

# Measurement of Electroweak Top Quark Production at DØ

by

Yun-Tse Tsai

Submitted in Partial Fulfillment  
of the Requirements for the Degree

Doctor of Philosophy

Supervised by

Professor Aran Garcia-Bellido

Department of Physics and Astronomy  
Arts, Sciences, and Engineering  
School of Arts and Sciences

University of Rochester  
Rochester, New York

2013

## Biographic Sketch

The author was born in Taipei, Taiwan on October 12th, 1982. She attended National Taiwan University in 2000, double majoring in Physics and Mathematics. She graduated with a Bachelor of Science and received the Dean's award in 2005. Based upon experimental research in particle physics, she earned a Master of Science in Physics in 2006, and soon thereafter came to the University of Rochester. After successful completion of the preliminary examination in September of 2007, she was awarded a Master of Arts in Physics in the following year. The author continued research in the field of particle physics under the supervision of Professor Aran Garcia-Bellido, which has culminated in this dissertation.

# Acknowledgments

I first thank my supervisor, Aran Garcia-Bellido, who has always guided me to the “big picture,” and provides helpful suggestions, comments, and encouragement.

I am extremely grateful to Ashok Das, who has always been kind, and willing to help me in every aspect of my studies.

I also thank the members of the  $D\bar{0}$  single-top group: Cecilia Gerber, Reinhard Schwienhorst, Ann Heinson, Victor Bazterra, and Liang Li, for their guidance in the single-top analyses, and Nathan, Mark, Jyoti, and Weigang for their cooperation in the work of the group. I am grateful to the  $D\bar{0}$  top group for the full analysis of the data: Andreas Jung, Viatcheslav Sharyy, Daniel Meister, and Oleksii Turkot, without whose assistance, the analysis would have taken a far longer time.

I also thank the  $D\bar{0}$  Matrix Element analyzers: Michael Wang and Yuji Enari for helping me in setting up the code, Gaston Gutierrez for providing me with the overall view of the method, and Thomas Gadfort and Zhenyu Ye for passing on to me their experience with these analyses. The Matrix Element analysis would not have succeeded without their help. And for the measurement of the cross section extraction, I am particularly grateful to Reinhard Schwienhorst for all the long discussions about the statistical methods. In addition, I thank Qizhong Li, who managed the  $D\bar{0}$  computing resources and helped me in my computing intensive work.

I thank Tom Ferbel and Amnon Harel of the  $D\bar{0}$  Rochester group, who offered many comments in my work. I am particularly thankful to Gianluca Petrillo, with whom I discussed many of the new ideas and the technical issues, for the friendship and assistance he has provided during my graduate career.

Last but not least, I thank my parents, my brother I-Chung, and all my friends for their support and confidence.

# Abstract

We present a new model-independent measurement of the electroweak single top-quark production cross section in proton-antiproton ( $p\bar{p}$ ) collisions at  $\sqrt{s} = 1.96$  TeV in  $9.7 \text{ fb}^{-1}$  of integrated luminosity collected with the DØ detector. Top quarks can be produced singly through the electroweak interaction when an off-shell (virtual)  $W$  boson in the  $s$ -channel decays to  $t\bar{b}$  quarks (“ $tb$ ” final state), or through the fusion of a virtual  $W$  boson with an incident virtual  $b$  quark in the  $t$ -channel to produce a top quark associated with a  $b$  and a first-generation quarks (“ $tqb$ ” final state). We select signal-like events, containing one energetic electron or muon, an imbalance in transverse momentum, and two or three jets, with one or two identified as candidates for originating from the fragmentation of  $b$  quarks. A discriminant based on the “Matrix Element” method is used to separate the signal from background, and a Bayesian approach is utilized to extract the cross sections for signals. The  $s$  and  $t$ -channel cross sections are extracted simultaneously, providing a way to measure both modes without assuming the Standard Model prediction for either. The  $s$  and  $t$ -channel cross sections for producing a single top quark are measured to be

$$\begin{aligned}\sigma(p\bar{p} \rightarrow tb + X) &= 1.13^{+0.37}_{-0.35} \text{ pb} \\ \sigma(p\bar{p} \rightarrow tqb + X) &= 2.14^{+0.55}_{-0.52} \text{ pb}.\end{aligned}$$

The probabilities to measure these values or larger of cross section in absence of signal are  $4.0 \times 10^{-4}$  for the  $s$ -channel and  $3.1 \times 10^{-6}$  for the  $t$ -channel, corresponding, respectively, to 3.4 and 4.5 standard deviation significance. These results are among the most accurate measurements to date, and are consistent with the expectations of the Standard Model of  $1.04 \pm 0.08$  and  $2.26 \pm 0.12$  pb, respectively.

## Contributors and Funding Sources

This work was supervised by Professor Aran Garcia-Bellido of the Department of Physics. The reconstruction algorithms described in Chapter 3 were developed by the DØ Algorithm and Physics Analyses Groups, with my contribution being the determination of the absolute calibration of the calorimeter response, which represents a sizable part of the correction to the energy scale for particles jets that is presented in Section 3.5.2. I covered a series of detector shifts during the data taking, with responsibility for data acquisition (DAQ) and the quality control of the central tracking system (tracker) from the end of 2009 to 2011, and was one of the on-call experts for the DAQ system from September 2010 to September 2011. The Monte Carlo (MC) simulations presented in this dissertation were generated by the DØ Common Sample Group. Part of the analysis code used in this dissertation was taken from the DØ top group, but I integrated this with my new code for use in future analyses.

My graduate study was supported by the University of Rochester and through a grant from the U.S. Department of Energy.

## Author's Contributions

My main contributions to the analysis of data commence with Chapter 5. I optimized the selection criteria to the signals, improved the MC modeling of signal and background contributions, and delivered the selected sample.

In addition to the Matrix Element (ME) method developed in previously by me colleagues, I established the  $t\bar{t}$  modeling, utilized the  $b$ -ID output information, and thereby improved its performance, as presented in Chapter 6. I also estimated the systematic uncertainties (Chapter 7), and, finally, extracted the results given in Chapter 8. I developed a discriminant sensitive to both the  $s$  and  $t$ -channel signals, which provides a way to measure both modes simultaneously without assuming the Standard Model prediction for either.

I measured the absolute response of the DØ calorimeter and contributed in calibrating jet energy scales, as presented in Appendix A.

# Table of Contents

<b>Biographic Sketch</b>	<b>ii</b>
<b>Acknowledgments</b>	<b>iii</b>
<b>Abstract</b>	<b>v</b>
<b>Contributors and Funding Sources</b>	<b>vi</b>
<b>Author's Contributions</b>	<b>vii</b>
<b>List of Tables</b>	<b>xv</b>
<b>List of Figures</b>	<b>xxi</b>
<b>List of Abbreviations</b>	<b>xxxvii</b>
<b>1 Introduction</b>	<b>1</b>
1.1 The Standard Model . . . . .	1
1.2 The Top Quark . . . . .	5
1.2.1 Production . . . . .	6
1.2.1.1 Strong Production of $t\bar{t}$ Pairs . . . . .	6
1.2.1.2 Electroweak Production of Top Quarks . . . . .	7
1.2.2 Decay . . . . .	10
1.3 Electroweak Top-Quark Production . . . . .	12
1.3.1 Motivation . . . . .	13

---

1.3.2	Event Signature . . . . .	16
1.3.3	Background Processes . . . . .	17
1.3.4	Analysis Overview . . . . .	21
<b>2</b>	<b>Experimental Apparatus</b>	<b>23</b>
2.1	The Tevatron Accelerator Complex . . . . .	23
2.1.1	The Initial Acceleration . . . . .	24
2.1.2	The Main Injector and The Antiproton Source . . . . .	24
2.1.3	The Tevatron . . . . .	25
2.2	The DØ Detector . . . . .	26
2.2.1	The Coordinate System . . . . .	26
2.2.2	The Tracking System . . . . .	28
2.2.3	The Calorimeter . . . . .	30
2.2.4	The Muon Spectrometer . . . . .	33
2.2.5	The Luminosity Monitor . . . . .	35
2.2.6	Trigger System and Data Acquisition . . . . .	36
<b>3</b>	<b>Object Reconstruction and Identification</b>	<b>38</b>
3.1	Tracks . . . . .	38
3.2	Primary Vertices . . . . .	39
3.3	Electrons . . . . .	40
3.4	Muons . . . . .	43
3.5	Jets . . . . .	45
3.5.1	Jet Reconstruction and Identification . . . . .	46
3.5.2	Jet Energy Scale . . . . .	48
3.6	Imbalance in Transverse Momentum . . . . .	49
3.7	$b$ Jets . . . . .	51
<b>4</b>	<b>Data and Simulation Samples</b>	<b>54</b>
4.1	Data Samples . . . . .	54
4.2	Monte Carlo Simulation . . . . .	55
4.3	Multijet Samples . . . . .	58

<b>5</b>	<b>Event Selection and Determination of Background</b>	<b>59</b>
5.1	Event Selection . . . . .	59
5.2	Modeling of the Simulated Samples . . . . .	62
5.2.1	Normalization of the NLO Cross Sections . . . . .	63
5.2.2	Monte Carlo Efficiency Corrections . . . . .	63
5.3	$W$ +Jets and Multijet Backgrounds . . . . .	65
5.4	Optimization of $b$ -ID . . . . .	68
5.5	Heavy-Flavor Scale Factor . . . . .	69
5.5.1	Extraction of Scale Factors . . . . .	73
5.5.2	Cross-Checks and Improvement on the Control Samples . .	76
5.5.3	Cross-Checks and Improvement Using Enriched Samples of $W$ +jets Events . . . . .	78
5.5.4	Cross-Checks for the Heavy-Flavor Scale Factor . . . . .	83
5.5.5	Cross-Checks and Improvement on the Signal Region . . .	86
5.5.6	Uncertainty for the Heavy Flavor Correction . . . . .	86
5.6	Comparison of Data with Simulation and Event Yields . . . . .	90
5.7	Total Acceptance for Signal $\mathcal{A}$ . . . . .	94
5.8	Cross-Check Samples . . . . .	98
<b>6</b>	<b>The Matrix Element Method</b>	<b>100</b>
6.1	General Concepts . . . . .	100
6.1.1	Probabilities . . . . .	101
6.1.2	Differential Cross Sections . . . . .	101
6.1.3	Description of Detector Response . . . . .	104
6.1.3.1	Jet Transfer Function . . . . .	105
6.1.3.2	Muon Transfer Function . . . . .	107
6.1.3.3	Electron Transfer Function . . . . .	108
6.1.3.4	Transfer Function for Jets Misidentified as Electrons	109
6.1.4	Normalization of the Differential Cross Section . . . . .	110
6.2	Implementation in Single Top-Quark Analysis . . . . .	111

6.2.1	Processes Parametrized via ME . . . . .	111
6.2.2	PDF and Factorization Scales . . . . .	114
6.2.3	The Phase Space . . . . .	114
6.2.3.1	The Dimensionality of Phase Space . . . . .	115
6.2.3.2	The Phase Space Transformation . . . . .	116
6.2.3.3	The Integration over Phase Space . . . . .	118
6.2.4	Modeling of $t\bar{t}$ Background . . . . .	118
6.2.4.1	Three Reconstructed Jets in $t\bar{t}$ Events . . . . .	119
6.2.4.2	Two Reconstructed Jets in $t\bar{t}$ Events . . . . .	121
6.3	Discriminants . . . . .	121
6.3.1	The ME Discriminant with $b$ -tagging Information . . . . .	123
6.3.1.1	The $P^{bl}$ -based Discriminant: Optimized for $t$ -channel	123
6.3.1.2	The B-weighted Discriminant: Optimized for $s$ - channel . . . . .	125
6.3.2	Transformation of Discriminant . . . . .	127
6.3.3	Performance of Discriminant and Output Distributions . .	128
6.3.4	Discriminant Performance on the Cross-Check Samples . .	130
<b>7</b>	<b>Systematic Uncertainties</b>	<b>136</b>
7.1	Normalization Systematic Uncertainties . . . . .	136
7.2	Shape-changing Systematic Uncertainties . . . . .	140
<b>8</b>	<b>Cross Section Measurement</b>	<b>143</b>
8.1	Bayesian Approach . . . . .	143
8.2	Calibration of the Method . . . . .	146
8.3	Expected Cross Section . . . . .	149
8.4	Measured Cross Section . . . . .	152
8.5	Model-independent Measurement . . . . .	155
8.6	Significance of Measurement . . . . .	157
<b>9</b>	<b>Conclusions and Outlook</b>	<b>166</b>

<b>Bibliography</b>	<b>169</b>
<b>A Absolute MPF Response Correction</b>	<b>183</b>
A.1 Missing $E_T$ Projection Fraction Method . . . . .	184
A.2 Corrections for Biases . . . . .	186
A.3 Results in the Data . . . . .	188
A.4 Uncertainties . . . . .	189
<b>B Trigger Efficiency Measurement</b>	<b>196</b>
<b>C Muon Angular Corrections</b>	<b>204</b>
C.1 Muon $\eta^{\text{det}}$ Corrections . . . . .	204
C.2 Muon Angular Cuts . . . . .	204
<b>D Control Plots</b>	<b>209</b>
<b>E Cross-Check Plots</b>	<b>221</b>
<b>F Differential Cross Section</b>	<b>224</b>
F.1 Hard Scatter Differential Cross Sections . . . . .	224
F.2 Phase Space . . . . .	225
F.3 Energy and Momentum Conservation and Neutrino Four-Momentum	226
F.4 The Full Integrals . . . . .	227
<b>G Supplements of Transfer Functions</b>	<b>229</b>
G.1 Jet . . . . .	229
G.2 Muons . . . . .	230
G.3 Electrons . . . . .	230
G.4 Fake Electrons . . . . .	243
<b>H The Normalization of the Probabilities</b>	<b>245</b>

<b>I</b>	<b>Integration Variable Remapping</b>	<b>248</b>
I.1	Jacobians . . . . .	248
I.1.1	Jacobian for Single Top-Quark Two-Jet Processes . . . . .	248
I.1.2	Jacobian for $W+2$ Jets Processes . . . . .	249
I.1.3	Jacobian for Diboson Two-Jet Processes . . . . .	249
I.1.4	Jacobian for $t\bar{t}$ Two-Jet Processes . . . . .	250
I.1.5	Jacobian for Single Top-Quark Three-Jet Processes . . . . .	251
I.1.6	Jacobian for $W+3$ Jets Processes . . . . .	252
I.1.7	Jacobian for $t\bar{t}$ 3 Jet Processes . . . . .	252
I.2	Jacobian Evaluation . . . . .	253
I.2.1	Jacobian about the $W$ mass squared, $s_{34}$ . . . . .	253
I.2.2	Jacobian about the top mass squared, $s_{345}$ . . . . .	255
I.2.3	Jacobian about the $Z$ (or the second $W$ ) mass squared, $s_{56}$ . . . . .	255
I.2.4	Jacobian about the second top mass squared, $s_{67}$ . . . . .	256
<b>J</b>	<b>Distribution Sampling</b>	<b>257</b>
J.1	Breit-Wigner Distribution Sampling . . . . .	257
J.2	Gaussian Distribution Sampling . . . . .	259
<b>K</b>	<b>The Yield Fractions in the Likelihood Functions</b>	<b>261</b>
<b>L</b>	<b>Different Types of Discriminants</b>	<b>267</b>
L.1	Basic Discriminant with no $b$ -ID Information . . . . .	267
L.2	$P^{bl}$ -based Matrix Element Discriminant . . . . .	267
L.3	$P^{bl \times bc}$ -based Matrix Element Discriminant . . . . .	268
L.4	B-weighted Matrix Element Discriminant . . . . .	268
L.5	$B^{bl \times bc}$ -weighted Matrix Element Discriminant . . . . .	268
L.6	CDF's Event Probability Discriminant . . . . .	268
L.7	Comparison of different discriminants . . . . .	269
<b>M</b>	<b>Updates from the Previous Matrix Element Analysis</b>	<b>273</b>

<b>N</b>	<b>Tables of the Normalization Systematic Uncertainties</b>	<b>275</b>
<b>O</b>	<b>Shape-Changing Systematic Uncertainties</b>	<b>284</b>

# List of Tables

1.1	The Standard Model fermions and their properties [1]. The electric charge is given in units of the charge of the electron. . . . .	3
1.2	The gauge bosons of the SM and their properties [1]. The electric charge is given in units of the charge of the electron. . . . .	3
1.3	Single top-quark cross sections . . . . .	11
1.4	Measured branching ratios for final states in $W$ boson decay [1]. .	11
4.1	Integrated luminosities for good quality data . . . . .	54
4.2	The parameters of the MC event generation. . . . .	56
4.3	Monte Carlo statistics . . . . .	57
5.1	Theoretical $K'$ -factors used to scale the ALPGEN background LLO calculations to NLO. . . . .	63
5.2	$\epsilon_{\text{fake-}\ell}$ and $\epsilon_{\text{real-}\ell}$ . . . . .	67
5.3	Matrix method yields . . . . .	67
5.4	The heavy-flavor correction factors . . . . .	75
5.5	Event yields in the control samples . . . . .	77
5.6	KS values and $\chi^2$ per bin of the JetBTagMVA distributions in two-jet control samples. . . . .	77
5.7	Event yields in the cross-check $W$ +jets samples . . . . .	79
5.8	KS values and $\chi^2$ per bin of the JetBTagMVA distributions in the $W$ +jets enriched ( $H_T < 175$ GeV) cross-check samples. . . . .	80
5.9	The heavy flavor scale factors derived with the three methods for the overall Run IIb and the combined electron and muon channels.	85

5.10	The heavy flavor scale factors derived with the second method, in which the event yields in the tagged and orthogonal samples are normalized to the data simultaneously, for the overall Run IIb and the combined electron and muon channels, but one-tagged and two-tagged samples separately. . . . .	85
5.11	Event yields in the signal samples . . . . .	86
5.12	KS values and $\chi^2$ per bin of the JetBTagMVA distributions in two-jet signal samples. . . . .	87
5.13	Pre-tagged event yields after selection. . . . .	91
5.14	Pre-tagged event yields with statistical uncertainty for each jet multiplicity and for all analysis channels combined. . . . .	92
5.15	Single-tagged event yields after selection. . . . .	93
5.16	Single-tagged event yields with statistical uncertainty for each jet multiplicity and for all analysis channels combined. . . . .	94
5.17	Double-tagged event yields after selection. . . . .	95
5.18	Double-tagged event yields with statistical uncertainty for each jet multiplicity and for all analysis channels combined. . . . .	96
5.19	Signal acceptances. . . . .	97
5.20	Combined signal acceptances. . . . .	97
5.21	Event yields after selection in the cross-check samples. . . . .	98
5.22	Event yields with statistical uncertainty in the cross-check samples, for all analysis channels combined. . . . .	99
6.1	The parton-level criteria applied in the phase space of the integration and in the MC samples. $q_i$ represents a final produced quark.	103
6.2	The detector level criteria applied in evaluating the normalization, corresponding to $\Theta_{acc}(x)$ . . . . .	110
6.3	The processes considered in this analysis in calculating signal and background ME probabilities. . . . .	112
6.4	Factorization scales used in the ME integrations and in MC samples.	115
6.5	The degrees of freedom in the ME integration. . . . .	116

6.6	The original and the transformed integration variables for each process. . . . .	117
6.7	The definitions of the signal and the background processes for each of the three signal-specific discriminants: $D_s$ , $D_t$ , and $D_{st}$ . . . . .	122
6.8	The $b$ -ID output weights implemented for jet-to-parton assignment for a process with two $b$ quarks in the final state, such as $tb$ . . . . .	124
6.9	The $b$ -ID output weights implemented for jet-to-parton assignment for a process with one $b$ and one light-flavored quarks in the final state, such as $tq$ . . . . .	124
6.10	The $b$ -ID output weights implemented for jet-to-parton assignment for a process with two light-flavored quarks in the final state, such as $Wgg$ . . . . .	125
6.11	The categories of the processes according to the number of the $b$ quarks in the final state. . . . .	126
7.1	A summary of the relative systematic uncertainties for each of the correction factors or normalizations. . . . .	142
8.1	The expected and observed significance computed using the asymptotic log-likelihood ratio approach. The $t$ -channel is assumed to have the cross section predicted in the SM when measuring the $s$ -channel cross section, and vice versa. . . . .	163
8.2	The expected and observed significance of the model-independent measurements. . . . .	163
A.1	Fitted parameters for the MPF response parameterization given in Equation (A.1.6). Run IIa parameterization is provided for reference.	188
G.1	Run IIa transfer-function parameters for light jets, $b$ jets, and soft muon tagged $b$ jets, for four regions of detector $ \eta $ . . . . .	234
G.2	Run IIb1 transfer-function parameters for light jets, $b$ jets, and soft muon tagged $b$ jets, for four regions of detector $ \eta $ . . . . .	235
G.3	Run IIb2 transfer-function parameters for light jets, $b$ jets, and soft muon tagged $b$ jets, for four regions of detector $ \eta $ . . . . .	236

G.4	Run IIb3 transfer-function parameters for light jets, $b$ jets, and soft muon tagged $b$ jets, for four regions of detector $ \eta $ . . . . .	237
G.5	Run IIa muon transfer-function parameters, for pre-2004-shutdown and post-2004-shutdown data taking periods, and for the cases with and without SMT hits associated with muon tracks. . . . .	241
G.6	Run IIb muon transfer-function parameters, for the cases with and without SMT hits associated with muon tracks. . . . .	241
G.7	The parameters of the fake electron transfer functions. . . . .	243
H.1	The normalization constants for the Run IIa samples. . . . .	245
H.2	The normalization constants for the Run IIb1 samples. . . . .	246
H.3	The normalization constants for the Run IIb2 samples. . . . .	246
H.4	The normalization constants for the Run IIb3 samples. . . . .	247
K.1	The coefficients, $c_i$ , of discriminants $D_s$ , $D_t$ , and $D_{st}$ for p17 two-jet single-tagged samples. . . . .	263
K.2	The coefficients, $c_i$ , of discriminants $D_s$ , $D_t$ , and $D_{st}$ for p17 three-jet single-tagged samples. . . . .	263
K.3	The coefficients, $c_i$ , of discriminants $D_s$ , $D_t$ , and $D_{st}$ for p17 two-jet double-tagged samples. . . . .	264
K.4	The coefficients, $c_i$ , of discriminants $D_s$ , $D_t$ , and $D_{st}$ for p17 three-jet double-tagged samples. . . . .	264
K.5	The coefficients, $c_i$ , of discriminants $D_s$ , $D_t$ , and $D_{st}$ for p20 two-jet single-tagged samples. . . . .	265
K.6	The coefficients, $c_i$ , of discriminants $D_s$ , $D_t$ , and $D_{st}$ for p20 three-jet single-tagged samples. . . . .	265
K.7	The coefficients, $c_i$ , of discriminants $D_s$ , $D_t$ , and $D_{st}$ for p20 two-jet double-tagged samples. . . . .	266
K.8	The coefficients, $c_i$ , of discriminants $D_s$ , $D_t$ , and $D_{st}$ for p20 three-jet double-tagged samples. . . . .	266
L.1	The summary table of the definitions of all the ME discriminants. . . . .	269

N.1	Systematic uncertainties for Run IIa Electron Channel Single-Tagged Two-Jet events. . . . .	276
N.2	Systematic uncertainties for Run IIa Electron Channel Double-Tagged Two-Jet events. . . . .	276
N.3	Systematic uncertainties for Run IIa Electron Channel Single-Tagged Three-Jet events. . . . .	277
N.4	Systematic uncertainties for Run IIa Electron Channel Double-Tagged Three-Jet events. . . . .	277
N.5	Systematic uncertainties for Run IIa Muon Channel Single-Tagged Two-Jet events. . . . .	278
N.6	Systematic uncertainties for Run IIa Muon Channel Double-Tagged Two-Jet events. . . . .	278
N.7	Systematic uncertainties for Run IIa Muon Channel Single-Tagged Three-Jet events. . . . .	279
N.8	Systematic uncertainties for Run IIa Muon Channel Double-Tagged Three-Jet events. . . . .	279
N.9	Systematic uncertainties for Run IIb Electron Channel Single-Tagged Two-Jet events. . . . .	280
N.10	Systematic uncertainties for Run IIb Electron Channel Double-Tagged Two-Jet events. . . . .	280
N.11	Systematic uncertainties for Run IIb Electron Channel Single-Tagged Three-Jet events. . . . .	281
N.12	Systematic uncertainties for Run IIb Electron Channel Double-Tagged Three-Jet events. . . . .	281
N.13	Systematic uncertainties for Run IIb Muon Channel Single-Tagged Two-Jet events. . . . .	282
N.14	Systematic uncertainties for Run IIb Muon Channel Double-Tagged Two-Jet events. . . . .	282
N.15	Systematic uncertainties for Run IIb Muon Channel Single-Tagged Three-Jet events. . . . .	283
N.16	Systematic uncertainties for Run IIb Muon Channel Double-Tagged Three-Jet events. . . . .	283

O.1	The yield differences on the shape-changing systematic uncertainties on the signals and the combined backgrounds. . . . .	285
-----	---	-----

# List of Figures

1.1	Representative leading-order Feynman diagrams for strong top-quark pair production from (a) quark annihilation ( $q\bar{q}$ ) and (b) gluon fusion ( $gg$ ) [2]. . . . .	7
1.2	Representative leading-order Feynman diagrams for electroweak single top-quark production for (a) $s$ -channel “ $tb$ ” mode, (b), (c), and (d) $t$ -channel “ $tqb$ ” modes, and (e) associated “ $tW$ ” mode. Diagrams with off-diagonal CKM matrix elements, such as $Wt\bar{s}$ or $Wt\bar{d}$ vertices, are suppressed due to the small values of their CKM matrix elements [2]. . . . .	9
1.3	The top quark decay and the final state, where $q$ and $\bar{q}'$ represents the quark and antiquark in the first and second generations [2]. .	12
1.4	Nomenclature for $t\bar{t}$ final states [2]. . . . .	12
1.5	Representative Feynman diagrams of single top-quark production, indicating the origin of the proportionality of the production cross section on $ V_{tb} ^2$ of the $Wtb$ vertex [2]. . . . .	13
1.6	Posterior probability density for $t$ -channel vs $s$ -channel single top-quark production in contours of equal probability density. The measured cross section and several theoretical predictions for new physics are shown for comparison. CL values represent the level of confidence for the previous measurement [3]. . . . .	15
1.7	Representative Feynman diagrams for $s$ -channel single top-quark production via a new boson: (a) a charged Higgs boson, and (b) a heavy $W'$ boson [2]. . . . .	15

1.8	Illustration for the final states in single top-quark events: (a) $s$ -channel, and (b) $t$ -channel [2]. The $b(\bar{b})$ quark from gluon splitting in the $t$ -channel is generally emitted along the beampipe and is not reconstructed. . . . .	16
1.9	Kinematic distributions of (a) transverse momentum ( $p_T$ ), and (b) the signed pseudorapidity ( $\eta \times Q(\text{electric charge of lepton})$ ) of partons in $t$ -channel single top-quark events, from the COMPHEP-SINGLETOP Monte Carlo simulation [4]. The contributions from $t$ and $\bar{t}$ events are antisymmetric in $\eta$ , and $\eta \times Q$ effectively flips and adds the contributions for antileptons and leptons in these events. . . . .	17
1.10	Illustration of the production cross sections for single top quarks and other processes [5]. The right $y$ -axis shows the cross sections relative to the single top-quark cross section. For details, see Table 4.3. . . . .	18
1.11	Representative Feynman diagrams for $W$ -boson production in association with quarks and gluons: (a) $Wb\bar{b}$ , (b) $Wb\bar{b}g$ , and (c) $Wq\bar{q}'g$ [2]. Among the (c) $Wq\bar{q}'g$ events, the light-flavored jet from gluon splitting can be misidentified as a $b$ -jet, and such events will pass our single top-quark selection criteria. . . . .	19
1.12	Illustration of multijet event production and misinterpretation [2].	20
1.13	Illustration of (a) $Z$ +jets and (b) $WW$ diboson production [2]. . .	20
2.1	A schematic overview of the Tevatron accelerator complex [6]. . .	24
2.2	Schematic profile of the DØ detector [7]. . . . .	27
2.3	Schematic profile of the central tracking system [7]. . . . .	28
2.4	The arrangement of the Silicon Microstrip Tracker [8]. . . . .	29
2.5	Isometric view of the central and two end calorimeters [8]. . . . .	31
2.6	Cross section of one quarter of the calorimeter [8]. Towers of different cell size are shown projected to the center of the detector. .	32
2.7	Exploded view of the muon drift-tube system [8]. . . . .	34
2.8	Exploded view of muon scintillation-detector system [8]. . . . .	35
2.9	Schematic overview of the trigger system. . . . .	36

3.1	An event display showing an electron, a muon, two $b$ -tagged jets, and the missing energy [9]. . . . .	40
3.2	An event display showing the presence of a muon [10]. . . . .	44
3.3	A schematic overview of the hadronization of a parton and the form of a jet [11]. . . . .	46
3.4	The absolute response of the calorimeter as a function of the jet energy. The details are described in Appendix A. . . . .	49
3.5	Examples of Jet energy scale (a) correction and (b) uncertainty for data as a function of jet pseudorapidity for $R_{\text{cone}} = 0.5$ jets [12]. .	50
3.6	Illustration of the secondary vertex [13]. . . . .	52
3.7	Examples of the $b$ -tagging input variables: (a) Counting Signed Impact Parameter Tagger (CSIP), (b) Jet Lifetime Probability (JLIP), and (c) the $\chi^2$ per degree of freedom of the secondary vertex (SVT $\chi^2_{\text{dof}}$ ) [14]. . . . .	52
3.8	The estimated $b$ -tagging efficiency of light-flavored jets parametrized in the central calorimeter (CC, continuous line), intercryostat detector (ICR, dot-dashed line) and end calorimeter (EC, dot-dot-dashed line) for the L2 (a) and Tight (b) operating points. The dotted black lines represent the fit uncertainty [14]. . . . .	53
5.1	The $\epsilon_{\text{fake-}\ell}$ for the inclusive $\geq 2$ jet bin versus the electron (left) and muon (right) $p_T$ [15]. . . . .	66
5.2	The figure of merit, $s/\sqrt{b}$ , versus the $b$ -tagging cut for the double-tagged sample (left) and the single-tagged sample (right). . . . .	69
5.3	The JetBTagMVA distributions for Run IIb e+jets (a) one-tag two-jet and (b) two-tag two-jet channels. . . . .	70
5.4	The JetBTagMVA distributions for Run IIb e+jets (a) one-tag two-jet and (b) two-tag two-jet $W$ +Jets enriched ( $H_T < 175$ GeV) samples. . . . .	71
5.5	The JetBTagMVA distributions for Run IIb e+jets (a) one-tag three-jet and (b) two-tag three-jet channels. . . . .	72
5.6	The JetBTagMVA distributions for Run IIb e+jets tagged (at least one tagged) three-jet $t\bar{t}$ enriched samples. . . . .	72

5.7	ME discriminant without the correction in the control region, for electron and muon combined, one-tag (left) and two-tag (right) channels. . . . .	74
5.8	The JetBTagMVA distributions in the control samples for (a) one-tag two-jet, and (b) two-tag two-jet channels, without the new heavy-flavor correction (left column) and with the correction (right column). . . . .	75
5.9	JetBTagMVA distributions in one-tag two-jet control samples, without (upper row) and with (lower row) the heavy-flavor correction. . . . .	78
5.10	JetBTagMVA distributions in two-tag two-jet control samples, without (upper row) and with (lower row) the heavy-flavor correction. . . . .	79
5.11	The background-subtracted data in the control sample, without (upper row) and with (lower row) the heavy-flavor correction, for one-tag (left) and two-tag (right) channels. . . . .	80
5.12	JetBTagMVA distributions in the $W$ +jets enriched cross-check samples and one-tag channel, without (upper row) and with (lower row) the heavy-flavor correction. . . . .	81
5.13	JetBTagMVA distributions in the $W$ +jets enriched cross-check samples and two-tag channel, without (upper row) and with (lower row) the heavy-flavor correction. . . . .	82
5.14	Heavy flavor scale factors (measured with the second method) versus $b$ -ID operating points without (left) and with (right) the heavy-flavor correction, for the overall Run IIb and the combined electron and muon channels, but one-tagged, two-tagged, and inclusive tagged samples separately. . . . .	85
5.15	JetBTagMVA distributions in one-tag two-jet signal samples, without (upper row) and with (lower row) the heavy-flavor correction. . . . .	88
5.16	JetBTagMVA distributions in two-tag two-jet signal samples, without (upper row) and with (lower row) the heavy-flavor correction. . . . .	89
5.17	The background-subtracted data in the signal sample, without (upper row) and with (lower row) the heavy-flavor correction. . . . .	90
5.18	Plot key. . . . .	92

5.19	The transverse mass of the $W$ boson from the top quark for pre-tagged (left), single-tagged (central), and double-tagged (right) for Run IIb, electron channel, two-jet events. . . . .	93
5.20	The transverse mass of the $W$ boson for $W$ +jets (left) and $t\bar{t}$ (right) enriched samples, for the Run IIb electron channel. . . . .	99
6.1	Schematic representation of the ME method . . . . .	103
6.2	Distributions in $\Delta E = E_{jet} - E_{parton}$ for $b$ quarks in the range $ \eta^{\text{det}}  < 0.4$ . . . . .	106
6.3	Representative Feynman diagrams corresponding to single top quark, with two jets in the final state: $u\bar{d} \rightarrow tb$ (left), and $u\bar{b} \rightarrow tq$ (right). . . . .	112
6.4	Representative Feynman diagrams corresponding to background with two jets in the final state: starting with the upper left, they are $u\bar{d} \rightarrow Wbb$ , $sg \rightarrow Wcg$ , $u\bar{d} \rightarrow Wgg$ , $u\bar{u} \rightarrow WW$ , $u\bar{d} \rightarrow WZ$ , $gg \rightarrow ggg$ , and $u\bar{u} \rightarrow t\bar{t}$ processes. . . . .	113
6.5	Representative Feynman diagrams corresponding to single top-quark, with three jets in the final state: $u\bar{d} \rightarrow tbq$ (left), $ug \rightarrow tqb$ (central), and $ub \rightarrow tqg$ (right). . . . .	114
6.6	Representative Feynman diagrams corresponding to the backgrounds with three jets in the final state: $u\bar{d} \rightarrow Wbbg$ (left), $dg \rightarrow Wugg$ (central), and $u\bar{u} \rightarrow t\bar{t}$ (right). . . . .	114
6.7	Monte Carlo distributions in $p_T$ (left) and $\eta$ (right) for $b$ and light quarks in $t\bar{t}$ events that are matched to reconstructed jets (“Reco b” and “Reco l”), and for (“Missing b” and “Missing l”) from a $t\bar{t}$ ALPGEN sample with full $D\bar{O}$ reconstruction. . . . .	120
6.8	MC distributions in energy for (i) $W$ bosons that decay into $q'\bar{q}$ , but provide only one reconstructed decay product ( $W$ parton), (ii) the partons from this $W$ decay that are reconstructed (Matched Parton), and (iii) the corresponding reconstructed jets (Matched jet). . . . .	120
6.9	The priors for unobserved $W$ bosons for $t\bar{t}$ events containing two jets in the final states. . . . .	121
6.10	The $s$ -channel B-MED for signal and background before (left) and after (central) the bin transformation, and the transformation function (right). . . . .	127

- 6.11 The data-MC comparisons of the  $s$ -channel B-MED for the Run II electron and muon combined samples. The first and the second rows show the results of the two-jet and the three-jet events, respectively. The left, the central and the right columns show the results of the single-tagged, the double-tagged, and the combined-tagged events. The signal is normalized to the SM expectation. . . . . 128
- 6.12 The data-MC comparisons of the  $s$ -channel B-MED with log scale for the Run II electron and muon combined samples. The first and the second rows show the results of the two-jet and the three-jet events, respectively. The left, the central and the right columns show the results of the single-tagged, the double-tagged, and the combined-tagged events. The signal is normalized to the SM expectation. . . . . 129
- 6.13 The data-MC comparisons of the  $t$ -channel  $P^{bl}$ -MED for the Run II electron and muon combined samples. The first and the second rows show the results of the two-jet and the three-jet events, respectively. The left, the central and the right columns show the results of the single-tagged, the double-tagged, and the combined-tagged events. The signal is normalized to the SM expectation. . . . . 129
- 6.14 The data-MC comparisons of the  $t$ -channel  $P^{bl}$ -MED for the Run II electron and muon combined samples. The first and the second rows show the results of the two-jet and the three-jet events, respectively. The left, the central and the right columns show the results of the single-tagged, the double-tagged, and the combined-tagged events. The signal is normalized to the SM expectation. . . . . 130
- 6.15 Individual background rejection vs signal efficiency of the  $s$ -channel B-MED for the Run II electron and muon combined samples. The first and the second rows show the results of the two-jet and the three-jet events, respectively. The left column shows the results of the single-tagged events, while the right column the double-tagged ones. . . . . 131

6.16	Individual background rejection vs signal efficiency of the $t$ -channel $P^{bl}$ _MED for the Run II electron and muon combined samples. The first and the second rows show the results of the two-jet and the three-jet events, respectively. The left column shows the results of the single-tagged events, while the right column the double-tagged ones. . . . .	132
6.17	Comparisons of B-MED outputs for the $s$ -channel signal and the individual backgrounds for Run II, combining electron and muon channels for two-jet doubly- $b$ -tagged events. . . . .	133
6.18	Comparisons of $P^{bl}$ _MED outputs in the $t$ -channel signal and the individual backgrounds for Run II, combining electron and muon channels two-jet singly- $b$ -tagged events. . . . .	134
6.19	Data and MC comparisons for the $s$ -channel B-MED for the combined electron and muon $W$ +jets cross-check event sample. The left, the central and the right panels show the results of the single-tagged, the double-tagged, and the combined-tagged events, respectively. . . . .	134
6.20	Data and MC comparisons for the $s$ -channel B-MED for the combined electron and muon $t\bar{t}$ cross-check event sample. The left, the central and the right panels show the results of the single-tagged, the double-tagged, and the combined-tagged events, respectively. .	135
6.21	Data and MC comparisons for the $t$ -channel $P^{bl}$ _MED for the combined electron and muon $W$ +jets cross-check event sample. The left, the central and the right panels show the results of the single-tagged, the double-tagged, and the combined-tagged events, respectively. . . . .	135
6.22	Data and MC comparisons for the $t$ -channel $P^{bl}$ _MED for the combined electron and muon $t\bar{t}$ cross-check event sample. The left, the central and the right panels show the results of the single-tagged, the double-tagged, and the combined-tagged events, respectively. .	135
7.1	The effects of the shape-changing systematic uncertainties on the ME discriminant for Run IIb e+jets two-jet double-tagged sample.	141

- 8.1 An example of the posterior probability density function. The mode (peak position) is the measured value, while the width is the uncertainty. . . . . 146
- 8.2 An example of shape-changing systematic uncertainties. In each bin, the prior p.d.f.  $\pi(\mathbf{a}, \mathbf{b})$  is sampled as a Gaussian with different positive and negative widths,  $\delta_{ibin}^+$  and  $\delta_{ibin}^-$ , and with the mean equal to the predicted yields of the nominal sample. . . . . 147
- 8.3 Each plot contains 10,000 entries, consisting of the peak of the posterior p.d.f. for each pseudo-data sample for the  $s$ -channel. The ensemble average of the measured cross sections is written in each plot, and it follows the different injected signal cross sections. The input cross sections are 0.5 pb (top left), 0.75 pb (top right), 1.04 pb (the SM prediction, middle left), 1.5 pb (middle right), 2.5 pb (bottom left), 3.5 pb (bottom right). . . . . 148
- 8.4 The ensemble average of measured cross section as a function of the input  $s$ -channel cross sections. The band shows the ensemble average of the 68% intervals of the posteriors, and this interval is used as the uncertainty of the value of the cross section in the fit. 149
- 8.5 Each plot contains 10,000 entries, consisting of the peak of the posterior p.d.f. for each pseudo-data sample for the  $t$ -channel. The ensemble average of the measured cross sections is written in each plot, and it follows the different injected signal cross sections. The input cross sections are 1.5 pb (top left), 2 pb (top right,) 2.26 pb (the SM prediction, middle left), 3.5 pb (middle right), 5 pb (bottom left), 7 pb (bottom right). . . . . 150
- 8.6 The ensemble average of measured cross section as a function of the input  $t$ -channel cross sections. The band shows the ensemble average of the 68% intervals of the posteriors, and this interval is used as the uncertainty of the value of the cross section in the fit. 151
- 8.7 Distributions of the measured cross sections (left), the measured negative uncertainties (central), and the measured positive uncertainties (right) for the  $s$ -channel B-MED pseudo-data samples, where the SM cross section, 1.04 pb, is used as the input signal cross section. 151

8.8	Distributions of the measured cross sections (left), the measured negative uncertainties (central), and the measured positive uncertainties (right) for the $t$ -channel $P^{bl}$ _MED pseudo-data samples, where the SM cross section, 2.26pb, is used as the input signal cross section. . . . .	151
8.9	Measured result for $s$ -channel single top-quark cross section measurement. . . . .	152
8.10	Measured result for $t$ -channel single top-quark cross section measurement. . . . .	153
8.11	The data-MC comparisons of the $s$ -channel B-MED for the overall Run II data, with all the analysis channels combined. The left figure shows the overall region, while the right figure zooms into the signal-enriched region. The hatched area is the posterior $\pm 1$ SD uncertainty on the total background prediction. The signal contribution is scaled to the measured result. . . . .	153
8.12	The data-MC comparisons of the $t$ -channel $P^{bl}$ _MED for the overall Run II data, with all the analysis channels combined. The left figure shows the overall region, while the right figure zooms into the signal-enriched region. The hatched area is the posterior $\pm 1$ SD uncertainty on the total background prediction. The signal contribution is scaled to the measured result. . . . .	154
8.13	The posterior $\pm 1$ SD uncertainty on the background prediction versus the ME discriminant output for (a) $s$ -channel and (b) $t$ -channel. . . . .	154
8.14	The data after subtracting the background versus (a) $s$ -channel and (b) $t$ -channel ME discriminants. The signal contributions are scaled to the measured cross sections. The hatched bands show the posterior uncertainty on the background prediction, and both the $s$ and $t$ -channel contributions are visible above the $\pm 1$ SD hatched band. . . . .	155

8.15	The data-MC comparisons of the mixed discriminant with log scale for the Run II electron and muon combined samples. The upper and lower rows show the results of the two-jet and the three-jet events, respectively. The left and right columns show the results of the single-tagged and the double-tagged events. The bins between 0 and 1 show the $s$ -like category, while the bins between 1 and 2 show the $t$ -like category. The $s$ and $t$ -channel contributions are scaled to the measured results. . . . .	156
8.16	Expected results for model-independent measurements on the $s$ and $t$ -channel cross sections: (a) 2D posterior p.d.f., shown along with the 1, 2 and 3 SD contours of probability, (b) 1D posterior p.d.f. for the $s$ -channel, and (c) 1D posterior p.d.f. for the $t$ -channel. . .	158
8.17	Observed results for model-independent measurements on the $s$ and $t$ -channel cross sections: (a) 2D posterior p.d.f., shown along with the 1, 2 and 3 SD contours of probability, (b) 1D posterior p.d.f. for the $s$ -channel, and (c) 1D posterior p.d.f. for the $t$ -channel. . .	159
8.18	Significance of $s$ -channel cross section measurement. The $t$ -channel is assumed to have the cross section predicted in the SM. . . . .	164
8.19	Significance of $t$ -channel cross section measurement. The $s$ -channel is assumed to have the cross section predicted in the SM. . . . .	164
8.20	Significance of the model-independent $s$ -channel cross section measurement. . . . .	165
8.21	Significance of the model-independent $t$ -channel cross section measurement. . . . .	165
9.1	Correlation expected for cross sections based on MC studies of pairs of discriminants: (a) BDT vs ME, (b) BNN vs ME, and (c) BDT vs BNN [16]. . . . .	167
A.1	Absolute MPF response for $R_{\text{cone}} = 0.7$ jets (left) and for $R_{\text{cone}} = 0.5$ jets (right) as a function of $E'$ . The solid lines indicate the fit to the function in Equation (A.1.6). The lower plots show the relative difference of the points with respect to the fitted function of the overall Run IIb data. . . . .	189

A.2	Absolute MPF response for $R_{\text{cone}} = 0.7$ jets as a function of $E'$ . The solid lines indicate the fit to the function in Equation (A.1.6). The lower plots show the relative difference of the points with respect to the fitted function, with a yellow band showing statistical uncertainty of the fit. . . . .	190
A.3	Absolute MPF response for $R_{\text{cone}} = 0.5$ jets as a function of $E'$ . The solid lines indicate the fit to the function in Equation (A.1.6). The lower plots show the relative difference of the points with respect to the fitted function. . . . .	191
A.4	Comparison of absolute responses measured with Run IIb1 and Run IIb4 data using the events with exactly one primary vertex. .	192
A.5	The relative difference of the absolute MPF responses for $R_{\text{cone}} = 0.7$ jets (left) and for $R_{\text{cone}} = 0.5$ jets (right) as a function of $E'$ . The solid lines indicate the fit to the function in Equation (A.1.6). The yellow band shows the statistic uncertainty of the overall Run IIb fit.	192
A.6	Relative uncertainties on the absolute MPF response measurement in data for $R_{\text{cone}} = 0.7$ jets as a function of $E'$ . . . . .	193
A.7	Relative uncertainties on the absolute MPF response measurement in data for $R_{\text{cone}} = 0.5$ jets as a function of $E'$ . . . . .	194
B.1	Run IIb1 electron channel: Ratios of Super-OR fired events to the inclusive trigger fired events in “Data-multijet” (left column); ratios of Super-OR corrected MC yields to the 100% MC yields (central column); ratios of the previous two ratios, namely the inclusive trigger efficiency (right column). The rows show these ratios for the six chosen variables. . . . .	198
B.2	Run IIb1 muon channel: Ratios of Super-OR fired events to the inclusive trigger fired events in “Data-multijet” (left column); ratios of Super-OR corrected MC yields to the 100% MC yields (central column); ratios of the previous two ratios, namely the inclusive trigger efficiency (right column). The rows show these ratios for the six chosen variables. . . . .	199

B.3	Run I Ib2 electron channel: Ratios of Super-OR fired events to the inclusive trigger fired events in “Data-multijet” (left column); ratios of Super-OR corrected MC yields to the 100% MC yields (central column); ratios of the previous two ratios, namely the inclusive trigger efficiency (right column). The rows show these ratios for the six chosen variables. . . . .	200
B.4	Run I Ib2 muon channel: Ratios of Super-OR fired events to the inclusive trigger fired events in “Data-multijet” (left column); ratios of Super-OR corrected MC yields to the 100% MC yields (central column); ratios of the previous two ratios, namely the inclusive trigger efficiency (right column). The rows show these ratios for the six chosen variables. . . . .	201
B.5	Run I Ib3 electron channel: Ratios of Super-OR fired events to the inclusive trigger fired events in “Data-multijet” (left column); ratios of Super-OR corrected MC yields to the 100% MC yields (central column); ratios of the previous two ratios, namely the inclusive trigger efficiency (right column). The rows show these ratios for the six chosen variables. . . . .	202
B.6	Run I Ib3 muon channel: Ratios of Super-OR fired events to the inclusive trigger fired events in “Data-multijet” (left column); ratios of Super-OR corrected MC yields to the 100% MC yields (central column); ratios of the previous two ratios, namely the inclusive trigger efficiency (right column). The rows show these ratios for the six chosen variables. . . . .	203
C.1	The muon detector $\eta$ distributions for the Run I Ib2 two-jet samples. The left plot shows the distribution before the bin-by-bin muon detector $\eta$ reweighting, while the right one shows the one after the reweighting. As indicated in these plots, the data-MC agreement is improved after reweighting. . . . .	204
C.2	The mismodeled $\Delta\phi(\mu, \cancel{E}_T)$ distribution for Run I Ib muon two-jet channel at the pre-tagged stage. All the Run I Ib1, I Ib2, and I Ib3 simulation have the same features. . . . .	205
C.3	The muon related variables for the Run I Ib2 muon two-jet channel.	206

C.4	The $\Delta\phi(\mu, \cancel{E}_T)$ and Lepton $\eta^{\text{det}}$ with the cut Lepton $\chi^2$ Probability $> 0.05$ . The simulation improves. . . . .	207
C.5	Events with $\Delta\phi(\mu, \cancel{E}_T) > 2.95$ . . . . .	207
C.6	Two-dimensional distributions: The muon track curvature significance versus $\Delta\phi(\mu, \cancel{E}_T)$ (upper row), and the $\Delta\phi(\mu, \cancel{E}_T)$ versus the lepton $\eta^{\text{det}}$ (lower row), for the data (left column), the $tb$ signal (central column), and $wlp$ simulated sample (right column). . . .	208
C.7	The distributions of $\Delta\phi(\mu, \cancel{E}_T)$ and Lepton $\eta^{\text{det}}$ with the final triangle and trapezoid cuts. . . . .	208
D.1	The transverse momentum of the lepton for pre-tagged (left), single-tagged (central), and double-tagged (right) for Run IIb, electron and muon channels, two-jet and three-jet events. . . . .	210
D.2	The pseudorapidity of the lepton for pre-tagged (left), single-tagged (central), and double-tagged (right) for Run IIb, electron and muon channels, two-jet and three-jet events. . . . .	211
D.3	The missing transverse energy for pre-tagged (left), single-tagged (central), and double-tagged (right) for Run IIb, electron and muon channels, two-jet and three-jet events. . . . .	212
D.4	The transverse energy of the leading jet for pre-tagged (left), single-tagged (central), and double-tagged (right) for Run IIb, electron and muon channels, two-jet and three-jet events. . . . .	213
D.5	The transverse energy of the second leading jet for pre-tagged (left), single-tagged (central), and double-tagged (right) for Run IIb, electron and muon channels, two-jet and three-jet events. . . . .	214
D.6	The pseudorapidity of the leading jet for pre-tagged (left), single-tagged (central), and double-tagged (right) for Run IIb, electron and muon channels, two-jet and three-jet events. . . . .	215
D.7	The pseudorapidity of the second leading jet for pre-tagged (left), single-tagged (central), and double-tagged (right) for Run IIb, electron and muon channels, two-jet and three-jet events. . . . .	216
D.8	The scalar transverse energy sum for pre-tagged (left), single-tagged (central), and double-tagged (right) for Run IIb, electron and muon channels, two-jet and three-jet events. . . . .	217

D.9	The pseudorapidity of the light quark jet times lepton charge for single-tagged (left) and double-tagged (right) for Run IIb, electron and muon channels, two-jet and three-jet events. . . . .	218
D.10	The angular distance $\Delta R$ between the leading two jets for pre-tagged (left), single-tagged (central), and double-tagged (right) for Run IIb, electron and muon channels, two-jet and three-jet events. . . . .	219
D.11	The transverse mass of the $W$ boson from the top quark for pre-tagged (left), single-tagged (central), and double-tagged (right) for Run IIb, electron and muon channels, two-jet and three-jet events. . . . .	220
E.1	Cross-check plots for several variables in the $W$ +Jets enriched samples. . . . .	222
E.2	Cross-check plots for several variables in the $t\bar{t}$ enriched samples. . . . .	223
G.1	Distributions in $\Delta E$ and transfer functions for light quarks in the range $ \eta^{\text{det}}  < 0.4$ for Run IIb1. . . . .	231
G.2	Distributions in $\Delta E$ and transfer functions for $b$ quarks in the range $ \eta^{\text{det}}  < 0.4$ for Run IIb1. . . . .	232
G.3	Distributions in $\Delta E$ and transfer functions for $b$ quarks with soft muons in the range $ \eta^{\text{det}}  < 0.4$ for Run IIb1. . . . .	233
G.4	Transfer functions for light quark jets for different parton energies and for the following detector regions: (1) $ \eta^{\text{det}}  < 0.4$ , (2) $0.4 <  \eta^{\text{det}}  < 0.8$ , (3) $0.8 <  \eta^{\text{det}}  < 1.6$ , (4) $1.6 <  \eta^{\text{det}}  < 2.5$ . . . . .	238
G.5	Transfer functions for $b$ quark jets for different parton energies and for the following detector regions: (1) $ \eta^{\text{det}}  < 0.4$ , (2) $0.4 <  \eta^{\text{det}}  < 0.8$ , (3) $0.8 <  \eta^{\text{det}}  < 1.6$ , (4) $1.6 <  \eta^{\text{det}}  < 2.5$ . . . . .	239
G.6	Transfer functions for light quark jets for different parton energies and for the following detector regions: (1) $ \eta^{\text{det}}  < 0.4$ , (2) $0.4 <  \eta^{\text{det}}  < 0.8$ , (3) $0.8 <  \eta^{\text{det}}  < 1.6$ , (4) $1.6 <  \eta^{\text{det}}  < 2.5$ . . . . .	240
G.7	The muon transfer functions for different parton transverse momenta for Run IIb; the upper plots are the transfer functions with SMT hits, while the lower plots are the ones without SMT hits. . . . .	242
G.8	The electron transfer functions for different true electron energies. . . . .	243
G.9	The fake electron transfer functions for different parton energies. . . . .	244

L.1	Background rejection vs signal efficiency of the $s$ -channel discriminant for the Run II electron and muon combined samples. The first and the second rows show the results of the two-jet and the three-jet events, respectively. The left column shows the results of the single-tagged events, while the right column the double-tagged ones. The $P^{bl \times bc}$ discriminant is not plotted, for it is very similar to the $P^{bl}$ discriminant. . . . .	270
L.2	The figure of merit, $s/\sqrt{b}$ vs the cutoff on discriminants, of the $s$ -channel discriminant for the Run II electron and muon combined samples. The first and the second rows show the results of the two-jet and the three-jet events, respectively. The left column shows the results of the single-tagged events, while the right column the double-tagged ones. The $P^{bl \times bc}$ discriminant is not plotted, for it is very similar to the $P^{bl}$ discriminant. . . . .	271
O.1	The effects of the shape-changing systematic uncertainties on the ME $tb$ discriminant for Run IIa e+jets two-jet single-tagged sample.	286
O.2	The effects of the shape-changing systematic uncertainties on the ME $tb$ discriminant for Run IIa e+jets two-jet double-tagged sample.	286
O.3	The effects of the shape-changing systematic uncertainties on the ME $tb$ discriminant for Run IIa e+jets three-jet single-tagged sample.	287
O.4	The effects of the shape-changing systematic uncertainties on the ME $tb$ discriminant for Run IIa e+jets three-jet double-tagged sample.	287
O.5	The effects of the shape-changing systematic uncertainties on the ME $tb$ discriminant for Run IIa $\mu$ +jets two-jet single-tagged sample.	288
O.6	The effects of the shape-changing systematic uncertainties on the ME $tb$ discriminant for Run IIa $\mu$ +jets two-jet double-tagged sample.	288
O.7	The effects of the shape-changing systematic uncertainties on the ME $tb$ discriminant for Run IIa $\mu$ +jets three-jet single-tagged sample.	289
O.8	The effects of the shape-changing systematic uncertainties on the ME $tb$ discriminant for Run IIa $\mu$ +jets three-jet double-tagged sample. . . . .	289
O.9	The effects of the shape-changing systematic uncertainties on the ME $tb$ discriminant for Run IIb e+jets two-jet single-tagged sample.	290

O.10	The effects of the shape-changing systematic uncertainties on the ME $tb$ discriminant for Run IIb $e$ +jets two-jet double-tagged sample.	290
O.11	The effects of the shape-changing systematic uncertainties on the ME $tb$ discriminant for Run IIb $e$ +jets three-jet single-tagged sample.	291
O.12	The effects of the shape-changing systematic uncertainties on the ME $tb$ discriminant for Run IIb $e$ +jets three-jet double-tagged sample.	292
O.13	The effects of the shape-changing systematic uncertainties on the ME $tb$ discriminant for Run IIb $\mu$ +jets two-jet single-tagged sample.	293
O.14	The effects of the shape-changing systematic uncertainties on the ME $tb$ discriminant for Run IIb $\mu$ +jets two-jet double-tagged sample.	293
O.15	The effects of the shape-changing systematic uncertainties on the ME $tb$ discriminant for Run IIb $\mu$ +jets three-jet single-tagged sample.	294
O.16	The effects of the shape-changing systematic uncertainties on the ME $tb$ discriminant for Run IIb $\mu$ +jets three-jet double-tagged sam- ple. . . . .	295

# List of Abbreviations

$\eta^{\text{det}}$	Detector Pseudorapidity
$\ell$	Electron or Muon
$\eta$	Pseudorapidity
$\cancel{E}_T$	Imbalance in Transverse Momentum
$\nu$	Neutrino
$\phi$	Azimuthal Angle in the Transverse Plane
$\mathbf{p}$	Vector Momentum
$p_T$	Transverse Momentum
$p_{tot}^z$	Longitudinal Momentum of the Total System in the Lab Frame
$\sigma$	Cross section
$CP$ -violation	Charge Conjugation and Parity violation
$dca$	Transverse Impact Parameter, or Distance of Closest Approach in the Transverse Plane
$E$	Energy
$p^z$	Longitudinal Momentum Component
$q$	Quark
AA	Alternate Algorithm
AC	Angular Corrections
ATLAS	A Toroidal LHC Apparatus
BDT	Boosted Decision Trees
BTag	$b$ -tagging Efficiency Correction Factor
CC	Central Calorimeter
CDF	Collider Detector Facility
CFT	Central Fiber Tracker
CH Calorimeter	Coarse Hadronic Calorimeter
CKM matrix	Cabibbo-Kobayashi-Maskawa matrix
CMS	Compact Muon Solenoid

---

CPS	Central Preshower Detector
CSIP	Counting Signed Impact Parameter Tagger
CTT	Central Track Trigger
EC	Endcap Calorimeter
EM Calorimeter	Electromagnetic Calorimeter
EW	Electroweak
FCNC	Flavor-changing neutral current
FH Calorimeter	Fine Hadronic Calorimeter
FPS	Forward Preshower Detector
GeV	Gega Electronvolt, equivalent to $1.602176565(35) \times 10^{10}$ Joule. In this dissertation, $\hbar$ and $c$ are set to be 1, and GeV also represents masses and momenta, instead of $\text{GeV}/c^2$ and $\text{GeV}/c$ . 1 GeV is equivalent to $1.78 \times 10^{-27}$ kg and $5.344286 \times 10^{-10}$ kg·m/s.
HTF	Histogram Track Finding
ICD	Intercryostat Detector
ILC	International Linear Collider
IP	Impact Parameter
ISR	Final-state Radiation
ISR	Initial-state Radiation
JER	Jet Energy Resolution
JES	Jet Energy Scale
JETID	Jet Reconstruction and Identification
JLIP	Jet Lifetime Probability
JSSR	Jet Shifting, Smearing, and Removal
KS Value	Kolmogorov-Smirnov Value
L1	Level 1 Trigger System
L2	Level 2 Trigger System
L3	Level 3 Trigger System
LHC	Large Hadron Collider
Linac	Linear Accelerator
LLR	Log-likelihood Ratio
LO	Leading-order
MC	Monte Carlo
MDT	Mini Drift Tube
ME	Matrix Element

---

MED	Matrix Element Discriminant
MI	Main Injector
MJ	multijet
MPF	Missing $E_T$ Projection Fraction
MVA	Multivariate Analysis
NLO	Next-to-leading order
NN	Neural Network
NNLO	Next-to-next-to-leading order
p.d.f.	Probability Density Function
PDF	Parton Distribution Function
PDT	Proportional Drift Tube
PMT	Photo-multiplier Tube
pQCD	perturbative QCD
QCD	Quantum Chromodynamics
QED	Quantum Electrodynamics
RF	Random Forests of Decision Trees
SDC	Flavor-dependent Jet Energy Scale
SM	The Standard Model of particle physics
SMT	Silicon Microstrip Tracker
STT	Silicon Track Trigger
SVT	Secondary Vertex Tagger
VC	Vertex Confirmation
VLPC	Visible Light Photon Counter
DØ	The DØ Detector or The DØ Collaboration

# 1 Introduction

## What is matter made of?

This question has been asked since ancient times. Particle physics aims to understand the elementary constituents of matter and energy, and the interactions among them. It is our current understanding that the fundamental structure of matter reflects the existence of subatomic particles, namely, quarks and leptons, and the dynamics of these particles are summarized in a theory known as the Standard Model of particle physics (SM).

Experimentally, high energy is required to probe the elementary particles at the smallest distances, and this requires the development of high energy accelerators. In this dissertation, we present the measurement of the electroweak production of single top quarks in proton-antiproton collisions at a center-of-mass energy of 1.96 TeV. The data was collected at the DØ experiment, one of the multi-purpose detectors located at the Tevatron proton-antiproton collider at Fermilab.

In this chapter, we start with a brief description of the Standard Model and of the top quark in Sections 1.1 and 1.2, respectively. The measurement of single top-quark production is addressed in Section 1.3, where we discuss the motivation for this measurement (Section 1.3.1), the event signature (Section 1.3.2), and the main background processes (Section 1.3.3). Finally, we outline the study in Section 1.3.4.

## 1.1 The Standard Model

The Standard Model (SM) of particle physics [17] is a theory describing interactions among particles in terms of relativistic quantum fields. In quantum field

theory, particles are regarded as excited states of a quantized field, and different type of particles correspond to different fields. Among the many quantum field theories, the ones that require Lagrangians to be invariant under a phase transformation, or gauge transformation, are named gauge theories. Formulated in 1970s, the SM is the simplest of the gauge theories. According to this model, all matter is made of fundamental point-like spin- $\frac{1}{2}$  fermions: six quarks and six leptons. Interactions between these fermions are considered to involve exchanges of spin-1 bosons, with the internal symmetries formulated as the unitary group  $SU(3) \times SU(2) \times U(1)$ . The Standard Model encompasses the three fundamental interactions, namely, the electromagnetic, weak and strong forces, but not gravity. Gravity is a factor of  $10^{32}$  times smaller than the weak interaction, which is the weakest among the interactions considered in the SM, and on the scale of current experiments in particle physics, gravity is negligible for the scope of our discussion.

The properties of elementary fermions are summarized in Table 1.1. Being spin- $\frac{1}{2}$  particles, they comply with the Pauli exclusion principle. Each particle has a corresponding antiparticle, which has the same mass and lifetime as its partner, but opposite electric charge and magnetic moment. Antiparticles are denoted by placing bars above the particle symbols. The quarks and leptons are grouped in three “generations,” and particles in the same generation have relatively similar mass and related quantum properties. The particles in the first generation rarely decay, and all ordinary matter is comprised of such particles. On the other hand, the particles in the higher generations are unstable, can only be produced at very high energies, and eventually decay into particles of the first generation. Such decay transitions violate conservation of the “flavor” of the generations, as discussed below.

Among the leptons ( $\ell$ ), the muon ( $\mu$ ) and tau lepton ( $\tau$ ) are the massive versions of the higher-generation electron ( $e$ ). These charged leptons interact via the electromagnetic and weak forces. The neutral leptons, or neutrinos, are expected to be massless in the Standard Model, however, recent experimental results show they have small but finite mass [18, 19]. Neutrinos interact only via the weak force, and are therefore hard to detect. In experiments such as DØ, their presence is inferred by an imbalance in transverse momentum in a measured event (as will be discussed in Section 3.6), because they escape without detection.

Quarks interact via electromagnetic, weak, and strong interactions. In addi-

	Electric Charge	1st Generation	2nd Generation	3rd Generation
Leptons	-1	electron ( $e$ ) $m_e = 0.511$ MeV	muon ( $\mu$ ) $m_\mu = 105.7$ MeV	tau ( $\tau$ ) $m_\tau = 1776.82 \pm 0.16$ MeV
	0	electron neutrino ( $\nu_e$ ) $m_{\nu_e} < 2.05$ eV	muon neutrino ( $\nu_\mu$ ) $m_{\nu_\mu}$ is small but non-zero	tau neutrino ( $\nu_\tau$ ) $m_{\nu_\tau}$ is small but non-zero
Quarks	+2/3	up ( $u$ ) $m_u = 2.3^{+0.7}_{-0.5}$ MeV	charm ( $c$ ) $m_c = 1.275 \pm 0.025$ GeV	top ( $t$ ) $m_t = 173.5 \pm 0.6 \pm 0.8$ GeV
	-1/3	down ( $d$ ) $m_d = 4.8^{+0.7}_{-0.3}$ MeV	strange ( $s$ ) $m_s = 0.095 \pm 5$ GeV	bottom ( $b$ ) $m_b = 4.65 \pm 0.03$ GeV

**Table 1.1** The Standard Model fermions and their properties [1]. The electric charge is given in units of the charge of the electron.

tion to fractional electric charges, quarks carry quantum-chromodynamics (QCD) “color charges” of the strong interaction, expressed as red, green, and blue, and their antiquarks carry the corresponding anticolors [17]. Unlike leptons, quarks other than the top quark (see Section 1.2) do not exist as free particles, but are always bound to one another, forming color-neutral particles (hadrons).

The properties of gauge bosons, defined as force carriers that mediate the electromagnetic, weak, and strong interactions, are summarized in Table 1.2.

Particle	Electric Charge	Mass (GeV)	Interaction
Photon ( $\gamma$ )	0	0	Electromagnetic
$W$ boson ( $W^\pm$ )	$\pm 1$	$80.385 \pm 0.015$	Weak
$Z$ boson ( $Z^0$ )	0	$91.1876 \pm 0.0021$	Weak
Gluon ( $g$ )	0	0	Strong (QCD)

**Table 1.2** The gauge bosons of the SM and their properties [1]. The electric charge is given in units of the charge of the electron.

Electromagnetic interactions are mediated by photon exchange between particles with electric charges, such as electrons and nuclei. The interaction corresponds to the  $U(1)$  symmetry of quantum electrodynamics (QED) [17].

The weak interactions are mediated by charged  $W^\pm$  and neutral  $Z^0$  vector bosons, exchanges between all quarks and leptons. The fact that these bosons are very massive is reflected in the very short range of these interactions. At energies above the  $W$  mass, the SM effectively unifies the electromagnetic and weak interactions into a single electroweak (EW) force. The electroweak symmetry

$SU(2) \times U(1)$  is broken, which results in very different masses for the mediating photon and the  $W$  and  $Z$  bosons, and which is accommodated by the Higgs mechanism [20, 21, 22], in which the presence of the Higgs field breaks the EW symmetry. The Higgs boson that corresponds to an excitation of the Higgs field is likely to have recently been observed at the Large Hadron Collider (LHC) in Geneva, Switzerland, but further verifications are proceeding to measure if the observed particle indeed has spin-zero, and conforms to all other expectations of the SM.

The coupling strength of the EW interaction among the up and down quarks of the electroweak current couples “rotated” quark states that correspond to mixed states of quark flavor. Specifically, with six quark flavors, the rotation can be expressed by a unitary  $3 \times 3$  matrix, known as the Cabibbo-Kobayashi-Maskawa (CKM) matrix [23],

$$V_{\text{CKM}} = \begin{pmatrix} V_{ud} & V_{us} & V_{ub} \\ V_{cd} & V_{cs} & V_{cb} \\ V_{td} & V_{ts} & V_{tb} \end{pmatrix}. \quad (1.1.1)$$

As for any  $3 \times 3$  matrix, we can define three Euler angles and one phase angle, and the latter introduces the possibility of the simultaneous violation of Charge Conjugation and Parity conservation ( $CP$ -violation) in EW processes [24]. The currently measured magnitudes of the CKM matrix elements are as follows [1],

$$V_{\text{CKM}} = \begin{pmatrix} 0.97425 \pm 0.00022 & 0.2252 \pm 0.0009 & (4.15 \pm 0.49) \times 10^{-3} \\ 0.230 \pm 0.011 & 1.006 \pm 0.023 & (40.9 \pm 1.1) \times 10^{-3} \\ (8.4 \pm 0.6) \times 10^{-3} & (42.9 \pm 2.6) \times 10^{-3} & 0.89 \pm 0.07 \end{pmatrix}. \quad (1.1.2)$$

Some of the elements are measured directly from particle decays, while others are obtained assuming unitarity of the matrix.

The strong interaction (QCD) is mediated by gluons that couple to color-charged particles (quarks and gluons), and is described by an  $SU(3)$  symmetry group. Unlike quarks, gluons carry both color and anticolor, and are postulated to belong to an octet of states, where the octet arises from the 9 combination of three colors and three anticolors, excluding a color singlet with no net color. QCD is the strongest of the fundamental interactions (a factor of  $\approx 10^{39}$  stronger than gravity), and the strength increases as the distance of the interacting objects increases.

As color is not a physically observable quality, any quarks or gluons produced in high energy collisions transform to color-neutral hadrons, or “hadronize,” as the final states evolves in time. Experimentally, when a quark or gluon is produced in a collision, it will generate a shower of hadrons, called a “jet,” that can be detected with the color quantum number of the final state being identical to that of the initial colliding objects, as will be discussed in Section 3.5.

While QCD processes cannot be calculated exactly, but approximation techniques based on perturbation theory are available, in which as asymptotic series can be given in terms of the “coupling strength” of the interaction. The coupling strength of the strong interaction, denoted as  $\alpha_S$ , decreases with increasing transverse momentum (scale) of the elementary collision, and perturbative QCD (pQCD) at leading, and next-to-leading order (LO and NLO) are available for most production processes.

Predictions for EW and QCD interactions based on the SM have been verified by experiment. Nevertheless, the SM is incomplete, as it does not include gravity, nor does it involve “dark matter” and “dark energy [25].” In addition, the SM assumes that neutrinos are massless, but recent experiments show that neutrinos are massive [18, 19]. This provides motivation to search for physics beyond the SM.

## 1.2 The Top Quark

First observed at the Tevatron collider in 1995 [26, 27], the top quark plays a key role in the study of fundamental interactions, the parameters, of the SM, and the EW symmetry breaking. The confirmation of the existence of the top quark verifies the prediction within the framework of the  $SU(3) \times SU(2) \times U(1)$  symmetry. As the most massive of all known elementary particle ( $\simeq 173.5$  GeV, as indicated in Table 1.1), the top quark probes physics at a much higher energy scale than other fermions, and may open a window on new physics.

The production of top quarks at colliders provides us with opportunities to study precisely the strong and EW interactions. Moreover, the top quark mass constrains the Higgs mechanism. Since it is expected to have an exceedingly short lifetime of  $0.5 \times 10^{-24}$  s, an order of magnitude smaller than hadronization

timescales [28], the top quark decays as an essentially free particle, imparting its kinematic and spin properties to its decay products.

We briefly discuss top-quark production and decay in Section 1.2.1 and Section 1.2.2, respectively. In addition, as the study in this dissertation focuses on EW production, the production of single top quarks is explored separately in Section 1.3.

### 1.2.1 Production

When a proton and an antiproton collide, a hard interaction (or hard scattering) with large momentum transfer can place between the constituents (also known as “partons”) of the proton and of the antiproton. The initial partons can be valence quarks, sea quarks, or gluons. The valence quarks of a particle are the quarks that most reflect its quantum numbers; for example, the proton is considered to be composed of the  $u$ ,  $u$ , and  $d$  valence quarks. Nevertheless, there are also “sea” quarks (in the form of virtual quark-antiquark pairs) and gluons within a hadron. Typically, valence quarks of a particle carry most of its momentum, while sea quarks and gluons carry less.

The likelihood of an interaction between particles is specified by the term “cross section,” denoted as “ $\sigma$ .” Namely, the production rate for any given production process is quantified by the value of its cross section. The unit of cross section is a barn (b), and it is equal to  $10^{-28} \text{ m}^2$ . The larger the  $\sigma$ , the more it that process to take place.

#### 1.2.1.1 Strong Production of $t\bar{t}$ Pairs

As mentioned before, top quarks can be produced as  $t\bar{t}$  pairs via the strong interaction, or singly via the electroweak interaction. At the Tevatron, the leading order (LO) production of a  $t\bar{t}$  occurs dominantly (85%) via quark-antiquark ( $q\bar{q}$ ) annihilation, as shown in Figure 1.1(a), where the quark and the antiquark originate from the valence quarks in the colliding proton and antiproton, respectively.

At the center-of-mass energies of the Tevatron, gluons often do not carry sufficient energy to induce top pair production through gluon-gluon interactions. As a consequence, top-quark pair production via gluon ( $gg$ ) fusion, as shown in Figure 1.1(b), is suppressed (to 15% of the total rate). The predicted production cross

section at next-to-next-to-leading order (NNLO) in pQCD is close to 7.5 pb at the Tevatron at a center-of-mass energy  $\sqrt{s} = 1.96$  TeV [29, 30, 31, 32]. The most recent measurement, combining the results from the CDF and DØ experiments, yields  $\sigma_{t\bar{t}} = 7.65 \pm 0.42$  pb for a top-quark mass of 172.5 GeV [33].

At the Large Hadron Collider, for  $\sqrt{s} = 7, 8$  TeV, the lack of valence antiquarks suppresses the  $q\bar{q}$  annihilation, and the fractions of the  $q\bar{q}$  annihilation and  $gg$  fusion contributions to top-quark pair production are approximately reversed to 15% and 85%, respectively. The two multipurpose ATLAS and CMS experiments at the LHC obtain a combined result of  $\sigma_{t\bar{t}} = 173.3 \pm 10.1$  pb at  $\sqrt{s} = 7$  GeV for a top-quark mass of 172.5 GeV [34], in agreement with the prediction  $\sigma_{t\bar{t}} = 167^{+17}_{-18}$  pb [35].

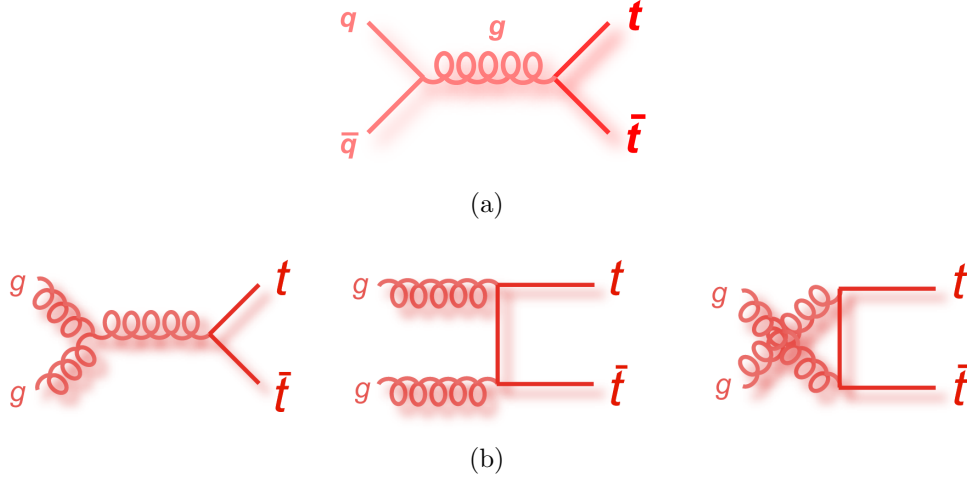


**Figure 1.1** Representative leading-order Feynman diagrams for strong top-quark pair production from (a) quark annihilation ( $q\bar{q}$ ) and (b) gluon fusion ( $gg$ ) [2].

### 1.2.1.2 Electroweak Production of Top Quarks

Top quarks can also be produced singly without their antiparticle partners via the electroweak interaction. Despite that such weak interactions have far smaller coupling strengths than the strong interaction, the large mass scales involved and the kinematics bring the production cross section of a single top quark to approximately one-half of the cross section for  $t\bar{t}$  pair. Classified according to the virtuality of the participating  $W$  boson, (the square of the four momentum

of the  $W$  boson,  $q_W^2$ ), we can define three channels of inclusive single top-quark production,  $s$ -channel,  $t$ -channel, and associated  $tW$  production, as indicated in Figure 1.2, where inclusive reflects that these states can be accompanied by any number of  $X$  additional gluons or photons radiated in the process. Here,  $s$  and  $t$  refer to the partonic kinematic invariants for the process  $p_1 + p_2 \rightarrow p_3 + p_4$ , where the partons are represented by their four-momenta  $p_i$ , with  $s = (p_1 + p_2)^2$ , and  $t = (p_1 - p_3)^2$ . Charge conjugate processes (the production of antitop quarks) are expected to have the same diagrams and rates at the Tevatron. Throughout this dissertation, the charge conjugate processes are included, unless mentioned explicitly to the contrary.

The two-body process  $q\bar{q} \rightarrow t\bar{b}$  in Figure 1.2(a) is referred to as the  $s$ -channel or  $t\bar{b}$  mode [36, 37, 38, 39, 40], where the  $W$  boson is timelike ( $q_W^2 = s \geq (m_t + m_b)^2 \geq 0$ ). This is also often termed  $W^*$  production, with an initial-state quark-antiquark pair annihilating into an off-shell virtual  $W$  boson, which then decays into a top and a  $b$  quark. Except for colinear production, the final state  $b$  quark must recoil against the top quark with large transverse momentum. Because  $W$  bosons do not have strong interactions, the initial state of the  $s$ -channel must be a color singlet, which limits the number of initial color combinations and therefore the production rate. For a top quark mass of  $m_t = 173$  GeV, the predicted NNLO cross section is  $1.04 \pm 0.08$  pb at  $\sqrt{s} = 1.96$  TeV at the Tevatron [41] and  $4.56^{+0.19}_{-0.18}$  pb at the LHC [42]. The  $s$ -channel cross section increases slowly with center-of-mass energy, but the LHC  $pp$  collider can only provide the initial antiquark from the sea quarks, which suppresses  $s$ -channel production. As a consequence, the  $s$ -channel single top-quark cross section increases by only about a factor of 4 at the LHC relative to that at the Tevatron. With much more background contamination at the LHC, it is difficult to measure the  $s$ -channel cross section, and the Tevatron therefore provides a unique opportunity to perform this measurement. In addition, the  $s$ -channel cross section can be calculated more reliably than the  $t$ -channel, because the quark and antiquark distribution functions in the energy scale of the Tevatron and LHC are well known [37]. Unlike for the  $t$ -channel, which we discuss below, the  $s$ -channel simulation at LO is essentially identical in kinematic properties to the approximation at NLO [43].

The process  $q'b \rightarrow tq$  or  $q'g \rightarrow tq\bar{b}$  is referred to as  $t$ -channel, single top-quark production or  $tqb$  final state [44, 40, 45, 46, 47], as the  $W$  boson is spacelike ( $q_W^2 = t < 0$ ), with imaginary (virtual) mass. In the  $q'b \rightarrow tq$  subprocess indicated

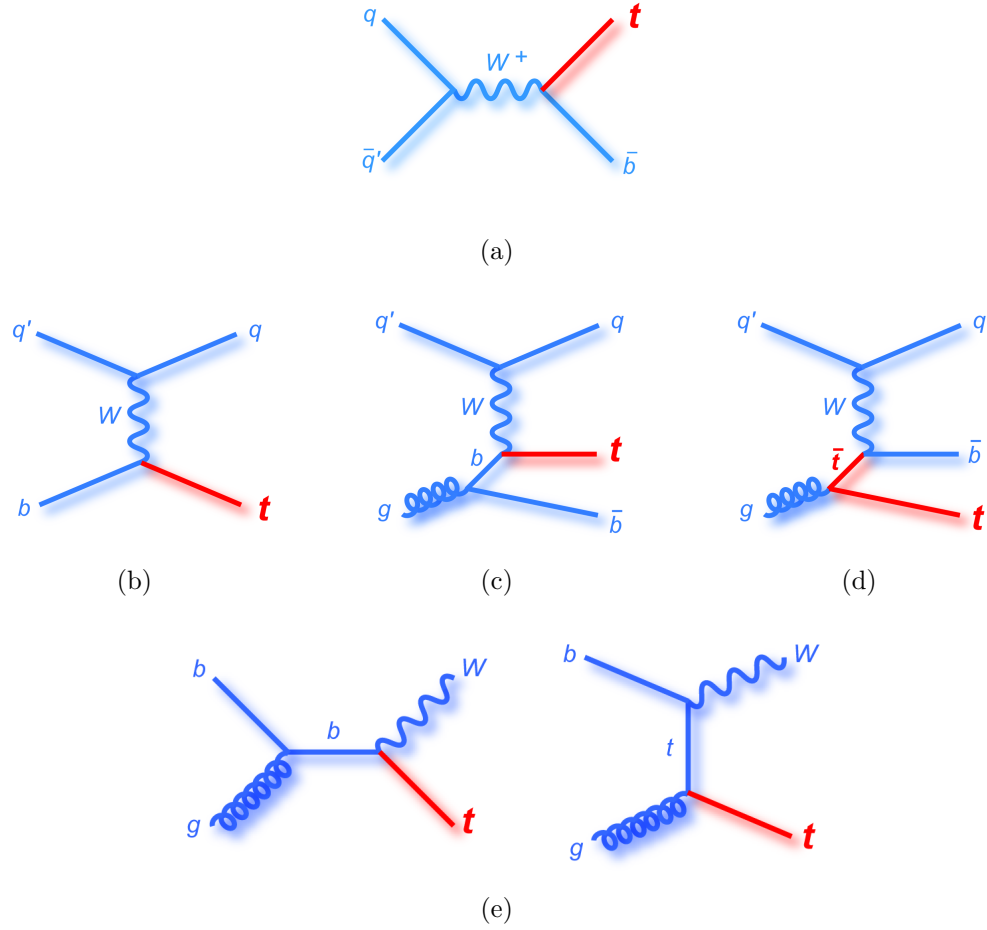


**Figure 1.2** Representative leading-order Feynman diagrams for electroweak single top-quark production for (a)  $s$ -channel “ $tb$ ” mode, (b), (c), and (d)  $t$ -channel “ $tqb$ ” modes, and (e) associated “ $tW$ ” mode. Diagrams with off-diagonal CKM matrix elements, such as  $Wt\bar{s}$  or  $Wt\bar{d}$  vertices, are suppressed due to the small values of their CKM matrix elements [2].

in Figure 1.2(b), a  $b$  quark from the sea in the proton or antiproton couples with the virtual  $W$  boson, producing a top quark. In the  $q'g \rightarrow tq\bar{b}$  subprocess, as illustrated in Figure 1.2(c), one of the  $b$  quarks, arising from gluon splitting, couples to a virtual  $W$  boson and produces a top quark, whereas the other  $b$  quark continues along the original direction of the incident gluon, and has small transverse momentum. Since the second subprocess dominates the cross section, the  $t$ -channel is also known as  $W$ -gluon fusion. For  $m_t = 173$  GeV, the predicted cross section for all  $t$ -channel contributions is  $2.26 \pm 0.12$  pb at the Tevatron ( $\sqrt{s} = 1.96$  TeV) [41], and  $64.6^{+2.1+1.5}_{-0.7-1.7}$  pb at the LHC ( $\sqrt{s} = 7$  TeV) [48]. The  $t$ -channel cross section is the largest of the three modes of single top-quark production at both the Tevatron and LHC, and, owing to the fact that the  $W$ -gluon fusion is greatly enhanced at very high energies, the single top-quark production is far larger at the LHC [44]. This is mainly due to the gluon color-octet nature in the initial state, and that the number of color combinations in the  $t$ -channel is therefore greater than that in the  $s$ -channel, and leads to a larger cross section for  $t$ -channel production. Additional gluon radiation affects significantly the kinematics of the inclusive  $t$ -channel  $qtb$  final states (i.e.  $qtb + X$ ) [43], and therefore NLO Monte Carlo (MC) simulation must be used in this analysis [49, 4], as will be discussed in Section 4.2.

The process  $bg \rightarrow tW$  of Figure 1.2(e), referred to as associated  $t$  and  $W$  production or, simply,  $tW$  [41, 50], has an on-shell  $W$  boson ( $q_W^2 = m_W^2$ ) produced together with a top quark. The predicted cross section for this process is  $0.28 \pm 0.06$  pb at the Tevatron [41] and  $15.6 \pm 0.4^{+1.0}_{-1.2}$  pb at the LHC [50]. Associated production is kinematically suppressed at the Tevatron due to the presence of the two massive particles in the final state, and is ignored in this study.

The predicted single top quark inclusive production cross sections and their most recent measurements are summarized in Table 1.3.

### 1.2.2 Decay

Assuming that there are three quark generations, the unitarity of the  $3 \times 3$  CKM matrix, together with the available measurements constrain the  $|V_{tb}|$  element to be very close to unity [1]. Consequently, the probability of the top quark to decay into a  $W$  boson and a  $b$  quark is nearly 100%. As listed in Table 1.4, the  $W$  boson can decay into one of the three charged-lepton-neutrino ( $\ell\nu_\ell$ ) pairs and into three colored doublets of up and down ( $u\bar{d}$ ) quarks and of charm and strange

Inclusive Channel	$s$ -channel ( $t\bar{b} + X$ )	$t$ -channel $[(tq + X) + (tq\bar{b} + X)]$	$tW$ ( $tW + X$ )
Tevatron Prediction ( $\sqrt{s} = 1.96$ TeV)	$1.04 \pm 0.08$ [41]	$2.26 \pm 0.12$ [41]	$0.28 \pm 0.06$ [41]
CDF	$1.81^{+0.63}_{-0.58}$ [51]	$1.49^{+0.47}_{-0.42}$ [51]	—
DØ	$0.98 \pm 0.63$ [3]	<b><math>2.9 \pm 0.59</math></b> [3]	—
LHC Prediction ( $\sqrt{s} = 7$ TeV)	$4.56^{+0.19}_{-0.18}$ [42]	$64.6^{+2.1+1.5}_{-0.7-1.7}$ [48]	$15.6 \pm 0.4^{+1.0}_{-1.2}$ [50]
ATLAS	—	<b><math>83 \pm 4^{+20}_{-19}</math></b> [52]	<i><math>16.8 \pm 2.9 \pm 4.9</math></i> [53]
CMS	—	<b><math>67.2 \pm 6.1</math></b> [54]	<i><math>16^{+5}_{-4}</math></i> [55]

**Table 1.3** The predicted and latest-measured inclusive production cross sections for single top-quark final states at the Tevatron and LHC [41, 51, 3, 42, 48, 50, 52, 53, 54, 55]. The units are in pb. The bold line indicates observation at more than five standard deviations of confidence, while the italics show evidence with confidence of more than three standard deviations.

( $c\bar{s}$ ) quarks. As indicated in Figure 1.3, the final state of top-quark decay can contain either  $\ell\nu b$  or  $q\bar{q}'b$  systems, where  $q$  and  $\bar{q}'$  denote quarks in the first and second generations (“light-flavored quarks<sup>1</sup>”).

Decay Mode	Branching Ratio
$W \rightarrow e\nu$	$(10.75 \pm 0.13)\%$
$W \rightarrow \mu\nu$	$(10.57 \pm 0.15)\%$
$W \rightarrow \tau\nu$	$(11.25 \pm 0.20)\%$
$W \rightarrow \text{quarks}$	$(67.60 \pm 0.27)\%$

**Table 1.4** Measured branching ratios for final states in  $W$  boson decay [1].

Events from  $t\bar{t}$  production contain therefore two  $W$  bosons and two  $b$  quarks, and can be classified according to the  $W$  decay products, as shown in Figure 1.4. First, 10.5% of the  $t\bar{t}$  events contain two charged leptons, two neutrinos, and two  $b$  quarks ( $\bar{\ell}\nu_{\ell}b\ell'\bar{\nu}_{\ell'}\bar{b}$ ), and are denoted as “dilepton” final states. The second class of events, referred to as “ $\ell$ +jets,” contain a charged lepton, its neutrino, two light-flavored and two  $b$  quarks (either  $q\bar{q}'b\ell^{-}\bar{\nu}_{\ell}\bar{b}$  or  $\ell^{+}\nu_{\ell}bq\bar{q}'\bar{b}$ ). The third class of “all-jets” or, as often mistermied, “all-hadronic” channels provide four

<sup>1</sup>The mass and properties of the charm quark are in fact between the other light-flavored quarks,  $u$ ,  $d$ ,  $s$ , and the heavy-flavored quark,  $b$ . For this study, we categorize it as a light-flavored quark unless explicitly mentioned.

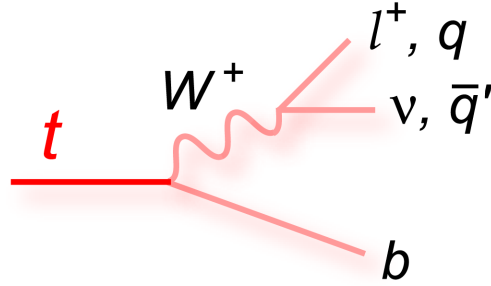


**Figure 1.3** The top quark decay and the final state, where  $q$  and  $\bar{q}'$  represents the quark and antiquark in the first and second generations [2].

light-flavored and two  $b$  quarks ( $q\bar{q}'bq''\bar{q}'''\bar{b}$ ).

### Top Pair Decay Channels

$\bar{c}s$	<div style="display: flex; flex-direction: column; align-items: center;"> <div style="background-color: #d9ead3; padding: 2px;">electron+jets</div> <div style="background-color: #a6d854; padding: 2px;">muon+jets</div> <div style="background-color: #f4cccc; padding: 2px;">tau+jets</div> </div>	all-hadronic			
$\bar{u}d$					
$\tau^-$	$e\tau$	$\mu\tau$	$\tau\tau$	tau+jets	
$\mu^-$	$e\mu$	$\mu\mu$	$\mu\tau$	muon+jets	
$e^-$	$e e$	$e\mu$	$e\tau$	electron+jets	
$W$ decay	$e^+$	$\mu^+$	$\tau^+$	$u\bar{d}$	$c\bar{s}$

**Figure 1.4** Nomenclature for  $t\bar{t}$  final states [2].

## 1.3 Electroweak Top-Quark Production

Single top-quark production was first observed by the DØ and CDF collaborations [56, 57]. As discussed in the previous section, single top quarks at the Tevatron are produced essentially via the  $s$  and  $t$ -channel processes, and both collaborations have performed measurements focusing on these two individual

channels [3, 58, 51]. In particular, DØ observed  $t$ -channel production at a five standard deviation level of confidence [3]. In this dissertation, we present the final measurement of the single top-quark production cross section at DØ based on the full Tevatron Run II data sample.

### 1.3.1 Motivation

Measuring the single top-quark production cross section provides a direct determination of  $|V_{tb}|$ , an indirect measurement of the width and lifetime of the top quark, and a window to physics beyond the Standard Model. We summarize below a few interesting aspects that motivate this measurement.

Both the  $s$  and  $t$ -channel single top-quark production involves a  $Wtb$  vertex, as indicated in Figure 1.5, and the production cross section is proportional to the  $Wtb$  coupling strength  $|V_{tb}|^2$ . Hence, the measurement of these cross sections directly determines  $|V_{tb}|$ , with most minimal assumptions concerning the structure of the CKM matrix. The assumption that the top quark decays 100% of the time to  $Wb$  only requires  $|V_{tb}|^2 \gg |V_{td}|^2 + |V_{ts}|^2$ , but does not constrain the number of elementary fermion generations (i.e. to three in the Standard Model) nor the unitarity of the CKM matrix, assuming there is no forth generation. Moreover, this measurement is complementary to using the ratio of branching fractions in top-quark decay, where the unitarity of the  $3 \times 3$  CKM matrix has to be assumed [59].

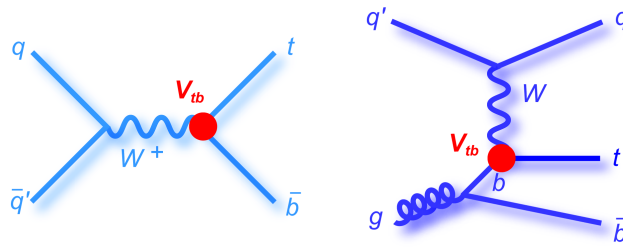


**Figure 1.5** Representative Feynman diagrams of single top-quark production, indicating the origin of the proportionality of the production cross section on  $|V_{tb}|^2$  of the  $Wtb$  vertex [2].

The total decay width of the top quark,  $(\Gamma)$ , reflecting the probability per unit time for the top quark to decay, can be extracted indirectly by comparing

the production cross section using the prediction in the SM with that measured in data [60, 61, 62]. The lifetime of the top quark then follows from width:  $\tau_t = \hbar c/\Gamma$ .

As discussed in Section 1.2, the top quark decays through the weak interaction without hadronizing, preserving thereby its properties in its decay products. Hence, the polarization of the top quark can be measured from the angular distributions of its decay products. In the SM, single top quarks are produced via the  $V - A$  electroweak interaction are nearly 100% left-handed polarized. However, if single top quarks can be produced through other mechanisms, such as flavor-changing neutral current (FCNC) or new charged Higgs bosons, or if the top quark couples anomalously to the  $W$  boson, the polarization can be affected. Measuring the polarization provides therefore another check for the presence of contributions to the structure of the  $Wtb$  vertex beyond the SM [63].

Although  $CP$  violation can be accommodated in the SM, its effect on top-quark production and decay is minimal. However, other models provide significant  $CP$  violation [64, 65]. At the Tevatron,  $CP$  violation can be measured by comparing the production cross section of top quarks to that of antitop quarks [66], which, for the initial  $p\bar{p}$   $CP$  eigenstate, are expected to be identical.

Other physics scenarios beyond the SM predict larger cross sections of single top quark production than expected in the SM, that would manifest themselves differently in  $s$  and  $t$ -channels [67], as shown in Figure 1.6. The  $s$ -channel is sensitive to new particles, such as charged Higgs [68] and  $W'$  bosons [69, 70, 71], as illustrated in Figure 1.7, while the  $t$ -channel is affected by anomalous  $Wtb$  couplings [72, 73, 74] and flavor-changing neutral currents [75, 76, 77]. Measuring the single top-quark production cross section precisely, as well as the  $s$  and  $t$ -channels individually, can therefore help to disentangle different models of physics beyond the SM.

As the Tevatron was shut down in September, 2011, the measurement of single top-quark production cross section is a legacy of the  $p\bar{p}$  collider at a center-of-mass energy of 1.96 TeV. In particular, the  $s$ -channel production rate is comparatively low at the LHC (Table 1.3), and with a much larger background contamination, which will make it very difficult to measure the  $s$ -channel cross section. Hence, the measurement at the Tevatron is a unique opportunity to study single top-quark production in the  $s$ -channel for the near future.

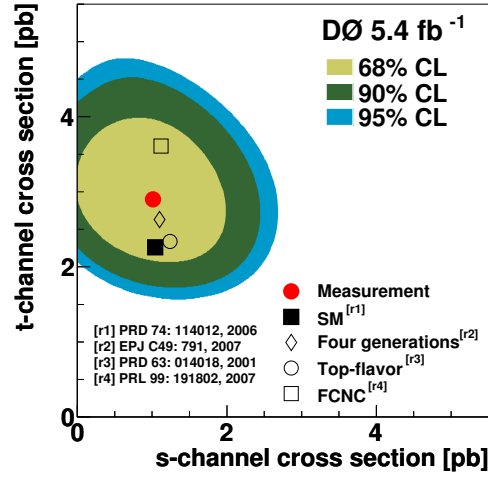


**Figure 1.6** Posterior probability density for  $t$ -channel vs  $s$ -channel single top-quark production in contours of equal probability density. The measured cross section and several theoretical predictions for new physics are shown for comparison. CL values represent the level of confidence for the previous measurement [3].

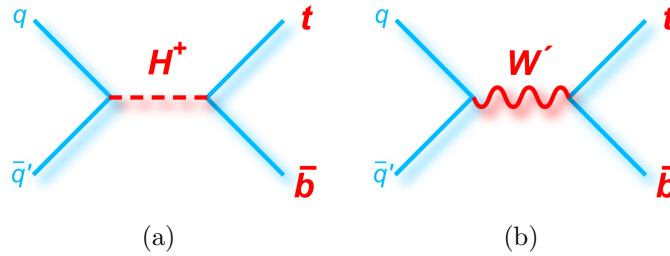


**Figure 1.7** Representative Feynman diagrams for  $s$ -channel single top-quark production via a new boson: (a) a charged Higgs boson, and (b) a heavy  $W'$  boson [2].

### 1.3.2 Event Signature

About 32,000 single top-quark events are expected to have been produced in Tevatron Run II. However, with the overwhelming background, measuring the production cross section remains challenging. Nevertheless, we can exploit the unique properties of the single top-quark events to select samples with reduced background, and thereby separate the signals from background.

Figure 1.8 shows the decay chain for single top-quark events. Based on the fact that the background from multijet events produced via the strong interaction is overwhelming at the Tevatron, and that, by requiring a lepton in the analysis, such events can be greatly reduced, we consider only the events that contain an isolated lepton in the final state, namely, the events with leptonic  $W$  decays. Specifically, we only analyze the “ $\ell$ +jets” events with  $\ell$  being an electron or a muon in the final state. This also includes some  $W \rightarrow \tau\nu_\tau$  decays when the  $\tau$  lepton decays to  $e\nu_e\nu_\tau$  or  $\mu\nu_\mu\nu_\tau$ . The  $W \rightarrow \tau\nu_\tau \rightarrow \text{hadrons} + \nu_\tau\nu_\tau$  are not included in the analysis because they are difficult to reconstruct.

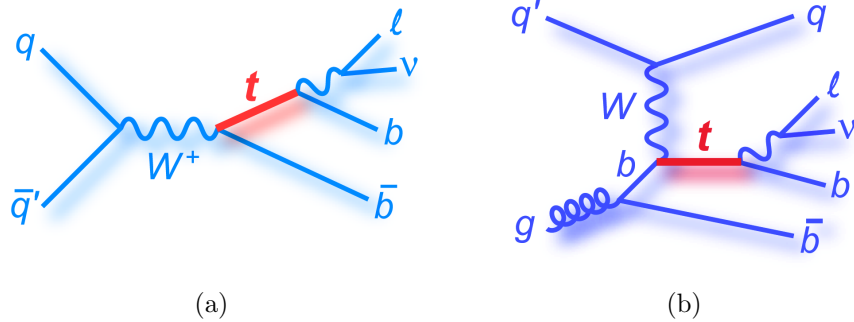


**Figure 1.8** Illustration for the final states in single top-quark events: (a)  $s$ -channel, and (b)  $t$ -channel [2]. The  $b(\bar{b})$  quark from gluon splitting in the  $t$ -channel is generally emitted along the beam pipe and is not reconstructed.

Owing to the fact that the top quark is very massive, it is produced nearly at rest in the center of mass reference frame, and its decay products do not have any much preferred directions. Furthermore, the lighter decay products can be highly boosted and have large transverse momenta ( $p_T$ ). In brief, a single top event candidate has a high- $p_T$  electron or muon, a neutrino inferred by a large imbalance in  $p_T$  in the event, two or three high- $p_T$  jets, two of which are candidates for originating from the  $b$  quark (also known as  $b$ -jets or  $b$ -tagged jets). We discuss

the reconstruction of these final-state objects and event selections in Chapters 3 and 5, respectively.

Typically, the  $b$ -quark produced through the  $s$ -channel recoils with large  $p_T$  against the top quark in the central region of the detector. The  $s$ -channel event therefore tends to have both  $b$ -jets reconstructed. In contrast, the  $b$  quark from gluon splitting in the  $t$ -channel tends to have low transverse momentum, and to be emitted in the very forward (or backward) region of the detector, as shown in Figure 1.9(a). The  $t$ -channel events therefore normally contain only one reconstructed  $b$ -jet. Empirically, the direction of the light quark in the  $t$ -channel event is found to have a peak near pseudorapidity  $|\eta| = 1.5$ , where  $\eta = -\ln \tan \frac{\theta}{2}$ , and  $\theta$  is the polar angle of an object relative to the collision axis. The expected distributions are shown in Figure 1.9(b) [40]. The  $\eta$  is a very powerful variable for distinguishing  $t$ -channel events from background.

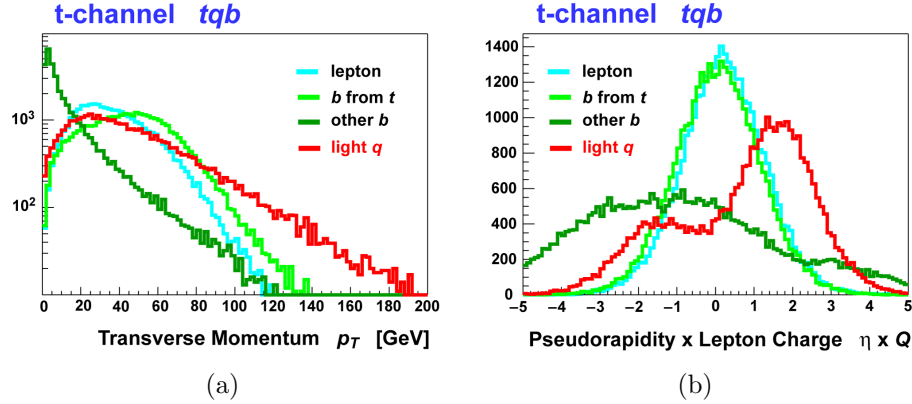


**Figure 1.9** Kinematic distributions of (a) transverse momentum ( $p_T$ ), and (b) the signed pseudorapidity ( $\eta \times Q$  (electric charge of lepton)) of partons in  $t$ -channel single top-quark events, from the CompHEP-SINGLETOP Monte Carlo simulation [4]. The contributions from  $t$  and  $\bar{t}$  events are antisymmetric in  $\eta$ , and  $\eta \times Q$  effectively flips and adds the contributions for antileptons and leptons in these events.

### 1.3.3 Background Processes

Events that have the same final-state objects as the single top-quark events, or mimic the signal final state through misreconstruction, fall into the selected samples and produce a background for the analysis. Indistinguishable background sources arise from  $W$  boson production in association with quarks or gluons

( $W$ +jets) and from  $t\bar{t}$  production, while more minor contributions correspond to multijet (MJ) production via the strong interaction,  $Z$  boson production in association with quarks and gluons ( $Z$ +jets), and  $WW$ ,  $WZ$ ,  $ZZ$  diboson production. The rates for background processes are illustrated in Figure 1.10. We briefly discuss these background events below in this section, and the simulation and the modeling in Chapters 4 and 5.

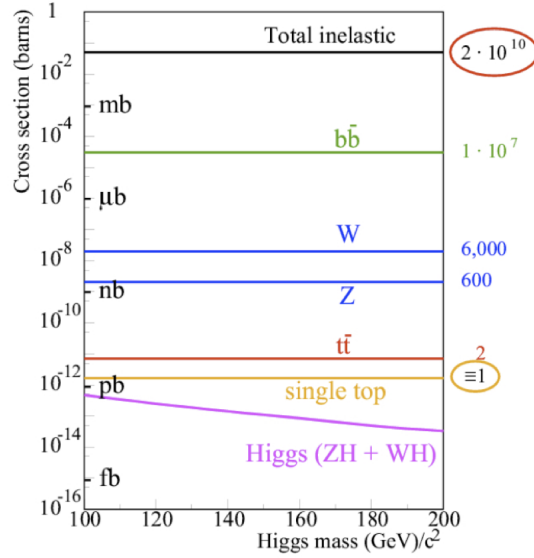


**Figure 1.10** Illustration of the production cross sections for single top quarks and other processes [5]. The right  $y$ -axis shows the cross sections relative to the single top-quark cross section. For details, see Table 4.3.

$W$ +jets production, as shown in Figure 1.11, is the main background contribution in this analysis. For events containing  $W \rightarrow \ell\nu_\ell$  decay and a few jets, the  $W$ +jets events have the same final-state objects as signal. Most of  $W$  boson production involves light-flavored quarks, and identifying jets that originate from  $b$  quarks greatly reduces therefore background from these events. The  $W$ +jets events contaminating the final selected sample (using  $b$ -tagging criteria) are mainly the ones with  $b$ -jets, as indicated in Figures 1.11(a) and 1.11(b), and with light-flavored jets misidentified as  $b$ -jets, as shown in Figure 1.11(c).

The  $t\bar{t}$  events falling in our selected samples are from the “dilepton” or “ $\ell$ +jets” final states. The dilepton events enter the two-jet samples when one of the leptons is not reconstructed, whereas the  $\ell$ +jets events enter the three-jet samples as a quark is missed, or a merged jet is formed from two quark jets. Applying  $b$ -jet

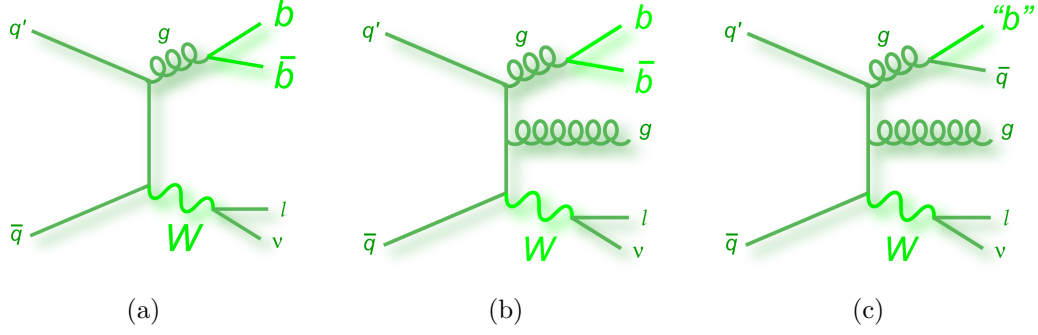


**Figure 1.11** Representative Feynman diagrams for  $W$ -boson production in association with quarks and gluons: (a)  $Wb\bar{b}$ , (b)  $Wb\bar{b}g$ , and (c)  $Wq\bar{q}'g$  [2]. Among the (c)  $Wq\bar{q}'g$  events, the light-flavored jet from gluon splitting can be misidentified as a  $b$ -jet, and such events will pass our single top-quark selection criteria.

identification cannot reduce the  $t\bar{t}$  contamination since there are two  $b$ -jets in both final states. The selected  $t\bar{t}$  events are discussed in Section 6.2.4.

When a jet in multijet events is misreconstructed as an electron, or a  $b$  quark produces an isolated muon through its weak decay, when the imbalance in transverse momentum in events is large, and when one or two of the jets are  $b$ -jets or are mistagged as  $b$ -jets, these kinds of multijet event can be selected into our samples, as can be seen from in Figure 1.12. The probability for all these three conditions to hold is small; however, with the overwhelming production rate of multijet events at the Tevatron, there is still a significant fraction of such events that fall into the selected signal samples. The impact of the multijet contribution is more evident in the candidate sample with an electron and two jets, as it is easier to misreconstruct a jet as an electron than as a muon, and the MJ events with lower jet multiplicity have larger production rates.

A  $Z$  boson can decay into two charged leptons (3.37% for each of  $e^+e^-$ ,  $\mu^+\mu^-$ , and  $\tau^+\tau^-$  pairs), two neutrinos (20%), or  $q\bar{q}'$  pairs (69.9%). When the  $Z$  boson in a  $Z$ +jets event decays into two charged leptons and one of them is not reconstructed, as demonstrated in Figure 1.13(a), the event will appear to have a large imbalance in transverse momentum, and enter our selected samples. As for  $W$ +jets processes, most of the  $Z$  bosons are produced in association with light-flavored quarks. With the smaller  $Z$ +jets production cross section, the low misreconstruction rate, and required  $b$ -jet identification, the  $Z$ +jets contribution to the selected samples is negligibly small.

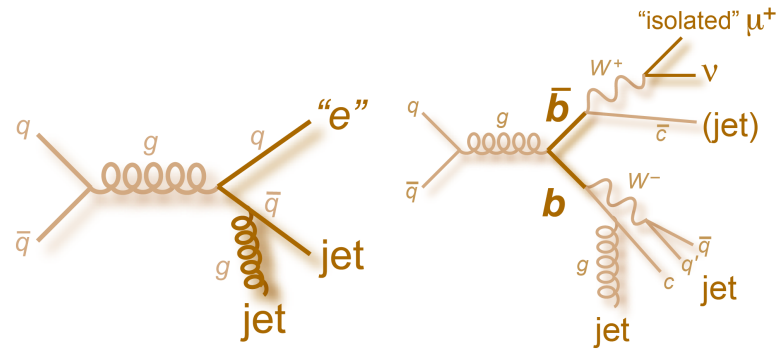


**Figure 1.12** Illustration of multijet event production and misinterpretation [2].

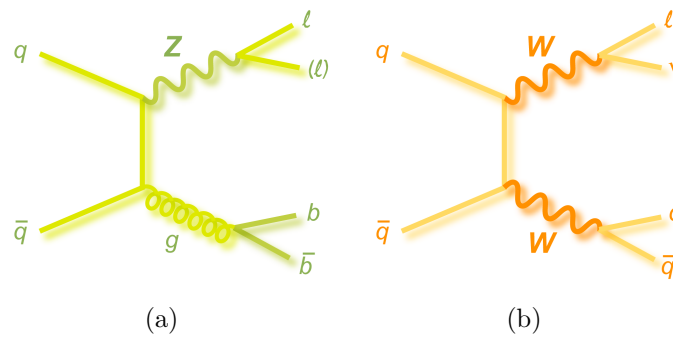


**Figure 1.13** Illustration of (a) Z+jets and (b) WW diboson production [2].

An example of  $WW$  diboson production is illustrated in Figure 1.13(b). If one of the bosons decays leptonically and the other decays into  $q\bar{q}'$  pairs, and the jet decay products are identified as  $b$ -jets, the event will pass the selections for our analysis. Moreover, because diboson production rates are small and only a small fraction of jets mimic  $b$ -jets, the contribution of such events to background is very small.

### 1.3.4 Analysis Overview

In this analysis, we measure the individual cross sections for  $s$  and  $t$ -channel single top-quark production, using all the Tevatron Run II data collected at DØ ( $9.7 \text{ fb}^{-1}$ ). While ATLAS and CMS have observed  $t$ -channel production at the LHC [52, 54], and have an evidence for the associated  $tW$  channel [53, 55], it will be difficult for these experiments to measure the  $s$ -channel. The measurement of the  $s$ -channel cross section is therefore one of the important legacy measurements at the Tevatron, and for that reason the DØ analysis is optimized to search for this channel.

The  $s$ -channel single top-quark cross section measurement is well motivated; however, owing to its small cross section and large background contamination, it is also extremely challenging at the Tevatron. We first select events as done for all the single top-quark processes, by requiring an isolated electron or muon, a large imbalance in transverse momentum, two or three jets, among which one or two jets are  $b$ -tagged. In the final selected samples, the background is approximately a factor of 50 that of the  $s$ -channel signal, and a factor of 30 that of the  $t$ -channel. Moreover, the uncertainties on the background processes are larger than the expected signal. To measure the production cross section, the expected rate for signal must clearly exceed the uncertainty on the background, which requires additional background rejection to obtain a purer sample of signal events.

However, kinematic properties of the single top-quark events are not very distinct, and there is not a single kinematic variable, such as the  $p_T$  of the leading jet (i.e., largest  $p_T$ ) that can be used to distinguish the signals from background. To obtain a signal-enriched sample, different multivariate analysis (MVA) techniques, such as Boosted Decision Trees (BDT), Neural Network (NN), and Matrix Element method (ME), have been developed [78, 79], exploiting multiple kinematic properties of the signal. A final discriminant is formed accordingly to ensure

that the expected signal is large enough to make the measurement possible in the signal-enriched region.

The ME method is used to establish the discriminant in this analysis. While the other MVA techniques seek to distinguish signal from background using an optimized set of kinematic distributions of simulated samples of pure signal and pure background events, the ME method has an intrinsically different approach. For each event, the ME method takes the theoretical prediction from the matrix element, and evaluates a probability that it can be described by any given theoretical process. Throughout the evaluation, all correlations among the final-state particles can be retained. The combined probabilities for all signal and background processes are used to form a likelihood ratio that is used as the final discriminant. The ME method is particularly powerful for processes in which the NLO kinematic distributions can be reproduced by models at LO, such as in  $s$ -channel single top-quark production. In addition, because the ME method accounts for all correlations in the hard scattering, it can provide information orthogonal to other MVA techniques, improving thereby the sensitivity of the combined results.

From the ME discriminant, we extract the signal cross section using a Bayesian approach. The signal-enriched region is sensitive to the desired cross section, while the signal-depleted region constrains the uncertainties on background. All the statistical and systematic uncertainties, and their correlations, are taken into account in the process. Ensembles of MC pseudo-experiments are also studied to validate the measurement and calibrate the result, if needed. Finally, the significance of this measurement is assessed according to standard statistical methods.

We discuss elements of the Tevatron accelerator and the DØ detector in Chapter 2. The reconstruction of physical objects and the simulation of signal and background samples are described in Chapters 3 and 4, respectively. The analysis of the single top-quark production begins with event selections in Chapter 5, followed by the Matrix Element method in Chapter 6. Systematic uncertainties on this measurement are given in Chapter 7. Then, Chapter 8 presents the extraction of the cross section. Finally we draw conclusions from our measurement in Chapter 9.

## 2 Experimental Apparatus

High collision energies are required to probe the fundamental properties of matter and its elementary constituents at small distances. Such energies can be attained through particle accelerators by accelerating charged particles in electromagnetic fields, and colliding them either with a fixed target or another beam of particles.

In this study, the data analyzed were collected at the DØ detector at the Tevatron collider. The Tevatron, located at the Fermi National Accelerator Laboratory (Fermilab) in the outskirts of Chicago, is the final element of a complex system, a synchrotron that accelerates injected protons and antiprotons, in opposite directions within a single 6.28 km ring, to an energy of 0.98 TeV. The protons and antiprotons are made to collide at the two points in the ring, where the CDF and DØ experiments are located. Each of these experiments is a cylindrical multi-purpose detector that is used to measure the positions, charges, energies, and momenta of the particles produced in the  $p\bar{p}$  collisions.

We summarize the properties of the accelerator system in Section 2.1, and the subsystems of the DØ detector used to study the particles produced in the collisions in Section 2.2.

### 2.1 The Tevatron Accelerator Complex

With beams of protons and antiprotons colliding at a center-of-mass energy of 1.96 TeV ( $10^{12}$  eV), the Tevatron was the most energetic facility in the world until the LHC started operating at CERN in 2009. Figure 2.1 shows a schematic view of the accelerator complex at Fermilab. A chain of five accelerators and two storage rings were interconnected to reach 0.98 TeV per beam.

## FERMILAB'S ACCELERATOR CHAIN

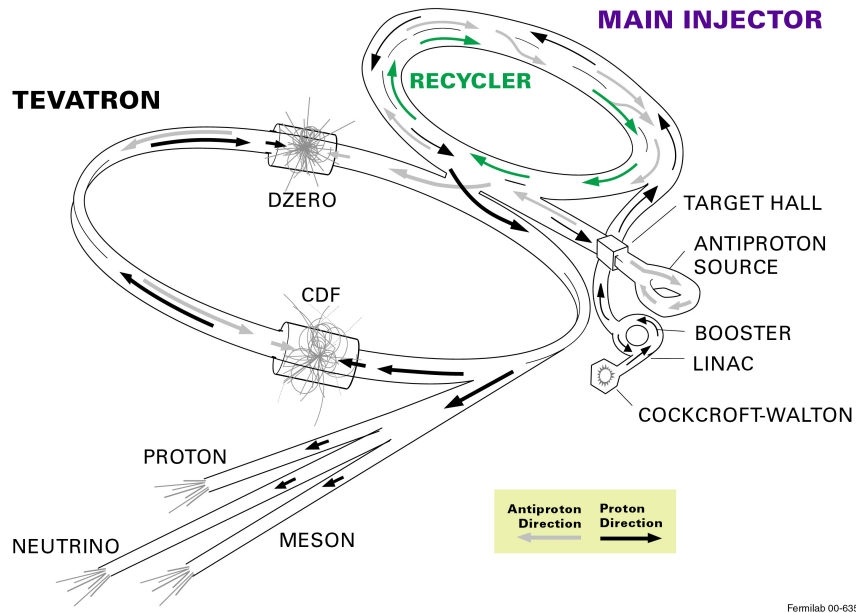


**Figure 2.1** A schematic overview of the Tevatron accelerator complex [6].

### 2.1.1 The Initial Acceleration

Starting with a bottle of hydrogen gas, a Cockcroft-Walton preaccelerator ionizes  $H_2$  molecules into  $H^-$  ions and accelerates these ions to 750 keV. A 150-meter linear accelerator (or “Linac”) subsequently accelerates the  $H^-$  ions up to an energy of 400 MeV, after which the ions are injected into the Booster, the first synchrotron in the accelerator chain, with a radius of 75-meter. A carbon foil strips the electrons from the  $H^-$  ions at injection, and leaves bare circulating protons. The intensity of the proton beam is increased by merging additional protons into the circulating beam, and, eventually, using a series of radio frequency (RF) cavities, the protons are accelerated from 400 MeV to 8 GeV

### 2.1.2 The Main Injector and The Antiproton Source

The protons extracted from the Booster are transferred into the Main Injector (MI), a synchrotron with a 500-meter radius. The Main Injector accelerates the protons from 8 to 120 GeV, and then produces antiprotons by directing the beam

into a nickel target (see below). In a later step, the MI accelerates the protons from the Booster and the antiprotons from the Recycler to 150 GeV, and then injects them in opposite directions into the Tevatron.

The proton-nickel collisions produce a large number of particles that are filtered through a pulsed magnet mass-charge spectrometer to select the small fraction ( $10^{-5}$ ) of the desired antiprotons. A lithium-current lens then focuses the beam. To reduce the momentum spread in each bunch, the antiproton beam is gradually “debunched” in the Debuncher (a triangular synchrotron). Subsequently, the Accumulator, housed in the same tunnel as the Debuncher, “stacks” the antiprotons from the Debuncher over a period of a few hours. In the mean time, the spread in transverse momentum is reduced using stochastic “cooling.” The antiprotons are periodically transferred from the Accumulator to the Recycler, which sits on top of the Main Injector. The Recycler uses both stochastic cooling and electron cooling systems [80] to further cool the antiprotons than the Accumulator is capable of doing, providing thereby more compact, brighter  $\bar{p}$  bunches. Finally, the antiprotons are injected into the Main Injector which accelerates them to 150 GeV, as mentioned above.

### 2.1.3 The Tevatron

The Tevatron is a superconducting synchrotron that accelerates the injected protons and the antiprotons simultaneously up to 980 GeV, while the field in the superconducting dipole magnets, operated at 4 K in a bath of liquid helium, increases to a final value of 4.2 T, as the power from the RF field of superconducting cavities is transferred to the beams. The counter-circulating beams are focused in a narrow collision region by special quadrupole magnets near the CDF and DØ detectors.

During the period of collisions, also known as a “store,” the proton and antiproton beams in the Tevatron have 36 bunches each, and the bunches cross every 396 ns. There are about  $2.7 \times 10^{11}$  protons and  $7.0 \times 10^{10}$  antiprotons per bunch, giving an instantaneous luminosity ( $\mathcal{L}_{\text{inst}}$ ) of about  $200 \times 10^{30} \text{ cm}^{-2}\text{s}^{-1}$ . The instantaneous luminosity is defined as,

$$\mathcal{L}_{\text{inst}} = \frac{f N_p N_{\bar{p}}}{A}, \quad (2.1.1)$$

where  $f$  is the bunch crossing frequency, and  $N_p$  and  $N_{\bar{p}}$  are the number of particle per bunch, and  $A$  is the effective cross-sectional area of the beams. In particular,  $A$  can be expressed in terms of the transverse widths of the proton and antiproton beams, and the luminosity in the Tevatron can be written as

$$\mathcal{L}_{\text{inst}} = \frac{f N_p N_{\bar{p}}}{2\pi(\sigma_p^2 + \sigma_{\bar{p}}^2)} F, \quad (2.1.2)$$

where  $\sigma_p$  ( $\sigma_{\bar{p}}$ ) is the effective standard deviation of the proton (antiproton) beam distribution at the interaction point in the detector, and  $F$  is a factor that can depend on the bunch length and interaction point. For Tevatron Run II,  $\sigma_p$  and  $\sigma_{\bar{p}}$  are about 25-30  $\mu\text{m}$ , and the “form factor” is  $F = 0.7$  [81]. The instantaneous luminosity during the run exceeded  $400 \times 10^{30} \text{ cm}^{-2}\text{s}^{-1}$  at the beginning of stores. After the collisions, the instantaneous luminosity decreased, and the store usually ended within  $\approx 24$  hours.

## 2.2 The DØ Detector

The multi-purpose DØ detector sketched in Figure 2.2, consists of three major sub-systems: a tracking detector for measuring momenta of charged particles and identifying the vertices of interactions, a uranium-liquid argon calorimeter for measuring the energies of electromagnetic and hadronic showers, and a muon spectrometer for measuring muon momenta. In this section, we first introduce the coordinate system used at the DØ experiment, and sequentially discuss the most important aspects of the subcomponents of the detector. More details on the DØ detector can be found in Ref. [8].

### 2.2.1 The Coordinate System

A cylindrical coordinate system, with the origin at the center of the detector, is used to describe positions in the DØ experiment. The positive  $z$  direction is defined along the direction of the incoming proton, which are circulating clockwise in the ring, and the  $x$  and  $y$  axes point vertically upwards and towards the center of the Tevatron ring, respectively.

Owing to the fact that the detector components are almost symmetrically distributed in azimuthal angle,  $\phi = \tan^{-1} \frac{y}{x}$ , we use a cylindrical coordinate system

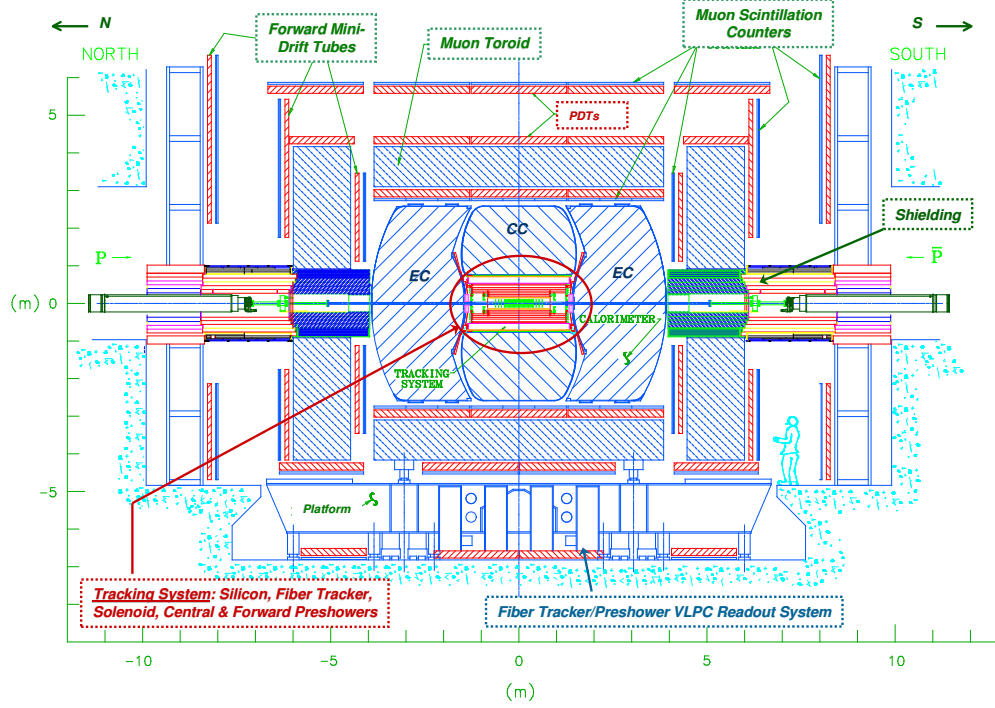


**Figure 2.2** Schematic profile of the DØ detector [7].

$(r, \theta, \phi)$ , where the polar angle  $\theta = \tan^{-1} \frac{r}{z}$  and  $r = \sqrt{x^2 + y^2}$ , instead of a Cartesian system to describe measurements. Furthermore, since hard scatters take place between partons within protons and antiprotons, the longitudinal momentum of the colliding objects (in the  $z$  direction) is unknown. Assuming conservation of transverse momentum in the collision, we represent the final objects using variables invariant under Lorentz boosts in the  $z$  direction. In particular, we choose the transverse momentum (the momentum in the  $(x, y)$  plane,  $p_T$ ), the pseudorapidity ( $\eta$ ), and the azimuthal angle in the transverse plane ( $\phi$ ), and the observed energy ( $E$ ) to describe the kinematic properties of all objects.

The pseudorapidity is defined as  $\eta = -\ln \tan \frac{\theta}{2}$  or  $\eta = \frac{1}{2} \ln \left( \frac{|\mathbf{p}| + p^z}{|\mathbf{p}| - p^z} \right)$ , where  $|\mathbf{p}|$  is the magnitude of the momentum vector, and  $p^z$  is its longitudinal component, and rapidity is defined as  $y = \frac{1}{2} \ln \left( \frac{E + p^z}{E - p^z} \right)$ . The difference in  $\eta$  between any two objects is invariant to Lorentz transformations along the  $z$  direction. In practice, the rapidity is often replaced with the angular variable pseudorapidity, which equals the rapidity for massless particles.

Pseudorapidity of particles in the final state is calculated with respect to the

measured position of each vertex. In studying different regions of the detector, it is more convenient to use the detector pseudorapidity ( $\eta^{\text{det}}$ ), which reflects  $\eta$  measured relative to the center of the detector.

### 2.2.2 The Tracking System

The central tracking system of the innermost detector is designed to reconstruct trajectories of charged particles and the interaction vertices within  $|\eta^{\text{det}}| < 3$ . Surrounding the beryllium beam pipe, it consists of a silicon microstrip tracker (SMT) and a central fiber tracker (CFT). The entire tracking system resides within a 2 T solenoidal superconducting magnet that produces a magnetic field along the  $z$  direction that bends the trajectories of charged particles in the  $(r, \phi)$  plane. The polarity of the superconduction is reversed at regular intervals to minimize the impact of any detector asymmetries related to the direction of the field. The charge and momentum of the particle are determined from the direction and the transverse radius of curvature of the trajectories. The expected resolution of the central tracking system is  $\delta p_T \approx 0.5$  GeV at  $p_T = 10$  GeV and  $|\eta| = 0$ .

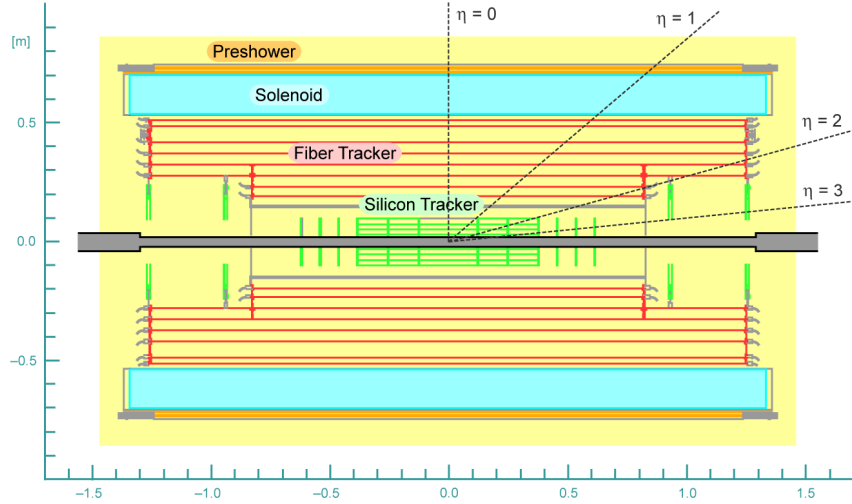


**Figure 2.3** Schematic profile of the central tracking system [7].

The inner-most part of the central tracking system shown in Figure 2.3 is the SMT, which consists of wafers of n-type silicon etched with many p-type silicon strips. A passing charged particle ionizes the silicon and creates electron-hole

pairs. Upon application of a reverse-bias voltage, the ionized electrons drift across the wafer and are collected and read out electronically at the edge of each unit.

There are both single-sided and double-sided SMT modules. For the latter, the two surfaces are implanted with p-type and n-type silicon strips respectively. Moreover, the strips in one surface are aligned at a small stereo angle with respect to the other surface, providing a three dimensional measurement of position.

Figure 2.4 shows the three subdetectors of the SMT: the central barrels, the F disks and the H disks. The design maximizes the number of particles that meet the silicon surface at a right angle, for a  $\approx 25$  cm wide Gaussian-distributed collision profile along the beam axis. Entering the silicon wafer at right angle reduces the area of charge deposition, and results in a more precise measurement of position and of the momenta of particles emitted in the collision.

The central barrels are constructed of six modules, and interspersed with six F disks, while the forward and backward regions each have three F disks and two large-diameter H disks. The barrel modules have five concentric layers of silicon detectors, in which the strips are aligned along the beam axis, providing  $(r, \phi)$  measurements. The F and H disks are made of 12 double-sided and 24 single-sided wedges, respectively, and are used to measure both the  $(r, \phi)$  and  $(r, z)$  components of a particle trajectory.

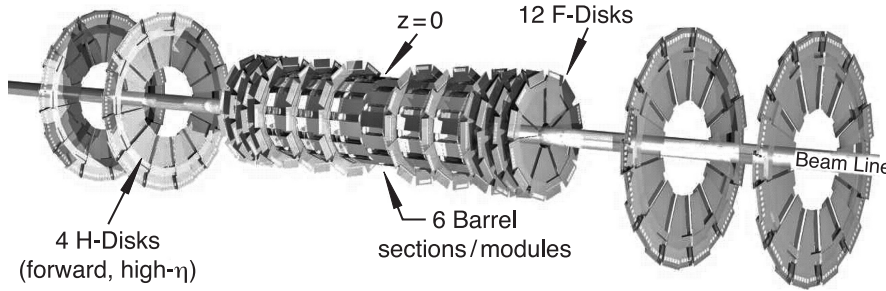


**Figure 2.4** The arrangement of the Silicon Microstrip Tracker [8].

Among the five silicon layers in the central barrels, the innermost one (Layer-0) was added in 2005 to cope with the expected increase in instantaneous luminosity [82]. This “radiation hard” layer improves the vertexing capability by adding a tracking point close to the interaction region.

The SMT has 50 and 62.5  $\mu\text{m}$  pitch stripes for the p and n-types silicon channels, respectively, a coverage of up to  $|\eta^{\text{det}}| \approx 3$ , and provides  $\approx 20 \mu\text{m}$

spatial resolution.

The CFT is made of scintillating fibers mounted on eight concentric cylinders outside the SMT, providing coverage for  $|\eta^{\text{det}}| < 1.7$ . When a charged particle penetrates a fiber, the scintillator emits light through a rapid fluorescence. Read-out fibers are coupled to waveguides that transport the scintillation light to visible light photon counters (VLPC) for processing.

Each cylindrical layer consists of a doublet layer of fibers oriented along the beam axis and a second doublet layer at a stereo  $+3^\circ$  or  $-3^\circ$  angle in  $\phi$ . Starting with the innermost layer, the  $+3^\circ$  and  $-3^\circ$  layers are alternated. Moreover, to accommodate the forward SMT H disks, the two innermost cylinders are 1.66 m long, while the outer six are 2.52 m long. A  $100\ \mu\text{m}$  resolution is achieved by the CFT alone.

### 2.2.3 The Calorimeter

Photons, electrons, and hadrons interact with nuclei in the medium of sampling calorimeters and these interactions produce cascades (showers) of particles. Calorimeters are designed to measure the energy these showers of particles deposit in the sensitive regions of the detectors. A high energy electron penetrating material of large atomic number (e.g., uranium) initially radiates photons in a process known as Bremsstrahlung. A radiated high energy photon penetrating the material further will produce an electron and positron pair. Hence, both electrons and photons of high energy produce extensive electromagnetic showers (i.e., with an increasing numbers of lower-energy electrons and photons as the shower develops). On the other hand, high energy hadrons such as charged pions interact with nuclei of the material via the strong force. This interaction produces secondary hadronic particles and a subsequent hadronic shower (a large number of hadronic particles, but also photons from decays of hadrons). Once the particles in the electromagnetic and hadronic showers have sufficiently low energies, their dominant interaction with the calorimeter material will be through ionization of atoms, which can also be detected.

DØ has preshower detectors, located between the solenoid and the calorimeter, that are used to initiate particle (especially electromagnetic) showers. They consist of layers of scintillators and lead: the lead induces high energy photons or electrons to begin showering and the scintillators provide a sampling of deposited

energy and a measurement of position. The central preshower (CPS) and forward preshower (FPS) detectors cover the regions  $|\eta^{\text{det}}| < 1.3$  and  $1.4 < |\eta^{\text{det}}| < 2.5$ , respectively. They also improve photon and electron identification and background rejection by enhancing the spatial matching of charged tracks with showers in the calorimeter.

The calorimeter is comprised of a central calorimeter (CC) and two end calorimeters (EC), as shown in Figure 2.5. The central calorimeter covers a range up to  $|\eta^{\text{det}}| = 1$ , while the end calorimeters extend the coverage to  $|\eta^{\text{det}}| \approx 4$ . Most calorimeter cells have transverse dimensions of  $\eta^{\text{det}} \times \phi$  of  $0.1 \times 0.1$  rad, except in the most forward regions of  $\eta$ , where they are  $0.2 \times 0.2$  rad, as shown in Figure 2.6. All three calorimeters are contained within their separate cryostats, which are cooled with liquid nitrogen to keep the detector temperature  $< 90$  K. These modules are constructed from alternating layers of absorbing material (mainly uranium) that induces the electromagnetic and hadronic showers, and sampling material (liquid argon) where the ionization is measured.

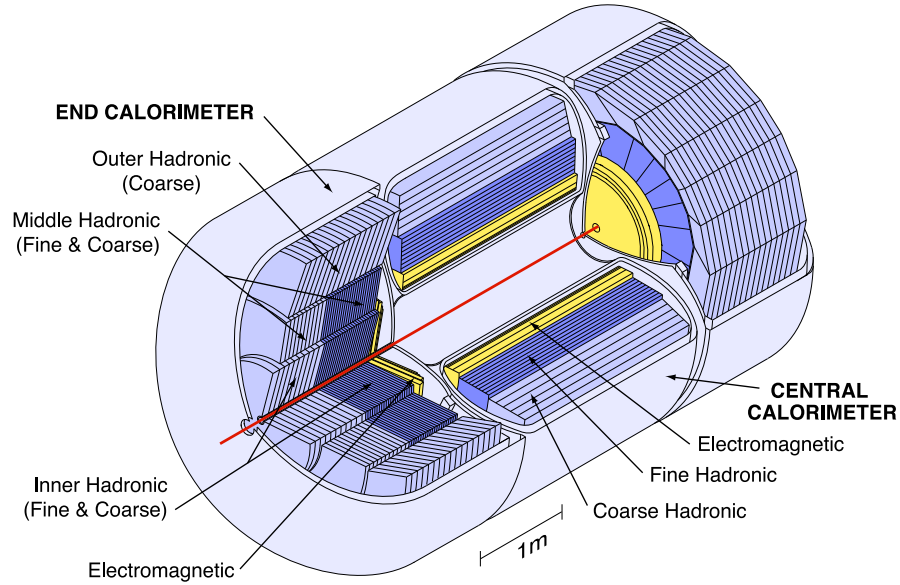


**Figure 2.5** Isometric view of the central and two end calorimeters [8].

Each of the calorimeter modules contain four layers of electromagnetic (EM) calorimeter cells, followed outwards by three layers of fine hadronic (FH) calorimeter cells and a final layer of coarse hadronic (CH) cells. The layer arrangement is required because hadronic showers transverse typically an order of magnitude

longer distances in depth than electromagnetic showers. With this kind of arrangement, electromagnetic and hadronic showers are expected to deposit most of their energies in the EM and hadronic layers, respectively. In addition, the peaks of electromagnetic showers occur in the third layer of the EM calorimeter, this layer is therefore segmented into finer cell sizes of  $0.05 \times 0.05$  rad. The absorbers are made of 4 mm thick plates of depleted uranium in the EM layers, and 6 mm thick plates of uranium-niobium (2%) alloy in the FH layers, and copper (CC) or stainless steel (EC) in the CH layer. The sampling material consists of 2.3 mm gaps of liquid argon.

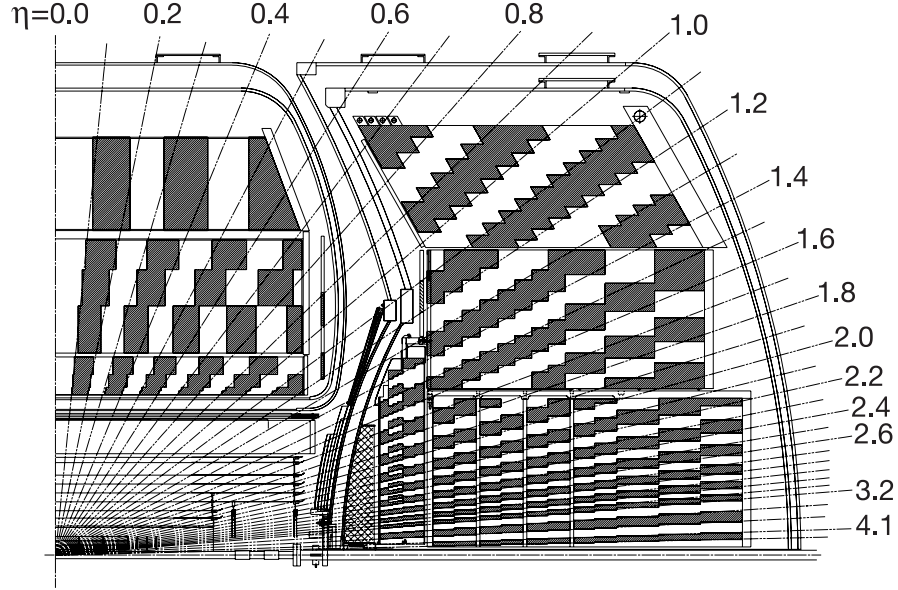


**Figure 2.6** Cross section of one quarter of the calorimeter [8]. Towers of different cell size are shown projected to the center of the detector.

To compensate for the lack of shower sampling in the region between the cryostats, a so-called intercryostat detector (ICD) is instrumented between the CC and EC ( $1.1 \leq |\eta^{\text{det}}| \leq 1.5$ ). The ICD consists of scintillating tiles mounted on the outer wall of the EC cryostats that are read out using photomultiplier tubes (PMT).

The energy resolution of the electromagnetic and hadronic calorimeter can be

parametrized as follows,

$$\left(\frac{\sigma(E)}{E}\right)^2 = C^2 + \frac{S^2}{E} + \frac{N^2}{E^2}, \quad (2.2.1)$$

where  $C$  is an energy independent term that reflects the uncertainty of the overall calibration,  $S$  reflects the fluctuation from energy sampling and deposition, and  $N$  reflects the instrumental noise. Different constants are needed for describing electrons, photons, and hadronic particles. The energy resolutions are about 4% and 15% for electrons and jets with  $p_T = 40$  GeV. We will use this parametrization to model detector effects in the ME analysis in Section 6.1.3.3.

### 2.2.4 The Muon Spectrometer

Only energetic muons and neutrinos are expected not to be absorbed in the calorimeter. In particular, muons pass through the calorimeter because they do not interact via the strong force, but they nevertheless can ionize and often emit bremsstrahlung. The DØ muon spectrometer is consequently located outside of the calorimeter.

The muon detector consists of three parts: the central muon system ( $|\eta^{\text{det}}| < 1$ ), the forward muon system ( $1 < |\eta^{\text{det}}| < 2$ ), and a toroidal magnet of 1.8 T. Both of the muon systems use wire drift tubes and scintillation counters. The drift tubes are arranged in three layers, where layer A is located between the calorimeter and the toroidal magnet, and layers B and C are outside the magnet.

The drift tubes are made of rectangular aluminum tubes, filled with a gas mixture. Each tube has an anode wire at the center, which gives information on position of the muon trajectory, and vernier cathode pads positioned above and below the anode. When a charged particle passes through the tube, the gas is ionized and electrons liberated by ionization drift toward the anode. The drift time and charge deposition are recorded and used to determine the position of the deposited ionization (“hit”).

The central muon detector is instrumented with proportional drift tubes (PDT) as shown in Figure 2.7. The PDT contain a gas mixture of 84% argon, 8% methane, and 8% CF<sub>4</sub>, which is optimized for faster drift times of the high instantaneous-luminosity environment of Run II. Because the drift time of the

PDT (750 ns) is still longer than the bunch crossing time at the Tevatron, two additional layers of scintillators, the A- $\phi$  scintillators (situated between the calorimeter and layer A) and the “cosmic-cap” scintillators (located outside the layer C) shown in Figure 2.8, are used to trigger muon events and reject cosmic muons. Furthermore, the A- $\phi$  scintillators are also used to reject any other particles that emerge from the calorimeter. The coverage of the bottom scintillators is reduced because the detector is supported there from the ground.

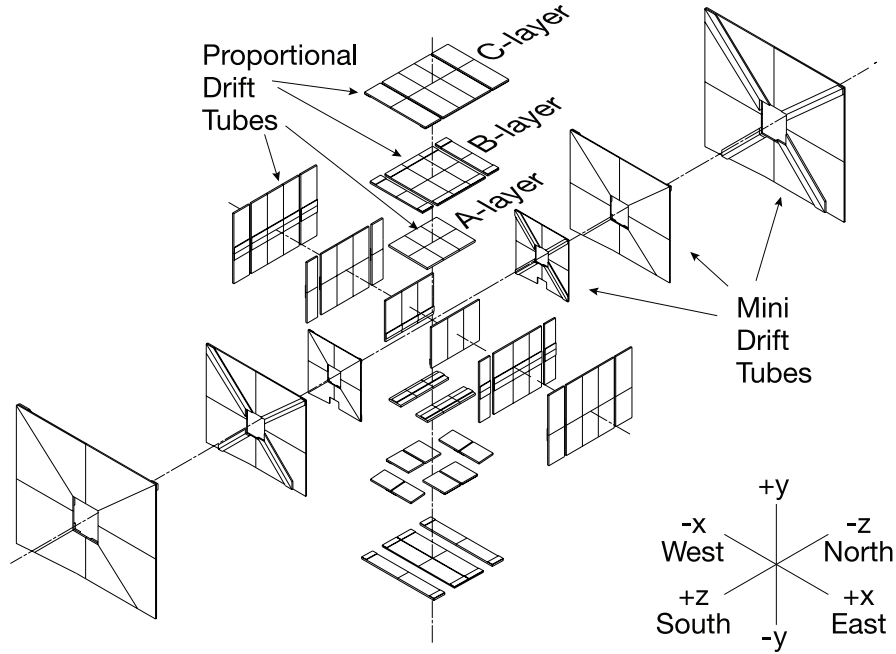


**Figure 2.7** Exploded view of the muon drift-tube system [8].

The forward muon detector is instrumented with mini drift tubes (MDT) and scintillation counters. Although the drift time of the MDT is only 60 ns, the scintillators are also used to trigger on muon events and to reject cosmic muons and other backgrounds.

The toroidal magnet provides the momentum measurement, with trajectories always bending in the  $(r, z)$  plane of the muon systems. This offers cleaner matching to central tracks and helps reject muons from  $\pi/K$  decays. The external muon system also helps to improve momentum resolution for high momentum muons detected in the central tracker.

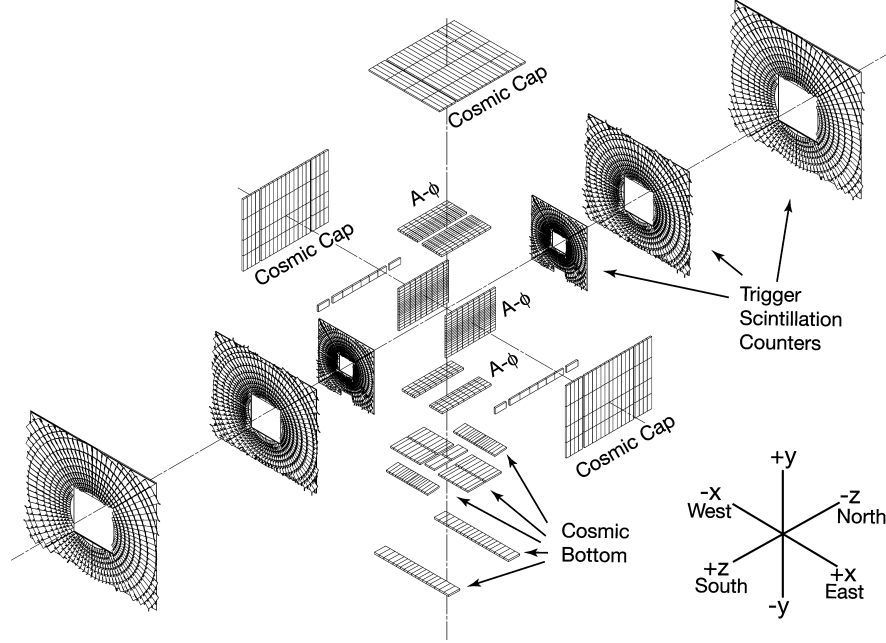


**Figure 2.8** Exploded view of muon scintillation-detector system [8].

### 2.2.5 The Luminosity Monitor

The luminosity monitor is used to determine the Tevatron luminosity at the DØ interaction region, which is accomplished through measuring the rate of inelastic  $p\bar{p}$  collisions. The cross section for these collisions is dominated by soft processes, where no high  $p_T$  particles are produced. In addition, most of the particles produced in these processes are emitted from the interaction point close to or inside the beam pipe, and are not observed.

The two luminosity monitors are therefore situated at  $z = \pm 140$  cm relative to the center of the detector, close to the beam pipe, and cover the range of  $2.4 < |\eta^{\text{det}}| < 4.4$ . The monitors are made of scintillators, and the light from the scintillating medium is recorded using PMT.

To distinguish the  $p\bar{p}$  interactions from collisions in the beam halo, the  $z$  coordinate of the interaction vertex is calculated from the difference in time-of-flight between the  $+z$  and  $-z$  luminosity monitors. Particles produced from the  $p\bar{p}$  interactions have smaller time-of-flight difference than those from the beam halo. The overall uncertainty on integrated luminosity is 4.3-6.1%.

### 2.2.6 Trigger System and Data Acquisition

The 1.7 MHz beam crossing frequency at the Tevatron is much larger than the rate that can be written to tape, and is impractical to analyze. A three-level trigger system, illustrated in Figure 2.9, is therefore required to determine in real time which events are interesting enough to record. The trigger system is designed to select events containing leptons or jets of large  $p_T$ , and reduce the rate down to  $\approx 150$  Hz. The trigger list is updated over time to accommodate the changes in running conditions, most of all, the increasing instantaneous luminosity.

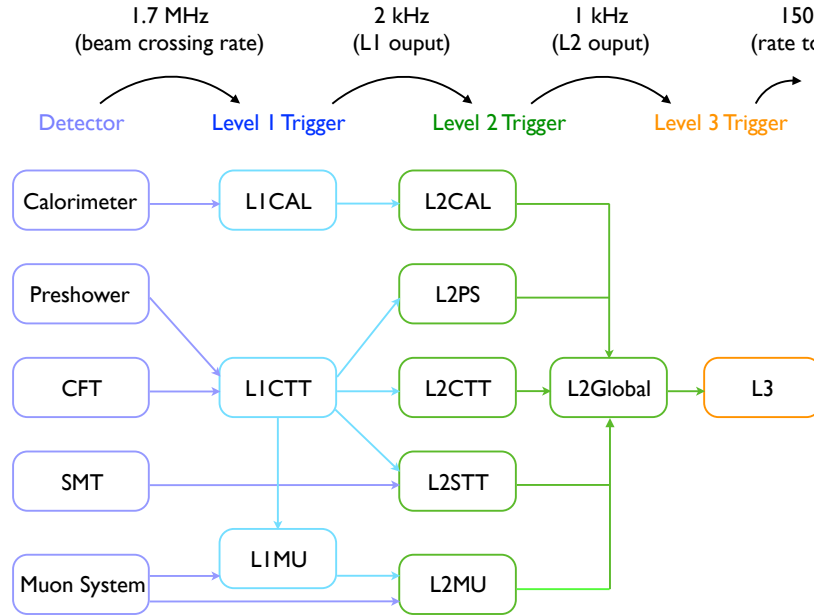


**Figure 2.9** Schematic overview of the trigger system.

The first stage (Level 1 or L1), of the trigger system comprises a collection of hardware trigger elements, and examines every event for interesting features, including tracks, energy depositions, and muon transverse momenta. It takes less than  $3.5 \mu\text{s}$  to make a decision, and sends about 2000 events per second to the second stage (Level 2).

To reconstruct the trajectories of charged particles, the Level 1 central track trigger (L1CTT) uses fast discriminator data from the CFT, the central and forward preshower detectors. It compares the hits in  $4.5^\circ$  sectors in the transverse plane with predefined hit maps that represent the curvature paths imposed by the magnetic field.

The Level 1 calorimeter trigger (L1CAL) is used to look for patterns of energy deposition exceeding programmed limits on  $p_T$ . The trigger inputs consist of energies from electromagnetic and hadronic trigger towers, where each tower is defined by  $\Delta\eta \times \Delta\phi = 0.2 \times 0.2$ . Electron triggers, use the  $p_T$  of the electromagnetic towers, while jet triggers, the sum of the electromagnetic and hadronic towers.

Looking for patterns consistent with muons, the Level 1 muon trigger (L1MU) exploits hit information from muon chambers, muon scintillators, and tracks from the L1CTT. This allows the L1MU to match an object from the muon detector with tracks in the tracking system.

The Level 2 (L2) trigger refines the data from the L1 trigger to form physical objects, and then combines data from different subdetectors to examine event-wide correlations and make global decisions. It is used to reduce the event rate to  $\approx 1000$  Hz, and to send the events to the third stage, Level 3 (L3) trigger.

The L2 trigger decisions are made for charged tracks, calorimeter objects (electrons and jets), and muon candidates. In addition to the CTT tracks, it includes information from the silicon track trigger (STT), which improves momentum resolution. The STT also helps to tag heavy-flavor decays by providing the impact parameters of reconstructed tracks relative to the beam axis. The L2 calorimeter trigger (L2Cal) identifies jets and electrons/photons by forming clusters using trigger towers. Moreover, it calculates the vector sum  $p_T$  from the individual trigger tower passed on from L1 to reconstruct the imbalance in transverse momentum (often called  $\cancel{E}_T$ ) for each event. The L2 muon trigger (L2MU) uses calibration and more precise timing information to improve the quality of muon candidates. Finally, the L2 global trigger provides decisions by creating and examining the global physical objects.

The Level 3 trigger (L3) implements a simplified event reconstruction algorithm that relies on the high-precision calorimeter readout and the position of the primary vertex. Using a farm of computers, it provides decisions on whether the events passing the L2 trigger should be saved on tape for offline analyses. The final recorded event rate is, in fact, reduced to  $\approx 150$  Hz, as planned.

## 3 Object Reconstruction and Identification

As described in Section 2.2.6, the trigger system selects events interesting enough to be recorded. To obtain the objects used in the analysis, the recorded events are subsequently processed through reconstruction software. In general, the software finds hits in the subdetectors, reconstructs tracks in the central tracker and clusters in the calorimeter, and combines the tracks and the calorimeter clusters to form physical objects, such as electrons, muons, and jets. In this chapter, we describe the reconstruction of tracks and track vertices, as well as the final-state objects involved in the single top-quark analysis: electron, muons, jets, imbalance in transverse momentum (accounting for escaping neutrinos), and jets originating from  $b$  quarks ( $b$ -jets).

### 3.1 Tracks

The reconstruction of electrons and muons requires track matching, and jet reconstruction can be improved significantly by combining calorimeter and tracking information.

As a charged particle passes through the tracking system, it leaves a small amount of energy in the layers of the detectors. This energy is reconstructed into hits in each layer, indicating the location of the particle. The track is then reconstructed from these hits by two steps. First, two tracking algorithms, the histogram track finding (HTF) and the Alternate Algorithm (AA), are exploited to combine the hits into a track. The HTF uses the curvature and the direction of the track at the origin [83], while the AA reconstructs tracks taking the missing hits and the primary vertices into account [84]. The track candidates are passed to a track fitter based on a Kalman Filter algorithm [85]. Refitting and smoothing

all the track candidates, the Kalman Filter algorithm reconstructs the final track parameters with proper uncertainties [85].

## 3.2 Primary Vertices

The primary vertex represents the location of a collision between the proton and the antiproton that is the origin of the particles produced in the collision. Reliable vertex reconstruction is needed to distinguish hard interactions from small  $p_T$  inelastic scattering (also known as the underlying event or minimum bias interaction).

The main challenges of the primary vertex reconstruction are the capabilities to discriminate tracks from secondary vertices, which correspond to decaying heavy hadrons, and additional inelastic scatterings close to the primary vertex. This situation gets worse as the instantaneous luminosity increases and the combinatorics with increased numbers of hits create fake particles. To accommodate to these situations, an adaptive primary vertex algorithm [86] is developed and used to reconstruct the primary vertex at DØ.

First of all, the tracks with a minimum transverse momentum of 0.5 GeV and at least two hits in the acceptance region of the SMT are selected to find the primary vertex. All the tracks of a cluster within 2 cm in  $z$ -axis are fitted into a common vertex with the Kalman filter vertex fitting algorithm, which in turn removes the track with the highest  $\chi^2$  contribution to the vertex until the total  $\chi^2$  per degree of freedom is smaller than 10. Among the remaining tracks, only the ones whose closest distances in  $(x, y)$  plane are within 5 standard deviations of the beam spot calculated in the previous step are further selected. With these selected tracks, the uncertainties of the tracks are reweighted according to their  $\chi^2$  distributions, and the vertex is fitted iteratively until it converges.

There are usually several vertices reconstructed in a single event. To figure out the hard scattering vertex, the transverse momenta of the tracks at each vertex are used. Since the tracks originating from the inelastic interactions tend to have lower transverse momenta, the probability that a track comes from an inelastic interaction is calculated from data accordingly, and the overall probability that a vertex represents an inelastic interaction is also evaluated. The vertex with the lowest inelastic probability is therefore considered as the primary vertex.

### 3.3 Electrons

Electrons are expected to deposit most of their energy in the electromagnetic calorimeter, but being charged particles, they also leave ionization in the central tracking system. They can therefore be reconstructed by matching a cluster of energy in the EM calorimeter with a track in the trackers, as illustrated in Figure 3.1.

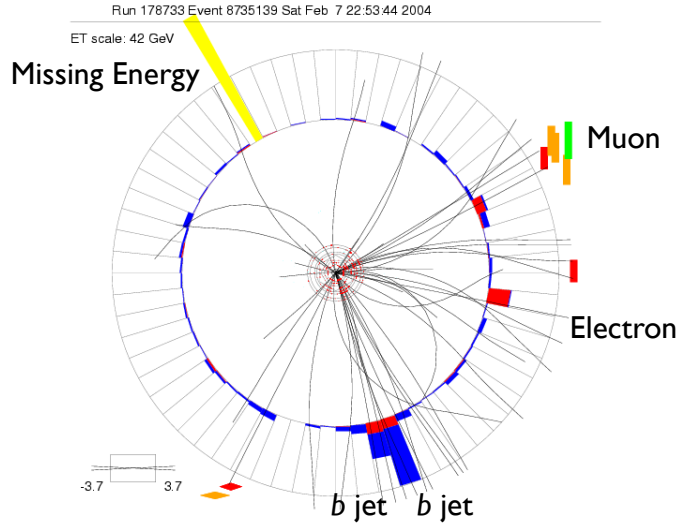


**Figure 3.1** An event display showing an electron, a muon, two  $b$ -tagged jets, and the missing energy [9].

The reconstruction of electrons starts with clustering nearby EM calorimeter towers, where a tower is defined by adding the energies measured in calorimeter cells<sup>1</sup> of all four EM layers plus the first hadronic layer. Around the tower with the highest transverse energy ( $E_T$ ), adjacent towers with  $E_T > 50$  MeV in a cone of radius  $R = \sqrt{(\Delta\eta)^2 + (\Delta\phi)^2} = 0.2$  are added up, forming an EM cluster. Energy deposits in the preshower detectors are also added to the EM cluster and used to determine its direction if they lie within a window of  $\eta \times \phi = 0.05 \times 0.05$  of the center of the EM cluster. Because the energy resolution of electrons is poor in the intercroystat region, the EM objects with a detector pseudorapidity between 1.1 and 1.5 are rejected.

<sup>1</sup>The energy has to be above the noise threshold, which is determined using the T42 algorithm [87].

Electrons and photons are expected to deposit most of their energies in a cone of radius 0.2, while jets have significant deposits outside the 0.2 cone. Therefore, the EM objects are required to be isolated,

$$f_{iso} = \frac{E_{tot}(R < 0.4) - E_{EM}(R < 0.2)}{E_{EM}(R < 0.2)} < 0.2, \quad (3.3.1)$$

where  $E_{tot}(R < 0.4)$  is the total energy in all the towers (except those in the coarse hadronic calorimeter) within a cone of radius 0.4 around the direction of the cluster, and  $E_{EM}(R < 0.2)$  is the energy in the EM calorimeter within a cone of radius 0.2. Moreover, since the energy deposition for electrons and photons mainly takes place in the EM calorimeter, the electromagnetic fraction of an EM object has to be greater than 0.9,

$$f_{EM} = \frac{E_{EM}(R < 0.2)}{E_{tot}(R < 0.2)} > 0.9. \quad (3.3.2)$$

In addition, electrons are distinguished from photons by matching to a track in the central tracking system. Quantitatively, the probability of  $\chi_{\text{spat}}^2$  is required to be greater than 0,

$$p(\chi_{\text{spat}}^2) > 0, \quad (3.3.3)$$

where  $\chi_{\text{spat}}^2$  determines how well a track matched to an EM cluster in space, and is defined as follows,

$$\chi_{\text{spat}}^2 = \left( \frac{\delta\phi}{\sigma_\phi} \right)^2 + \left( \frac{\delta z}{\sigma_z} \right)^2. \quad (3.3.4)$$

$\delta\phi$  in Equation (3.3.4) represents the difference in  $\phi$  between the extrapolated track impact and the EM cluster at the third layer of the EM calorimeter, the layer with the best granularity,  $\delta z$  is the difference in  $z$ -axis between the vertices calculated from the track and from the EM cluster, and  $\sigma_\phi$  and  $\sigma_z$  are the root-mean-squares (RMS) of the experimental distributions of the corresponding quantities [88].

The main background sources which mimic electrons are high  $p_T$  electrons coming from photons ( $\gamma \rightarrow e^+e^-$ ) and jets dominated by a leading  $\pi^0$  which decays to two photons ( $\pi^0 \rightarrow \gamma\gamma$ ). To further discriminate electrons from the backgrounds, a boosted decision tree (BDT) is introduced. The information used in the BDT classifier is listed below:

- **Shower shape:** The EM fraction, as defined in Equation (3.3.2), tends to

be close to one for real electrons, and small for jets. Moreover, a covariance matrix is built up to describe the shower shape, and the correlations between energies deposited in different calorimeter cells. The longitudinal shape is reflected through the fraction of energy deposited in each layer of the calorimeter. The transverse shape is described by several variables in the third layer of the electromagnetic calorimeter. In addition, the total energy and the longitudinal position of the primary vertex are included, accounting for the dependence on the energy and impact parameter. A  $\chi^2$  is evaluated from this matrix for each electron candidate, quantifying how consistent the shower shape of the candidate is with that of an electron [89].

- **Calorimeter isolation:** Since electrons tend to be within narrower cones than jets, the calorimeter isolation for an EM object, as defined in Equation (3.3.1), is also used in the BDT classifier.
- **$E_{cal}/p_{trk}$ :** The momentum of electrons measured in the tracker is expected to be consistent with the energy measured in the EM calorimeter, since electrons are expected to deposit most of their energies in the EM calorimeter. Decays of  $\pi^0 \rightarrow \gamma\gamma$  matching with random tracks tend to have large values of  $E_{cal}/p_{trk}$ , because the matched tracks are likely to have low  $p_T$ . On the other hand, the charged hadrons are expected to deposit most of their energies in the hadronic calorimeter, and therefore their  $E_{cal}/p_{trk}$  values are usually small.
- **Track isolation:** The track isolation variable is defined as the total  $p_T$  of the reconstructed tracks within a hollow cone of  $0.05 < R < 0.4$  around the candidate electron. This variable is used to reduce the  $\pi^0$  produced in association with charged hadrons [90].
- **Track matching:** The quality of matching a track to an EM cluster can be quantified as the probabilities of the  $\chi^2$  in terms of the spatial and kinematic phase space distances. The former is described in Equation (3.3.4), and the latter is defined as,

$$\chi_{\text{EM-track}}^2 = \left( \frac{\delta\phi}{\sigma_\phi} \right)^2 + \left( \frac{\delta z}{\sigma_z} \right)^2 + \left( \frac{E_{cal}/p_{trk} - 1}{\sigma_{E_{cal}/p_{trk}}} \right)^2, \quad (3.3.5)$$

where  $E_{cal}/p_{trk}$  is defined above and  $\sigma_{E_{cal}/p_{trk}}$  is the RMS of the associated experimental distribution.

Data samples containing real and fake electrons are used to train the BDT classifier. A clean sample of  $Z \rightarrow ee$  events is used as the sample of real electrons, whereas a sample containing dijet events is used to obtain the fake electrons. Owing to different signal to background ratios and resolution of input variables, the BDT classifier is constructed separately in four combinations: central and end calorimeter, high and low instantaneous luminosity [91].

Electrons are identified by the BDT discriminant ranging between -1 and 1. Two categories of electrons are defined with different qualities. The “loose isolated” electrons are required to have the discriminant value larger than -0.96, while the “tight isolated” electrons have the discriminant value greater than -0.22. The tight criterion is used to define the electrons in the analysis, and the loose one is to define the orthogonal sample for the multijet background modeling. The details of the electron selection is presented in Section 5.1.

The calibration of electron energy is implemented through the response of each EM calorimeter cell, and the corrections for energy loss in detector material [92]. An additional calibration is obtained using  $Z \rightarrow e^+e^-$  events, with the electron energy corrected to match the accepted invariant mass of the  $Z$  boson.

### 3.4 Muons

Muons are expected to pass through all the detector material inside the muon detector, and, being charged particles, they too leave ionization in the central tracking system, and can be reconstructed and identified through the combination of information from the muon detector and the central tracking system, as illustrated in Figure 3.2, where the former identifies muons, and the latter finds tracks and provides precise momentum resolution.

Starting with objects reconstructed in the muon detector, or “local muons,” the muon candidates are required to match to a track in the central tracking system. To reduce the background sources, such as muons from heavy flavor hadrons (the hadrons containing  $b$  or  $c$  quarks) decays, cosmic muons, and tracks and muon detector hits produced by other particles, a series of requirements are

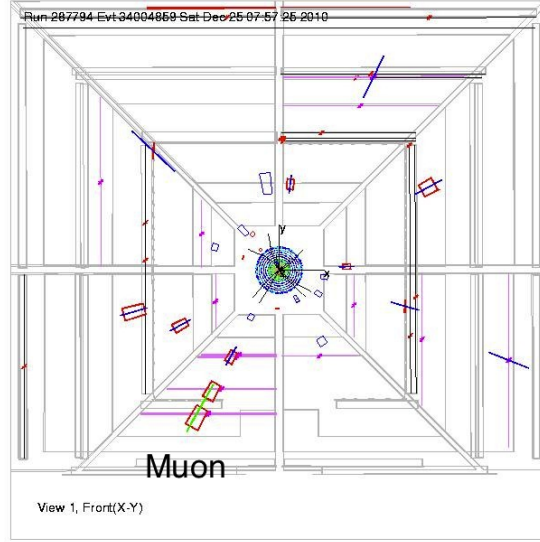


**Figure 3.2** An event display showing the presence of a muon [10].

applied. The muon identification therefore includes three parts: the local muon, the matching track, and the isolation criteria.

To suppress the charged hadrons which pass through the calorimeter and enter the muon detector, the local muons must have at least two A layer wire hits, at least one A- $\phi$  scintillator hit, and at least two wire hits in B or C layers. For the forward muon ( $|\eta^{\text{det}}| > 1$ ), at least one cosmic cap scintillator hit is also required [93]. Cosmic muons are rejected by requiring all the scintillator hits within a timing window of 10 ns from the expected time when a muon from the hard interaction point arrives to the detector [93]. The track quality relies on the track characteristics: the number of hits in the SMT or CFT systems, the  $\chi^2$  per degree of freedom of the central track fit, and the transverse impact parameter (distance of closest approach in the transverse plane, or  $dca$ ) with respect to the beamline ( $z$ -axis). The tracks matched to the muon candidates have to fulfill the following requirement [93]:

- The absolute value of  $dca$  is less than 0.2 cm.
- If the track has SMT hits, the absolute value of  $dca$  should be less than 0.04 cm.
- The  $\chi^2$  per degree of freedom is smaller than 9.5.

- There are at least 2 CFT hits on the track.

The muons fulfilling the above requirements are referred to as “loose isolated muons.” A “tight isolated muon” is a loose isolated muon with two additional isolation requirements. The isolation requirements are used to distinguish prompt muons (muons from electroweak processes) from secondary muons (muons from heavy flavor hadron decays). Since the secondary muons tend to be surrounded by additional hadronic activities from the  $b$  or  $c$  quark fragmentation, the prompt muons can be selected based on the information of tracks or calorimetric energy depositions around. The isolation criteria are therefore defined as follows [93],

- $\sum_{\text{tracks} \in \Delta R < 0.5} p_T(\text{track}) < 0.1 \times p_T(\mu)$ , where the left hand side is the scalar sum of transverse momenta of all tracks inside a  $\Delta R(\text{track}, \mu) < 0.5$  cone around the muon track and with  $\Delta z_0(\text{track}, \mu) < 0.2$  cm. The muon track itself is not included.  $p_T(\mu)$  denotes the transverse momentum of the muon itself, and this  $p_T(\mu)$  scale provides more powerful rejection in the low- $p_T$  region and higher efficiency in the high- $p_T$  region.
- $\sum_{\text{clusters} \in 0.1 < \Delta R < 0.4} E_T(\text{cluster}) < 0.1 \times p_T(\mu)$ , where the left hand side represents the scalar sum of transverse energies of all calorimeter clusters inside a hollow cone  $0.1 < \Delta R(\text{cluster}, \mu) < 0.4$  around the muon. Only the cluster from the fine hadronic and electromagnetic calorimeters are taken into account.

The details of the muon selection in this analysis are described in Section 5.1.

The muon momentum is determined by the track curvature. Using  $Z \rightarrow \mu^+ \mu^-$  and  $J/\psi \rightarrow \mu^+ \mu^-$  events, the muon momentum is calibrated to match the  $Z$  and  $J/\psi$  invariant masses [94].

### 3.5 Jets

Quarks and gluons evolve and hadronize immediately after production, eventually forming showers of mesons and baryons, as illustrated in Figure 3.3. The energies of these hadrons are mainly contained within the hadronic calorimeter, and jet reconstruction algorithms cluster these energy depositions into jets such that the kinematic properties (e.g., momenta and energies) of the jets can be related to the

corresponding properties of the original partons. In particular, when many soft gluons are radiated and are not included in the jet, the jet energy is mismeasured. Jet algorithms need to be “infrared safe.” Similarly, soft gluons can split into highly collimated  $q\bar{q}$  systems, and reconstructed jets must be also “collinear safe,” to account for these collimated quarks.

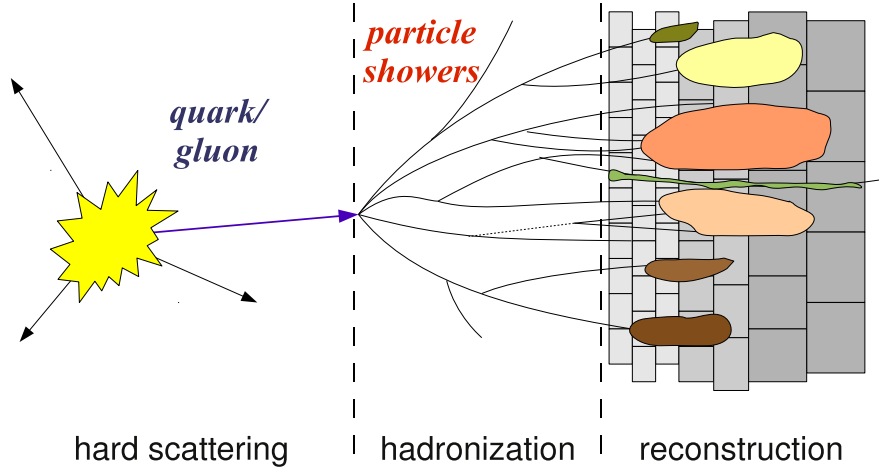


**Figure 3.3** A schematic overview of the hadronization of a parton and the form of a jet [11].

### 3.5.1 Jet Reconstruction and Identification

The DØ experiment reconstructs jets using the Run II midpoint cone algorithm [95, 96], which forms jets by associating together particles lying within a cone of a specific radius. The reason for using a cone structure is due to the radiation pattern of the initial energetic partons. Most of the DØ analyses use jets with a cone size of  $R_{\text{cone}} = 0.5$ .

Starting with a calorimeter cell, which is considered as a massless object, a four-momentum can be defined by the measured energy in the cell and the direction with respect to the primary vertex. A calorimeter tower is built from a space of  $\eta \times \phi = 0.1 \times 0.1$  containing the cells above some noise threshold. A tower with  $p_T > 500$  MeV initiates a precluster, and any other towers with  $p_T > 1$  MeV and within  $\Delta R < 0.3$  from the initial tower are combined with the precluster. Making use of preclusters instead of towers improves the collinear safety. While

the preclusters with  $p_T < 1$  GeV are removed, the remaining ones are used as seeds to form “proto-jets.” Looping over the preclusters ordered by decreasing  $p_T$ , if the distance<sup>2</sup>  $\Delta R(y, \phi) = \sqrt{(\Delta y)^2 + (\Delta \phi)^2}$  between the precluster and the closest proto-jet is smaller than  $R_{\text{cone}}/2$ , then the precluster is added to the proto-jets. If not, the precluster is considered as a new proto-jet candidate. The four-momenta of all towers within  $\Delta R(y, \phi) < R_{\text{cone}}$  around the candidate are summed (in the  $E$ -scheme [95]), leading to a new candidate centroid. This procedure is repeated iteratively until the centroid is stable. Next, each  $p_T$ -weighted average  $(y, \phi)$  midpoint between any pair of proto-jets satisfying  $R_{\text{cone}} < \Delta R(y, \phi) < 2R_{\text{cone}}$  is considered as a seed of a proto-jet, and the procedure of forming stable proto-jets is repeated with such a seed. This makes the jet algorithm insensitive to the soft radiation. Finally, in order to avoid double counting of energies, the merging/splitting algorithm is applied. If the overlapping energy of two proto-jets is more than 50% of the  $p_T$  of the lower- $p_T$  proto-jet, the two proto-jets are merged, and the centroid of the merged proto-jet is re-calculated. If the overlap is less than 50%, the two proto-jets are split: each overlapping tower is assigned to the closest proto-jet in terms of  $\Delta R(y, \phi)$ . The final jets with  $p_T > 6$  GeV are used in physics analyses.

In order to remove fake jets resulting from the calorimeter noise and the reconstruction biases, additional jet quality requirements are applied [97]. First, the fraction of the jet energy deposited in the coarse hadronic calorimeter has to be less than 0.4 and 0.46 in the central and end calorimeter, respectively. Second, the electromagnetic fraction of a jet is required to be greater than 5%, in order to avoid jets dominated by the hadronic noise. Similarly, it has to be less than 95% to differentiate from the EM objects. Third, the jet has to be confirmed by the Level 1 trigger [98],

$$R_{\text{L1}} = \frac{p_T^{\text{L1}}}{p_T^{\text{non-CH jet}}} > 0.5, \quad (3.5.1)$$

where  $p_T^{\text{L1}}$  is the sum of the scalar  $p_T$ s from the 100 hottest L1 towers in a cone of  $\Delta R < 0.5$  around the jet, and  $p_T^{\text{non-CH jet}}$  is the vector  $p_T$  sum over all reconstructed tower assigned to the jet, excluding the coarse hadronic calorimeter. To cope with the increasing instantaneous luminosity in the Run IIb data taking, for the Run IIb samples in particular, the jet has to contain at least two tracks

---

<sup>2</sup>The jet algorithm uses the rapidity  $y$ , which is invariant under the Lorentz boost along the  $z$  direction, as mentioned in Section 2.2.1.

associated with the primary vertex (also known as “jet vertex confirmation”). The purpose of selecting the vertex confirmed jets is to reject the particle jets coming from previous crossings or multiple interactions.

### 3.5.2 Jet Energy Scale

It is essential to have a good understanding of the jet energy scale and resolution in all precision measurements, and these uncertainties are the main limitations to the measurement of the single top-quark cross section.

The jet energy scale correction calibrates the jet energy measured in the detector to the energy of the final state particle jet. The calibration can be represented as follows [99, 12],

$$E_{\text{jet}}^{\text{corr}} = \frac{E_{\text{jet}}^{\text{meas}} - E_{\text{O}}}{R_{\text{jet}} k_{\text{R}} S_{\text{jet}}} k_{\text{O}} C_{\text{res}}, \quad (3.5.2)$$

where  $E_{\text{jet}}^{\text{corr}}$  is the corrected jet energy, calibrated so that it is equal on average to the energy of all particles that are produced inside the jet cone.  $E_{\text{jet}}^{\text{meas}}$  is the measured (reconstructed) jet energy.  $E_{\text{O}}$  represents the offset energy correction, arising from the energy deposit associated with instrumental noises, additional  $p\bar{p}$  interactions (multiple interactions in the same bunch crossing), and previous crossings (pile-ups).  $R_{\text{jet}}$  is the average calorimeter response to the energy deposits by the particles that make up the jet, as shown in Figure 3.4.  $S_{\text{jet}}$  denotes the showering correction which corrects for the energy migration inside and outside the jet cone, as a result of the finite size of the calorimeter cells. The factors  $k_{\text{O}}$  and  $k_{\text{R}}$  are the corrections for biases introduced from the determination of the offset energy  $E_{\text{O}}$  and the detector response  $R_{\text{jet}}$ . The residual correction factor,  $C_{\text{res}}$ , is estimated from the closure studies, and is found to be one. The overall jet energy scale corrections and uncertainties are illustrated in Figure 3.5.

The jet energy scale correction mentioned above depends on the jet kinematic properties, such as the jet  $p_{\text{T}}$  and the detector pseudorapidity  $\eta^{\text{det}}$ . However, it is found that the jet energy scale correction also depends on the topological configuration of the jet. For example, jets originate from different flavors of partons have different angular spectra of particles in the reconstructed jet cones. Furthermore, jets produced via different processes have different parton flavor compositions. Specifically, the ratio between the  $b$  and light-flavored jet responses and the ratio between the quark and gluon jet responses are different in the data and the

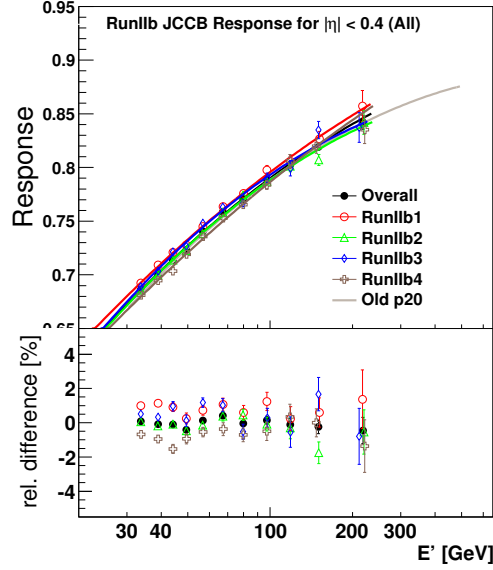


**Figure 3.4** The absolute response of the calorimeter as a function of the jet energy. The details are described in Appendix A.

simulated samples. As a consequence, an additional flavor-dependent jet energy scale is derived and applied on the simulated events [100], making the simulation appropriately reflect the data.

After calibrating the jet energy, the jet energy resolution is measured using the  $\gamma + \text{jet}$  and  $Z + \text{jet}$  events [101, 102]. Compared to the jet resolution measured in the data, the simulated jet resolution is smeared to reproduce the resolution in the data.

### 3.6 Imbalance in Transverse Momentum

Neutrinos, or other particles that escape detection, can be inferred from energy and momentum conservation in the collision. As the momenta of the incoming partons in the  $z$  direction in Tevatron collisions are unknown, only the imbalance in transverse momentum in an event, often called the “missing transverse energy” ( $\cancel{E}_T$ ), can be calculated, indicating the possible presence of such particles.

The vector  $\cancel{E}_T$  in an event is computed by summing vectorially over all the projected energy deposited above some noise thresholds in the calorimeter cells in the

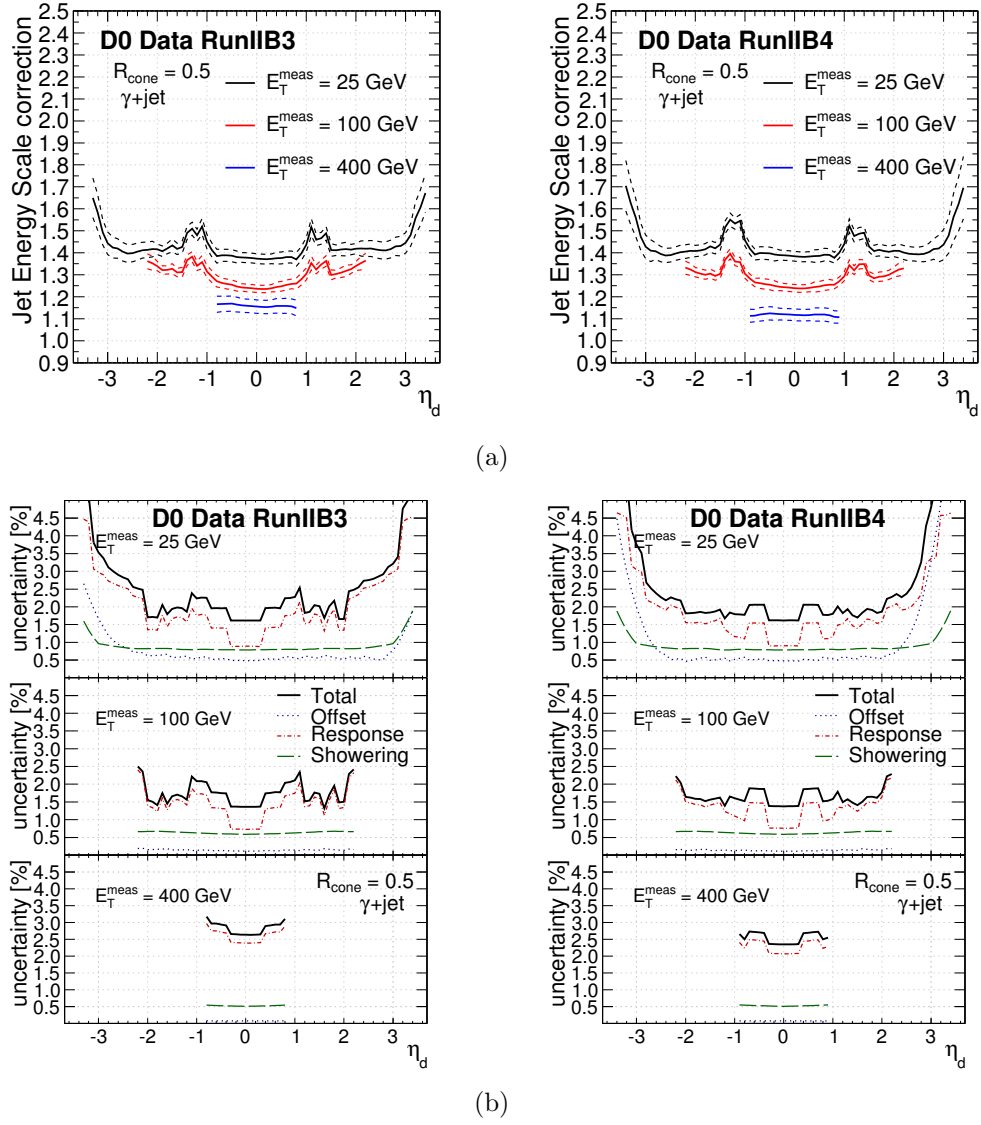


**Figure 3.5** Examples of Jet energy scale (a) correction and (b) uncertainty for data as a function of jet pseudorapidity for  $R_{\text{cone}} = 0.5$  jets [12].

transverse plane. (The cells in the coarse hadronic calorimeter are excluded, in order to reduce the effect of noise.) Moreover, the corrections for well-reconstructed objects, such as electrons, muons, and jets, are considered separately:

$$\vec{E}_T = - \sum_i \vec{p}_i^{\text{cell}} - \sum_j \left( \vec{p}_j^{\text{object}} - \sum_{k_j} \vec{p}_{k_j}^{\text{cell}} \right), \quad (3.6.1)$$

where  $\vec{p}_i^{\text{cell}}$  is the energy deposited in each calorimeter cell  $i$ , with the direction given by the coordinate of each cell,  $\vec{p}_j^{\text{object}}$  represents the  $p_T$  of the reconstructed object  $j$  with all corrections applied, and  $\vec{p}_{k_j}^{\text{cell}}$  is the original  $p_T$  in the cell  $k_j$  that belongs to a reconstructed object  $j$ . (The corrections also take account of the energy loss by muons in the calorimeter through ionization.)

### 3.7 $b$ Jets

The single top-quark processes always contain up to two  $b$  quarks in the final states, while the main background process,  $W$ +jets, overwhelmingly produces two light jets in the final state. Hence, identifying jets that originate from  $b$ -quarks, also known as “ $b$ -tagging,” significantly reduces background. The  $b$ -tagging algorithm distinguishes  $b$  jets from light-flavored jets (originated from light-flavored quarks and gluons) by utilizing the fact that  $b$ -hadrons have relatively long lifetimes ( $\approx 10^{-12}$  s) and therefore can travel several millimeters before decaying. Specifically,  $b$ -jet identification is based on presence of tracks with origins displaced from the primary vertex, and the reconstruction of a “secondary vertex” with a large transverse impact parameter, as illustrated in Figure 3.6.

A jet has to first be “taggable,” ensuring there is sufficient track information to apply the  $b$ -tagging algorithm. A taggable jet is a calorimeter jet matched to a track jet within  $\Delta R < 0.5$ , where the track jet consists of at least two tracks, with  $\Delta R < 0.5$  between them, each track has at least one SMT hit, and at least one track has  $p_T > 1$  GeV.

Among the taggable jets, a combined multivariate method is exploited to separate  $b$ -jets and light-flavored jets [103]. Simulated  $b\bar{b}$  dijet and inclusive dijet samples are used as the signal and background samples in the MVA training. First, six random forests of decision trees (RF) are trained. Five of the RFs

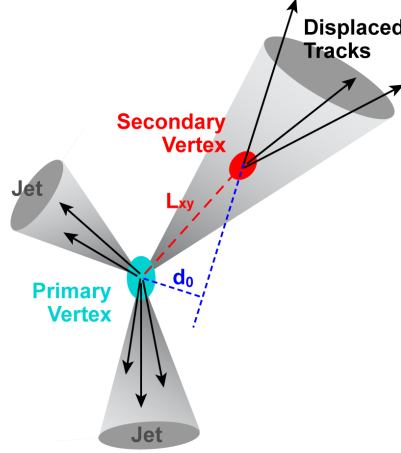


**Figure 3.6** Illustration of the secondary vertex [13].

are trained with the secondary vertex tagger (SVT) variables, while the other is trained with the variables related to impact parameters (IPs). The SVT [104] reconstructs secondary vertices using tracks with large impact parameter significance, and the variables related to the secondary vertex, such as the decay length significance and the  $\chi^2$  per degree of freedom of the secondary vertex, are calculated accordingly. The IP-variables, the Jet Lifetime Probability (JLIP) [105] and the Counting Signed Impact Parameter Tagger (CSIP) [106], represent the probability that all tracks in a jet originate from the primary vertex, and the number of tracks above a given signed IP threshold. As illustrated in Figure 3.7, these input variables are sensitive to the separation of  $b$ -jets and light-flavored jets. After the six RFs are obtained, their outputs are fed into a neural network (NN), and the NN output is taken as the final discriminant of the  $b$ -tagging algorithm.

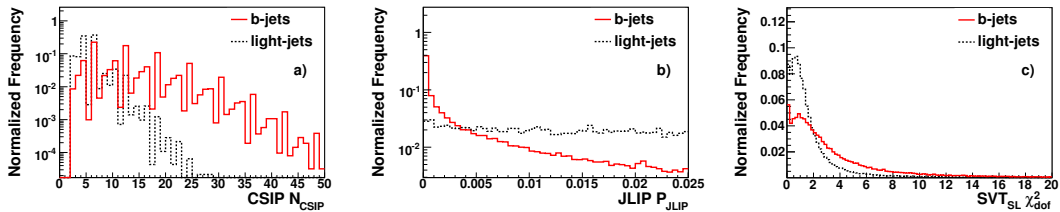


**Figure 3.7** Examples of the  $b$ -tagging input variables: (a) Counting Signed Impact Parameter Tagger (CSIP), (b) Jet Lifetime Probability (JLIP), and (c) the  $\chi^2$  per degree of freedom of the secondary vertex (SVT  $\chi^2_{\text{dof}}$ ) [14].

Light-flavored jets can be reconstructed with high-impact parameter tracks or displaced vertices, owing to resolution and misreconstruction effects. These effects lead to the secondary vertex reconstructed in the direction opposite to the direction of the corresponding jet. The determination of the light-flavor mistag rate or fake rate relies on this feature, and twelve  $b$ -tagging operating points are defined corresponding to different fake rates, as illustrated in Figure 3.8.

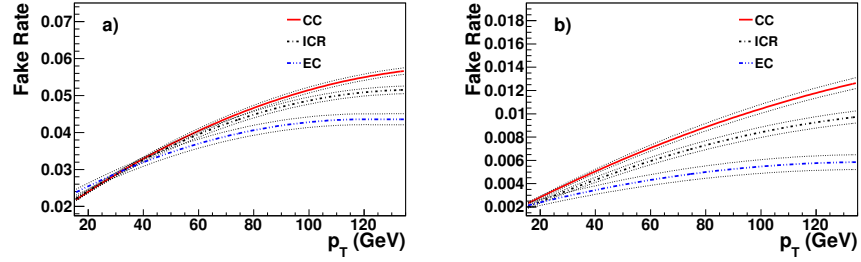


**Figure 3.8** The estimated  $b$ -tagging efficiency of light-flavored jets parametrized in the central calorimeter (CC, continuous line), intercryostat detector (ICR, dot-dashed line) and end calorimeter (EC, dot-dot-dashed line) for the L2 (a) and Tight (b) operating points. The dotted black lines represent the fit uncertainty [14].

The  $b$ -tagging criterion in this analysis is optimized to the  $s$ -channel single top events, as described in Section 5.4. Furthermore, the  $b$ -tagging output values are found to be helpful in separating the signal and background events, as discussed in Section 6.3.1.

## 4 Data and Simulation Samples

The full Tevatron Run II data sample, corresponding to  $9.7 \text{ fb}^{-1}$ , is analyzed in this study. We use Monte Carlo simulation to model the single-top-quark  $s$ -channel and main background events, and model the multijet background using an orthogonal data sample.

### 4.1 Data Samples

The data was collected with the DØ detector in two run periods: Run IIa data taken between August 2002 and February 2006, and the Run IIb collected from June 2006 until September 2011, with an increasingly higher instantaneous luminosity. Out of  $11.9 \text{ fb}^{-1}$  of delivered integrated luminosity,  $9.7 \text{ fb}^{-1}$  was recorded and classified as being of sufficiently good data quality for use in analysis. Table 4.1 lists each run period and the corresponding integrated luminosity.

Data Sample	Dates	Trigger Version	Integrated Luminosity [ $\text{pb}^{-1}$ ]
Run IIa	Jul. 26, 2002 - Feb. 22, 2006	v8 - v14	1078.81
Run IIb1	Jun. 9, 2006 - Aug 4, 2007	v15.00 - v15.83	1217.67
Run IIb2	Oct. 28, 2007 - Jun. 13, 2009	v15.90 - v16.29	3039.84
Run IIb3	Sept. 15, 2009 - July 18, 2010	v16.30 - v16.64	1994.27
Run IIb4	Sept. 15, 2010 - Sept. 30, 2011	v16.65 - v16.99	2403.91
Run IIb		v15 - v16	8655.69
Run II		v8 - v16	9734.5

**Table 4.1** Integrated luminosities for good quality data for each run period used in this analysis. These numbers are calculated from unrescaled jet triggers.

In this analysis, we use an “inclusive” trigger requirement, which means no explicit trigger is required. Events that might have failed a certain trigger require-

ment can be collected by others. As a result, we have 100% trigger efficiency. The systematic uncertainty for this method is described in Appendix B.

The Run IIa samples are not re-analyzed in this study. They are directly taken from Ref. [107] with their normalizations and scale factors unchanged and used for the cross section measurement. In the following sections, we will focus on the Run IIb samples, but will mention the Run IIa samples when the treatment of these two samples is different.

## 4.2 Monte Carlo Simulation

Monte Carlo simulations are used to model signal and background events, and different Monte Carlo generators are used to simulate different hard-scattering processes:

- Single top quark: The CompHEP-SINGLETOP event generator, which produces final state partons matching those from NLO calculations [49].
- $t\bar{t}$ ,  $W$ +jets and  $Z$ +jets: The ALPGEN Leading-Order event generator [108].
- Diboson ( $WW$ ,  $WZ$ ,  $ZZ$ ): PYTHIA [109].

The top quark mass is set to 172.5 GeV, close to the current world average of  $173.18 \pm 0.94$  GeV. The leading-order parton distribution function, CTEQ6L, is used for all the MC simulated samples, except for the  $t$ -channel single top-quark events. The PDF set for the  $t$ -channel MC samples is CTEQ6M, in which both  $\alpha_S$  and the evolution of the PDFs are evaluated at next-to-leading-order. This is due to the fact that the NLO contribution of the  $t$ -channel production is significant, and a NLO PDF set is required correspondingly. Moreover, because we are selecting the phase space where the two quarks annihilate into a state close to the top quark mass shell, we choose the factorization scale,  $Q$ , to be  $m_t$  for the  $s$ -channel [110]. On the other hand, owing to the significant NLO effect, the factorization scale of the  $t$ -channel,  $m_t/2$ , is pragmatically chosen by matching the LO cross section to the NLO one [110]. Moreover, the SINGLETOP generator simulates the decays of the top quarks and the  $W$  bosons from the top quarks, ensuring the spins are properly transferred, and therefore the angular distributions are well described. The parameters of the MC simulation are summarized in Table 4.2, and the cross

sections, branching fractions, and the initial numbers of events generated are shown in Table 4.3.

Process Category	Generator	PDF	Factorization Scale Q
$s$ -channel	CompHEP-SINGLETOP	CTEQ6L1	$m_{top}$
$t$ -channel	CompHEP-SINGLETOP	CTEQ6M	$m_{top}/2$
$t\bar{t}$	ALPGEN	CTEQ6L1	$\sqrt{\sum(m^2 + p_T^2)}$
$W$ +Jets, $Z$ +Jets	ALPGEN	CTEQ6L1	$\sqrt{m_V^2 + \sum(m^2 + p_T^2)}$
Diboson	PYTHIA	CTEQ6L1	$\sqrt{m_V^2 + \sum(m^2 + p_T^2)}$

**Table 4.2** The parameters of the MC event generation. The  $m_V$  is the mass of the vector boson ( $W$  or  $Z$ ) that decays leptonically. The  $\sum$  in this table extends to all final state partons (including the heavy quarks, excluding the  $W$  boson decay products). Namely, the  $\sum$  sums over the  $m^2$  and the  $p_T$  of the final state partons except the  $W$  boson decay products.

All the simulated events mentioned above are interfaced with PYTHIA for parton showering, hadronization, underlying events, and initial and final-state radiation. The PYTHIA modified version of Tune A [111, 112, 113] is chosen, and we estimate systematic uncertainties with other tunes as described in Section 7.1. In addition, we use TAUOLA [114] to decay the tau leptons, and EVTGEN [115] to decay  $b$  hadrons. Moreover, in order to model the noise and pile-up events, the “zero bias” data events, collected during beam crossings but without any trigger requirement, are overlaid on all the MC simulated events.

A few parton level cuts are applied on the  $W$ +jets MC samples to avoid the divergence in calculations of the cross section: the generated partons are required to have  $p_T > 8$  GeV and a separation of  $\Delta R > 0.4$ . After PYTHIA showering, any particle jet with  $p_T > 8$  GeV is required to match an ALPGEN parton, except in the highest parton multiplicity (inclusive) sample where additional (unmatched) particle jets are allowed (MLM matching [116]). All ALPGEN  $W$ +jets samples have undergone a process of heavy-flavor (HF) skimming. Events containing heavy-flavored partons generated by PYTHIA in the region of phase space where they are also generated by ALPGEN in the hard process have been removed in order to avoid double counting of heavy flavor production [117].

All generated MC events are processed through the GEANT [118] simulation of the DØ detector to model the detector and reconstruction effects. Because of

Event Type	The Monte Carlo Event Sets					
	Cross Section [pb]	Branching Fraction	No. of Run IIa Events	No. of Run IIb1 Events	No. of Run IIb2 Events	No. of Run IIb3 Events
Signals						
$t\bar{t} \rightarrow \ell + \text{jets}$	$1.04^{+0.04}_{-0.04}$	$0.3240 \pm 0.0032$	0.6M	1.6M	0.8M	4.9M
$tq\bar{b} \rightarrow \ell + \text{jets}$	$2.26^{+0.12}_{-0.12}$	$0.3240 \pm 0.0032$	0.6M	0.8M	0.8M	4.5M
<b>Signal total</b>	<b><math>3.30^{+0.16}_{-0.16}</math></b>	<b><math>0.3240 \pm 0.0032</math></b>	<b>1.2M</b>	<b>2.4M</b>	<b>1.6M</b>	<b>9.4M</b>
Backgrounds						
$t\bar{t} \rightarrow \ell + \text{jets}$	$7.46^{+0.48}_{-0.67}$	$0.4380 \pm 0.0044$	1.5M	3.1M	2.1M	1.5M
$t\bar{t} \rightarrow \ell\ell$	$7.46^{+0.48}_{-0.67}$	$0.1050 \pm 0.0010$	1.5M	1.5M	2.2M	1.4M
<b>Top pairs total</b>	<b><math>7.46^{+0.48}_{-0.67}</math></b>	<b><math>0.5430 \pm 0.0054</math></b>	<b>3.0M</b>	<b>4.6M</b>	<b>4.3M</b>	<b>2.9M</b>
$Wb\bar{b} \rightarrow \ell\nu b\bar{b}$	90.5	$0.3240 \pm 0.0032$	2.7M	26M	8.3M	11.4M
$Wc\bar{c} \rightarrow \ell\nu c\bar{c}$	260	$0.3240 \pm 0.0032$	2.7M	26M	16.8M	22.7M
$Wj\bar{j} \rightarrow \ell\nu j\bar{j}$	23,831	$0.3240 \pm 0.0032$	55M	213M	303M	314M
<b>W+jets total</b>	<b>24,182</b>	<b><math>0.3240 \pm 0.0032</math></b>	<b>60.4M</b>	<b>280M</b>	<b>328M</b>	<b>348M</b>
$Zb\bar{b} \rightarrow \ell\ell b\bar{b}$	38.7	$0.03366 \pm 0.00002$	0.7M	8.1M	8.2M	18.7M
$Zc\bar{c} \rightarrow \ell\ell c\bar{c}$	106	$0.03366 \pm 0.00002$	0.7M	15.7M	8.6M	18.5M
$Zj\bar{j} \rightarrow \ell\ell j\bar{j}$	7,032	$0.03366 \pm 0.00002$	14M	69.9M	54.5M	74.5M
<b>Z+jets total</b>	<b>7,177</b>	<b><math>0.03366 \pm 0.00002</math></b>	<b>15.4M</b>	<b>94M</b>	<b>71.3</b>	<b>112M</b>
$WW \rightarrow \text{anything}$	$11.6 \pm 0.4$	$1.0 \pm 0.0$	2.0M	5.5M	4.6M	4.7M
$WZ \rightarrow \text{anything}$	$3.25 \pm 0.11$	$1.0 \pm 0.0$	1.0M	5.4M	4.6M	2.0M
$ZZ \rightarrow \text{anything}$	$1.33 \pm 0.04$	$1.0 \pm 0.0$	1.0M	3.7M	4.6M	1.7M
<b>Diboson total</b>	<b><math>16.2 \pm 0.6</math></b>	<b><math>1.0 \pm 0.0</math></b>	<b>4.0M</b>	<b>14.6M</b>	<b>13.8M</b>	<b>8.4M</b>

**Table 4.3** The cross sections, branching fractions, and initial numbers of events in the Monte Carlo event samples. The symbol  $\ell$  stands for electron plus muon plus tau decays. Note the cross sections listed in this table are from the NLO calculations, not the LO one generated by ALPGEN. We will normalize the LO ALPGEN MC samples to the NLO in the analysis, as explained in Section 5.2.1. To reduce the statistical fluctuation, we usually generate a lot of events, and assign a weight on each event to make the effective events (so-called the “yields”) fit the prediction.

the different detector effects and the calibration in each sub-run period, we also separate the Run IIb MC samples into three run periods, Run IIb1, IIb2, and IIb3, where the Run IIb3 MC samples are used to model the combined Run IIb3 and IIb4 data.

### 4.3 Multijet Samples

Unlike other background samples, multijet events are modeled using data. This is because the probability of misidentifying a jet as a lepton is extremely small. In practice, this would require generating a prohibitively large number of multijet events, most of which would be rejected by our selection criteria. Furthermore, there is no MC generator which can satisfyingly describe the multijet events with the precision needed to study such rare events.

To model the multijet events, an orthogonal data sample is selected by reversing the lepton isolation requirements. The selection criteria and the background determination of these events will be further discussed in Section 5.1 and Section 5.3, respectively.

## 5 Event Selection and Determination of Background

Since we are searching for single top-quark signals in  $\ell\nu$ +jets final states, as discussed in Section 1.3.2, we select events with an isolated lepton, significant  $\cancel{E}_T$ , and two or more jets.

The selected events, also known as “pre-tagged,” are dominated by  $W$ +jets background. The  $t\bar{t}$  contribution is next largest, and becomes more significant for large jet multiplicities.

Finally, we require one or two jets originating from  $b$  quarks, dictated by the fact that the signal events have two  $b$ -quarks in the final states. This requirement is achieved by applying  $b$ -ID cuts, and significantly improves the signal purity in the final selected samples, the single-tagged and the double-tagged samples.

This selection describes the details of the event selection and the background modeling, starting with a list of the selection cuts in Section 5.1. In Section 5.2, we briefly discuss the default DØ MC corrections, which are provided by the  $V$ +jets group and used to bring the MC simulation match to the data. The  $W$ +jets and multijet normalizations and corrections are described in Section 5.3, and we present the  $b$ -ID cut optimization and heavy-flavor simulation modeling in Sections 5.4 and 5.5, respectively. We summarize the predicted numbers of events and the signal acceptances in Sections 5.6 and 5.7, and finally show cross-check samples in Section 5.8.

### 5.1 Event Selection

The energy of the  $s$ -channel single top-quark events is harder and more centrally distributed than the  $t$ -channel events; therefore, we slightly tighten the selection

criteria in this analysis, by raising the lepton and jet  $p_T$  cut from 15 to 20 GeV, and narrowing the jet  $|\eta^{\text{det}}|$  cut from 3.4 to 2.5, with respect to what was used in the previous inclusive single top-quark cross section measurement. The advantages of tightening the jet selection are that the systematic uncertainties on the jet energy scale, the jet energy resolution, and the jet identification are significantly reduced, and the multiple hard scattering and pile-up effects are diminished.

### Common selection for both electron and muon channels

- Good quality (for data)
- Instantaneous luminosity  $> 0$
- Use the inclusive trigger: no explicit trigger requirement
- Good primary vertex:  $|z_{PV}| < 60$  cm with at least three tracks attached
- Two, or three good and vertex confirmed jets with  $p_T > 20$  GeV and  $|\eta^{\text{det}}| < 2.5$
- The leading jet  $p_T > 25$  GeV
- Jet triangle cut of  $|\Delta\phi(\text{leading jet}, \cancel{E}_T)|$  vs.  $\cancel{E}_T$ , to clean up multijet events with soft jets:
  - $|\Delta\phi| < 1.5 + 0.0469 \cancel{E}_T$
- Missing transverse energy
  - $20 < \cancel{E}_T < 200$  GeV in events with exactly two good jets
  - $25 < \cancel{E}_T < 200$  GeV in events with exactly three good jets
- Scalar sum of the transverse energies of all good jets, the lepton transverse momentum, and the missing transverse energy
  - $H_T(\text{all jets}, \text{lepton}, \cancel{E}_T) > 120$  GeV in events with exactly two good jets
  - $H_T(\text{all jets}, \text{lepton}, \cancel{E}_T) > 140$  GeV in events with exactly three good jets

### Electron channel selection

- Only one tight isolated electron (“emvPoint1\_eff”) with  $|\eta^{\text{det}}| < 1.1$  and  $p_T > 20$  GeV
- No additional loose electron with  $p_T > 10$  GeV

- No tight muon with  $p_T > 10$  GeV
- Electron coming from the primary vertex:  $|\Delta z(e, \text{PV})| < 1$  cm
- Electron triangle cuts of  $|\Delta\phi(e, \cancel{E}_T)|$  vs.  $\cancel{E}_T$ 
  - $|\Delta\phi| > 2.0 - 0.05 \cancel{E}_T$
  - $|\Delta\phi| > 1.5 - 0.03 \cancel{E}_T$
  - $|\Delta\phi| < 2.0 + 0.0476 \cancel{E}_T$

### Muon channel selection

- Only one tight isolated muon with  $p_T > 20$  GeV and  $|\eta^{\text{det}}| < 2.0$
- No additional loose muons with  $p_T > 10$  GeV.
- No loose electron with  $p_T > 10$  GeV
- Muon coming from the primary vertex:  $|\Delta z(\mu, \text{PV})| < 1$  cm
- Muon triangle cuts of  $|\Delta\phi(\mu, \cancel{E}_T)|$  vs.  $\cancel{E}_T$ 
  - $|\Delta\phi| > 1.4 - 0.0141 \cancel{E}_T$
  - $|\Delta\phi| < 2.5 + 0.0214 \cancel{E}_T$
- Muon track curvature significance cuts of  $|\text{TrackCurvSig}|$  vs.  $|\Delta\phi(\mu, \cancel{E}_T)|$ , where  $|\text{TrackCurvSig}| = \left| \frac{q/p_T}{\sigma(1/p_T)} \right|$ , and  $q$  and  $p_T$  are the charge and transverse momentum of the charged track associated with the muon

$$\frac{b(|\Delta\phi| - a)}{\pi - a} < |\text{TrackCurvSig}|, \quad \text{where } (a, b) = (2.9, 10) \quad (5.1.1)$$

- Muon trapezoid cuts of  $|\Delta\phi(\mu, \cancel{E}_T)|$  vs.  $|\eta_\mu^{\text{det}}|$

$$\begin{cases} |\Delta\phi| < 2.8 & \text{for } |\eta_\mu^{\text{det}}| > 1.5 \\ \frac{2.8 - |\Delta\phi|}{2(\pi - 2.8)} + 1.5 > |\eta_\mu^{\text{det}}| & \text{for } 1.0 < |\eta_\mu^{\text{det}}| < 1.5 \end{cases} \quad (5.1.2)$$

The muon track curvature significance and trapezoid cuts are needed to reject events with poorly measured muons that cause an excess in data over background model in the  $\Delta\phi$  distributions. The details are discussed in Appendix C.2.

**Orthogonal samples selection** for modeling the multijet backgrounds: all the selection cuts listed above are kept except for the lepton requirements, which are replaced with

### Electron channel

- Only one loose electron (“emvPoint05\_eff”) that fails the tight electron criteria (“emvPoint1\_eff.”)
- No second loose electron is allowed in any  $|\eta^{\text{det}}|$  region. (Note, this requirement rejects all events with a tight isolated electron, thus keeping this sample orthogonal to the main one.)

### Muon channel

- Events with a tight isolated muon are rejected. This ensures orthogonality.
- Jets near the muon are removed and the  $\cancel{E}_T$  of the event is corrected accordingly.

We divide the selected events into 32 nonoverlapping samples, referred to as analysis channels, that depend on run period (Run IIa, Run IIb1, Run IIb2, and Run IIb3b4), the flavor of the lepton (electron or muon, labeled as  $e$ +jets or  $\mu$ +jets), jet multiplicity (two or three), and the number of jets identified as candidates for originating from  $b$  quarks (number of single-tagged or double-tagged jets). After applying all the corrections and  $b$ -tagging described in Sections 5.2 to 5.4, and confirming the similarity of kinematic distributions in all Run IIb periods, the events from Run IIb1, IIb2, and IIb3b4 are merged together. There are consequently 16 analysis channels in the end.

## 5.2 Modeling of the Simulated Samples

To model the expected numbers of events and distributions in the selected samples, we apply several corrections to account for NLO effects and differences in event reconstruction efficiencies between simulated events and the data.

### 5.2.1 Normalization of the NLO Cross Sections

We normalize all the simulated event samples to the integrated luminosity of our data. The cross section for  $W$ +jets samples from ALPGEN is at leading-log order (LLO), and corrected with a phenomenological  $K'$ -factor [119, 120, 121, 122] to match the inclusive  $W$  cross section calculated at the next-to-leading order (NLO). In addition, the heavy-flavor samples are corrected by the ratio  $K'_{HF}$  of heavy to light NLO  $K'$ -factors obtained using MCFM [123]. Other corrections to the calculated  $W$ +jets cross section are described in Section 5.3. The uncertainty from higher order effects on the  $t\bar{t}$  yield is considered in Section 7.1. The cross section normalizations are shown in Table 5.1.

Correction Factors for $V$ +Jets and $t\bar{t}$ Cross Sections								
	$Wjj$	$Wcj$	$Wc\bar{c}$ and $Wb\bar{b}$	$Zjj$	$Zc\bar{c}$	$Zb\bar{b}$	$t\bar{t} \rightarrow \ell+\text{jets}$	$t\bar{t} \rightarrow \ell\ell$
Run IIa	1.246	1.648	$1.246 \times 1.47$	1.253	$1.253 \times 1.67$	$1.253 \times 1.52$		
Run IIb1	1.300	1.648	$1.300 \times 1.47$	1.313	$1.313 \times 1.67$	$1.313 \times 1.52$	1.430	1.392
Run IIb2	1.301	1.648	$1.301 \times 1.47$	1.308	$1.308 \times 1.67$	$1.308 \times 1.52$	1.442	1.380
Run IIb3	1.297	1.648	$1.297 \times 1.47$	1.310	$1.310 \times 1.67$	$1.310 \times 1.52$	1.423	1.375

**Table 5.1** Theoretical  $K'$ -factors used to scale the ALPGEN background LLO calculations to NLO. For a product of two factors, the first one,  $K'$ , is for the ratio of NLO to LLO, the second corresponds to the heavy-flavor scale factor  $K'_{HF}$ .

### 5.2.2 Monte Carlo Efficiency Corrections

Since reconstruction and selection efficiencies are different for MC simulations and data, several of the scale factors studied by the ID groups and integrated by the  $V$ +jets group are used to correct the MC samples, as summarized below.

- **Primary vertex position reweighting**

The distribution of the  $z$  position of the primary vertices is simulated with a Gaussian, and reweighted to match the distribution observed in the data.

- **Instantaneous luminosity reweighting**

The instantaneous luminosity distribution of each simulated sample is generated from the luminosity of the overlaid zero-bias events. We reweight

this distribution to match the data. Moreover, a second small instantaneous luminosity reweighting is applied on our selected samples, so that the luminosity profiles in the simulated samples exactly matches the data.

- **$W$   $p_T$  and  $Z$   $p_T$  distribution reweighting**

The inclusive  $W$   $p_T$  and  $Z$   $p_T$  reweightings are applied to correct these distributions at the generation level.

- **Lepton ID efficiency correction factor**

For both the lepton flavors, we apply scale factors on the simulated events to account for the difference of the lepton ID efficiencies between the data and the simulation, as described in Sections 3.3 and 3.4.

- **Jet shifting, smearing, and removal (JSSR)**

As mentioned in Section 3.5.2, the scale factors of the JSSR are applied on the simulated events to cope with the differences of the jet energy scale, the jet energy resolution, and the jet identification efficiencies between the data and the simulation.

- **Muon angular corrections**

In the muon channel, an additional mismodeling correction is applied on all the simulated samples as a function of muon detector pseudorapidity such that the simulation matches the data. The details of this correction are described in Appendix C.1.

- **Taggability and  $b$ -tagging efficiency correction factor**

To increase the signal purity, we require one or two  $b$ -tagged jets in the final selected samples. Jets are first required to be “taggable” and then required to be “tagged,” by directly imposing a requirement on the  $b$ -ID MVA output. To correctly model the taggability in the simulated events, the “taggability” scale factors, parametrized with jet  $p_T$  and  $\eta$  [124] in the pre-tagged sample, are applied on all the selected jets. The overall taggability correction for an event can therefore be written as

$$w_{\text{taggability}} = \prod_{i=1}^{N_{\text{taggable jets}}} SF_{\text{tagga},i} \prod_{j=1}^{N_{\text{untaggable jets}}} \overline{SF}_{\text{tagga},j}, \quad (5.2.1)$$

where  $SF_{tagga}$  and  $\overline{SF}_{tagga}$  are the taggability scale factors and anti-scale factors defined as follows,

$$\begin{aligned} SF_{tagga} &= \frac{\text{Taggability(Data)}}{\text{Taggability(MC)}} \\ \overline{SF}_{tagga} &= \frac{1 - \text{Taggability(Data)}}{1 - \text{Taggability(MC)}}. \end{aligned} \quad (5.2.2)$$

Furthermore, the tag-rate scale factors are applied on the taggable jets, accounting for the difference of the tag rate between the data and the simulation. The tagging scale factors are evaluated as follows,

$$SF_f(p_T, \eta, x) = \frac{TRF_f^i(p_T, \eta) - TRF_f^{i+1}(p_T, \eta)}{\epsilon_f^i(p_T, \eta) - \epsilon_f^{i+1}(p_T, \eta)}, \quad (5.2.3)$$

where  $TRF_f^i$  represents the tag-rate function with jet flavor  $f$  at the  $i$ th  $b$ -tagging operating point, and  $\epsilon_f^i$  is the tag efficiency of a simulated jet with flavor  $f$  at the  $i$ th operating point.

### 5.3 $W$ +Jets and Multijet Backgrounds

The theoretical  $W$ +jets cross sections have large uncertainties, specially for  $W$ +heavy-flavor jets, which constitute the main background in this analysis. In addition, the multijet background, modeled by an orthogonal data samples of multijet-enriched events, provides the distributions of the multijet events, but not their normalization. The  $W$ +jets and multijet backgrounds are therefore normalized simultaneously to the data.

The  $W$ +jets and multijet normalization is performed using the pre-tagged samples, where the signal fraction is less than 0.3%, and should not bias the background expectation. The “matrix method” is used to extract the normalizations [125]. Two data samples are defined, the *tight* sample, which is our pre-tagged data sample, and the *loose* sample, where the same selection are applied, but requiring only loose lepton quality.

Using the *loose* sample, we measure the efficiency  $\epsilon_{\text{real-}\ell}$  for a real isolated lepton to pass the tight lepton selection in MC samples, and the efficiency  $\epsilon_{\text{fake-}\ell}$  for a fake isolated lepton to pass the tight lepton criteria in a multijet enriched

sample. To define the multijet enriched sample, we apply all the selection cuts, but reverse the  $\cancel{E}_T$  cut to  $\cancel{E}_T < 10$  GeV. The details of the efficiency measurement can be found in [15]. The following two equations can therefore be used:

$$N_{\text{loose}} = N_{\text{loose}}^{\text{fake-}\ell} + N_{\text{loose}}^{\text{real-}\ell} \quad (5.3.1)$$

$$N_{\text{tight}} = N_{\text{tight}}^{\text{fake-}\ell} + N_{\text{tight}}^{\text{real-}\ell} = \epsilon_{\text{fake-}\ell} N_{\text{loose}}^{\text{fake-}\ell} + \epsilon_{\text{real-}\ell} N_{\text{loose}}^{\text{real-}\ell}, \quad (5.3.2)$$

where  $N_{\text{loose}}$  and  $N_{\text{tight}}$  are the numbers of events in the loose and tight samples, respectively. By solving for  $N_{\text{loose}}^{\text{fake-}\ell}$  and  $N_{\text{loose}}^{\text{real-}\ell}$ , the  $W$ +jets and multijet contributions in the tight sample can be determined.

The efficiencies  $\epsilon_{\text{real-}\ell}$  and  $\epsilon_{\text{fake-}\ell}$  depends on lepton  $p_T$ ,  $\eta$ , and jet multiplicity, as illustrated in Figure 5.1. We use the constant values of  $\epsilon_{\text{real-}\ell}$  and  $\epsilon_{\text{fake-}\ell}$  measured in the inclusive  $\geq 2$  jet bin, and assign systematic uncertainties accounting for the dependencies. The results are listed in Table 5.2. The matrix method is solved for each jet multiplicity bin, and the multijet background is therefore obtained from the pre-tagged orthogonal sample, scaled to  $N_{\text{tight}}^{\text{fake-}\ell}$ . For the  $W$ +jets background, including  $Wb\bar{b}$ ,  $Wc\bar{c}$ ,  $Wcj$  and  $Wjj$  samples, is scaled to  $N_{\text{tight}}^{\text{real-}\ell}$ , after subtracting the expected number of the events coming from the other sources (diboson, single top-quark,  $t\bar{t}$ ) in each jet multiplicity bin of the tight sample:

$$N_{\text{tight}}^{W+\text{jets}} = N_{\text{tight}}^{\text{real-}\ell} - N^{st} - N^{t\bar{t}} - N^{\text{diboson}}, \quad (5.3.3)$$

The final results are shown in Table 5.3.

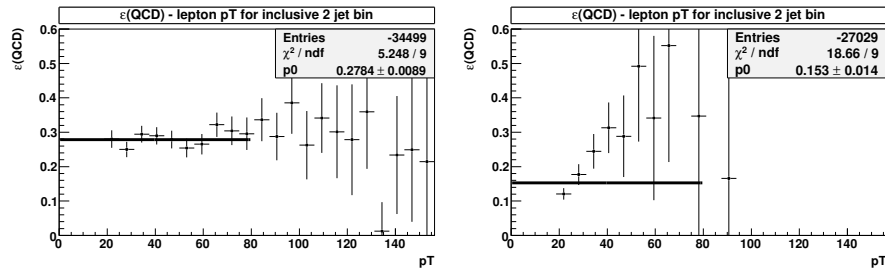


**Figure 5.1** The  $\epsilon_{\text{fake-}\ell}$  for the inclusive  $\geq 2$  jet bin versus the electron (left) and muon (right)  $p_T$  [15].

In addition to the normalization, the  $W$ +jets MC samples are reweighted to correct the mismodeling in some angular variables. This reweighting is derived by comparing the  $W$ +jets and the  $Z$ +jets MC samples to the data, after subtracting

Run period	$\epsilon_{\text{fake}-\ell}$	$\epsilon_{\text{fake}-\ell} \delta_{\text{stat}}$	$\epsilon_{\text{fake}-\ell} \delta_{\text{syst}}$	$\epsilon_{\text{real}-\ell}$	$\epsilon_{\text{real}-\ell} \delta_{\text{stat}}$	$\epsilon_{\text{real}-\ell} \delta_{\text{syst}}$
e+jets						
Run IIb1	0.308	$\pm 0.017$	$^{+0.015}_{-0.015}$	0.863	$\pm 0.002$	$\pm 0.014$
Run IIb2	0.283	$\pm 0.009$	$^{+0.008}_{-0.009}$	0.876	$\pm 0.002$	$\pm 0.006$
Run IIb3,4	0.264	$\pm 0.006$	$^{+0.015}_{-0.015}$	0.863	$\pm 0.002$	$\pm 0.007$
$\mu$ +jets						
Run IIb1	0.149	$\pm 0.029$	$^{+0.053}_{-0.055}$	0.911	$\pm 0.002$	$\pm 0.014$
Run IIb2	0.194	$\pm 0.020$	$^{+0.053}_{-0.054}$	0.896	$\pm 0.002$	$\pm 0.012$
Run IIb3,4	0.198	$\pm 0.016$	$^{+0.052}_{-0.054}$	0.891	$\pm 0.002$	$\pm 0.011$

**Table 5.2**  $\epsilon_{\text{fake}-\ell}$  and  $\epsilon_{\text{real}-\ell}$  as derived for all run periods with statistical and systematic uncertainties, as explained in Ref. [15].

W+jets and Multijet Background Normalization								
	Electron Channel				Muon Channel			
	$N_{\text{loose}}$	$N_{\text{tight}}$	$N_{\text{tight}}^{\text{fake}-\ell}$	$N_{\text{tight}}^{\text{real}-\ell}$	$N_{\text{loose}}$	$N_{\text{tight}}$	$N_{\text{tight}}^{\text{fake}-\ell}$	$N_{\text{tight}}^{\text{real}-\ell}$
Run IIb1								
2jet	14406	10942	827.1	10114.9	12778	10977	129.8	10847.2
3jet	2128	1602	130.1	1471.9	2059	1685	37.3	1647.7
Run IIb2								
2jet	37914	27101	2916.7	24184.3	29195	24518	453.4	24064.6
3jet	5664	3947	484.2	3462.8	4655	3706	128.5	3577.5
Run IIb3,4								
2jet	62315	40893	5678.8	35214.2	44660	37267	721.4	36545.6
3jet	9754	6092	1025.0	5067.0	7370	5902	189.9	5712.1

**Table 5.3** Matrix method yields in the electron and the muon channels for different run periods: the loose and tight selected events, and the expected contribution from events with a real and with a fake lepton.

all other backgrounds. It is performed sequentially in the following order:  $\eta(\text{Jet}_1)$ ,  $\eta(\text{Jet}_2)$ ,  $\Delta R(\text{Jet}_1, \text{Jet}_2)$ , and  $\eta(\text{Jet}_3)$  if applicable. The details of the reweighting are described in Appendix 5 of Ref. [107].

Finally, to address differences between data and heavy flavor backgrounds, including  $Wb\bar{b}$  and  $Wc\bar{c}$  samples, a heavy flavor correction is applied to all  $b$ -tagged jets in all samples as described in Section 5.5.

## 5.4 Optimization of $b$ -ID

In addition to the selections listed in Section 5.1, we apply the  $b$ -ID (also known as  $b$ -tagging) criteria on the pre-tagged samples to improve signal purity. In the previous analyses [126, 107], we selected events with one TIGHT  $b$  jet ( $b$ -tag NN output  $> 0.775$ , corresponding to  $b$ -tag MVA output  $> 0.225$ ) for the single-tagged samples, and events with two OLDLOOSE  $b$  jets ( $b$ -tag NN output  $> 0.5$ , corresponding to  $b$ -tag MVA output  $> 0.1$ ) for the double-tagged sample. To ensure the orthogonality between the single-tagged and double-tagged samples, in single-tagged samples, the events with a second jet passing the OLDLOOSE requirement were vetoed.

The  $b$ -tagging cuts used in the previous analyses were optimized to the inclusive single top-quark signals, the  $s$  and  $t$ -channels together; however, the  $t$ -channel has a cross section twice as large as the  $s$ -channel cross section, and thus dominates the cut determination. In this analysis, we re-determine the  $b$ -tagging cuts such that they are optimized for the  $s$ -channel.

Unlike the  $t$ -channel, the  $s$ -channel tends to have two central  $b$ -quarks in the final state, and these  $b$ -quarks are therefore more likely to be both reconstructed and  $b$ -tagged. The  $t$ -channel is likely to have only one  $b$ -quark in the final state, and therefore the single-tagged sample is the most sensitive in that measurement. As a result, we start with optimizing the  $b$ -tagging cut on the two-jet, double-tagged samples. Figure 5.2 shows the figure of merit,  $s/\sqrt{b}$ , versus the  $b$ -tagging cut on such a sample.  $s$  is the predicted number of events of our signal,  $s$ -channel single top-quark, while  $b$  is the predicted sum of all the backgrounds, except the  $t$ -channel single top-quark events. According to the figure, we select the events which have two jets passing the 0.075 (LOOSE) MVA  $b$ -tagging cut for the double-tagged sample.

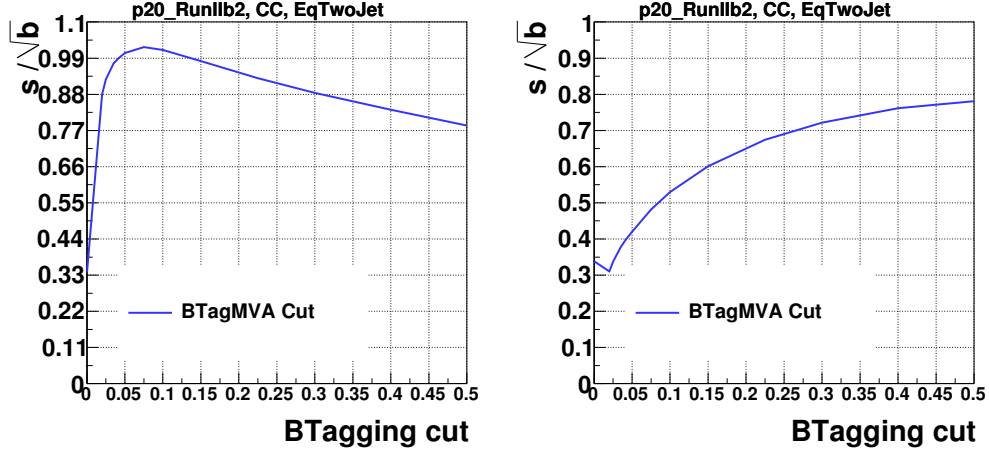


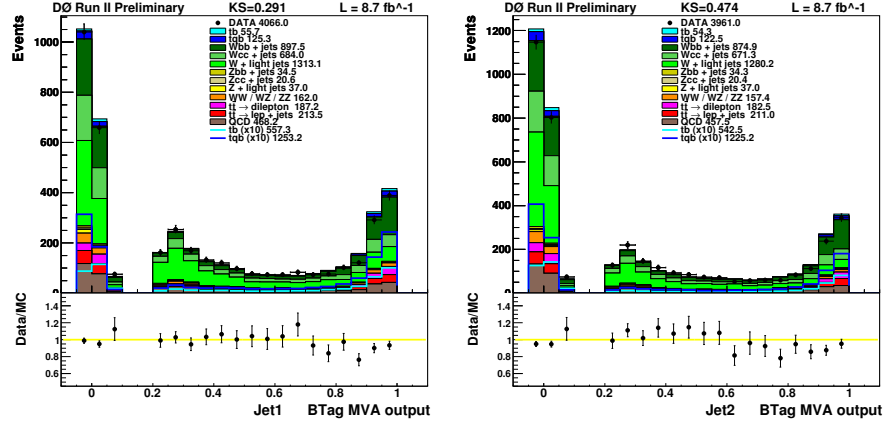
**Figure 5.2** The figure of merit,  $s/\sqrt{b}$ , versus the  $b$ -tagging cut for the double-tagged sample (left) and the single-tagged sample (right). In the single-tagged sample, the events with a second jet passing the LOOSE cut are vetoed to ensure the orthogonality between the single-tagged and double-tagged samples. The Run IIB2  $e$ +jets two-jet samples are used in these plots, but the other samples yield the same conclusions.

For the single-tagged sample, we keep the same cut, 0.225 MVA  $b$ -tagging output (TIGHT), as the previous analyses. This choice allows us to be nearly optimal and still keep enough statistics to train the multivariate methods in the next stage of the analysis. In the single-tagged sample, we veto events with another LOOSE tagged jet to keep orthogonality with the double-tagged sample.

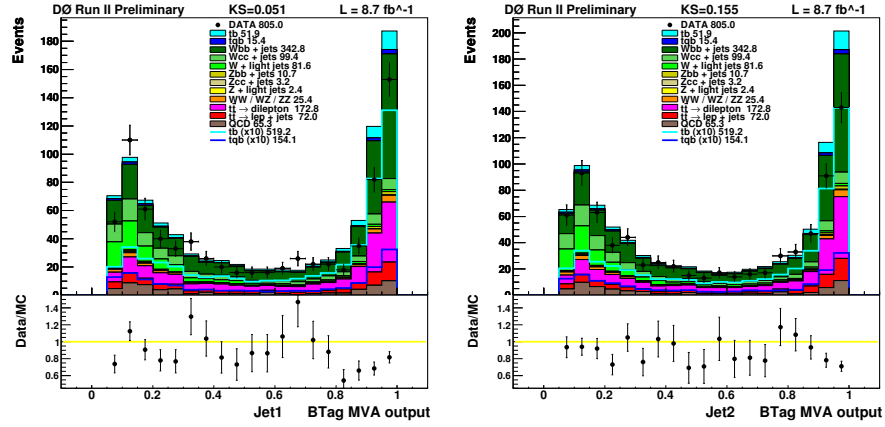
## 5.5 Heavy-Flavor Scale Factor

We observe disagreement between data and background predictions for  $b$ -tag MVA output values of  $\gtrsim 0.8$ , as shown in Figure 5.3. The overshoot of MC relative to data is specially large in the two-tag, two-jet sample. This is also true for enriched the  $W$ +jets sample of Figure 5.4, although it is not significant in the three-jet and  $t\bar{t}$ -enriched samples shown in Figures 5.5 and 5.6, respectively.

We suspect this disagreement comes from several factors: the known deviations in ALPGEN distributions for  $W+b\bar{b}/c\bar{c}$  with Tevatron data [127, 128] (arising from large uncertainties in the k-factors for the heavy flavor processes), and possible mismodeling of the  $b$ -tagging efficiencies for very pure  $b$  jets coming from gluon splitting, where there is not enough data to measure accurately the  $b$ -ID scale

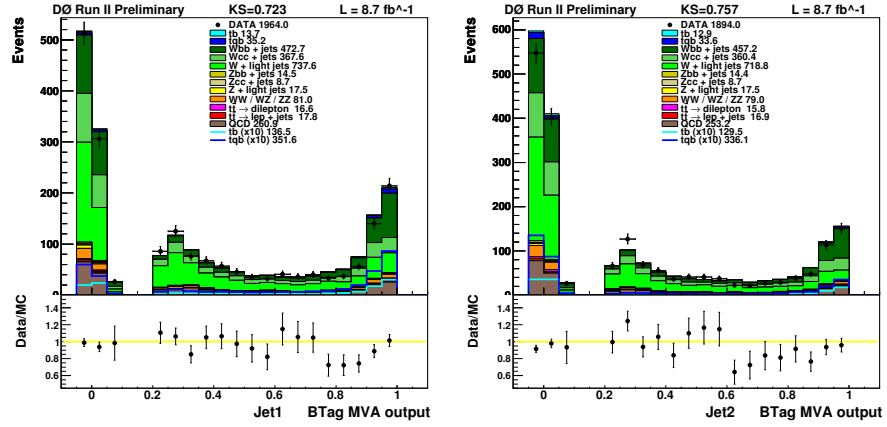


(a)

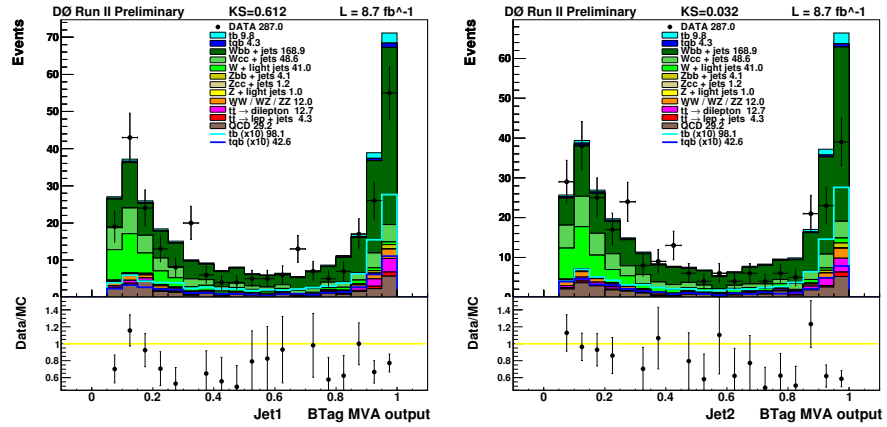


(b)

**Figure 5.3** The JetBTagMVA distributions for Run IIb e+jets (a) one-tag two-jet and (b) two-tag two-jet channels.



(a)



(b)

**Figure 5.4** The JetBTagMVA distributions for Run IIb e+jets (a) one-tag two-jet and (b) two-tag two-jet  $W$ +Jets enriched ( $H_T < 175$  GeV) samples.

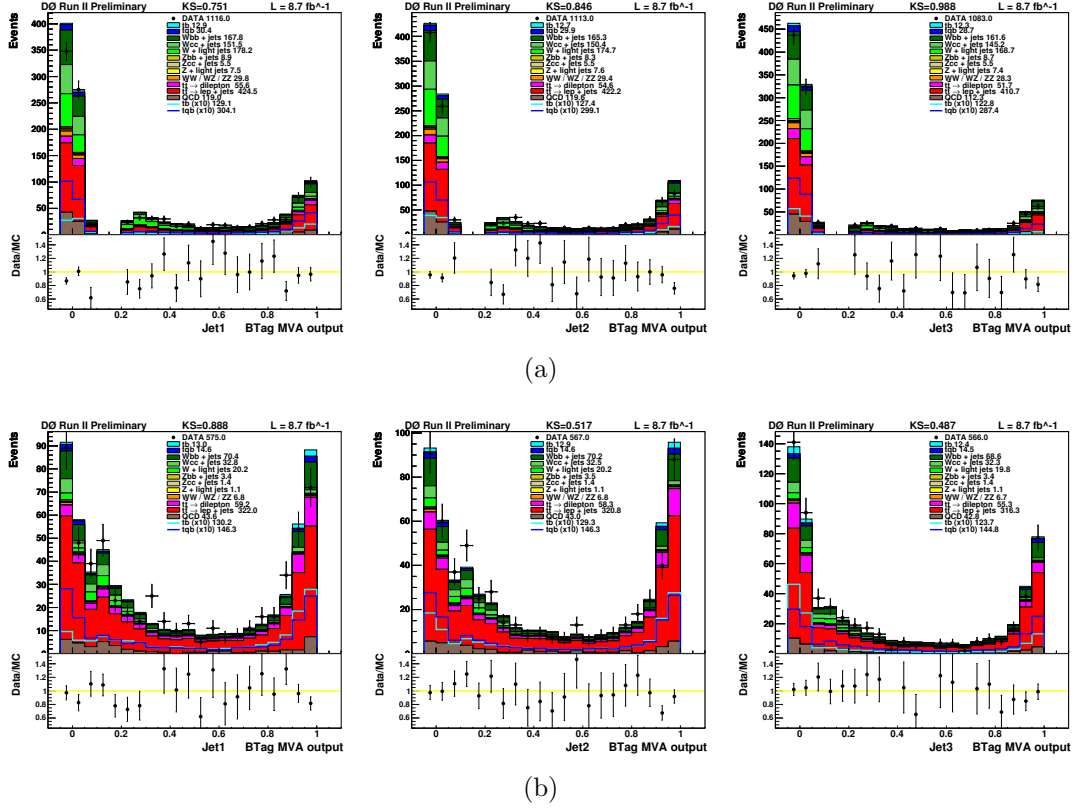


Figure 5.5 The JetBTagMVA distributions for Run IIb e+jets (a) one-tag three-jet and (b) two-tag three-jet channels.

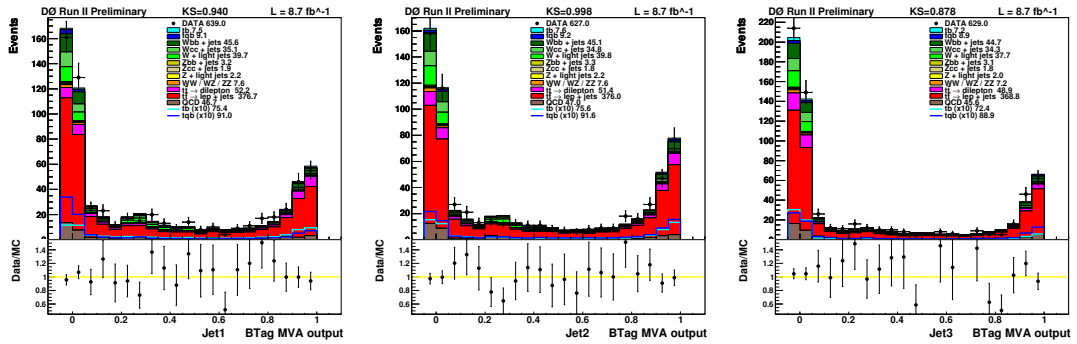


Figure 5.6 The JetBTagMVA distributions for Run IIb e+jets tagged (at least one tagged) three-jet  $t\bar{t}$  enriched samples.

factors to correct the simulation (the highest operating point provided by the  $b$ -ID group covers the  $b$ -ID output from 0.5 to 1).

Given that the disagreement is large in the signal region, for the most  $b$ -like jets, and in order to correct it, we need a region with very small signal but with enough heavy flavor contribution to have enough statistics to derive a scale factor. The basic Matrix Element discriminant, which does not use  $b$ -ID information, and does not depend on the simulation kinematics, as described in Chapter 6 and appendix L, can be used to select a background enriched sample with enough amount of backgrounds with  $b$ -jets, but very small signal, and not be biased by the disagreement we are trying to correct.

As shown in Figures 5.5 and 5.6 the agreement in the three jet channels (single and double tagged) is reasonable within the uncertainties. We have found no need to apply any correction on these channels, dominated by  $t\bar{t}$  contributions. We did however derive scale factors (following the same prescription described below), and found that the corrections only added larger uncertainties given the smaller statistics in these samples, and did not improve the data-background agreement in the control sample or in the  $t\bar{t}$ -enriched sample. Therefore, the following corrections are derived and applied exclusively on the two jet channel.

### 5.5.1 Extraction of Scale Factors

We define a control sample to correct the  $b$ -tag MVA distribution for jets in the two jet channels. These events are excluded from the signal samples and never used to measure the single top-quark cross section in the subsequent multivariate ME, BNN and BDT analyses. To limit contribution from single top-quark events, the control sample for each analysis channel is defined slightly differently. The one-tag two-jet channel is sensitive to both  $s$  and  $t$ -channel contributions, and events with  $MED_{st} < 0.12$  are selected for the control sample. For the two-tag two-jet channel, the  $s$ -channel contribution is dominant, while the  $t$ -channel is negligible, and the requirement of  $MED_s < 0.12$  is therefore utilized to define the control sample. These distributions are shown in Figure 5.7.

The MED cutoff at 0.12 in the ME output is chosen to assure sufficient statistics in the final output distribution used to measure the cross section. Even though this lower part of the discriminant contains very little signal (1% of the data), it would nevertheless contribute to constrain the backgrounds in the cross section

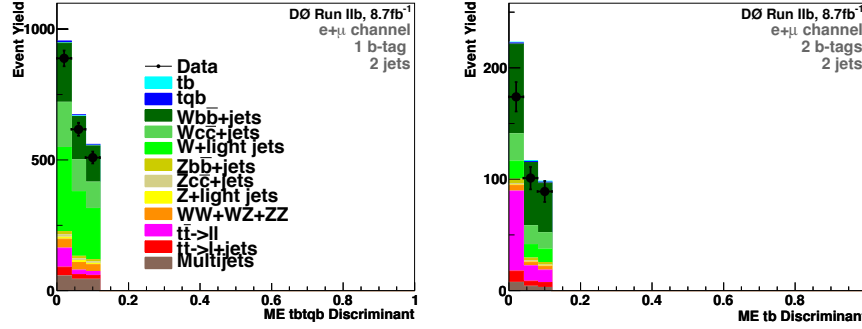


**Figure 5.7** ME discriminant without the correction in the control region, for electron and muon combined, one-tag (left) and two-tag (right) channels.

measurement. The total control sample amounts to 2848 data events (24.5% of the total data). We have tested that removing that portion from the final discriminant increases the error on the expected cross section from  $\pm 0.33$  pb to  $\pm 0.35$  pb, so it is an acceptable compromise to improve the data-background agreement and not degrade the measurement too much. The degradation comes from the fact that by carving out this control sample and removing those events from the lower part of the final discriminant used in the measurement, we diminish the statistical power of the data to constrain the backgrounds in this background-enriched region.

Once we have selected these control samples in the one and two tagged channels, and have removed them from the signal samples, we use them to measure a correction for the heavy-flavored jets ( $b$  and  $c$ ) in our two jet channels. We plot the  $b$ -ID output distribution for both jets in the events. That means that events with one  $b$ -tagged jet will contribute one entry and events with two  $b$ -tagged jets will have two entries in the  $b$  jet enriched region of the JetBTagMVA histogram. We then look only at the last two bins of this " $b$ -ID MVA output(all jets)" distribution, those with values between (0.90,0.95) and (0.95,1.0). We obtain a scale factor by dividing the light-flavor subtracted data over the heavy-flavor expectation. The number of light-flavored jets in these very high  $b$ -ID outputs is very small.

These factors are found to be channel dependent, we therefore derive a correction for the following separate channels: one-tag two-jet and two-tag two-jet channels (Run IIb periods and lepton flavors are merged), as listed in Table 5.4.

The JetBTagMVA output distributions in the control samples are shown in Figure 5.8. These plots show that the largest disagreement affects mostly the 0.9-1.0 region of the  $b$ -ID MVA output. We did try to extend the derivation of the scale factor to one more bin, in (0.8,0.9), but found that the statistics are much lower in this area, and the sample has more  $W$ +light-flavored jets, so the measured weight in this bin did not improve the agreement in the control region.

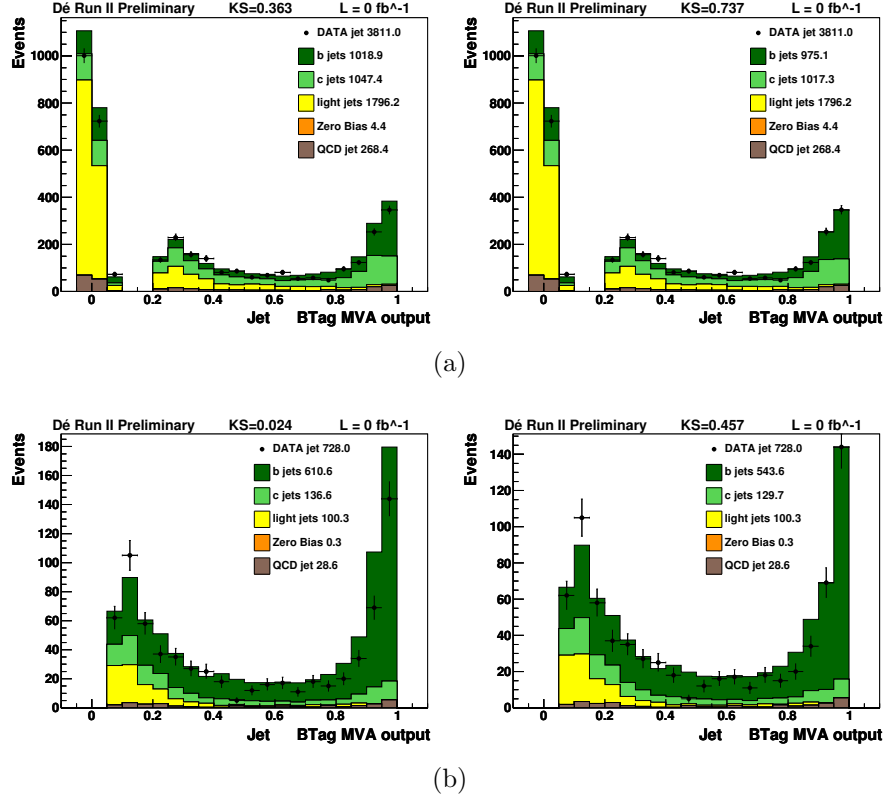


**Figure 5.8** The JetBTagMVA distributions in the control samples for (a) one-tag two-jet, and (b) two-tag two-jet channels, without the new heavy-flavor correction (left column) and with the correction (right column).

Channel	Heavy-Flavor Correction Scale Factor	
	$0.9 < \text{JetBTagMVA} < 0.95$	$0.95 < \text{JetBTagMVA} < 1.0$
one-tag, two-jet	$0.86 \pm 0.08$	$0.89 \pm 0.07$
two-tag, two-jet	$0.63 \pm 0.10$	$0.80 \pm 0.09$

**Table 5.4** The heavy-flavor correction factors, where the uncertainties come from the statistics in the control samples.

These scale factors are then applied to each heavy-flavored ( $b$  or  $c$ ) jet individually in all the simulated samples as a weight. If the heavy-flavored jet has a  $b$ -ID MVA output between 0.9 and 1.0, it will be scaled by the corresponding factor. If its  $b$ -ID MVA output is below 0.9, it is unaffected. If a second heavy-flavored jet in the same event is  $b$ -tagged and also has a  $b$ -ID MVA output above 0.9, it will also be weighted by the scale factor corresponding to its bin. Using this method, we derive the scale factors from a combined sample of  $b$ -tagged heavy-flavored jets and then apply it to each heavy-flavored jet individually.

In summary, we obtain and apply the corrections as follows:

1. Select a control region with  $MED_{st} < 0.12$  for the one-tag, two-jet channel, and  $MED_s < 0.12$  for the two-tag two-jet channel,
2. Plot the  $b$ -ID MVA output for all jets in the event in this control region (each jet contributes one entry, so two jet events contribute two entries); one plot for each channel (one-tag two-jet, and two-tag two-jet channel).
3. Define a scale factor of

$$\frac{\text{Data} - \text{light flavor simulation}}{\text{heavy flavor simulation}}$$

in the two largest output bins (0.90,0.95) and (0.95,1.0) for each channel.

4. Apply the scale factor as an event weight to every single heavy-flavored ( $b$  or  $c$ ) jet based on the value of the  $b$ -ID MVA output for that jet.
5. The weight is applied to all simulated samples for these two channels (one-tag two-jet, and two-tag two-jet channels).

### 5.5.2 Cross-Checks and Improvement on the Control Samples

We first perform a cross-check, or a “closure” test by applying the heavy-flavor correction to all the heavy-flavored jets in all the samples in the control region, to check that indeed the agreement between data and background agreement improves. Tables 5.5 and 5.6 show the event yields and the KS values (Kolmogorov-Smirnov values, which test the agreement of two distributions) for the comparison

of the JetBTagMVA distributions, while Figures 5.9 and 5.10 demonstrate the agreement in JetBTagMVA for data and MC. The MC modeling clearly improves when the heavy-flavor correction is implemented.

Yields in Events in the Control Samples				
	Run IIb Electron + Muon Two-Jet Channel			
	One-Tag		Two-Tag	
	no correction	corrected	no correction	corrected
$tb$	6.17	5.80	2.46	1.94
$tqb$	14.5	13.6	2.79	2.31
Background	2166	2093	432.9	363.7
Background+Signal	2187	2113	438.2	368.0
Data	2014	2014	364	364
(Data-Background)/Data	-7.5%	-3.9%	-18.9%	0.08%
(Data-All MC)/Data	-8.5%	-4.9%	-20.4%	-1.1%

**Table 5.5** Event yields in the control samples without and with the heavy-flavor correction. The “All MC” contribution includes all backgrounds and signals.

KS and $\chi^2$ Values in the Control Samples				
	Run IIb Electron + Muon Two-Jet Channel			
	One-Tag		Two-Tag	
	no correction	corrected	no correction	corrected
KS Value				
Jet1BTagMVA	0.275	0.751	0.967	0.731
Jet2BTagMVA	0.926	0.928	0.005	0.162
Jet1BTagMVA OP	0.514	0.835	0.995	0.956
Jet2BTagMVA OP	0.957	0.955	0.007	0.234
$\chi^2$ /Number of bins				
Jet1BTagMVA	2.835	2.225	2.831	1.891
Jet2BTagMVA	1.648	1.374	3.685	2.083
Jet1BTagMVA OP	2.885	1.648	3.423	1.448
Jet2BTagMVA OP	2.351	1.197	6.702	1.996

**Table 5.6** KS values and  $\chi^2$  per bin of the JetBTagMVA distributions in two-jet control samples. The “JetBTagMVA OP” distribution shows the JetBTagMVA outputs binned with the  $b$ -ID operating points.

We also look at background subtracted data and measure the difference in all the bins, as shown in Figure 5.11, and compare it with the status before the corrections.

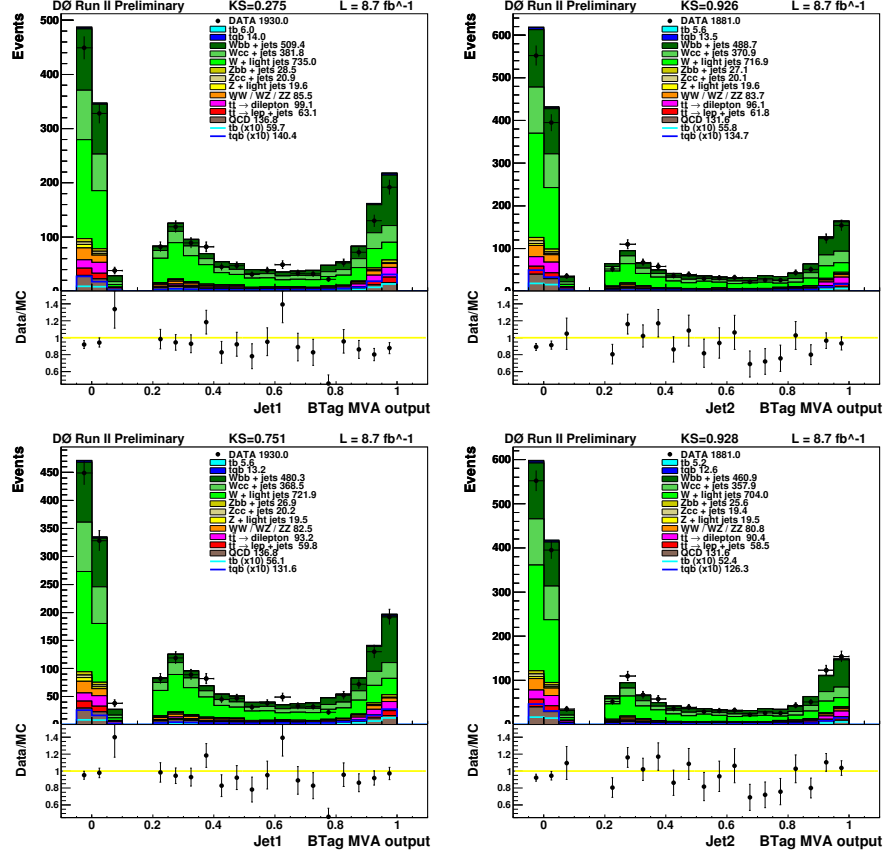
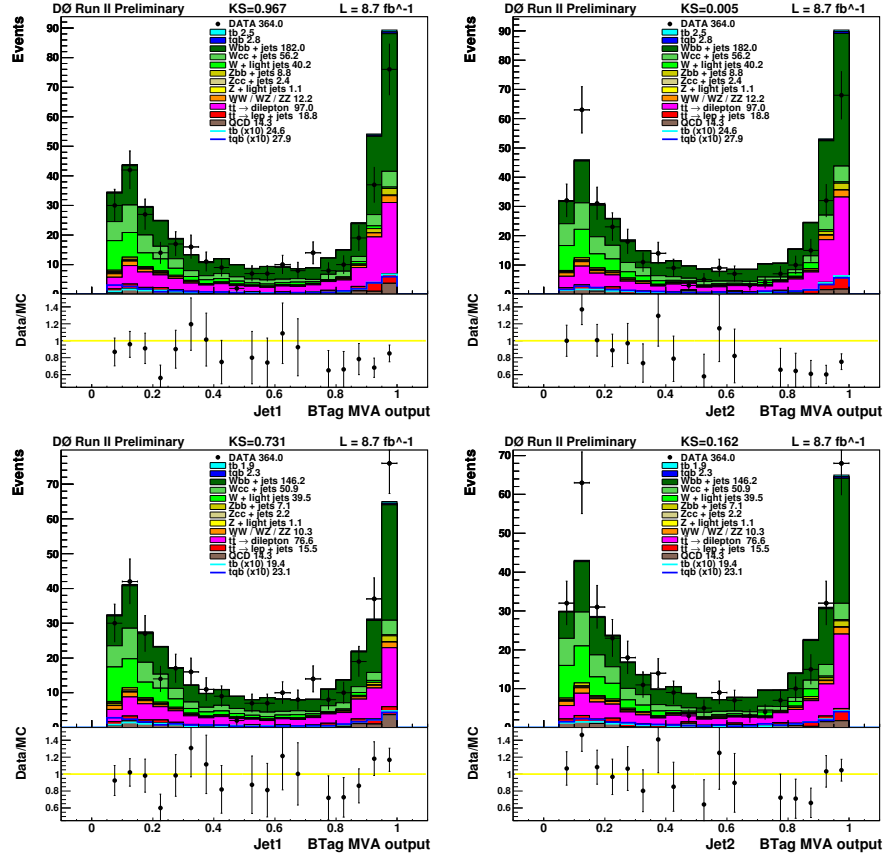


Figure 5.9 JetBTagMVA distributions in one-tag two-jet control samples, without (upper row) and with (lower row) the heavy-flavor correction.

### 5.5.3 Cross-Checks and Improvement Using Enriched Samples of $W$ +jets Events

The same kind of procedures are followed for the background enriched  $W$ +jets samples. The event yields in the background ( $W$ +jets) enriched samples are listed in Table 5.7, the KS values of the JetBTagMVA distributions are listed in Table 5.8, and the JetBTagMVA distributions are plotted in Figures 5.12 and 5.13, where the agreement also improves across all bins.



**Figure 5.10** JetBTagMVA distributions in two-tag two-jet control samples, without (upper row) and with (lower row) the heavy-flavor correction.

Yields in Events in the Cross-Check $W$ +Jets Samples				
	Run IIb Electron + Muon Two-Jet Channel			
	One-Tag		Two-Tag	
	no correction	corrected	no correction	corrected
$tb$	26.2	24.5	18.1	14.2
$tqb$	70.4	66.0	8.3	6.8
Background	3936	3808	618.3	527.2
Background+Signal	4032	3899	644.7	548.2
Data	3691	3691	534	534
(Data-Background)/Data	-6.6%	-3.2%	-15.8%	1.3%
(Data-All MC)/Data	-9.2%	-5.6%	-20.7%	-2.6%

**Table 5.7** Event yields in the cross-check  $W$ +jets samples without and with the heavy-flavor correction. The “All MC” contribution includes all backgrounds and signals.

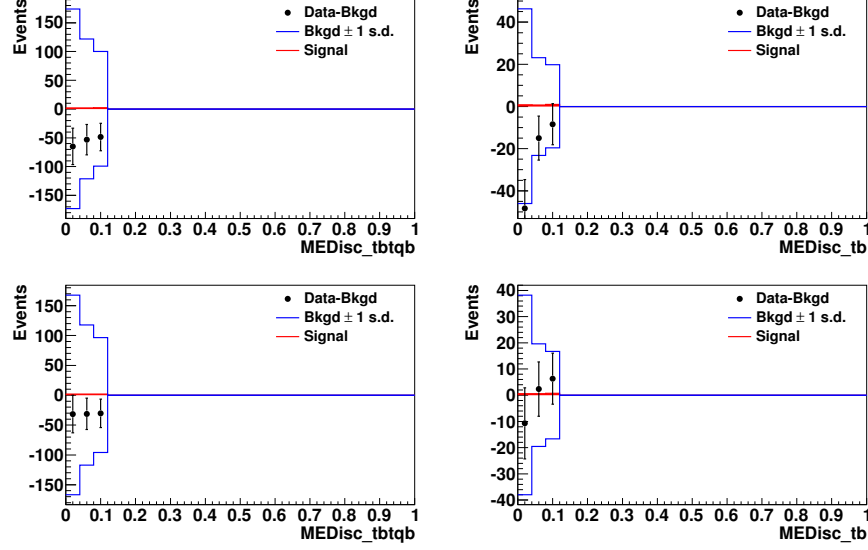


**Figure 5.11** The background-subtracted data in the control sample, without (upper row) and with (lower row) the heavy-flavor correction, for one-tag (left) and two-tag (right) channels.

KS and $\chi^2$ Values in the Cross-Check Samples				
	Run IIb $W$ +jets Cross-Check Sample, Electron + Muon Channel			
	One-Tag		Two-Tag	
	no correction	corrected	no correction	corrected
KS Value				
Jet1BTagMVA	0.339	0.977	0.542	0.781
Jet2BTagMVA	0.324	0.791	0.002	0.134
Jet1BTagMVA OP	0.853	1.000	0.875	0.988
Jet2BTagMVA OP	0.762	0.993	0.002	0.200
$\chi^2$ /Number of bins				
Jet1BTagMVA	2.664	1.542	2.733	1.385
Jet2BTagMVA	3.182	2.131	5.100	2.172
Jet1BTagMVA OP	3.679	1.431	4.819	1.567
Jet2BTagMVA OP	4.853	2.345	8.738	1.706

**Table 5.8** KS values and  $\chi^2$  per bin of the JetBTagMVA distributions in the  $W$ +jets enriched ( $H_T < 175$  GeV) cross-check samples. The “JetBTagMVA OP” distribution shows the JetBTagMVA outputs binned with the  $b$ -ID operating points.

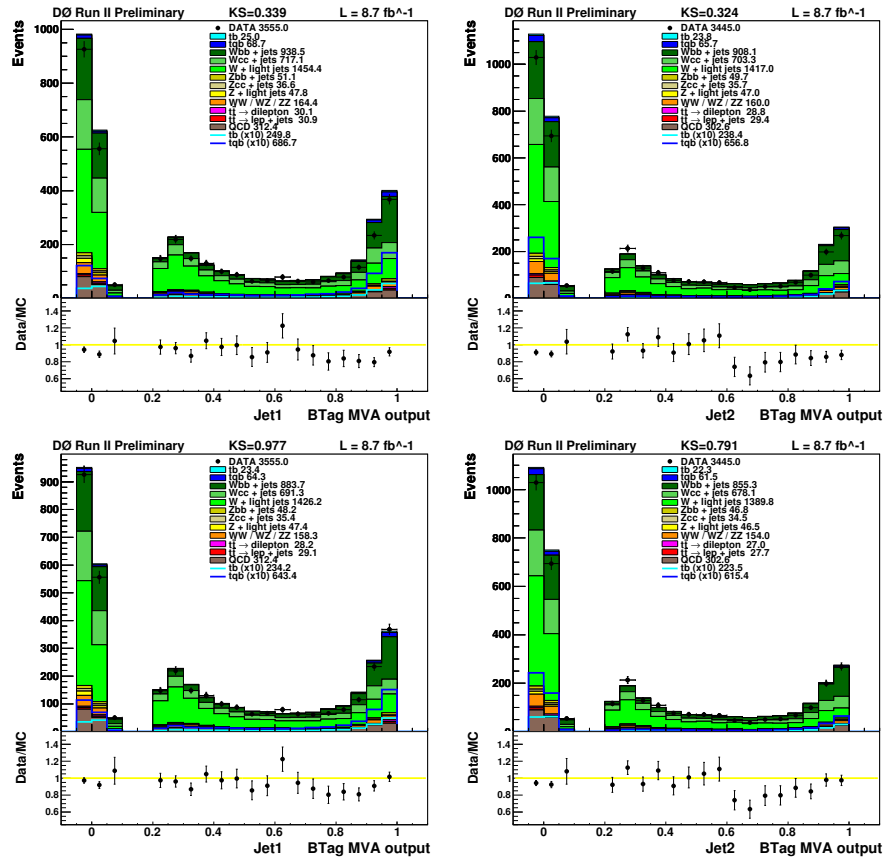
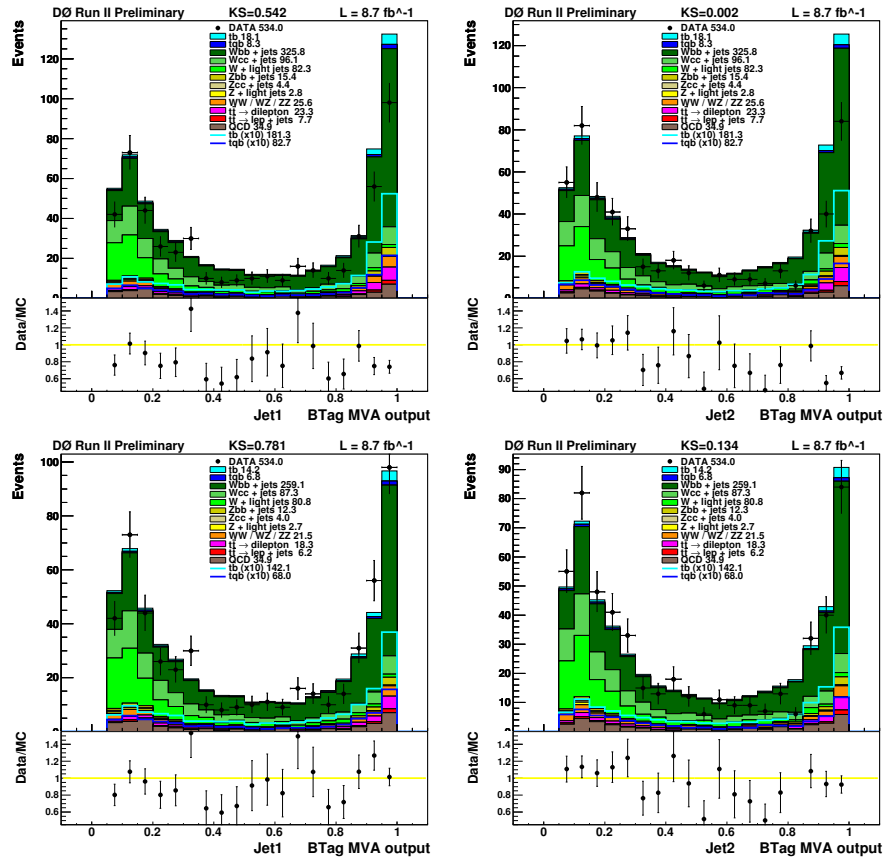


Figure 5.12 JetBTagMVA distributions in the  $W$ +jets enriched cross-check samples and one-tag channel, without (upper row) and with (lower row) the heavy-flavor correction.



**Figure 5.13** JetBTagMVA distributions in the  $W$ +jets enriched cross-check samples and two-tag channel, without (upper row) and with (lower row) the heavy-flavor correction.

### 5.5.4 Cross-Checks for the Heavy-Flavor Scale Factor

As another cross-check, we obtain the heavy-flavor scale factor, as in the previous analyses [107]. The heavy flavor scale factor is based on three methods described in Appendix 7 of Ref. [107], for two-jet events that pass the selection criteria of Section 5.1. The essence of these methods are summarized below.

#### 1. Heavy flavor scale factor measured in the zero-tag sample:

We measure  $\lambda_{HF}$  in a zero-tag sample, which consists of the two-jet events passing the selection described in Section 5.1, but failing the  $b$ -tagging requirement. This sample is completely orthogonal to the sample used to measure the single top-quark cross section. The following equation is used to derive  $\lambda_{HF}$ :

$$N^{(0)} = N_{wlp}^{(0)} + \lambda_{HF} N_{whp}^{(0)} \quad (5.5.1)$$

where  $N = N_{\text{data}} - N_{\text{multijet}} - N_{\text{non-wjets}}$ ,  $N_{wlp} = N_{wjj} + N_{wcj}$ , and  $N_{whp} = N_{wcc} + N_{wbb}$ . The superscript (0) indicates the events in the zero-tag sample.

#### 2. Heavy flavor scale factor measured in all the samples:

Using this method, we measure the heavy flavor scale factor by simultaneously normalizing the inclusive  $W$ +jets and heavy-flavored  $W$ +jets samples to the zero-tagged (0) and tagged (1, including the single-tagged and double-tagged) data samples:

$$\begin{aligned} N^{(0)} &= \lambda(N_{wlp}^{(0)} + \lambda_{HF} N_{whp}^{(0)}) \\ N^{(1)} &= \lambda(N_{wlp}^{(1)} + \lambda_{HF} N_{whp}^{(1)}) \end{aligned} \quad (5.5.2)$$

where  $\lambda$  is the  $W$ +jets normalization factor,  $\lambda_{HF}$  is the heavy flavor scale factor,  $N = N_{\text{data}} - N_{\text{multijet}} - N_{\text{non-wjets}}$ ,  $N_{wlp} = N_{wjj} + N_{wcj}$  and  $N_{whp} = N_{wcc} + N_{wbb}$ .

By solving Eq. 5.5.2, we obtain:

$$\lambda = \frac{N^{(0)}}{N_{wlp}^{(0)} + \lambda_{HF} N_{whp}^{(0)}}, \quad (5.5.3)$$

$$\lambda_{HF} = \frac{N^{(1)} N_{wlp}^{(0)} - N^{(0)} N_{wlp}^{(1)}}{N^{(0)} N_{whp}^{(1)} - N^{(1)} N_{whp}^{(0)}}. \quad (5.5.4)$$

### 3. Heavy flavor scale factor measured by fitting the $b$ -tagging output:

We also measure the heavy flavor scale factor by looking for the best agreement between the data and the simulation on a distribution that is sensitive to the heavy flavor contributions. The maximum value of the MVA  $b$ -tagging outputs in an event is chosen. We determine the best data-simulation agreement by minimizing the  $\chi^2$  defined below:

$$\chi^2(\lambda_{\text{HF}}) = \sum_i \frac{[N_i - \lambda(\lambda_{\text{HF}})(N_{\text{wlp},i} + \lambda_{\text{HF}}N_{\text{whp},i})]^2}{E_i^2 + E_{\text{wlp},i}^2 + E_{\text{whp},i}^2}, \quad (5.5.5)$$

where  $N_i = N_{\text{data},i} - N_{\text{multijet},i} - N_{\text{non-wjets},i}$ , and  $N_{\text{data},i}$ ,  $N_{\text{multijet},i}$  and  $N_{\text{non-wjets},i}$  are the event yields in the bin  $i$  of the  $b$ -tagging outputs for data, multijet and non  $W$ +jet events.  $N_{\text{wlp},i}$  and  $N_{\text{whp},i}$  are the event yields in the bin  $i$  of the  $W$ +light jets ( $Wcj$  and  $Wjj$ ) and of the  $W$ +heavy-flavored jets ( $Wb\bar{b}$  and  $Wc\bar{c}$ ), respectively.  $E_i$ ,  $E_{\text{wlp},i}$ , and  $E_{\text{whp},i}$  represent the  $i$ th bin errors. The function  $\lambda(\lambda_{\text{HF}})$  is constrained as follows,

$$\lambda(\lambda_{\text{HF}}) = \frac{\sum_i N_i}{\sum_i (N_{\text{wlp},i} + \lambda_{\text{HF}}N_{\text{whp},i})} \quad (5.5.6)$$

As shown in Table 5.9, the constant heavy flavor scale factors ( $\lambda_{\text{HF}}$ ) measured with these three methods were not consistent with unity, and if now measured on this corrected sample, all agree with 1.0 within 3%. Moreover, Table 5.10 shows the heavy flavor scale factor measured with the second method, but from different tagged channels. After applying the new correction, these scale factors measured from different tagged channels are consistent with unity within 10%, which is covered by the 20% uncertainty we assign as will be discussed in Section 5.5.6, whereas they can be 30% apart from 1 without the new correction. Finally, we examine the  $b$ -ID operating point dependency of the heavy flavor scale factor measured with the second method. Without the new correction, these heavy flavor scale factors have a huge dependency on the  $b$ -ID operating points and tagged channels, as shown in Figure 5.14, but those measured on the corrected samples are all consistent with unity.

Heavy Flavor Scale Factor for $W$ +jets Events				
Method	no correction		corrected	
	$\lambda$	$\lambda_{\text{HF}}$	$\lambda$	$\lambda_{\text{HF}}$
(1) Counting zero-tagged sample	1	$1.01 \pm 0.03$	1	$1.01 \pm 0.03$
(2) Counting tagged and orthogonal samples	$1.021 \pm 0.003$	$0.81 \pm 0.03$	$1.003 \pm 0.003$	$0.98 \pm 0.03$
(3) Minimizing $\chi^2$ of $b$ -tagging output distribution	$1.018 \pm 0.007$	$0.83 \pm 0.05$	$1.000 \pm 0.007$	$1.04 \pm 0.05$

**Table 5.9** The heavy flavor scale factors derived with the three methods for the overall Run IIb and the combined electron and muon channels.

Heavy Flavor Scale Factor for $W$ +jets Events Measured in Individual Samples				
Channel	no correction		corrected	
	$\lambda$	$\lambda_{\text{HF}}$	$\lambda$	$\lambda_{\text{HF}}$
Inclusive tagged channel	$1.021 \pm 0.003$	$0.81 \pm 0.03$	$1.003 \pm 0.003$	$0.98 \pm 0.03$
One-tagged channel	$1.016 \pm 0.004$	$0.85 \pm 0.03$	$1.007 \pm 0.004$	$0.95 \pm 0.04$
Two-tagged channel	$1.037 \pm 0.007$	$0.70 \pm 0.05$	$0.990 \pm 0.008$	$1.08 \pm 0.07$

**Table 5.10** The heavy flavor scale factors derived with the second method, in which the event yields in the tagged and orthogonal samples are normalized to the data simultaneously, for the overall Run IIb and the combined electron and muon channels, but one-tagged and two-tagged samples separately.

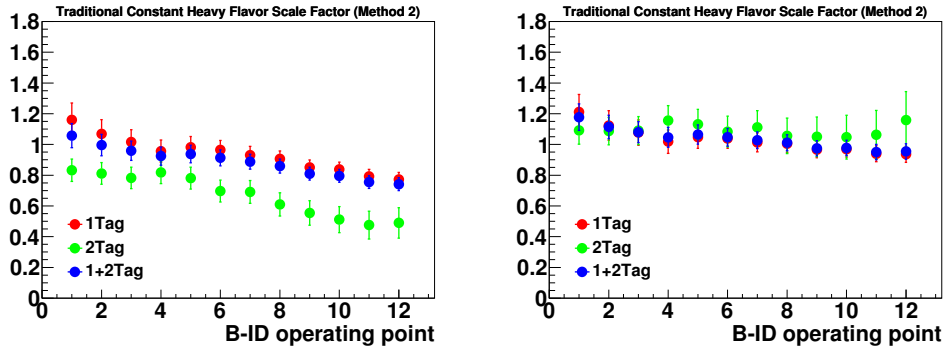


**Figure 5.14** Heavy flavor scale factors (measured with the second method) versus  $b$ -ID operating points without (left) and with (right) the heavy-flavor correction, for the overall Run IIb and the combined electron and muon channels, but one-tagged, two-tagged, and inclusive tagged samples separately.

### 5.5.5 Cross-Checks and Improvement on the Signal Region

Convinced that the scale factors improve agreement between data and simulation in the control sample, we apply the correction in to the region of signal, and perform the following cross-checks before extracting the cross section. First, we check event yields in the region of signal, as listed in Table 5.11, and examine the JetBTagMVA distributions in the signal region, including their KS values, listed in Table 5.12, and the impact on MC modeling in Figures 5.15 and 5.16. Finally, Figure 5.17 shows the background-subtracted data in the region of signal.

Yields in Events in Signal Samples				
	Run IIb Electron + Muon Two-Jet Channel			
	One-Tag		Two-Tag	
	no correction	corrected	no correction	corrected
$tb$	101.8	95.8	93.5	73.7
$tqb$	229.4	215.1	26.3	21.8
Background	5716	5523	1198	1011
Background+Signal	6047	5834	1318	1106
Data	5785	5785	1156	1156
(Data-Background)/Data	1.2%	4.5%	-3.6%	12.5%
(Data-All MC)/Data	-4.5%	-0.9%	-14.0%	4.3%

**Table 5.11** Event yields in the signal samples without and with the heavy-flavor correction. The “All MC” contribution includes all the backgrounds and signals.

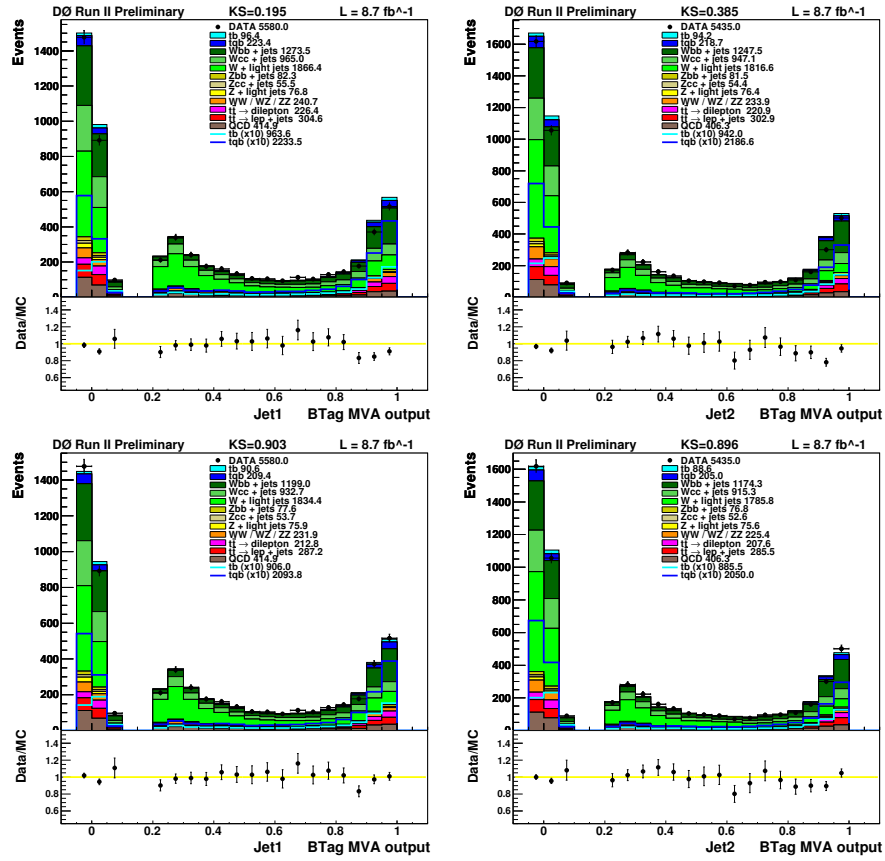
### 5.5.6 Uncertainty for the Heavy Flavor Correction

We estimate the uncertainty on the heavy-flavor correction from the statistical uncertainties used to derive the correction in each channel, which, from Table 5.4, suggest a 20% uncertainty on the heavy-flavor correction.

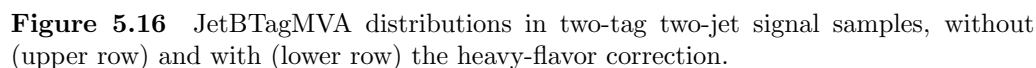
This uncertainty applies to all MC samples: including the signal and background, and is anticorrelated with the  $b$ -tagging uncertainty (on the scale factor applied to the simulation to correct the  $b$ -tagging efficiency). It is anticorrelated because when the  $b$ -tagging efficiency varies up, the MC simulation overshoots the

KS and $\chi^2$ Values in the Signal Samples				
	Run IIb Electron + Muon Two-Jet Channel			
	One-Tag		Two-Tag	
	correction	corrected	no correction	corrected
KS Value				
Jet1BTagMVA	0.195	0.903	0.033	0.637
Jet2BTagMVA	0.385	0.896	0.189	0.243
Jet1BTagMVA OP	1.000	1.000	0.106	0.997
Jet2BTagMVA OP	0.558	0.994	0.913	0.563
$\chi^2$ /Number of bins				
Jet1BTagMVA	1.929	0.898	3.202	1.721
Jet2BTagMVA	2.252	0.985	2.076	0.909
Jet1BTagMVA OP	3.048	1.807	6.151	1.718
Jet2BTagMVA OP	2.866	1.040	3.645	1.219

**Table 5.12** KS values and  $\chi^2$  per bin of the JetBTagMVA distributions in two-jet signal samples. The “JetBTagMVA OP” distribution shows the JetBTagMVA outputs binned with the  $b$ -ID operating points.



**Figure 5.15** JetBTagMVA distributions in one-tag two-jet signal samples, without (upper row) and with (lower row) the heavy-flavor correction.



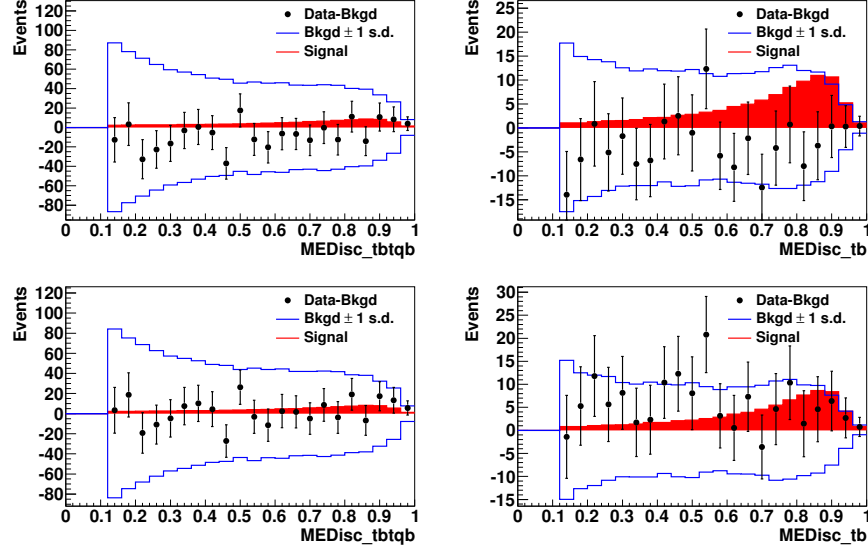


**Figure 5.17** The background-subtracted data in the signal sample, without (upper row) and with (lower row) the heavy-flavor correction.

data more, and the heavy-flavor correction factor is smaller in order to bring the MC simulation downward, and vice versa.

## 5.6 Comparison of Data with Simulation and Event Yields

After applying all the corrections to the MC samples, we attain good agreement between data and MC simulation, as shown in the control plots in Appendix D. The predicted number of events from each signal and background source, are summarized in Tables 5.13 to 5.18. All the MC processes except  $W$ +jets are normalized to the theoretical cross sections, as indicated in Tables 4.3 and 5.1. Since we normalize the  $W$ +jets and multijet backgrounds to the data, the total yields of the simulated samples matches exactly the number of events in the pre-tagged data samples.

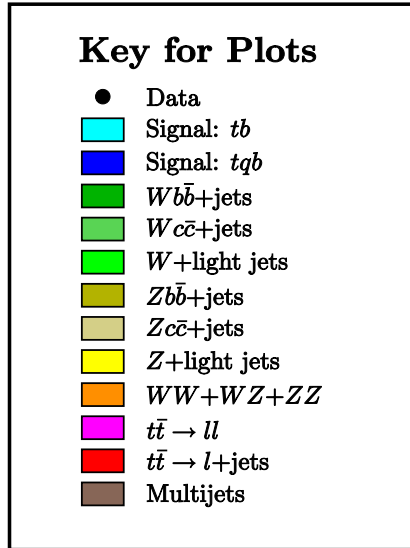
Figure 5.18 shows the color scheme used in the plots in this analysis and note.

Pre-tagged event yields								
	Run IIa, 1 fb <sup>-1</sup>				Run IIb, 8.7 fb <sup>-1</sup>			
	Electron Channel		Muon Channel		Electron Channel		Muon Channel	
	2 jets	3 jets	2 jets	3 jets	2 jets	3 jets	2 jets	3 jets
Signals								
$tb$	20	8.1	20	9.4	158	39	133	34
$tqb$	39	17	41	21	280	78	248	67
$tb + tqb$	59	25	61	31	439	117	382	102
Backgrounds								
$t\bar{t} \rightarrow \ell\ell$	48	35	45	37	539	175	398	132
$t\bar{t} \rightarrow \ell + \text{jets}$	28	109	20	108	579	1223	412	997
$Wb\bar{b}$	405	132	474	179	2680	501	2577	552
$Wc\bar{c}$	900	300	1104	418	5914	1151	5773	1273
$Wcj$	970	218	1122	284	4865	512	4442	537
$Wjj$	11073	2396	13952	3519	50530	5706	50841	6421
$Zb\bar{b}$	12	5.4	48	16	112	26	226	43
$Zc\bar{c}$	24	9.0	106	34	192	43	482	86
$Zjj$	359	89	1134	256	1618	223	3869	464
Diboson	307	81	371	114	2050	327	2057	329
Multijet	837	212	234	159	9423	1639	1305	356
Background Sum	14962	3586	18610	5125	78502	11526	72382	11192
Background + Signal	15021	3611	18672	5156	78941	11642	72764	11294
Data	15021	3611	18672	5156	78936	11641	72762	11293

**Table 5.13** Pre-tagged event yields after selection.

Pre-tagged event yields for combined signals and backgrounds						
	Electron+Muon, Run IIa + Run IIb					
	2 jets		3 jets		All Channels	
Signals						
$t\bar{b}$	333 ± 0.6		90 ± 0.3		423 ± 0.7	
$tq\bar{b}$	608 ± 1.2		184 ± 0.7		793 ± 1.4	
Backgrounds						
$t\bar{t}$	2069 ± 4.6	(1.1%)	2817 ± 6.0	(9.0%)	4886 ± 7.6	(2.3%)
$W$ +jets	157622 ± 111	(85%)	24099 ± 42	(77%)	181721 ± 118	(84%)
$Z$ +jets & diboson	12968 ± 19	(7.0%)	2147 ± 6.6	(6.8%)	15115 ± 20	(7.0%)
Multijet	11798 ± 51	(6.4%)	2365 ± 22	(7.5%)	14164 ± 56	(6.6%)
Background Sum	184457 ± 124		31428 ± 48		215885 ± 133	
Backgrounds + Signals	185398 ± 124		31703 ± 48		217101 ± 133	
Data	185391 ± 431		31701 ± 178		217092 ± 466	
$S(t\bar{b}) : B$	1:555		1:347		1:510	
$S(tq\bar{b}) : B$	1:303		1:171		1:272	

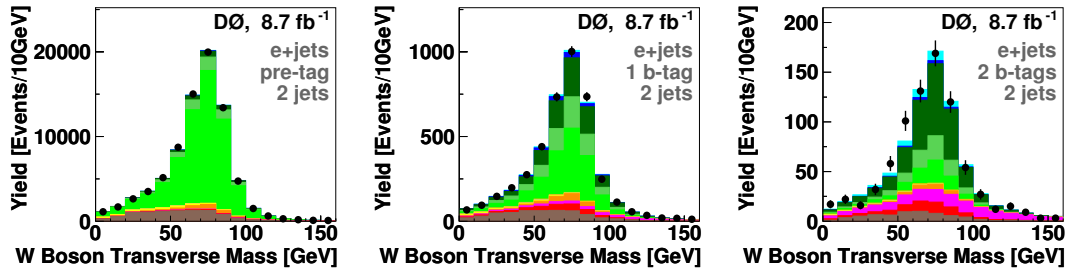
**Table 5.14** Pre-tagged event yields with statistical uncertainty for each jet multiplicity and for all analysis channels combined. The percentages are of the total background for each component.



**Figure 5.18** Illustration of the color scheme used in plots of signals and backgrounds in the single top-quark analyses.

Single-tagged event yields								
	Run IIa, 1 fb <sup>-1</sup>				Run IIb, 8.7 fb <sup>-1</sup>			
	Electron Channel		Muon Channel		Electron Channel		Muon Channel	
	2 jets	3 jets	2 jets	3 jets	2 jets	3 jets	2 jets	3 jets
Signals								
$t\bar{t}$	8.0	3.1	8.3	3.6	55	14	46	12
$tq\bar{b}$	16	6.9	17	8.6	121	32	108	28
$t\bar{t} + tq\bar{b}$	24	10	26	12	176	45	154	40
Backgrounds								
$t\bar{t} \rightarrow \ell\bar{\ell}$	20	15	19	16	188	61	138	46
$t\bar{t} \rightarrow \ell + \text{jets}$	11	44	8.0	44	211	450	153	369
$Wb\bar{b}$	126	43	149	58	880	176	865	196
$Wc\bar{c}$	64	25	75	34	684	158	660	174
$Wc\bar{j}$	77	26	88	23	633	73	590	74
$Wj\bar{j}$	135	40	167	58	701	112	721	125
$Zb\bar{b}$	4.0	2.0	17	5.6	35	9.8	75	16
$Zc\bar{c}$	1.4	0.9	8.0	3.3	21	6.0	56	12
$Zj\bar{j}$	5.1	1.7	13	4.3	39	8.1	62	12
Diboson	17	5.4	20	7.6	161	31	164	30
Multijet	31	9.4	13	14	492	130	87	35
Background Sum	492	211	577	267	4045	1215	3572	1091
Background + Signal	515	221	603	279	4221	1260	3726	1130
Data	482	191	592	256	4229	1188	3602	1094

Table 5.15 Single-tagged event yields after selection.


 Figure 5.19 The transverse mass of the  $W$  boson from the top quark for pre-tagged (left), single-tagged (central), and double-tagged (right) for Run IIb, electron channel, two-jet events.

Single-tagged event yields for combined signals and backgrounds						
	Electron+Muon, Run IIa + Run IIb					
	2 jets		3 jets		All Channels	
Signals						
$t\bar{b}$	118 ± 0.4		33 ± 0.2		150 ± 0.4	
$tqb$	262 ± 0.8		75 ± 0.4		337 ± 0.9	
Backgrounds						
$t\bar{t}$	747 ± 2.7	(8.6%)	1044 ± 3.7	(38%)	1791 ± 4.6	(16%)
$W$ +jets	6616 ± 19	(76%)	1395 ± 8.5	(50%)	8012 ± 21	(70%)
$Z$ +jets & diboson	700 ± 3.3	(8.1%)	156 ± 1.7	(5.6%)	855 ± 3.7	(7.5%)
Multijet	623 ± 12	(7.2%)	188 ± 6.3	(6.8%)	811 ± 13	(7.1%)
Background Sum	8685 ± 22		2784 ± 11		11469 ± 25	
Backgrounds + Signals	9065 ± 23		2891 ± 11		11956 ± 25	
Data	8905 ± 94		2729 ± 52		11634 ± 108	
$S(t\bar{b}) : B$	1:74		1:85		1:76	
$S(tqb) : B$	1:33		1:37		1:34	

**Table 5.16** Single-tagged event yields with statistical uncertainty for each jet multiplicity and for all analysis channels combined. The percentages are of the total background for each component.

## 5.7 Total Acceptance for Signal $\mathcal{A}$

All the selections described in Sections 5.1 and 5.4 are intended to maximize yield of signal, while minimizing background and the possibility of any mismodeling of the separate contributions.

The total “signal acceptance” is defined to contain the impact of both the branching fraction to each specific final state and the efficiency of the geometric and kinematic selections:

$$\mathcal{A} = \frac{\mathcal{B}}{\mathcal{N}_{\text{initial}}} \sum_{\mathcal{N}_{\text{selected}}} \varepsilon_{\text{corrections}}, \quad (5.7.1)$$

where  $\mathcal{B}$  is the branching fraction for the final state of interest,  $\mathcal{N}_{\text{initial}}$  the initial number of events generated in the MC sample,  $\mathcal{N}_{\text{selected}}$  the number of MC events selected, and  $\varepsilon_{\text{corrections}}$  are the correction factors accounting for any difference in selection efficiencies between data and the MC simulation, as discussed in

Double-tagged event yields								
	Run IIa, 1 fb <sup>-1</sup>				Run IIb, 8.7 fb <sup>-1</sup>			
	Electron Channel		Muon Channel		Electron Channel		Muon Channel	
	2 jets	3 jets	2 jets	3 jets	2 jets	3 jets	2 jets	3 jets
Signals								
$tb$	4.6	1.9	4.7	2.2	41	13	35	12
$tqb$	0.7	1.7	0.8	1.9	13	15	11	13
$tb + tqb$	5.3	3.5	5.5	4.1	54	28	46	25
Backgrounds								
$t\bar{t} \rightarrow \ell\ell$	10	9.8	10	11	137	61	104	47
$t\bar{t} \rightarrow \ell + \text{jets}$	2.5	21	1.8	22	59	328	43	269
$Wb\bar{b}$	33	12	34	15	273	72	254	77
$Wc\bar{c}$	5.0	2.3	4.3	3.1	91	33	88	36
$Wcj$	1.7	0.8	2.0	0.8	33	5.5	26	6.8
$Wjj$	3.0	1.8	3.7	2.5	48	15	52	18
$Zb\bar{b}$	0.4	0.7	3.1	1.6	8.7	3.6	21	6.4
$Zc\bar{c}$	0.0	0.1	0.6	0.3	2.9	1.5	7.0	2.9
$Zjj$	0.3	0.1	0.1	0.3	2.3	1.1	4.3	1.6
Diboson	1.8	0.8	2.8	1.1	21	7.0	23	7.2
Multijet	1.9	0.9	0.8	1.5	65	45	12	8.8
Background Sum	59	50	64	58	741	572	634	479
Background + Signal	65	54	69	62	794	600	680	504
Data	59	60	71	64	805	584	719	527

**Table 5.17** Double-tagged event yields after selection.

Double-tagged event yields for combined signals and backgrounds						
	Electron+Muon, Run IIa + Run IIb					
	2 jets		3 jets		All Channels	
Signals						
$tb$	$85 \pm 0.3$		$29 \pm 0.2$		$114 \pm 0.3$	
$tqb$	$26 \pm 0.2$		$32 \pm 0.3$		$57 \pm 0.4$	
Backgrounds						
$t\bar{t}$	$367 \pm 1.5$	(25%)	$767 \pm 3.0$	(66%)	$1134 \pm 3.4$	(43%)
$W$ +jets	$951 \pm 5.6$	(64%)	$300 \pm 3.2$	(26%)	$1252 \pm 6.5$	(47%)
$Z$ +jets & diboson	$100 \pm 0.9$	(6.7%)	$36 \pm 0.6$	(3.1%)	$136 \pm 1.1$	(5.1%)
Multijet	$80 \pm 4.2$	(5.3%)	$56 \pm 3.6$	(4.8%)	$135 \pm 5.6$	(5.1%)
Background Sum	$1498 \pm 7.3$		$1160 \pm 5.8$		$2658 \pm 9.3$	
Backgrounds + Signals	$1608 \pm 7.3$		$1220 \pm 5.8$		$2829 \pm 9.3$	
Data	$1654 \pm 41$		$1235 \pm 35$		$2889 \pm 54$	
$S(tb) : B$	1:18		1:40		1:23	
$S(tqb) : B$	1:58		1:37		1:46	

**Table 5.18** Double-tagged event yields with statistical uncertainty for each jet multiplicity and for all analysis channels combined. The percentages are of the total background for each component.

Section 5.2. The acceptance can also be written in the following form,

$$\mathcal{A} = \frac{\text{Yield in events}}{\sigma \times \mathcal{L}}, \quad (5.7.2)$$

in which  $\sigma$  is the predicted total production cross section and  $\mathcal{L}$  is the integrated luminosity, and the signal acceptance refers to Equation (5.7.2).

The final combined signal acceptance is:

$$\begin{aligned} \mathcal{A}(s\text{-channel } tb) &= 2.6\% \\ \mathcal{A}(t\text{-channel } tqb) &= 1.8\% \\ \mathcal{A}(s + t \text{ channels } tb + tqb) &= 2.0\%. \end{aligned} \quad (5.7.3)$$

For the  $s$ -channel, we obtain acceptances similar to those of the previous analysis [107], but using tighter selections. This is because  $s$ -channel jets have larger  $p_T$ , and the final state particles are emitted more centrally. The previous selections focused on  $t$ -channel production, which requires more acceptance for softer and more forward jets.

Signal Acceptance								
	Run IIa				Run IIb			
	Electron Channel		Muon Channel		Electron Channel		Muon Channel	
	2 jets	3 jets	2 jets	3 jets	2 jets	3 jets	2 jets	3 jets
PreTag								
<i>tb</i>	1.8%	0.72%	1.9%	0.86%	1.6%	0.42%	1.3%	0.37%
<i>tqb</i>	1.6%	0.70%	1.8%	0.90%	1.3%	0.39%	1.2%	0.34%
<i>tb + tqb</i>	1.7%	0.71%	1.8%	0.89%	1.4%	0.40%	1.2%	0.35%
OneTag								
<i>tb</i>	0.72%	0.28%	0.74%	0.33%	0.61%	0.15%	0.51%	0.13%
<i>tqb</i>	0.65%	0.28%	0.72%	0.35%	0.62%	0.16%	0.55%	0.14%
<i>tb + tqb</i>	0.67%	0.28%	0.72%	0.34%	0.62%	0.16%	0.54%	0.14%
TwoTag								
<i>tb</i>	0.41%	0.17%	0.42%	0.20%	0.46%	0.15%	0.39%	0.13%
<i>tqb</i>	0.03%	0.07%	0.03%	0.08%	0.07%	0.08%	0.06%	0.07%
<i>tb + tqb</i>	0.15%	0.10%	0.15%	0.11%	0.19%	0.10%	0.16%	0.09%
1,2 Tags								
<i>tb</i>	1.1%	0.44%	1.2%	0.52%	1.1%	0.30%	0.90%	0.26%
<i>tqb</i>	0.68%	0.35%	0.75%	0.43%	0.68%	0.24%	0.61%	0.21%
<i>tb + tqb</i>	0.82%	0.38%	0.88%	0.46%	0.80%	0.26%	0.70%	0.23%

**Table 5.19** Signal acceptances.

Combined Signal Acceptance			
	Run IIa+Run IIb, Electron+Muon		All Channels
	2 jets	3 jets	
PreTag			
<i>tb</i>	2.9%	0.88%	3.8%
<i>tqb</i>	2.6%	0.82%	3.4%
<i>tbtqb</i>	2.7%	0.84%	3.6%
1,2 Tags			
<i>tb</i>	2.0%	0.61%	2.6%
<i>tqb</i>	1.3%	0.48%	1.8%
<i>tbtqb</i>	1.5%	0.52%	2.0%

**Table 5.20** Combined signal acceptances.

## 5.8 Cross-Check Samples

To further check that the background is well-modeled in this analysis, two background-enriched control samples are examined. In addition to the standard selection cuts listed in Section 5.1, these cross-check samples are selected with the following requirements:

- **$W$ +Jets enriched sample:** Two jets, one  $b$ -tagged jet, and  $H_T < 175$  GeV.
- **$t\bar{t}$  enriched sample:** Three jets, at least one  $b$ -tagged jet, and  $H_T > 300$  GeV.

Tables 5.21 and 5.22 shows the event yields in these samples. Different kinematic variables are plotted in these enriched regions in Appendix E.

Event yields for the Cross-Check Samples								
	$W$ +Jets Samples				$t\bar{t}$ Samples			
	Run IIa, 1 fb <sup>-1</sup>		Run IIb, 8.7 fb <sup>-1</sup>		Run IIa, 1 fb <sup>-1</sup>		Run IIb, 8.7 fb <sup>-1</sup>	
	Electron	Muon	Electron	Muon	Electron	Muon	Electron	Muon
$t\bar{t}$	2.1	2.3	13	11	0.5	0.6	7.8	7.0
$tq\bar{b}$	5.2	6.0	34	32	1.0	1.1	9.4	8.0
$t\bar{t} \rightarrow \ell\bar{\ell}$	1.9	1.9	17	13	4.8	4.9	55	41
$t\bar{t} \rightarrow \ell + \text{jets}$	0.8	0.5	17	13	67	71	393	322
$Wb\bar{b}$	71	83	464	456	3.7	5.6	47	52
$Wc\bar{c}$	36	40	368	350	2.5	3.0	36	38
$Wcj$	49	59	385	356	1.2	0.6	12	11
$Wjj$	74	91	367	373	2.8	4.4	29	35
$Zb\bar{b}$	1.7	8.6	15	36	0.4	0.6	3.4	4.7
$Zc\bar{c}$	0.6	4.1	9.1	28	0.2	0.2	1.9	2.9
$Zjj$	2.1	6.7	18	32	0.2	0.3	2.3	3.1
Diboson	9.0	11	81	83	0.4	0.6	7.9	7.1
Multijet	19	7.0	271	54	0.9	2.5	50	9.6
Background Sum	266	314	2013	1796	84	94	638	525
Background + Signal	273	322	2060	1839	86	96	655	540
Data	270	321	2039	1652	73	98	667	613

**Table 5.21** Event yields after selection in the cross-check samples.

Event yields for the Cross-Check Samples				
	Electron+Muon, Run IIa + Run IIb			
	W+Jets Samples		$t\bar{t}$ Samples	
Signals				
$tb$	$29 \pm 0.2$		$16 \pm 0.1$	
$tqb$	$77 \pm 0.4$		$19 \pm 0.2$	
Backgrounds				
$t\bar{t}$	$65 \pm 0.8$	(1.5%)	$958 \pm 3.4$	(71%)
W+jets	$3626 \pm 14$	(83%)	$283 \pm 3.4$	(21%)
Z+jets & diboson	$346 \pm 2.4$	(7.9%)	$36 \pm 0.7$	(2.7%)
Multijet	$351 \pm 8.7$	(8.0%)	$64 \pm 3.9$	(4.7%)
Background Sum	$4388 \pm 17$		$1341 \pm 6.2$	
Backgrounds + Signals	$4494 \pm 17$		$1377 \pm 6.2$	
Data	$4282 \pm 65$		$1451 \pm 38$	
$S(tb) : B$	1:152		1:84	
$S(tqb) : B$	1:57		1:69	

**Table 5.22** Event yields with statistical uncertainty in the cross-check samples, for all analysis channels combined. The percentages are of the total background for each component.

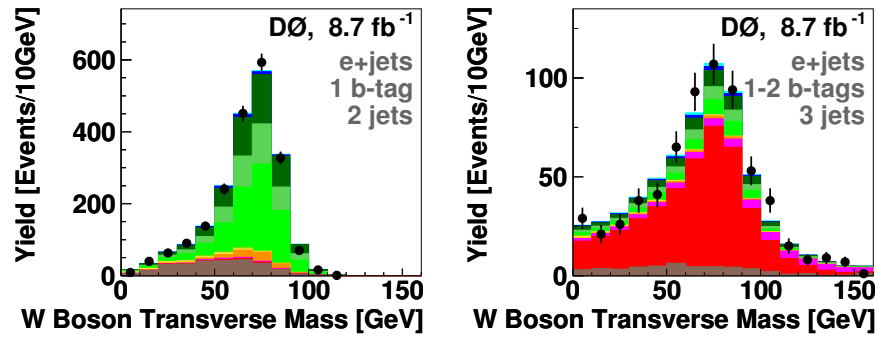


**Figure 5.20** The transverse mass of the W boson for W+jets (left) and  $t\bar{t}$  (right) enriched samples, for the Run IIb electron channel.

## 6 The Matrix Element Method

The Matrix Element (ME) method is unique among the analysis methods used in experimental particle physics in utilizing the theoretical predicted matrix element for a process to optimize the use of all the observed kinematic information in an event. A probability to observe an individual produced event is defined in terms of analytic expressions for signal and background, taking into account all detector effects.

The general concept of the ME method is presented in Section 6.1. The implementation specific to the single top-quark analysis is described in Section 6.2, and the discriminants based on this method are presented in Section 6.3. The details concerning the evaluation of the probabilities and prerequisite studies of the calculation are left to Appendices F to K.

### 6.1 General Concepts

Given a certain production hypothesis, the probability for observing an event can be calculated from the differential cross section, which is proportional to the corresponding square of the matrix element for the process. The matrix element is also known as the scattering amplitude, and it contains all the dynamic information for transition, which can be obtained from the relevant Feynman diagrams. In practice, this calculation requires all the four-momenta of initial and final elementary objects in the event. However, the incident parton four-momenta are not known, and only some of the four-momenta of the final-state objects can be reconstructed. To deal with this situation, we sum over all possibilities, taking any measured information into account, and integrating over all the phase space

for the collision using all prior knowledge of any parameters. The details of this procedure are described below.

### 6.1.1 Probabilities

The probability ( $P$ ) to observe an event produced in some elementary process with measured properties  $x$  in a detector can be defined as

$$P(x|\text{process}) = \frac{1}{\sigma^{\text{obs}}} \frac{d\sigma}{dx} \quad (6.1.1)$$

where  $d\sigma/dx$  is the differential cross section in terms of the observed variables, and  $\sigma^{\text{obs}}$  is the total observed cross section in the detector. These quantities are described further in Sections 6.1.2 and 6.1.4, respectively.

### 6.1.2 Differential Cross Sections

The differential probability for an event with  $n$  final state partons and their four-momenta  $y$  to be produced via any hard-scattering process is given by

$$d\sigma(p_1 p_2 \rightarrow y) = \frac{(2\pi)^4 |\mathcal{M}(p_1 p_2 \rightarrow y)|^2}{4\sqrt{(p_1 \cdot p_2)^2 - m_1^2 m_2^2}} d\Phi_n \quad (6.1.2)$$

where  $p_1$  and  $p_2$  are the initial parton variables, namely, the four-momenta of the incoming partons with masses  $m_1$  and  $m_2$ , and  $y$  are the four-momenta of the partonic final states.  $\mathcal{M}$  denotes the matrix element for the fundamental process, and  $d\Phi_n$  the element of  $n$ -body phase space for that final state, which is described more fully in Section 6.2.3 and Appendix F.2.

To evaluate the differential cross section,  $d\sigma(p\bar{p} \rightarrow y)$ , in  $p\bar{p}$  collisions, Equation (6.1.2) is convoluted with the parton density functions (PDF) for the incident hadrons, because the four-momenta of the specific colliding partons are unknown. Also, all possible flavor contributions of colliding partons to the process must be summed, yielding thereby the expression:

$$\frac{d\sigma}{dy}(p\bar{p} \rightarrow y) = \int_{\xi_1, \xi_2} \sum_{i,j} d\xi_1 d\xi_2 f_i(\xi_1, Q^2) f_j(\xi_2, Q^2) d\sigma(p_1(i) p_2(j) \rightarrow y) \quad (6.1.3)$$

where  $\xi_1$  and  $\xi_2$  are the momentum fractions of the incoming partons  $p_1(i)$  and  $p_2(j)$ , assuming that they are massless and moving along the beam axis (as detailed in Appendix F.1). The  $f_i(\xi_1, Q^2)$  denote the probability densities for having a parton of flavor  $i$  and momentum fraction  $\xi_1$  in the proton, evaluated at some chosen QCD factorization scale  $Q^2$ . Similarly,  $f_j(\xi_2, Q^2)$  denotes the analogous quantity from the antiproton.

The reconstructed objects in events correspond to charged leptons and evolved partonic jets. The difference between the initially produced objects in the hard collision and the reconstructed physical particles arises from parton evolution and hadronization, as well as from detector resolution. This is taken into account through a convolution of Equation (6.1.3) with a transfer function  $W(x, y)$  that describes the probability to reconstruct a produced state  $y$  as the final observed state  $x$  in the detector. As it is not known which jet originates from which parton, the integration has to be summed over all the possibilities of jet-to-parton assignments. Hence, the differential cross section for observing an event with reconstructed four-momenta,  $x$  can be written as

$$\frac{d\sigma}{dx}(p\bar{p} \rightarrow x) = \sum_{\substack{\text{jet-parton} \\ \text{assignments}}} \int_y \frac{d\sigma}{dy}(p\bar{p} \rightarrow y) W(x, y) dy. \quad (6.1.4)$$

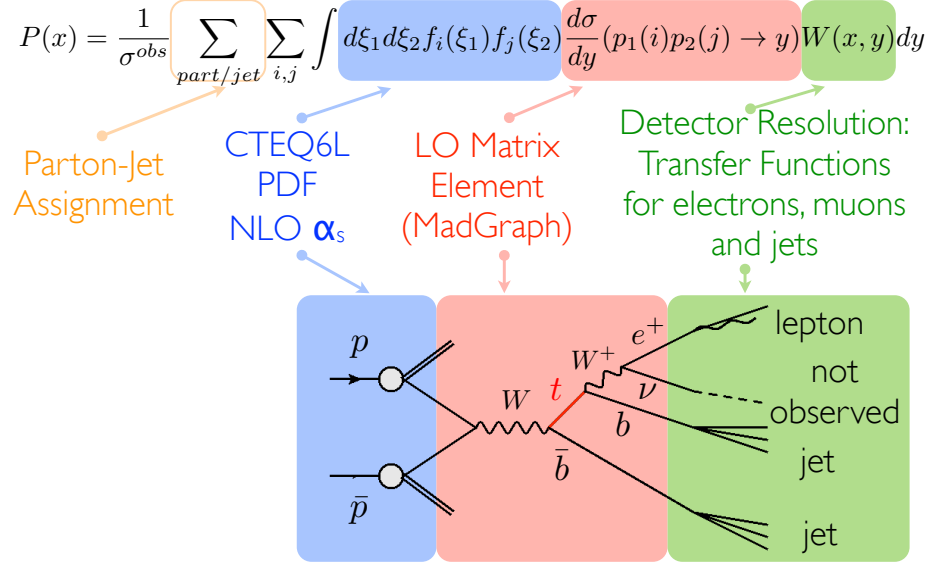
The scheme for integration is illustrated in Figure 6.1.

Several parton-level criteria are applied in the phase space of the integration in order to avoid singularities. As listed in Table 6.1, these criteria are less restrictive than the selection criteria. The differential cross section in Equation (6.1.4) will be effectively evaluated as follows,

$$\frac{d\sigma}{dx}(p\bar{p} \rightarrow x) = \sum_{\substack{\text{jet-parton} \\ \text{assignments}}} \int_y \frac{d\sigma}{dy}(p\bar{p} \rightarrow y) W(x, y) \Theta_{parton}(y) dy \quad (6.1.5)$$

where  $\Theta_{parton}(y)$  is cutoffs required on phase space to assure proper convergence of the leading-order calculation of the production cross section.

In summary, the differential cross section to observe an event in final state  $x$ ,

**Figure 6.1** Schematic representation of the ME method

Descriptions	ME Evaluation	MC Samples
Parton Isolation $\Delta R(q_i, q_j)$	$> 0.5$	$> 0.4$
Minimum Parton $p_T(q_i)$	$> 6 \text{ GeV}$	$> 8 \text{ GeV}$
Maximum Parton Pseudorapidity $ \eta(q_i) $	$< 2.5$ ( $< 3.4$ for Run IIa)	—
Minimum Lepton $p_T(\ell)$	$> 3 \text{ GeV}$	—

**Table 6.1** The parton-level criteria applied in the phase space of the integration and in the MC samples.  $q_i$  represents a final produced quark.

produced through some fundamental process described by  $y$ , can be evaluated as

$$\begin{aligned} \frac{d\sigma}{dx}(x) = & \sum_{\substack{\text{jet-parton} \\ \text{assignments}}} \sum_{i,j} \int_y f_i(\xi_1, Q^2) d\xi_1 f_j(\xi_2, Q^2) d\xi_2 \frac{(2\pi)^4 |\mathcal{M}(p_1(i)p_2(j) \rightarrow y)|^2}{4\sqrt{(p_1(i) \cdot p_2(j))^2 - m_1^2 m_2^2}} \\ & \delta^4 \left( p_1(i) + p_2(j) - \sum_{i=3}^{2+n} p_i \right) d\Phi_n W(x, y) \Theta_{parton}(y) \end{aligned} \quad (6.1.6)$$

where  $\delta^4(p_1(i) + p_2(j) - \sum_{i=3}^{2+n} p_i)$  is a Dirac  $\delta$ -function reflecting the conservation of energy and momentum in the reaction.

### 6.1.3 Description of Detector Response

As mentioned above, the transfer functions  $W(x, y)$  describe the probability of measuring a final state  $x$  in the detector when the partonic final state  $y$  is produced,

$$dP = W(x, y) dx. \quad (6.1.7)$$

The normalization condition for the transfer function in the region of acceptance for objects observed in the detector requires

$$\int_{observedx} W(x, y) dx = 1. \quad (6.1.8)$$

The transfer function factorizes into contributions from the individual final-state objects, and is taken as a  $\delta$ -function for well measured quantities, and a Gaussian-like function to account for resolution of the detector. In general, the angles of the final-state particles are assumed to be precisely measured, while energies or transverse momenta are not. The transfer functions can therefore depend on the energy or  $p_T$  of particles, especially important for the partonic sector. A major component of the resolution for jets is the correlation between jet and parton energies, which is obtained from MC studies, and incorporated into  $W(x, y)$ .

### 6.1.3.1 Jet Transfer Function

The  $D\bar{O}$  jet energy scale corrections are intended to make the jet energy correspond to the sum of energies of its individual particles, or to the “particle level,” and not to that of the initially produced nascent parton. As shown in Figure 6.2, from MC comparison studies of jet and parton energies, using fully simulated as well as partly simulated events, the energy differences between (corrected) jets and partons,  $\Delta E = E_{jet} - E_{parton}$ , are significant, and the distributions are not symmetric. Consequently, jet transfer functions are parametrized in terms of the energy difference, assuming a sum of two Gaussian for the distributions:

$$W_{jet}(E_x, E_y) = \frac{1}{\sqrt{2\pi}(c_2+c_3c_5)} \left\{ \exp \left[ -\frac{1}{2} \left( \frac{(E_x-E_y)-c_1}{c_2} \right)^2 \right] + c_3 \exp \left[ -\frac{1}{2} \left( \frac{(E_x-E_y)-c_4}{c_5} \right)^2 \right] \right\}. \quad (6.1.9)$$

The first Gaussian is to account for the shift in the energy, and the second one is for the asymmetry. It is also found that the parameters  $c_i$  are a function of parton energy. We assume a linear dependence of the  $c_i$  on  $E_y$  ( $E_{parton}$ ) [129]:

$$c_i = a_i + b_i \times E_y. \quad (6.1.10)$$

The energy response is different for light quarks and for  $b$  quarks, as well as for different regions of the detector. We therefore extract the parameters from separate studies of three quark varieties: light quarks ( $u$ ,  $d$ ,  $s$ ,  $c$ , and gluons),  $b$  quarks with a soft muon in the associated jet, and all other  $b$  quarks, and for four regions of pseudorapidity:  $|\eta^{\text{det}}| < 0.4$ ,  $0.4 < |\eta^{\text{det}}| < 0.8$ ,  $0.8 < |\eta^{\text{det}}| < 1.6$ , and  $1.6 < |\eta^{\text{det}}| < 2.5$ . The intervals of  $\eta^{\text{det}}$  we use differ slightly from those of previous transfer functions, and are defined through more recent studies of jet energy response [130].

The two run periods Run IIa and Run IIb are treated separately, since there are differences in jet resolution resulting from the detector upgrade in 2006. In this analysis, we rederive the Run IIb transfer functions using ALPGEN+PYTHIA  $t\bar{t}$  MC samples, taking account of the latest jet energy corrections. The updated parameters are listed in Tables G.2 to G.4 in Appendix G.1, and more details and plots are shown in the same Appendix.

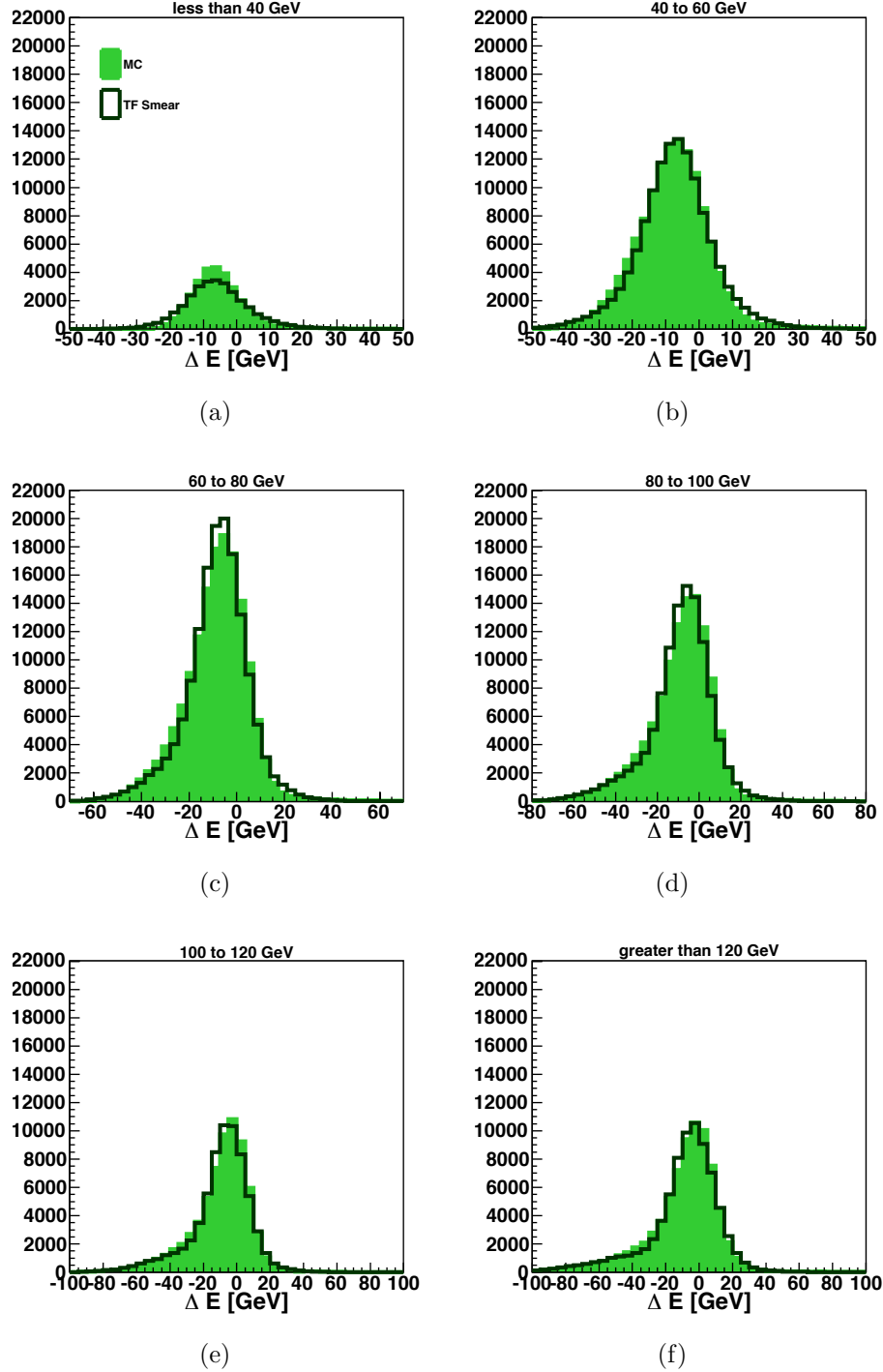


**Figure 6.2** Distributions in  $\Delta E = E_{jet} - E_{parton}$  for  $b$  quarks in the range  $|\eta^{\text{det}}| < 0.4$ . The filled histograms are the  $\Delta E$  distribution for fully simulated MC samples, while the open histograms correspond to just resolution-smeared partons, the energies both of which are smeared using the transfer functions. The events are generated using ALPGEN interfaced to PYTHIA  $t\bar{t}$  MC events, for  $150 \leq m_t \leq 190$  GeV (Appendix G.1). The excess for  $\Delta E < 0$  can be attributed to effects from hadronization and gluon radiation. The results for (a), (b), (c), (d), (e), and (f) are, respectively, for  $E_{parton} < 40$ , 40-60, 60-80, 80-100, 100-120, and  $> 120$  GeV.

### 6.1.3.2 Muon Transfer Function

The muon resolution in the central tracking detector depends on the track curvature in the magnetic field, which is proportional to the muon charge  $q$  divided by its transverse momentum,  $q/p_T$ . The muon transfer function is therefore described as a Gaussian in terms of  $q/p_T$  difference:

$$W_\mu \left( \left( \frac{q}{p_T} \right)_x, \left( \frac{q}{p_T} \right)_y \right) = \frac{1}{\sqrt{2\pi}\sigma} \exp \left[ -\frac{1}{2} \left( \frac{(q/p_T)_x - (q/p_T)_y}{\sigma} \right)^2 \right]. \quad (6.1.11)$$

Misidentification of muon charge is taken into account in the transfer function, but this analysis assumes that the muon charge is measured correctly.

As indicated above, the standard deviation  $\sigma$  for the muon transfer function depends on  $1/p_T$ , but also on  $\eta^{\text{det}}$ , especially for muons in the forward region ( $\eta^{\text{det}} > 1.4$ ),

$$\sigma = \begin{cases} \sigma_0 & \text{for } |\eta^{\text{det}}| \leq \eta_0^{\text{det}} \\ \sqrt{\sigma_0^2 + [c_0(|\eta^{\text{det}}| - \eta_0^{\text{det}})]^2} & \text{for } |\eta^{\text{det}}| > \eta_0^{\text{det}} \end{cases} \quad (6.1.12)$$

where  $\sigma_0$ ,  $c_0$ , and  $\eta_0^{\text{det}}$  are taken as a linear function of  $1/p_T$ :

$$\begin{aligned} \sigma_0 &= \sigma_0(0) + \sigma_0(1)/p_{Ty} \\ c_0 &= c_0(0) + c_0(1)/p_{Ty} \\ \eta_0^{\text{det}} &= \eta_0^{\text{det}}(0) + \eta_0^{\text{det}}(1)/p_{Ty}. \end{aligned} \quad (6.1.13)$$

The  $\eta$  dependence arises from the fact that muon identification at DØ relies just on CFT tracking, and since forward muon tracks cannot be measured in all layers of the tracking detector, and the resolution therefore degrades.

In addition,  $\approx 5\%$  of all muons have no hits in the inner SMT detector [131]. The track curvatures of these muons are consequently less precisely known, and the resolution is worse than for muons with hits in the SMT. The resolution can be improved by constraining these muon tracks to the primary vertices; however, the resolution of muons without information in the SMT remains different. The transfer functions for these kinds of muons are therefore obtained separately.

Moreover, the two major shutdowns of the DØ detector had impact on muon resolution. After the first shutdown in Fall 2004, the muon resolution degraded

by  $\approx 15\%$ , partially because of a reduction in magnetic field [131]. On the other hand, an additional inner tracker was installed during the second shutdown in Spring 2006, and the muon resolution was thereby improved. Different muon transfer functions apply therefore to these three separate periods.

The parameters of muon transfer functions are obtained from  $t\bar{t}$  and  $Z \rightarrow \mu\mu$  MC samples, and are listed in Tables G.5 and G.6 in Appendix G.2. More details can be found in Refs. [132, 131].

### 6.1.3.3 Electron Transfer Function

In analogy, to the jet transfer functions, the electron function is parametrized as a Gaussian distribution through an energy difference:

$$W_e(E_x, E_y) = \frac{1}{\sqrt{2\pi}\sigma} \exp \left[ -\frac{1}{2} \left( \frac{E_x - E_{center}}{\sigma} \right)^2 \right] \quad (6.1.14)$$

where

$$\begin{aligned} E_{center} &= 1.0002 \times E_y + 0.324 \text{ GeV}/c^2 \\ \sigma &= \sqrt{(0.028 \times E_{center})^2 + S^2 \times E_{center} + (0.4)^2} \\ S &= \left( 0.164 + \frac{0.122}{\sqrt{E_{center}}} \right) \exp \left( \frac{c_1}{\sin \theta} - c_1 \right) \\ c_1 &= 1.35193 - \frac{2.09564}{E_{center}} - \frac{6.98578}{E_{center}^2}. \end{aligned} \quad (6.1.15)$$

$E_{center}$  is the electron energy with all calibrations and corrections, except that determined through a fit to the  $Z$  mass distribution. This  $Z$  mass calibration brings the electron energy to the true value ( $E_y$ ), which is assumed to depend linearly on  $E_{center}$  [133].

In addition, the resolution in calorimeter energy at normal incidence is described as

$$\left( \frac{\sigma(E)}{E} \right)^2 = C^2 + \frac{S^2}{E} + \frac{N^2}{E^2} \quad (6.1.16)$$

where  $C$  is a constant term accounting for nonuniformity in response (intercalibration error),  $S$  is the term reflecting sampling fluctuations (intrinsic performance

of the calorimeter), and  $N$  is the noise term, arising, for example, from uranium activity, readout electronics, and the low- $p_T$  particle emission accompanying the hard collision (underlying event). A strong dependence of the energy resolution on the angle of incidence ( $\theta$ ) [134], regular an angular dependence in the sampling term:

$$S = \left( S_1 + \frac{S_2}{\sqrt{E}} \right) \times \frac{e^{c_1/\sin\theta}}{e^{c_1}}, \quad (6.1.17)$$

with

$$c_1 = S_3 - \frac{S_4}{E} - \frac{S_5^2}{E^2}. \quad (6.1.18)$$

All the above parameters were obtained by the DØ  $W$ -boson mass group using  $Z \rightarrow ee$  MC samples.

#### 6.1.3.4 Transfer Function for Jets Misidentified as Electrons

The transfer function for jets misidentified as electrons is applied only for the  $gg \rightarrow ggg$  process in the single top-quark analysis (Section 6.2.1), where a gluon is misidentified and reconstructed as an electron. It is parametrized as a bifurcated Gaussian,

$$W_{false-e}(E_x, E_y) = \frac{1}{\sqrt{2\pi}(\frac{c_2+c_3}{2})} \exp \left[ -\frac{1}{2} \left( \frac{(E_x - E_y) - c_1}{\sigma} \right)^2 \right], \quad (6.1.19)$$

with

$$\sigma = \begin{cases} c_2 & \text{for } E_x - E_y > c_1 \\ c_3 & \text{for } E_x - E_y < c_1 \end{cases} \quad (6.1.20)$$

where the mean and the widths have linear dependence on parton energy:

$$c_i = a_i + b_i \times E_y. \quad (6.1.21)$$

This transfer function is obtained from a special inclusive dijet MC sample ( $2 \rightarrow 2$  parton processes,  $p\bar{p} \rightarrow qq + X$ ,  $p\bar{p} \rightarrow qg + X$ , and  $p\bar{p} \rightarrow gg + X$ , as described in Section 5.2 in Ref. [99]). The parameters are listed in Table G.7 in Appendix G.4.

### 6.1.4 Normalization of the Differential Cross Section

The differential cross section described in Section 6.1.2 is normalized to retain the interpretation of a probability density in Equation (6.1.1), namely, as an integral over the observed events  $x$ , for the phase space relative to event selection:

$$\sigma^{obs} = \sum_{\substack{\text{jet-parton} \\ \text{assignments}}} \int_x \int_y \frac{d\sigma}{dy} (p\bar{p} \rightarrow y) W(x, y) \Theta_{parton}(y) \Theta_{acc}(x) dy dx \quad (6.1.22)$$

where  $\Theta_{acc}(x)$  denotes detector acceptance. Consequently, the difference in acceptance between signal and background is taken automatically into account in the probability density.

Description	Criteria
Isolation	$\Delta R > 0.5$
Lepton $p_T$	$p_T > 20 \text{ GeV}$
Lepton $\eta$	$ \eta^{\text{det}}  < 1.1(2.0) \text{ GeV for electron(muon)}$
Neutrino $p_T$	$20 (25) < p_T < 200 \text{ GeV for 2(3)-jet event}$
Leading jet $p_T$	$p_T > 25 \text{ GeV}$
Jet $p_T$	$p_T > 20 \text{ GeV}$
Jet $\eta$	$ \eta^{\text{det}}  < 2.5$

**Table 6.2** The detector level criteria applied in evaluating the normalization, corresponding to  $\Theta_{acc}(x)$ .

The normalization is evaluated using events generated with MadGraph, and smeared with the transfer functions that simulate the effects of the detector. The selection criteria on reconstructed objects are listed in Table 6.2, and the normalization constants for each process are listed in Appendix H. The statistical uncertainties are  $< 3\%$  in all processes.

## 6.2 Implementation in Single Top-Quark Analysis

Single top-quark production has a small cross section, and, even after  $b$ -tagging, the background events greatly dominate the signal. To improve the separation between sources of signal and background, several background as well as the signal are included in this ME analysis, as described below. However, the numerical integrations needed to evaluate the ME probabilities requires much CPU time. To reduce the computing time, the phase space is optimized for each process, which will be described in Section 6.2.3.

### 6.2.1 Processes Parametrized via ME

To determine signal in the data as effectively as possible, we include in the calculation of the background probabilities the ME formulations for the main background processes in our final sample. Table 6.3 lists all the background and signal ME transitions used in the analysis. Only the “two-jet” ( $2 \rightarrow 4$  processes) and “three-jet” ( $2 \rightarrow 5$  processes) events are considered for signal and background in this analysis. Not all possible Feynman diagrams are used to describe  $W$ +jets production, but each category contains the processes that give the largest contributions to our selected samples. For example, in the two jet sample, it was checked that  $Wcg$  production has a larger contribution than  $Wc\bar{c}$ , and is therefore selected for formulation through an ME term. The list represents a balance between all possible processes contributing to background and the computing time needed for each additional ME calculation. The fact that we cannot include all possible matrix elements makes the analysis less sensitive, but the current list covers many parts of the final phase space for our signal, and the main background from  $W$ +light-jets and  $W$ +heavy-flavor production,  $t\bar{t}$  production, where one or two jets are not reconstructed, as described in Section 6.2.4, the  $gg \rightarrow ggg$  process to model the multijet background, when a jet is misreconstructed as a lepton, and EW diboson production. The list is reduced in the three-jet sample because the combinatorial background is larger, and the background composition is dominated by  $W$ +jets and  $t\bar{t}$  events.

The matrix elements implemented in the analysis, as listed in Table 6.3, are obtained from the MadGraph leading-order ME generator [135], exploiting HELAS

Two Jets		Three Jets	
Name	Process	Name	Process
$tb$	$u\bar{d} \rightarrow t\bar{b} \rightarrow \ell^+ \nu_\ell b\bar{b}$	$tbq$	$u\bar{d} \rightarrow t\bar{b}g \rightarrow \ell^+ \nu_\ell b\bar{b}g$
$tq$	$ub \rightarrow td \rightarrow \ell^+ \nu_\ell b\bar{d}$	$tqb$	$ug \rightarrow td\bar{b} \rightarrow \ell^+ \nu_\ell b\bar{d}\bar{b}$
	$\bar{d}b \rightarrow t\bar{u} \rightarrow \ell^+ \nu_\ell b\bar{u}$		$\bar{d}g \rightarrow t\bar{u}\bar{b} \rightarrow \ell^+ \nu_\ell b\bar{u}\bar{b}$
		$tqq$	$ub \rightarrow tdg \rightarrow \ell^+ \nu_\ell b\bar{d}g$
			$\bar{d}b \rightarrow t\bar{u}g \rightarrow \ell^+ \nu_\ell b\bar{u}g$
$Wbb$	$u\bar{d} \rightarrow Wb\bar{b} \rightarrow \ell^+ \nu_\ell b\bar{b}$	$Wbbg$	$u\bar{d} \rightarrow Wb\bar{b}g \rightarrow \ell^+ \nu_\ell b\bar{b}g$
$Wcg$	$sg \rightarrow Wcg \rightarrow \ell\bar{\nu}_\ell c\bar{g}$	$Wugg$	$dg \rightarrow Wugg \rightarrow \ell\bar{\nu}_\ell u\bar{g}g$
$Wgg$	$u\bar{d} \rightarrow Wgg \rightarrow \ell^+ \nu_\ell g\bar{g}$		
$WW$	$u\bar{u} \rightarrow WW \rightarrow \ell\bar{\nu}_\ell c\bar{s}$		
$WZ$	$u\bar{d} \rightarrow WZ \rightarrow \ell^+ \nu_\ell b\bar{b}$		
$ggg$	$gg \rightarrow ggg$		
$t\bar{t}$	$u\bar{u} \rightarrow t\bar{t} \rightarrow \ell\bar{\nu}_\ell b\bar{b}W^+b$	$t\bar{t}$	$u\bar{u} \rightarrow t\bar{t} \rightarrow \ell\bar{\nu}_\ell b\bar{b}W^+b$

**Table 6.3** The processes considered in this analysis in calculating signal and background ME probabilities, including their charge-conjugate states that contain one charged lepton in the final state.

routines [136] to compute the helicity amplitudes of these “tree-level” Feynman diagrams.

Figures 6.3 to 6.6 show representative Feynman diagrams corresponding to the ME processes implemented in this analysis. The numbers labeling the initial and final-state partons reflect the standard convention; for example, we denote  $p_6$  as the four-momentum of fundamental object 6, which corresponds to the  $b$  quark in the  $tb$  process, but the gluon in the  $Wcg$  process.

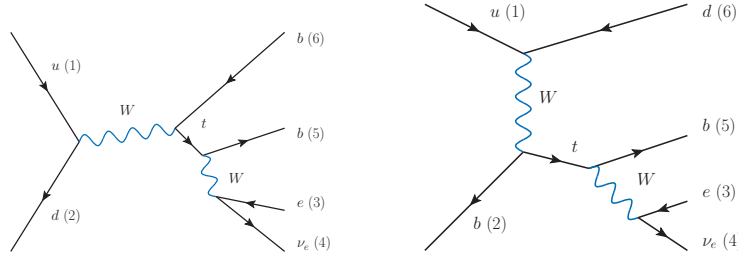


**Figure 6.3** Representative Feynman diagrams corresponding to single top quark, with two jets in the final state:  $u\bar{d} \rightarrow tb$  (left), and  $u\bar{b} \rightarrow tq$  (right).

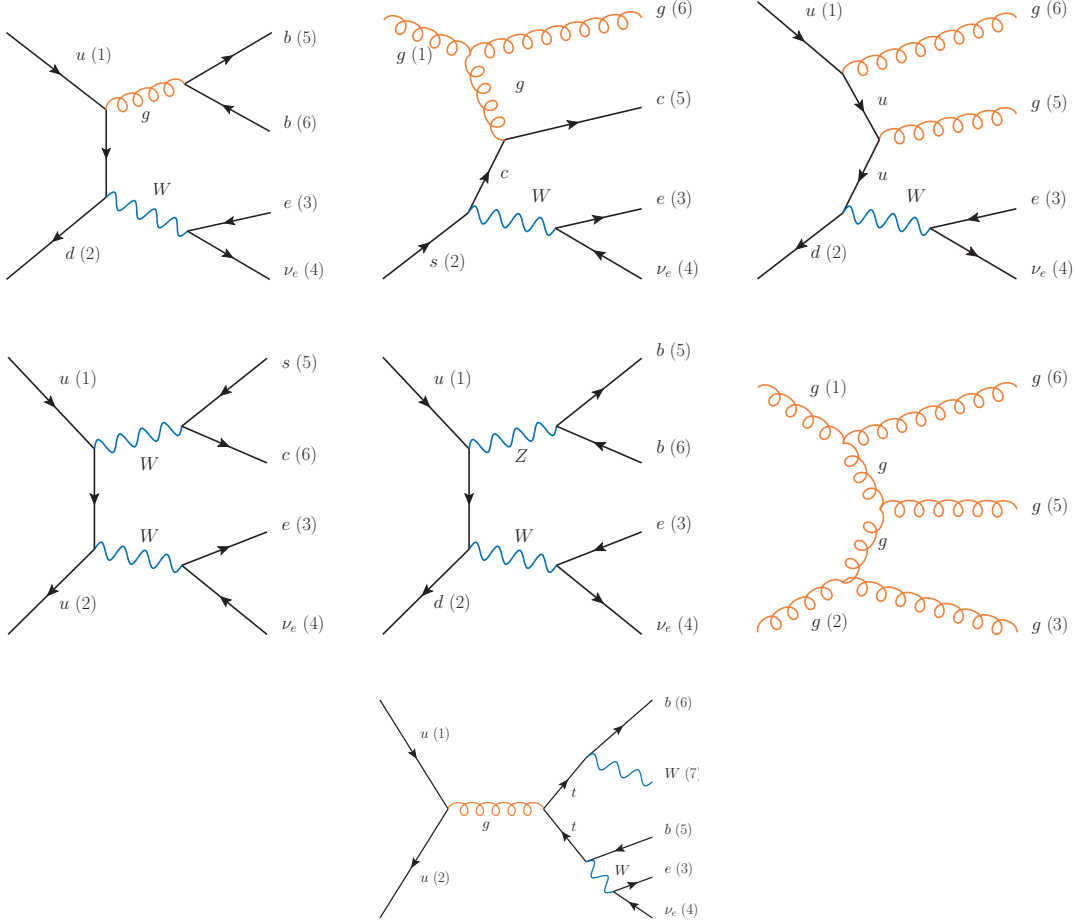


**Figure 6.4** Representative Feynman diagrams corresponding to background with two jets in the final state: starting with the upper left, they are  $u\bar{d} \rightarrow Wbb$ ,  $sg \rightarrow Wcg$ ,  $u\bar{d} \rightarrow Wgg$ ,  $u\bar{u} \rightarrow WW$ ,  $u\bar{d} \rightarrow WZ$ ,  $gg \rightarrow ggg$ , and  $u\bar{u} \rightarrow t\bar{t}$  processes.

In all processes, the top quark decays to a  $W$  boson and a bottom quark, and the generated  $W$  boson decays leptonically. The value of  $m_t$  is set to 172.5 GeV, which is very close to the current accepted value of 173.1 GeV, and consistent with what is used in the MC samples. Events in the electron and muon channels are evaluated using the same ME. Furthermore, the CKM matrix is assumed to be diagonal, and the subprocesses with first-generation incoming quarks ( $u\bar{d}$  and its conjugate) and second generation ( $c\bar{s}$  and its conjugate) are calculated using the same matrix elements, but with different parton distribution functions.

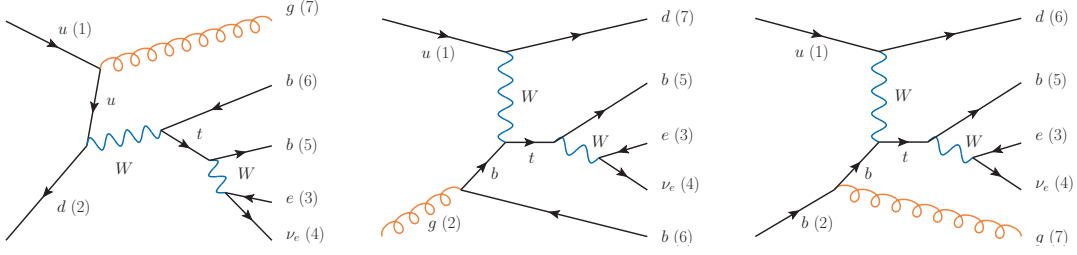


**Figure 6.5** Representative Feynman diagrams corresponding to single top-quark, with three jets in the final state:  $u\bar{d} \rightarrow tbg$  (left),  $ug \rightarrow tqb$  (central), and  $ub \rightarrow tqg$  (right).

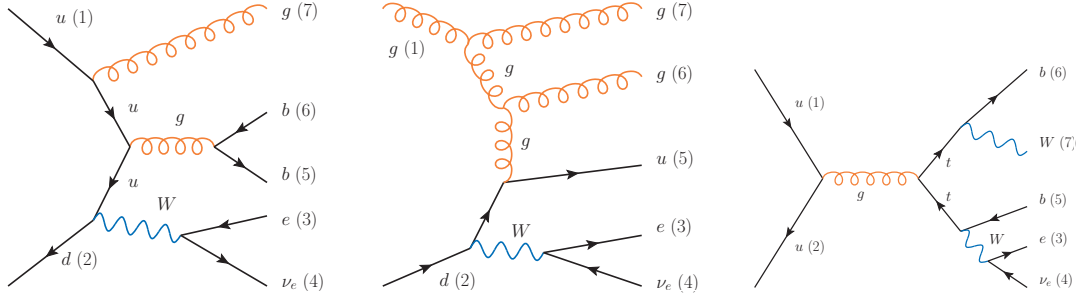


**Figure 6.6** Representative Feynman diagrams corresponding to the backgrounds with three jets in the final state:  $u\bar{d} \rightarrow Wbbg$  (left),  $dg \rightarrow Wugg$  (central), and  $u\bar{u} \rightarrow t\bar{t}$  (right).

### 6.2.2 PDF and Factorization Scales

The CTEQ6L parton distribution functions (PDF) are used in this analysis [137]. They are accessed via the LHAPDF library [138]. The CTEQ6L PDF have leading-order fits with two-loop  $\alpha_S$  corrections (next-to-leading order). We use NLO PDF to provide a better description of the incoming partons.

The QCD factorization scales in the ME calculations and used in the MC samples are listed in Table 6.4. In general, the scales are chosen to be consistent with the generated MC samples, except for the  $t\bar{t}$  process (as described in Section 6.2.4), for which we choose  $2m_{top}$  to approximate the scale used in the ALPGEN MC.

### 6.2.3 The Phase Space

To calculate the differential cross section  $d\sigma(p\bar{p} \rightarrow x)$  in Equation (6.1.5), or the probability in Equation (6.1.1), an integration has to be performed over the initial and the final phase space. This integration is highly time consuming, and

Process Category	Factorization Scale Q	MC Factorization Scale Q
$s$ -channel	$m_t$	$m_t$
$t$ -channel	$m_t/2$	$m_t/2$
$W$ +Jets, Diboson	$\sqrt{m_W^2 + \sum(m_i^2 + p_{T_i}^2)}$	$\sqrt{m_W^2 + \sum(m_i^2 + p_{T_i}^2)}$
$t\bar{t}$	$2m_t$	$\sqrt{\sum(m_i^2 + p_{T_i}^2)}$

**Table 6.4** Factorization scales used in the ME integrations and in MC samples. The  $\sum$  reflects a sum over all the final state partons with masses  $m_i$  and  $p_T = p_{T_i}$ .

we therefore impose a few constraints to reduce the dimensionality of the phase space, and perform a transformation to optimize integration time. The details are described below in Sections 6.2.3.1 and 6.2.3.2.

### 6.2.3.1 The Dimensionality of Phase Space

The  $n$ -body final-state phase space is defined by

$$d\Phi_n(p_1, \dots, p_n) = \prod_{i=1}^n \frac{d^4 p_i}{(2\pi)^3}. \quad (6.2.1)$$

Consider a  $2 \rightarrow n$  process, there are  $2 \times 4$  and  $n \times 4$  unknown quantities for the initial and the final states, respectively, or  $(2 + n) \times 4$  degrees of freedom.

However, with energy and momentum being conserved, we have four constraints. Furthermore, we assume:

1. The known masses of all the initial and final state partons. In particular, the masses of  $u$ ,  $d$ ,  $s$ ,  $c$  quarks, gluons and leptons are considered to have negligible mass,
2. The initial partons are moving along the  $z$ -axis, without any  $p_T$ ,
3. The directions of the final state partons are well-measured, except for neutrinos, which escape detection.

As listed in Table 6.5, for signal, we obtain  $n$  remaining dimensions of integration for a  $2 \rightarrow n$  process that contains a neutrino in the final state. Thus, for the

		Degrees of Freedom (DOF)
Particles:	2 initial and $n$ final state objects	$(2 + n) \times 4$
Constraints:	Energy and momentum conservation	-4
	All parton masses are known	$-(2 + n)$
	The initial partons moving along $z$ -axis	$-2 \times 2$
	The directions of final observable objects are well-measured	$-2 \times (n - 1)$
Remaining dimensions		$n$

**Table 6.5** The degrees of freedom in the ME integration. The direction of a parton corresponds to its polar angle and azimuth in spherical coordinate. Since we know the direction of the final state object, the integration over the unknown quantities is reduced by two degrees of freedom for each elementary observed object.

two-jet sample, we have four degrees of freedom, and in the three-jet sample we have five degrees of freedom. The phase space expression for initial-state objects, together with the ME is shown in Equation (6.1.3), and, for the final-state objects, we can write:

$$\begin{aligned}
 & d\Phi_n(p_1 + p_2; p_3, \dots, p_{n+2}) \\
 &= \delta^4(p_1 + p_2 - \sum_{i=3}^{n+2} p_i) \left( \prod_{i=3, i \neq 4}^{n+2} \delta^2(\Omega_i^y - \Omega_i^x) \frac{p_i^2 dp_i}{(2\pi)^3 2E_i} \right) \frac{d^3 p_4}{(2\pi)^3 2E_4} \quad (6.2.2)
 \end{aligned}$$

where  $\Omega_i$  is the element of solid angle for the  $i$ th particle, where we have redefined the phase space in terms of spherical coordinates (except for the neutrino). The details on the phase space are given in Appendix F.2.

### 6.2.3.2 The Phase Space Transformation

To minimize the computing time for the remaining integrations, it is desirable to transform the variables such that the integrand peaks as a function of the new integration variables. In fact, the matrix element contains Breit-Wigner terms in mass for the  $W$  and the top quark, and, except for detector resolution, contributes negligibly beyond the peak regions. Consequently, we choose the square of the invariant masses of the  $W$  and the top quark as integration variables, and sample the  $m_W^2$  and  $m_t^2$  according to Breit-Wigner expressions, instead of momenta of the remaining objects that tend to have very broad distributions and required therefore more sampling to obtain precise results.

In addition, we still need more variables to match the DOF of the variables

of phase space. We choose the magnitude of the momentum of certain final state quarks,  $|\mathbf{p}_i|$ , and the longitudinal momentum of the center of momentum of the total system in the lab frame,  $p_{tot}^z$  (we assume no transverse momentum for the total system, as discussed above), to simplify the kinematic formulation.

The evaluation of the differential cross section requires information on the four-momenta of the initial and final-state objects. Since we choose  $m_W^2$  and  $m_t^2$  as two integration variables, we have to solve sequential kinematic relationships for these four-momenta. Such kinematic equations are solved numerically, and the gain achieved from decreased computing time using these masses would be lost if the resultant kinematic equations were too complicated.

The integration variables we choose are uncorrelated, and optimized for different ME processes, as listed in Table 6.6. Furthermore, boundaries for these variables are adjusted to cover their allowed ranges at the Tevatron; for example, the magnitude of the momenta of quarks range from 0 to 980 GeV, or half the center-of-mass energy of the collisions.

Two Jets			
Category	Process	Original Phase Space	Final Integration
Single top quark	$tb, tq$	$d \mathbf{p}_3 d \mathbf{p}_5 d \mathbf{p}_6 dp_{tot}^z$	$ds_{34}ds_{345}d \mathbf{p}_6 dp_{tot}^z$
$W$ +Jets	$Wbb, Wcg, Wgg$	$d \mathbf{p}_3 d \mathbf{p}_5 d \mathbf{p}_6 dp_{tot}^z$	$ds_{34}d \mathbf{p}_5 d \mathbf{p}_6 dp_{tot}^z$
Dibosons	$WW, WZ$	$d \mathbf{p}_3 d \mathbf{p}_5 d \mathbf{p}_6 dp_{tot}^z$	$ds_{34}ds_{56}d \mathbf{p}_6 dp_{tot}^z$
Multijets	$ggg$	$d \mathbf{p}_3 d \mathbf{p}_5 d \mathbf{p}_6 dp_{tot}^z$	$d \mathbf{p}_3 d \mathbf{p}_5 d \mathbf{p}_6 dp_{tot}^z$ (no change)
Two top quarks	$t\bar{t}$	$d \mathbf{p}_3 d \mathbf{p}_5 d \mathbf{p}_6 d \mathbf{p}_7 d\cos\theta_7d\phi_7dp_{tot}^z$	$ds_{34}ds_{345}ds_{67}d \mathbf{p}_7 d\cos\theta_7d\phi_7dp_{tot}^z$

Three Jets			
Category	Process	Original Phase Space	Final Integration
Single top quark	$tbg, tqg, tqb$	$d \mathbf{p}_3 d \mathbf{p}_5 d \mathbf{p}_6 d \mathbf{p}_7 dp_{tot}^z$	$ds_{34}ds_{345}d \mathbf{p}_6 d \mathbf{p}_7 dp_{tot}^z$
$W$ +Jets	$Wbbg, Wugg$	$d \mathbf{p}_3 d \mathbf{p}_5 d \mathbf{p}_6 d \mathbf{p}_7 dp_{tot}^z$	$ds_{34}d \mathbf{p}_5 d \mathbf{p}_6 d \mathbf{p}_7 dp_{tot}^z$
Two top quarks	$t\bar{t}$	$d \mathbf{p}_3 d \mathbf{p}_5 d \mathbf{p}_6 d \mathbf{p}_7 dp_{tot}^z$	$ds_{34}ds_{345}ds_{67}d \mathbf{p}_7 dp_{tot}^z$

**Table 6.6** The original and the transformed integration variables for each process. The subscript numbers indicate the partons labeled in Figures 6.3 to 6.6, while  $p_{tot}^z$  denotes the longitudinal momentum of the total system in the lab frame.

Finally, a Jacobian determinant is required in the integration since we are making a change of variables. For example, the Jacobian for the single top-quark

two-jet process is defined as follows,

$$|J| = \begin{vmatrix} \frac{\partial s_{34}}{\partial |\mathbf{p}_3|} & \frac{\partial s_{34}}{\partial |\mathbf{p}_5|} & \frac{\partial s_{34}}{\partial |\mathbf{p}_6|} & \frac{\partial s_{34}}{\partial p_{tot}^z} \\ \frac{\partial s_{345}}{\partial |\mathbf{p}_3|} & \frac{\partial s_{345}}{\partial |\mathbf{p}_5|} & \frac{\partial s_{345}}{\partial |\mathbf{p}_6|} & \frac{\partial s_{345}}{\partial p_{tot}^z} \\ \frac{\partial |\mathbf{p}_6|}{\partial |\mathbf{p}_3|} & \frac{\partial |\mathbf{p}_6|}{\partial |\mathbf{p}_5|} & \frac{\partial |\mathbf{p}_6|}{\partial |\mathbf{p}_6|} & \frac{\partial |\mathbf{p}_6|}{\partial p_{tot}^z} \\ \frac{\partial p_{tot}^z}{\partial |\mathbf{p}_3|} & \frac{\partial p_{tot}^z}{\partial |\mathbf{p}_5|} & \frac{\partial p_{tot}^z}{\partial |\mathbf{p}_6|} & \frac{\partial p_{tot}^z}{\partial p_{tot}^z} \end{vmatrix} \quad (6.2.3)$$

where  $s_{34}$  and  $s_{345}$  are the squared invariant masses of the  $W$  and the top quark, respectively, and the  $|\mathbf{p}_i|$  denotes as the magnitude of the momentum (three-momentum) of particle  $i$ . The labels for particle indices  $i$  are indicated in Figures 6.3 to 6.6. Additional information about the Jacobian for each process can be found in Appendix I.

As mentioned above, we sample each of the mass variables according to Breit-Wigner forms, and moreover, use Gaussian sampling for each of the momenta. The details about these samplings are described in Appendix J.

### 6.2.3.3 The Integration over Phase Space

The final multidimensional integrals are calculated using the VEGAS Monte Carlo integration algorithm [139] from the GNU Scientific Library [140]. This algorithm searches for regions where the integrand has significant value, and the random sampling points are concentrated at these regions. As a result, the integration converges more quickly, and the overall computing time is greatly reduced.

## 6.2.4 Modeling of $t\bar{t}$ Background

A significant fraction of  $t\bar{t}$  events pass the single top-quark lepton+jets selections, corresponding approximately to the number of signal events. As a consequence, we include the  $t\bar{t}$  process in our discriminant to improve the separation between single top-quark signal and  $t\bar{t}$  background.

First,  $t\bar{t} \rightarrow \ell^\pm \nu q \bar{q}' b \bar{b}$  events should in principle end up in the four-jet bin. However, if one (or two) of the final-state jets is not detected or is merged with another jet, the event can fall into the three-jet (or the two-jet) bin. The dilepton  $t\bar{t} \rightarrow \ell^+ \nu \ell^- \bar{\nu} b \bar{b}$  events contain two leptons, two  $b$ -jets, and a large imbalance in

transverse momentum in the final state, but can shift to the two-jet  $\ell$ +jets bin if one of the leptons is not detected.

For all kinds of  $t\bar{t}$  events, one-to-one matching of a parton to a reconstructed jet cannot be assumed. In principle, some match of all reconstructed objects can be made to some of the final state particles, and integrate over the phase space of unreconstructed objects. For example, for the case of  $\ell$ +jets  $t\bar{t}$  events in the three-jet bin, the three reconstructed jets could be matched to three of the four particles, and integrate over the phase space of the fourth. However, this would require much more computing, as there will be 8 degrees of freedom and 24 jet-to-parton assignments. For a normal case of three jets, there are five degrees of freedom and 6 assignments. Consequently, assumptions and approximations are necessarily introduced to reduce computing time.

#### 6.2.4.1 Three Reconstructed Jets in $t\bar{t}$ Events

For a  $t\bar{t} \rightarrow \ell$ +jets event, four quarks are expected from the hard scattering. Ideally, there would be four reconstructed jets, and each one identified with a unique quark. However, for our analysis, the events of interest are those that contain only three jets. The  $t\bar{t} \rightarrow \ell$ +jets Monte Carlo events were therefore investigated to check what caused such events. Among the quarks from top-quark decays, 66% end up as one jet, 9% merge with the remnants of another quark and are reconstructed together as one jet, while 25% of the jets fail to reconstruct. Furthermore, 62% of the lost quarks correspond to light quarks from  $W$ -boson decays. These lost quarks can be attributed to their low value of reconstructed  $p_T$  or to their emission in the very forward directions. As a result, the corresponding jets do not pass the  $p_T$  threshold or the acceptance in  $\eta$ . Indeed, Figure 6.7, which shows the distributions in  $p_T$  and  $\eta$  for light and  $b$  quarks, suggests that the very low  $p_T$  is the main reason for a jet not being reconstructed, and it further suggests that light quarks are more likely to be lost since  $b$  quarks have larger  $p_T$  values.

Based on this study, we take the lost quark always to be one of the light quarks from  $W$ -boson decay. In addition, the original  $t\bar{t} \rightarrow \ell\nu q\bar{q}'b\bar{b}$  process is replaced by  $t\bar{t} \rightarrow \ell\nu W b\bar{b}$ , in which the  $W$  boson does not decay (“ $W$  parton”). In every jet-to-parton assignment, one of the three jets is matched to the  $W$  boson (“matched parton”). However, the energy difference between the  $W$  boson and the reconstructed jet is significant, since the energy of the lost quark is ignored in the

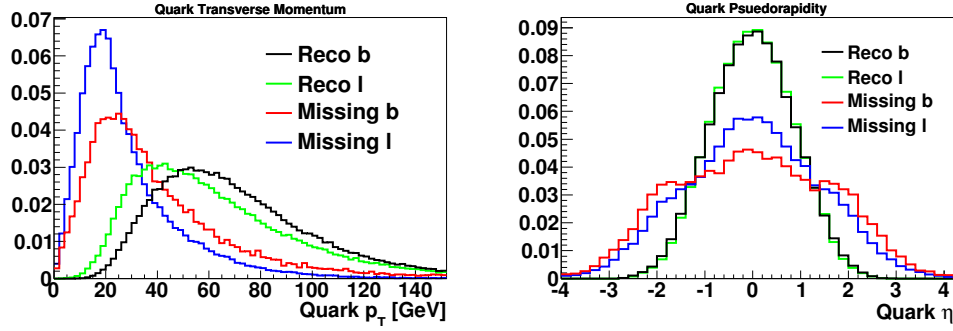


**Figure 6.7** Monte Carlo distributions in  $p_T$  (left) and  $\eta$  (right) for  $b$  and light quarks in  $t\bar{t}$  events that are matched to reconstructed jets (“Reco  $b$ ” and “Reco  $l$ ”), and for (“Missing  $b$ ” and “Missing  $l$ ”) from a  $t\bar{t}$  ALPGEN sample with full  $D\bar{O}$  reconstruction.

process. The combined effects of the new ME and the vanishing of the transfer function, makes the differential cross section unreasonably small for modelling the  $t\bar{t}$  decay. We therefore correct the energy difference between the  $W$  boson and its single (observed) decay product, using the energy distributions observed in Figure 6.8. The average value of the energy difference is added to that of the reconstructed jet to form the final jet. Using this approximation, we lose some sensitivity to the direction of the  $W$  boson, but reduce significantly the required computing time.

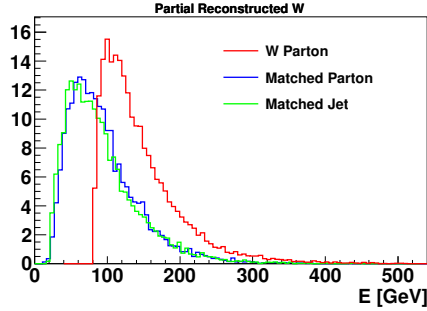


**Figure 6.8** MC distributions in energy for (i)  $W$  bosons that decay into  $q'\bar{q}$ , but provide only one reconstructed decay product ( $W$  parton), (ii) the partons from this  $W$  decay that are reconstructed (Matched Parton), and (iii) the corresponding reconstructed jets (Matched jet).

### 6.2.4.2 Two Reconstructed Jets in $t\bar{t}$ Events

For  $t\bar{t}$  events falling into the two-jet bin, the original  $t\bar{t} \rightarrow \ell\nu q\bar{q}'b\bar{b}$  diagram is replaced by  $t\bar{t} \rightarrow \ell\nu W b\bar{b}$ , in which the  $W$  boson that is supposed to decay is completely lost. The two reconstructed jets are matched to the two  $b$  quarks from  $t$  and  $\bar{t}$  decays, and we integrate over the phase space of the unobserved  $W$  boson assuming a prior based on lepton+jets and dilepton MC  $t\bar{t}$  events in two-jet final states shown in Figure 6.9. These priors are used to constrain  $W$  bosons in the regions of phase space where they are likely to be lost, and, with this constraint, the analysis of the two-jet events can be kept orthogonal to that of three-jet events. This approximation provides 7 degrees of freedom and two jet-to-parton assignments that help to minimize computing time.

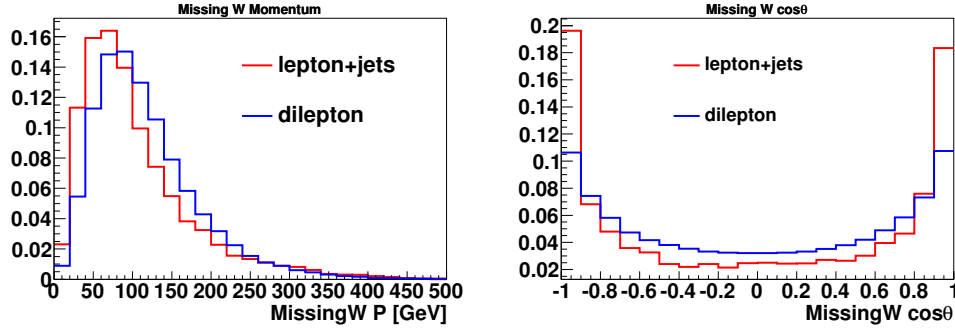


**Figure 6.9** The priors for unobserved  $W$  bosons for  $t\bar{t}$  events containing two jets in the final states. The priors are obtained separately for  $t\bar{t} \rightarrow \text{lepton+jets}$  and  $t\bar{t} \rightarrow \text{dilepton}$  MC samples. The “lepton+jets” and the “dilepton” priors are applied in proportion to their contributions to the background to two-jet selected samples of single top-quark candidates.

## 6.3 Discriminants

The measurement of single top-quark production depends critically on selecting a powerful discriminant for distinguishing between the two hypotheses  $H = H_0$  (background) and  $H = H_1$  (signal). In the matrix element analysis, it is a matter of choice for how to define a discriminant for the event probabilities of Equation (6.1.1). Following the Neyman-Pearson lemma [141], which states that the

likelihood ratio is the best choice for distinguishing among alternative assumptions, we use the likelihood ratio for our discriminant:

$$D(x) = \mathcal{L}R(x) = \frac{\mathcal{L}(S|x)}{\mathcal{L}(S|x) + \mathcal{L}(B|x)} \quad (6.3.1)$$

where the  $\mathcal{L}(S|x)$  and the  $\mathcal{L}(B|x)$  are, respectively, the signal and the background likelihood functions for each event with reconstructed final state  $x$ . The likelihood function is defined as

$$\mathcal{L}(H|x) = \sum_{H \text{ proc } i} c_i P_{\text{general},i}(x) \quad (6.3.2)$$

where  $H$  is either the signal or the background hypothesis, and  $c_i$  and  $P_{\text{general},i}$  refer to the fraction of yields and the probability density for each process  $i$  (evaluated, for example, from the ME integration in Equation (6.1.1)). The signal likelihood is defined specifically for each of the single top-quark production modes, as well as for inclusive production, assuming the SM ratio for the  $s$  and  $t$ -channel cross sections. In particular, the  $t$ -channel single top-quark processes are included in the background when forming the  $s$ -channel discriminant, and vice versa. We have therefore three signal-specific discriminants,  $D_s$ ,  $D_t$ , and  $D_{st}$  (sum of  $s$  and  $t$ ), with slightly different background processes, as listed in Table 6.7.

	Signal		Background	
	Two Jets	Three Jets	Two Jets	Three Jets
$D_s$ or $D_{tb}$	$tb$	$tbq$	$tq, Wbb, Wcg, Wgg,$ $WW, WZ, ggg, t\bar{t}$	$tqb, tqg, Wbbg,$ $Wugg, t\bar{t}$
$D_t$ or $D_{tq}$	$tq$	$tqb, tqg$	$tb, Wbb, Wcg, Wgg,$ $WW, WZ, ggg, t\bar{t}$	$tbq, Wbbg,$ $Wugg, t\bar{t}$
$D_{st}$ or $D_{tbtq}$	$tb, tq$	$tbq, tqb, tqg$	$Wbb, Wcg, Wgg,$ $WW, WZ, ggg, t\bar{t}$	$Wbbg, Wugg, t\bar{t}$

**Table 6.7** The definitions of the signal and the background processes for each of the three signal-specific discriminants:  $D_s$ ,  $D_t$ , and  $D_{st}$ .

The yield fraction,  $c_i$ , is proportional to the yield of the corresponding process  $i$  in our final sample, with all contributions normalized to unity. The values and the details of the yield fractions used in this analysis are listed in Tables K.1

to K.8 of Appendix K.

The  $P_{general,i}$  can be any of the three types of probabilities,  $P_i(x)$ ,  $P_i^{bl}(x)$ , and  $B_i P_i(x)$ , as discussed below, and in greater detail in Appendix L.

### 6.3.1 The ME Discriminant with $b$ -tagging Information

The Matrix Element method uses all the kinematic information available to produce the event probability  $P(x)$  of Equation (6.1.1) for each process. However, in addition to the object four-momenta, we have other variables that are not utilized in this method. In particular, the jet  $b$ -ID variable that provides significant separation between  $b$ -flavored and other jets. We include this variable in the analysis to improve the sensitivity of the measurement.

Two general methods are used to incorporate jet  $b$ -tagging information in the discriminant: (i) using  $b$ -ID output of the jets as a weight on each of the jet-parton permutations, before the event probability is established, and (ii) applying a similar weight to the event probability (while treating all jet-parton permutations equally). The difference in these two methods arises from the fact that the  $s$ -channel contains two  $b$ -quarks in the final state and no light quarks, the  $b$ -tagging information therefore does not help assign one jet to  $t \rightarrow Wb$  and the other jet to the initial  $b$  quark for in each permutation. Conversely, in  $t$ -channel events the final state contains typically only one  $b$ -jet and one or more light jets, the  $b$ -tagging information therefore helps to give more weight to the correct  $b$ -jet to  $b$ -quark permutation. Although the correct assignment of  $b$ -jets in the  $s$ -channel is neglected in this discriminant, the added  $b$ -ID information helps to separate signal from backgrounds that contain light quarks.

A general discussion of all the discriminants and their optimization can be found in Appendix L.

#### 6.3.1.1 The $P^{bl}$ -based Discriminant: Optimized for $t$ -channel

The most straightforward way to use output of the  $b$ -ID is to introduce a weight for each jet-to-parton assignment. As mentioned in Section 6.1.2, the probability

of Equation (6.1.1) runs over the sum of all the jet-to-parton assignments,

$$P = \sum_{\substack{\text{jet-parton} \\ \text{assignments (k)}}} \frac{d\sigma_k}{\sigma}. \quad (6.3.3)$$

When a  $b$  quark is matched to a  $b$ -like jet, the jet-to-parton assignment should have a higher weight in the final set of probabilities. Similarly, an assignment should also have a larger weight when a light-flavored quark matches properly to a light jet.

We use the output value from the MVA  $b$ -tagger (the variable JetBTagMVA in Section 5.5) to approximate the probability of a jet with a given  $b$ -ID output,  $b_l$  ( $b$ -jets relative to light-jets), to correspond to a  $b$  quark.

Jet-to-parton Assignment	$b$ quark	$b$ quark	weight
Assignment 1	Jet1	Jet2	$b_{l,1} \times b_{l,2}$
Assignment 2	Jet2	Jet1	$b_{l,1} \times b_{l,2}$

**Table 6.8** The  $b$ -ID output weights implemented for jet-to-parton assignment for a process with two  $b$  quarks in the final state, such as  $tb$ . The  $b_{l,k}$  variable corresponds to the probability of the  $b$ -ID output of the  $k^{th}$  jet.

Jet-to-parton Assignment	$b$ quark	light quark	weight
Assignment 1	Jet1	Jet2	$b_{l,1} \times (1 - b_{l,2})$
Assignment 2	Jet2	Jet1	$(1 - b_{l,1}) \times b_{l,2}$

**Table 6.9** The  $b$ -ID output weights implemented for jet-to-parton assignment for a process with one  $b$  and one light-flavored quarks in the final state, such as  $tq$ . The  $b_{l,k}$  variable corresponds to the probability of the  $b$ -ID output of the  $k^{th}$  jet.

The calculation of such weights is shown in Tables 6.8 to 6.10. Equation (6.3.3) can therefore be modified as follows for any specific process ( $tb$ ,  $tq$ , etc.)

$$P^{bl} = \frac{\sum_m w_m d\sigma_m}{(\sum_m w_m) \sigma} \quad (6.3.4)$$

where  $w_m$  is the weight of the  $m$ -th jet-to-parton assignment in Tables 6.8 to 6.10,

Jet-to-parton Assignment	light quark	light quark	weight
Assignment 1	Jet1	Jet2	$(1 - b_{l,1}) \times (1 - b_{l,2})$
Assignment 2	Jet2	Jet1	$(1 - b_{l,1}) \times (1 - b_{l,2})$

**Table 6.10** The  $b$ -ID output weights implemented for jet-to-parton assignment for a process with two light-flavored quarks in the final state, such as  $Wgg$ . The  $b_{l,k}$  variable corresponds to the probability of the  $b$ -ID output of the  $k^{th}$  jet.

and  $d\sigma_m$  is the differential cross section,  $\int_y d\sigma(p\bar{p} \rightarrow y)W(x, y)$ , evaluated according to the  $m$ -th assignment.

Finally, the signal and background likelihoods are defined as:

$$\mathcal{L}(H|x) = \sum_{H \text{ proc } i} c_i P_i^{bl}(x) \quad (6.3.5)$$

where  $P_i^{bl}$  is given in Equation (6.3.4) for a given ME process  $i$ , such as  $tb$  or  $t\bar{t}$ , etc.

The  $t$ -channel discriminant explicitly for two-jet events is as follows:

$$P^{bl} \text{MED}_t(x) = \frac{c_{tq} P_{tq}^{bl}(x)}{\sum_{i=tq, Wbb, Wcg, Wgg, WZ, WW, t\bar{t}, ggg, tb} c_i P_i^{bl}(x)}. \quad (6.3.6)$$

Similarly, the  $t$ -channel discriminant for three-jet events takes this form:

$$P^{bl} \text{MED}_t(x) = \frac{c_{tqb} P_{tqb}^{bl}(x) + c_{tqg} P_{tqg}^{bl}(x)}{c_{tqb} P_{tqb}^{bl}(x) + c_{tqg} P_{tqg}^{bl}(x) + c_{Wbbg} P_{Wbbg}^{bl}(x) + c_{Wugg} P_{Wugg}^{bl}(x) + c_{t\bar{t}} P_{t\bar{t}}^{bl}(x) + c_{tbg} P_{tbg}^{bl}(x)} \quad (6.3.7)$$

where  $P^{bl}$  is defined in Equation (6.3.4).

### 6.3.1.2 The B-weighted Discriminant: Optimized for $s$ -channel

To exploit  $b$ -ID information for  $s$ -channel final states, we introduce a weight  $B(x)$  to describe the probability for an event to originate from a process with  $n$   $b$  quarks. We again use  $b_l$ , the  $b$ -ID output for each jet, to quantify the flavor weight  $B$  for

a given event:

$$B(x) = \begin{cases} b_{l,1st} \times b_{l,2nd} & \text{for processes with two } b \text{ quarks in final state} \\ b_{l,1st} \times (1 - b_{l,2nd}) & \text{for processes with one } b \text{ quark in final state} \\ (1 - b_{l,1st}) \times (1 - b_{l,2nd}) & \text{for processes with no } b \text{ quarks in final state} \end{cases} \quad (6.3.8)$$

where  $b_{l,1st}$  and  $b_{l,2nd}$  are the largest and next largest  $b_l$  values in an event for the processes categorized in Table 6.11.

Final State Category		Processes
Two $b$ quarks	$tb, Wbb, WZ, t\bar{t}$ (two and three jets), $tbq, tqb, Wbbq$	
One $b$ quark	$tq, tqg$	
No $b$ quarks	$Wcg, Wgg, WW, ggg, Wugg$	

**Table 6.11** The categories of the processes according to the number of the  $b$  quarks in the final state.

The new signal and background likelihood functions are established by replacing  $P(x)$  with  $B(x)P(x)$ ,

$$\mathcal{L}(H|x) = \sum_{H \text{ proc } i} c_i B_i(x) P_i(x). \quad (6.3.9)$$

The  $B$  weight does not affect jet-parton matching, as it corresponds to an overall weight for each event that affects equally all possible jet-parton assignments.

Explicitly, the  $s$ -channel discriminant for two-jet events can be written as

$$B - MED_s(x) = \frac{c_{tb} b_{l,1} b_{l,2} P_{tb}(x)}{b_{l,1} b_{l,2} \left( \sum_{i=tb, Wbb, WZ, t\bar{t}} c_i P_i(x) \right) + c_{tq} b_{l,1} (1 - b_{l,2}) P_{tq}(x) + (1 - b_{l,1}) (1 - b_{l,2}) \left( \sum_{i=Wcg, Wgg, WW, ggg} c_i P_i(x) \right)} \quad (6.3.10)$$

and for three jet events:

$$B - MED_s(x) = \frac{c_{tbq} b_{l,1} b_{l,2} P_{tbq}(x)}{b_{l,1} b_{l,2} \left( \sum_{i=tbq, tqb, Wbbq, t\bar{t}} c_i P_i(x) \right) + c_{tqg} b_{l,1} (1 - b_{l,2}) P_{tq}(x) + c_{Wugg} (1 - b_{l,1}) (1 - b_{l,2}) P_{Wugg}(x)} \quad (6.3.11)$$

This B-weighted ME Discriminant (B-MED) has the best performance of the

discriminants tried for the  $s$ -channel. The definitions and comparisons with the other discriminants can be found in Appendix L.

### 6.3.2 Transformation of Discriminant

The distribution binned in discriminant output is used to measure the cross section, as presented in Chapter 8. However, to reduce statistical fluctuations, we transform the distribution in discriminant output ( $X_D$ ) to ensure the presence of at least 64 expected background events in every bin. Specifically, the binning of the distribution is changed such that the background follows a  $k/x$  form from 0 to 0.8, a linear function in  $X_D$  from 0.8 to 0.95, and has at least 64 effective events in each bin above 0.95, as illustrated in Figure 6.10. The value of  $k$  is chosen to normalize the area of the function to unity, with the slope and intercept of the linear term are constrained to make the overall transformation a continuous function of  $X_D$ .

Following the transformation, all bins containing finite predictions for signal or containing data also have finite expected background contributions. This avoids the possibility of overestimating the signal cross section caused by fluctuations of the background in the signal-like region of the discriminant. For the analysis channels with low statistics, we leave some of the bins empty, while keeping at least 64 background events in each of the filled bins.

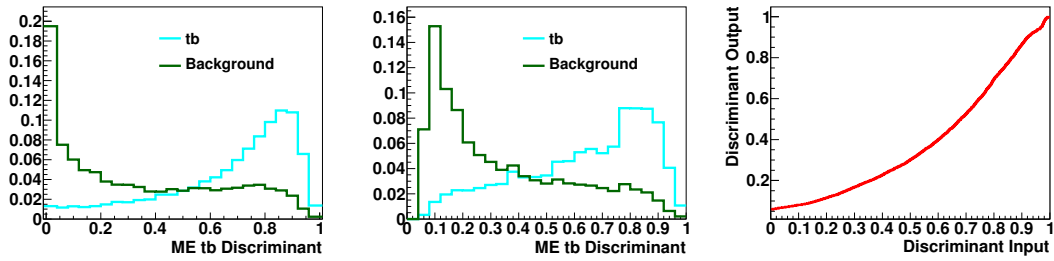


**Figure 6.10** The  $s$ -channel B-MED for signal and background before (left) and after (central) the bin transformation, and the transformation function (right).

### 6.3.3 Performance of Discriminant and Output Distributions

As shown in Figures 6.11 to 6.14, the data to MC comparisons of the  $s$ -channel B-MED and the  $t$ -channel  $P^{bl}$ -MED indicate acceptable overall agreement. Figures 6.15 to 6.18 provides, respectively, efficiencies for rejection of background versus acceptance of signal and discriminant outputs for each source of signal and background. The discrimination is good between the single top-quark signal and background from  $W$ +jets, diboson, multijet background. However, it is less powerful for distinguishing one signal from another, and from  $t\bar{t}$  background. The similarity of topologies in the  $s$ -channel and  $t$ -channel single top-quark events makes it difficult to distinguish one from the other. The separation against  $t\bar{t}$  is also not optimal, likely because of assumptions and approximations made to describe how four quarks from the final state end up as two or three reconstructed jets.

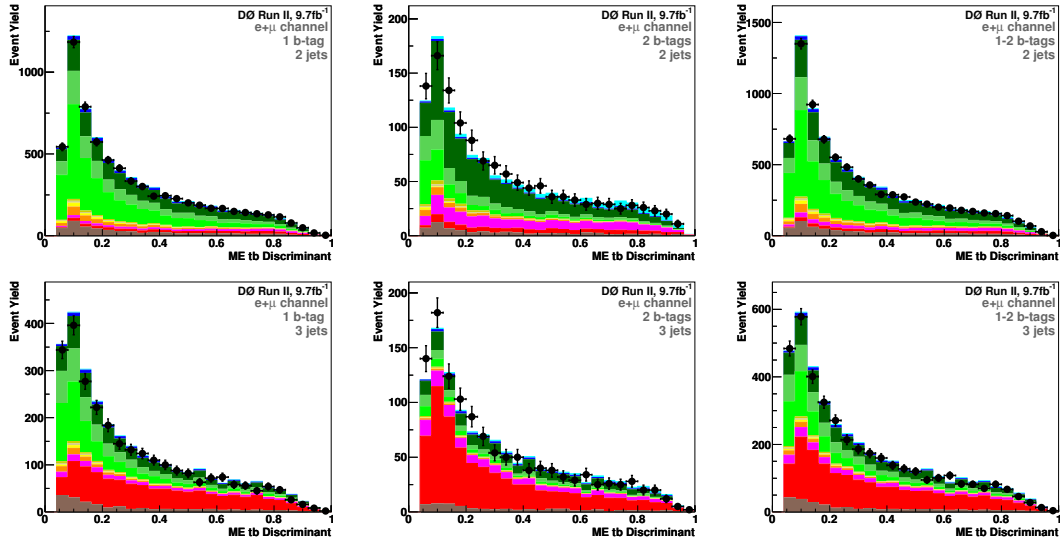


**Figure 6.11** The data-MC comparisons of the  $s$ -channel B-MED for the Run II electron and muon combined samples. The first and the second rows show the results of the two-jet and the three-jet events, respectively. The left, the central and the right columns show the results of the single-tagged, the double-tagged, and the combined-tagged events. The signal is normalized to the SM expectation.

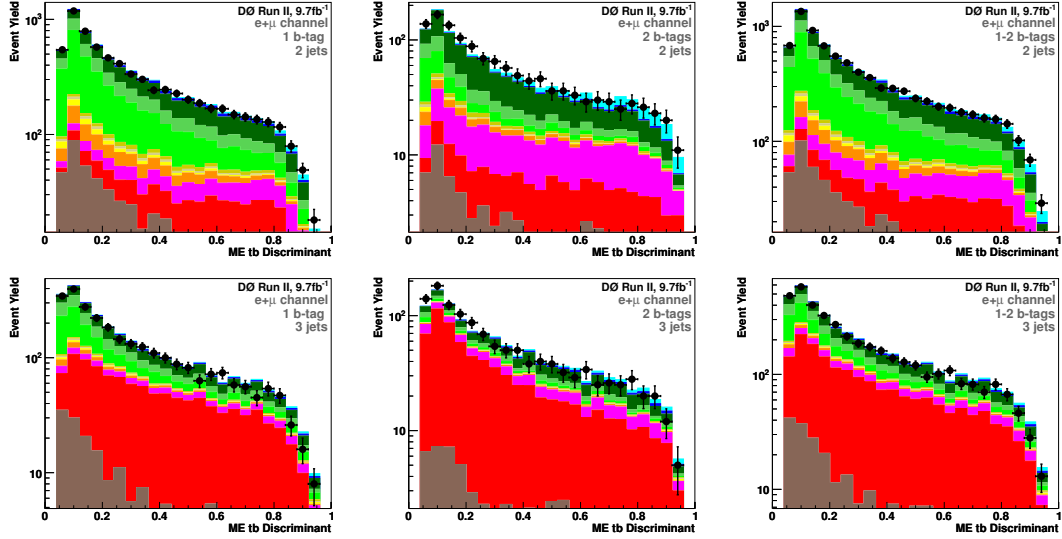


**Figure 6.12** The data-MC comparisons of the  $s$ -channel B-MED with log scale for the Run II electron and muon combined samples. The first and the second rows show the results of the two-jet and the three-jet events, respectively. The left, the central and the right columns show the results of the single-tagged, the double-tagged, and the combined-tagged events. The signal is normalized to the SM expectation.

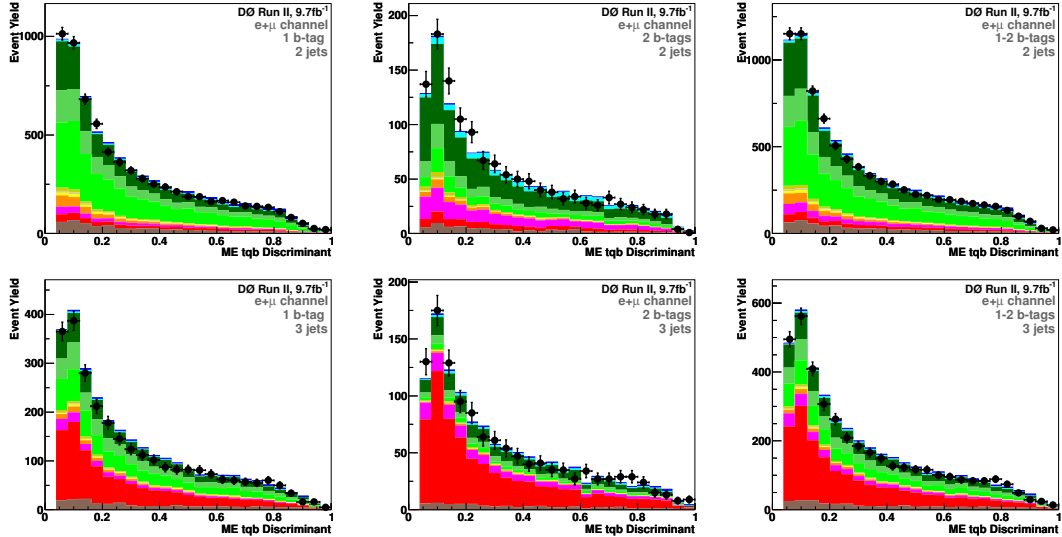


**Figure 6.13** The data-MC comparisons of the  $t$ -channel  $P^{bl}$ \_MED for the Run II electron and muon combined samples. The first and the second rows show the results of the two-jet and the three-jet events, respectively. The left, the central and the right columns show the results of the single-tagged, the double-tagged, and the combined-tagged events. The signal is normalized to the SM expectation.

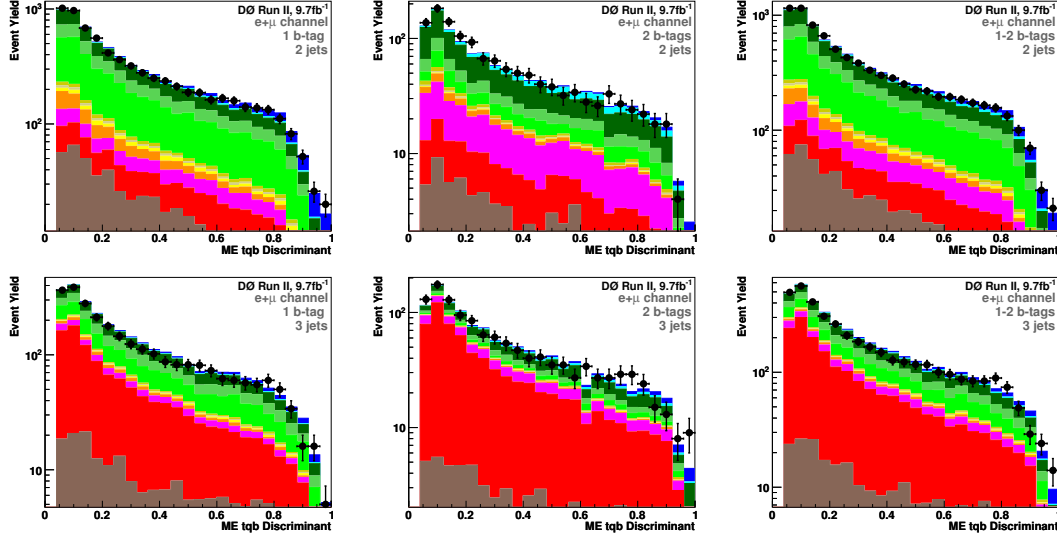


**Figure 6.14** The data-MC comparisons of the  $t$ -channel  $P^{bl}_{MED}$  for the Run II electron and muon combined samples. The first and the second rows show the results of the two-jet and the three-jet events, respectively. The left, the central and the right columns show the results of the single-tagged, the double-tagged, and the combined-tagged events. The signal is normalized to the SM expectation.

### 6.3.4 Discriminant Performance on the Cross-Check Samples

In addition to the good agreement found in comparisons of data with MC events for the nominal analysis samples, it is also important to check whether the models used for background are valid. Two background-dominated control samples are selected therefore to verify the quality of the modeling of the background, as mentioned in Section 5.8. The two main backgrounds ( $W$ +jets and  $t\bar{t}$ ) are tested separately in these samples. The control samples use the standard selections, but in addition with the criteria:

- **$W$ +jets enriched sample:** Two jets, one  $b$ -tagged jet, and  $H_T < 175$  GeV.
- **$t\bar{t}$  enriched sample:** Three jets, at least single-tagged, and  $H_T > 300$  GeV.

As shown in Figures 6.19 to 6.22, reasonable agreement is observed between the data and the MC predictions for the two backgrounds. We conclude therefore that our background is well modeled.

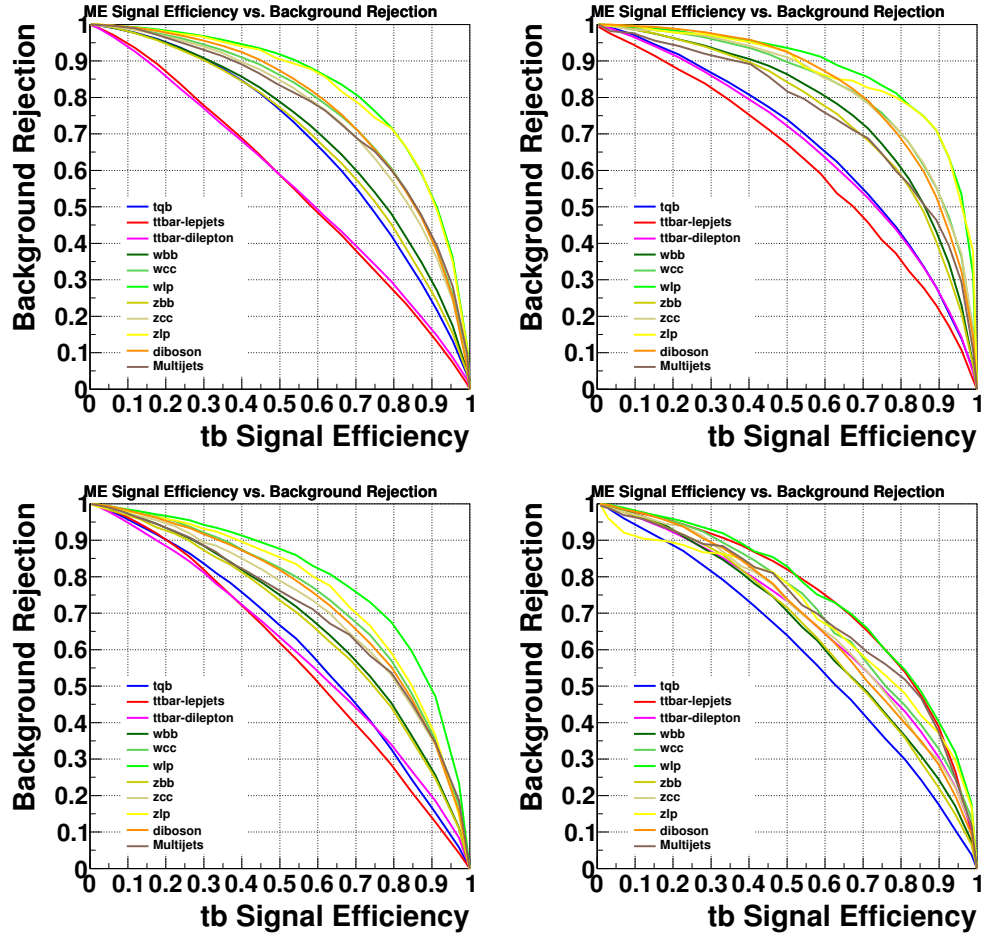


**Figure 6.15** Individual background rejection vs signal efficiency of the  $s$ -channel B-MED for the Run II electron and muon combined samples. The first and the second rows show the results of the two-jet and the three-jet events, respectively. The left column shows the results of the single-tagged events, while the right column the double-tagged ones.

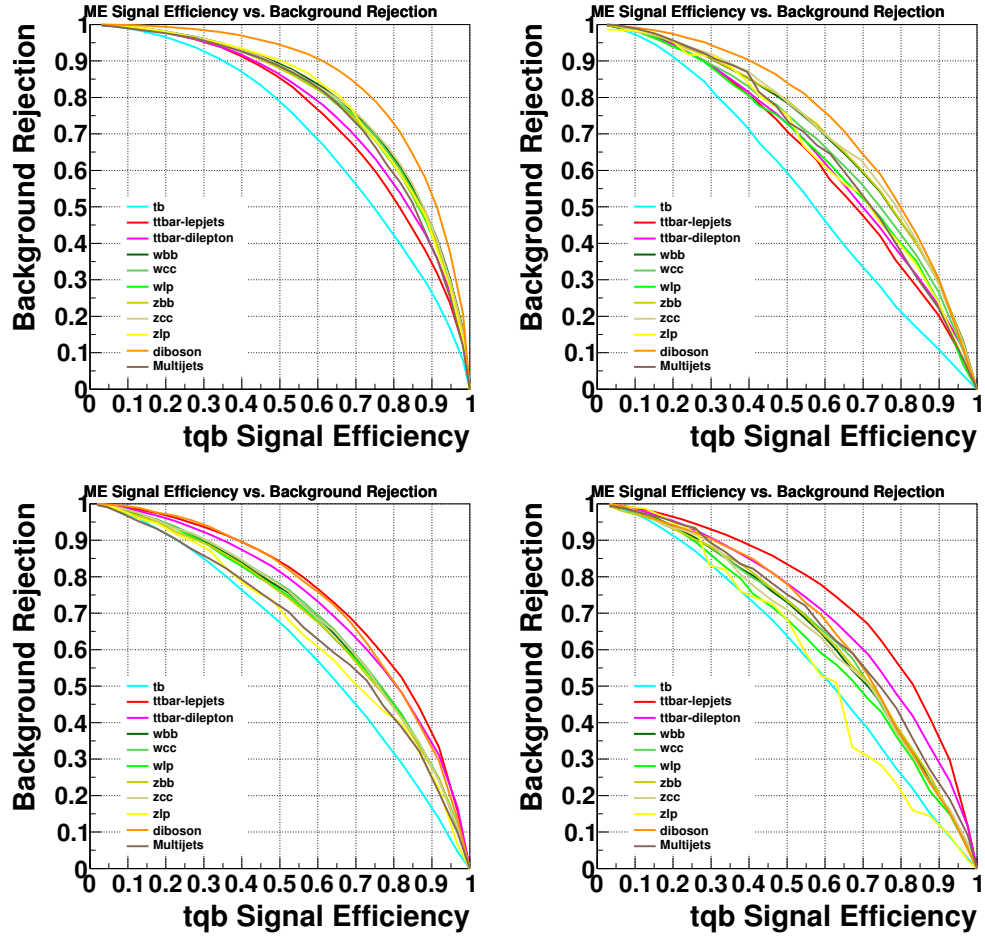


**Figure 6.16** Individual background rejection vs signal efficiency of the  $t$ -channel  $P^{bl}_{MED}$  for the Run II electron and muon combined samples. The first and the second rows show the results of the two-jet and the three-jet events, respectively. The left column shows the results of the single-tagged events, while the right column the double-tagged ones.

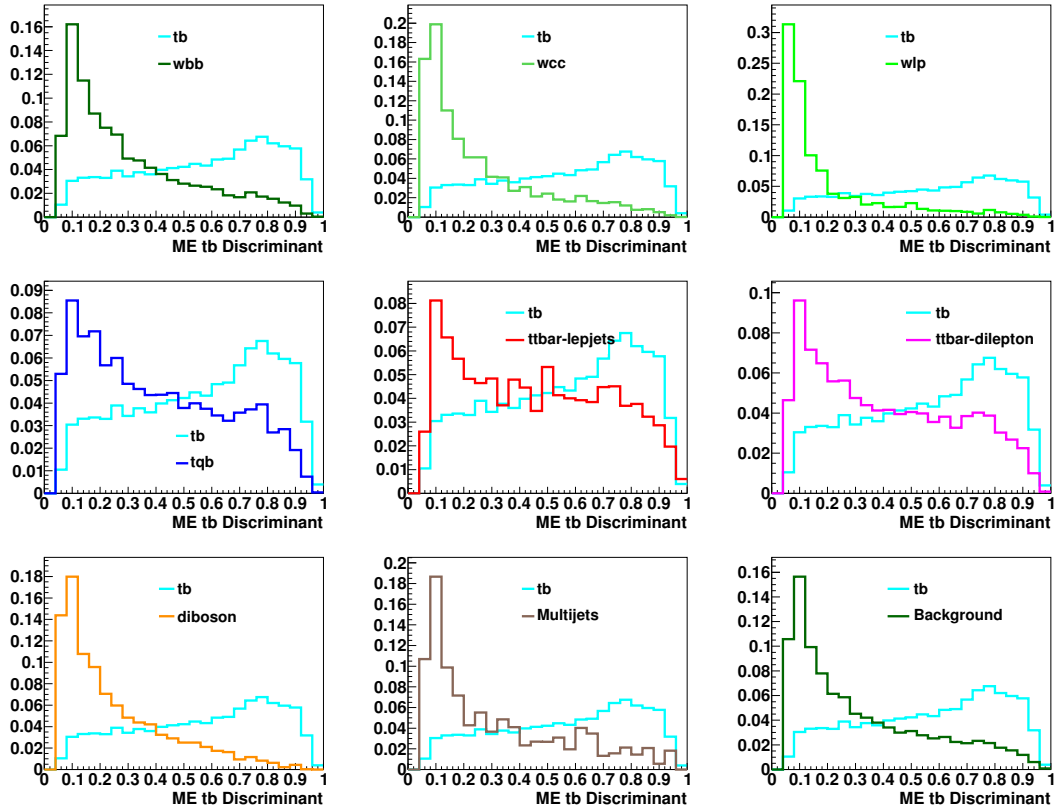


**Figure 6.17** Comparisons of B-MED outputs for the  $s$ -channel signal and the individual backgrounds for Run II, combining electron and muon channels for two-jet doubly- $b$ -tagged events.

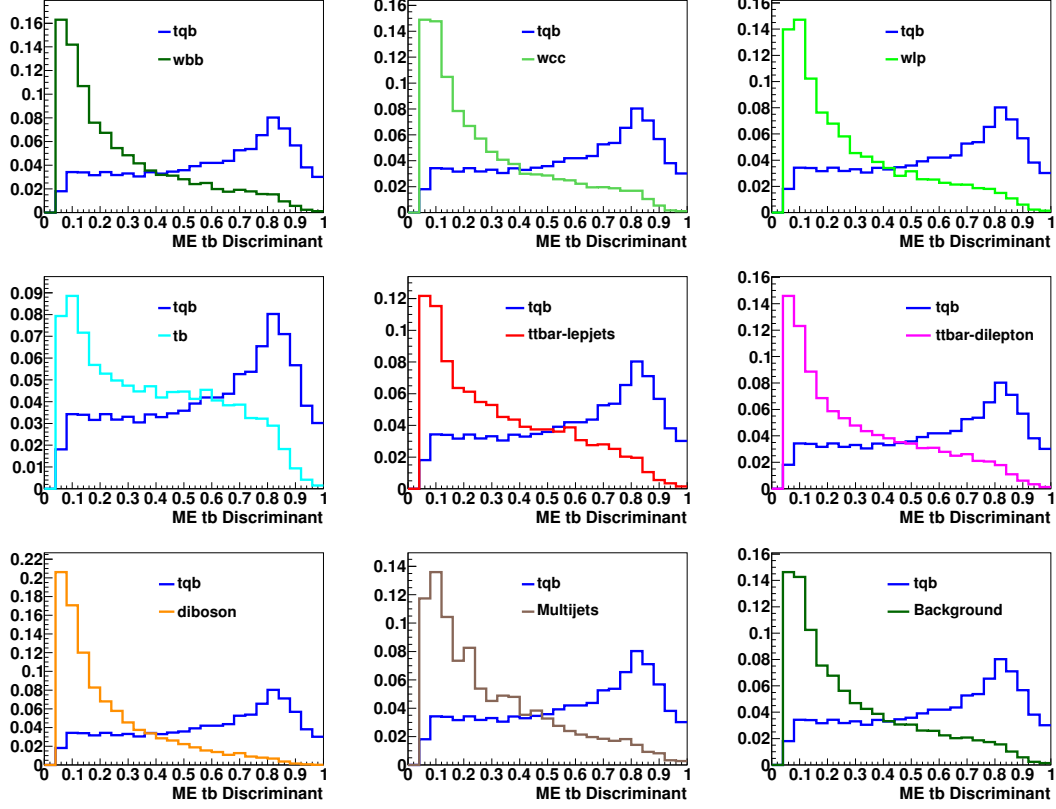


**Figure 6.18** Comparisons of  $P^{bl}$ -MED outputs in the  $t$ -channel signal and the individual backgrounds for Run II, combining electron and muon channels two-jet singly- $b$ -tagged events.

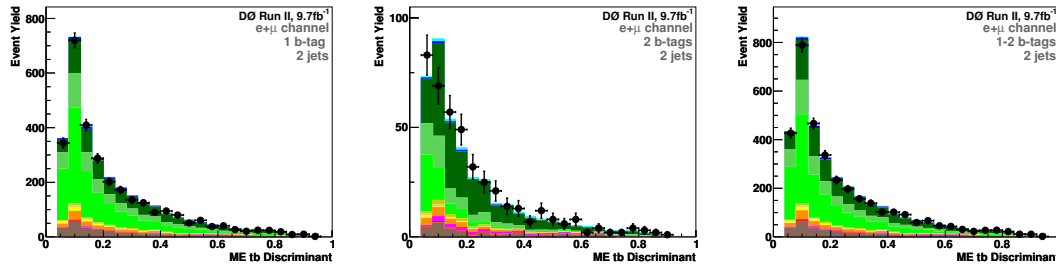


**Figure 6.19** Data and MC comparisons for the  $s$ -channel B-MED for the combined electron and muon  $W$ +jets cross-check event sample. The left, the central and the right panels show the results of the single-tagged, the double-tagged, and the combined-tagged events, respectively.

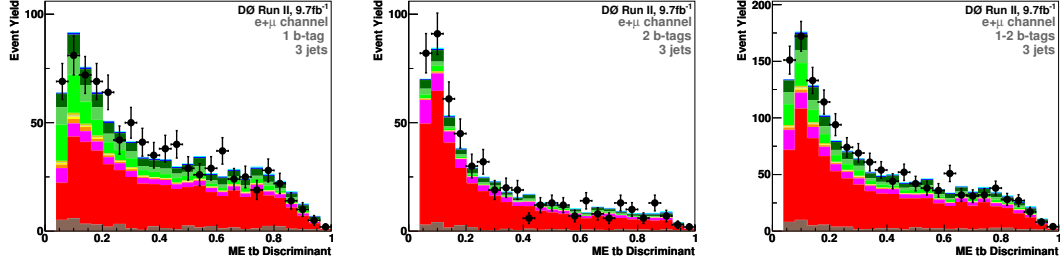


**Figure 6.20** Data and MC comparisons for the  $s$ -channel B-MED for the combined electron and muon  $t\bar{t}$  cross-check event sample. The left, the central and the right panels show the results of the single-tagged, the double-tagged, and the combined-tagged events, respectively.

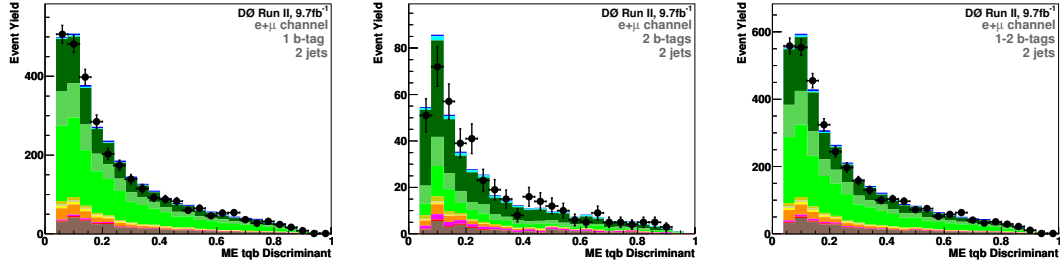


**Figure 6.21** Data and MC comparisons for the  $t$ -channel  $P^{bl}$ -MED for the combined electron and muon  $W$ +jets cross-check event sample. The left, the central and the right panels show the results of the single-tagged, the double-tagged, and the combined-tagged events, respectively.

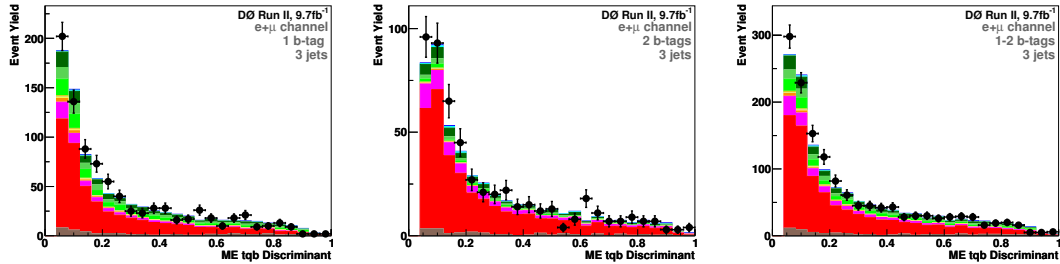


**Figure 6.22** Data and MC comparisons for the  $t$ -channel  $P^{bl}$ -MED for the combined electron and muon  $t\bar{t}$  cross-check event sample. The left, the central and the right panels show the results of the single-tagged, the double-tagged, and the combined-tagged events, respectively.

## 7 Systematic Uncertainties

Before performing the final cross section measurement, the effects of systematic uncertainties are investigated, and then integrated into the measurement via Bayesian approach, as will be discussed in Chapter 8. The systematic uncertainties considered in this analysis are categorized in two classes: one only affecting the overall normalization, and the other affecting both the normalization and the shapes of the kinematic and therefore the discriminant distributions. We briefly discuss these systematics in Sections 7.1 and 7.2, respectively, and summarize the effects in Table 7.1.

### 7.1 Normalization Systematic Uncertainties

The normalization systematic uncertainties, such as a theoretical cross section, affect only the overall scale, and have an uniform size across all bins of the discriminant. The one standard-deviation fluctuations for each systematic variation, background sample, and analysis channel are listed in Appendix N, and are combined proportionally to each background contribution for the cross section measurement.

- **Integrated luminosity:** This uncertainty comes from the uncertainty on the measured inelastic  $p\bar{p}$  cross section, and affects the signal,  $t\bar{t}$ ,  $Z$ +jets, and diboson yields, for these MC samples are normalized to the integrated luminosity.
- **Theoretical cross sections:** This uncertainty is due to the choices of the renormalization and factorization scales and the uncertainties of the top-mass and the PDFs. The uncertainties on the single top-quark and  $t\bar{t}$  cross

sections are calculated in Refs. [41, 29]. Furthermore, the one on the single top-quark signal is not included in the cross section measurement, but in the measurement of  $|V_{tb}|$ . The uncertainties on the diboson and  $Z$ +jets cross sections are calculated at NLO using the MCFM generator [123].

- **Branching fractions:** The uncertainty on the branching fractions for  $W$  boson decay is 1.5% [142].
- **Parton distribution functions:** The systematic effect of changing the parton distribution functions on the signal acceptance is estimated by using forty CTEQ PDF sets and measuring the change in the signal acceptance:

$$\sigma_{PDF} = \sqrt{\sum_{i=1}^{40} (A_{nominal} - A_i)^2} \quad (7.1.1)$$

where  $A_i$  is the signal acceptance from the  $i$ th PDF set, and  $A_{nominal}$  is the one from the default PDF set. The PDF uncertainties for the  $t\bar{t}$ ,  $Z$ +jets, and diboson backgrounds are already included in the uncertainties of the corresponding theoretical cross sections.

- **Trigger efficiency:** We use an inclusive trigger and have an efficiency close to 100%. An uncertainty of 5% (3% for Run IIb electron channel) is assigned, as demonstrated in Appendix B. The uncertainties are treated as uncorrelated between the Run IIa and the Run IIb, and between the  $e$ +jets and  $\mu$ +jets channels.
- **Instantaneous luminosity reweighting:** The procedure to match the luminosity profile in the simulation to that in the data, uses overlaid zero bias events increasing the weight of MC events with high luminosity. In order to limit the statistical fluctuations because of large individual weights, the maximum allowed weight in the luminosity reweighting procedure has been set to 3. All MC samples have been reweighted without any maximum limit on the weight and the difference in the efficiency with the default case (maximum weight equals to 3) is used as the systematic uncertainty. In all cases, we determine that 1% systematic error is a conservative choice for this source.

- **Primary vertex modeling and selection:** The  $z$  distribution of the primary vertices in the MC samples is reweighted to match that in the data [143, 144] with a negligible uncertainty of 0.05%, but the difference in primary vertex selection efficiency between the MC and the data gives an uncertainty of 1.4%.
- **Electron reconstruction and identification efficiency:** This is estimated from the uncertainty on the electron identification efficiency measurement, the “Tag and Probe” and template fit methods [145]. The values are taken from the studies of the EM-ID group [145].
- **Muon reconstruction and identification efficiency:** Since a prompt muon candidate for a  $D\bar{O}$  analysis is defined by a combination of the muon identification in the muon system, the track reconstruction in the central track, and the identification requirement, as mentioned in Section 3.4, the uncertainty of the muon reconstruction and identification is obtained by adding the uncertainties of these three requirements in quadrature. The values are provided by the Muon-ID group [146].
- **Jet Fragmentation and higher-order effects:** As mentioned in Section 4.2, PYTHIA is used as the default hadronization model for all the MC samples. By comparing the predicted events from ALPGEN+PYTHIA and ALPGEN+HERWIG MC generators, we can evaluate the uncertainty coming from the jet fragmentation (including both the hadronization and underlying event models) and apply it on the single top-quark,  $Z$ +jets, and di-boson samples. In particular, the default  $t\bar{t}$  MC samples, generated with ALPGEN+PYTHIA are compared with the ones generated with the NLO generator MC@NLO to estimate the higher order effects. We combine the jet fragmentation and higher-order effects uncertainties for the  $t\bar{t}$  events by comparing the ALPGEN+PYTHIA and MC@NLO+HERWIG samples.
- **Initial-state and final-state radiation:** The uncertainty coming from the ISR/FSR is estimated by comparing the default  $t\bar{t}$  samples and the ones generated with the PYTHIA parameters that are tuned to ISR/FSR upward/downward variations.
- **Color Reconnection:** The uncertainty on the color reconnection is measured by taking the difference between PYTHIA TuneApro and TuneACRpro,

where TuneACRpro includes the explicit color reconnection model [147].

- **$b$ -jet fragmentation:** The uncertainty is due to the fact that the PYTHIA  $b$ -jet modeling in DØ simulation is tuned to  $e^+e^-$  data. The size is taken from Ref. [148], where the difference between the Large Electron-Positron Collider (LEP) and the SLAC Large Detector (SLD) parametrization is measured.
- **$W$ +jets and multijet normalization:** The uncertainty for the Run IIa samples is estimated by the method described in Appendix 4 of Ref. [107], while the one for the Run IIb samples is evaluated from the error propagation of the matrix method according to the measured  $\epsilon_{QCD}$  and  $\epsilon_{sig}$  [149, 125].
- **Taggability efficiency:** For the Run IIa samples, the uncertainty estimation on the taggability efficiency is described in Appendix 6 of Ref. [107]. For the Run IIb samples, it is estimated from the difference between the data and the MC samples in the closure test of the taggability measurement [124].
- **Heavy-flavor correction:** This uncertainty for the Run IIa samples is described in Appendix 7 of Ref. [107]. For the Run IIb samples, an overall correction to the high  $b$ -ID output is performed in an orthogonal sample, as described in Section 5.5. The systematic uncertainty for this procedure stems from the statistics of the orthogonal sample in the different channels and is 20%. This uncertainty is treated as fully anti-correlated with respect to the uncertainty on the  $b$ -ID scale factor corrections (described in Section 7.2). It is anticorrelated because a higher  $b$ -ID efficiency results in a larger downward correction in the high discriminant output of the  $b$ -tagger. This scale factor is applied to all  $b$ -tagged jets with high  $b$ -ID output, not just to the  $W/Z$ +jets samples. Therefore, this systematic uncertainty in Run IIb affects all samples.
- **Relative  $b$ /light jet response:** This uncertainty is treated in the normalization-only category for the Run IIa samples [107, 150]; for the Run IIb samples, however, the flavor-dependent jet energy scale is applied, and the systematic falls into the shape-changing category. The Run IIa uncertainties and the corresponding Run IIb ones are correlated.
- **Sample statistics:** The uncertainty comes from the finite size of the data and the MC samples, and is taken into account in each bin of the final

discriminant distributions.

## 7.2 Shape-changing Systematic Uncertainties

The shape-changing systematic uncertainties, such as the jet energy scale, affect both the normalization and the shape of the discriminant distributions; namely, the sizes vary bin-to-bin. To estimate these uncertainties, in general, we raise and lower each of the uncertainty sources by one standard deviation, and repeat the whole analysis. The sources of the shape-changing uncertainties considered are listed below:

- **Jet energy scale** (JES, Section 3.5.2)
- **Jet energy resolution** (JER, Section 3.5.2)
- **Jet reconstruction and identification** (JETID, Section 3.5.1): The uncertainty, in particular, is determined by turning off the JETID correction factors, and is symmetrized with respect to the nominal samples.
- **Jet vertex confirmation** (VC, Section 3.5.1)
- **Flavor-dependent jet energy scale** (SDC, Section 3.5.2)
- **$V$ +jets angular corrections** (AC, Section 5.3)
- **$b$ -tagging efficiency correction factor** (BTag, Section 5.2.2): The uncertainty is treated as anti-correlated with respect to the uncertainty on the heavy-flavor correction, as described in Section 5.5.

Figure 7.1 illustrates the comparisons between the shifted and nominal samples. The plots show the effect of varying each systematic effect by  $\pm 1$  standard deviation on the Matrix Element discriminant for the sum of the signal and simulated backgrounds samples. The nominal sample is at unity.

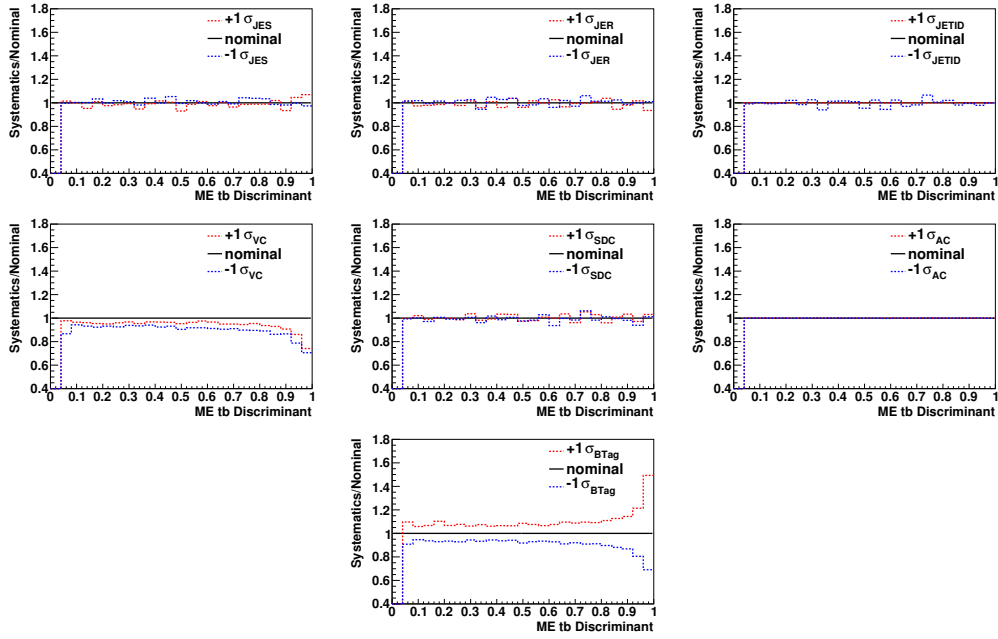


**Figure 7.1** The effects of the shape-changing systematic uncertainties on the ME discriminant for Run IIb e+jets two-jet double-tagged sample. The  $y$ -axis shows the ratio of the systematic shifted sample to the nominal sample. For the JETID uncertainty, we take the downward-shifted variation and symmetrize it when measuring the cross section. The large size of the BTag relative uncertainty in the high discriminant region is due to the fact that the bin contents of all the nominal and the two systematics samples are quite small.

Relative Systematic Uncertainties	
<b>Components for Normalization</b>	
Integrated luminosity	4.3%
$t\bar{t}$ cross section	9.0%
$Z$ +jets cross section	3.3%
Diboson cross sections	7.0%
Branching fractions	1.5%
Parton distribution functions	2.0%
(signal acceptances only)	
Triggers	(3.0-5.0)%
Instantaneous luminosity reweighting	1.0%
Primary vertex selection	1.4%
Color reconnection	1.0%
Electron identification	0.7%
Muon identification	1.7%
Jet fragmentation and higher order effects	(0.7-7.0)%
Initial-and final-state radiation	(0.8-10.9)%
$b$ -jet fragmentation	2.0%
Taggability	2.0%
Heavy-flavor correction	20.0%
$W$ +jets normalization to data	(1.1-2.5)%
Multijet normalization to data	(9.2-42.1)%
<b>Components for Normalization and Shape</b>	
Jet reconstruction and identification	(0.1-1.4)%
Jet energy resolution	(0.3-1.1)%
Jet energy scale	(0.1-1.2)%
Flavor-dependent jet energy scale	(0.1-1.3)%
Vertex confirmation	(4.5-10.5)%
$b$ tagging, single-tagged	(1.0-6.6)%
$b$ tagging, double-tagged	(7.3-8.8)%
Angular correction	0.1%

**Table 7.1** A summary of the relative systematic uncertainties for each of the correction factors or normalizations. The uncertainty shown is the error on the correction or the efficiency, before it has been applied to the MC or data samples.

## 8 Cross Section Measurement

The Matrix Element method establishes a discriminant to distinguish the signal and the background events, and the resulting binned distribution of the discriminant is used for all the cross section measurements. We might lose information by using the binned discriminant; however, using the unbinned likelihood function requires a fit and there will be an additional uncertainty from the fit. To extract the cross section, a Bayesian approach is utilized, taking all the statistical and systematic uncertainties and their correlations into account. This section starts with an introduction to the Bayesian approach. Before applying it to the data, we perform ensemble tests to validate and calibrate our method as described in Section 8.2. We present the results with the data and the significance of the measurement in Sections 8.4 and 8.6, respectively.

### 8.1 Bayesian Approach

In Bayesian statistics, if we want to determine an unknown parameter (or parameters)  $\sigma$ , and have a set of a measured properties  $\mathbf{D}$  whose probability density function depends on this parameter  $\sigma$ , we can find the degree of belief for  $\sigma$  in the posterior p.d.f.  $p(\sigma|\mathbf{D})$ ,

$$p(\sigma|\mathbf{D}) = \frac{L(\mathbf{D}|\sigma)\pi(\sigma)}{\int L(\mathbf{D}|\sigma')\pi(\sigma')d\sigma'} \quad (8.1.1)$$

where  $L(\mathbf{D}|\sigma)$  is the likelihood function (i.e. the joint p.d.f.) assuming the parameter  $\sigma$ , and  $\pi(\sigma)$  is the prior p.d.f. for  $\sigma$ . This equation comes from Bayes' theorem,  $p(\sigma|\mathbf{D}) = \frac{p(\mathbf{D}|\sigma)p(\sigma)}{p(\mathbf{D})}$ . The denominator of Equation (8.1.1) preserves the normalization of the posterior to unity.

In each bin of the discriminant outputs, specifically, the likelihood to observe a count  $D$  with a known mean count  $d$  is given by the Poisson distribution:

$$L(D|d) = \frac{e^{-d}d^D}{\Gamma(D+1)} \quad (8.1.2)$$

where  $\Gamma$  is the Gamma function, and is equal to  $D!$  when  $D$  is an integer. We use the Poisson distribution in this form in order to permit the use of non-integer counts for expected scenarios, in which the  $D$  is set to the predicted yield.

The mean count  $d$  is a sum of the predicted contributions from the signal and the  $N$  different backgrounds,

$$d = \alpha\mathcal{L}\sigma + \sum_{i=1}^N b_i \equiv a\sigma + \sum_{i=1}^N b_i \quad (8.1.3)$$

where  $\alpha$  is the signal acceptance,  $\mathcal{L}$  the integrated luminosity,  $\sigma$  the signal production cross section – the quantity of interest –  $b_i$  the predicted yield of the  $i$ th background source, and  $a \equiv \alpha\mathcal{L}$  the effective luminosity for the signal.

All the  $M$  statistically independent bins of the discriminant output distributions are combined by replacing the likelihood with the product of all the single-bin likelihoods,

$$L(\mathbf{D}|\mathbf{d}) \equiv L(\mathbf{D}|\sigma, \mathbf{a}, \mathbf{b}) = \prod_{j=1}^M L(D_j|d_j) \quad (8.1.4)$$

where  $\mathbf{D}$  and  $\mathbf{d}$  denote vectors of the observed and the mean counts in  $M$  signal-bins, and  $\mathbf{a}$  and  $\mathbf{b}$  represent vectors of the effective luminosity for the signal and the background prediction yields.

The prior p.d.f. in Bayesian statistics is not unique, and it reflects the degree of belief about  $\sigma$  of the experimenter's. Specifically, our prior p.d.f.  $\pi(\sigma, \mathbf{a}, \mathbf{b})$  encodes our knowledge of  $\sigma$ ,  $\mathbf{a}$  and  $\mathbf{b}$ . Assuming any prior knowledge of  $\mathbf{a}$  and  $\mathbf{b}$  is independent of the signal cross section  $\sigma$ , the joint prior p.d.f. can therefore be factorized:

$$\begin{aligned} \pi(\sigma, \mathbf{a}, \mathbf{b}) &= \pi(\mathbf{a}, \mathbf{b}|\sigma)\pi(\sigma) \\ &= \pi(\mathbf{a}, \mathbf{b})\pi(\sigma). \end{aligned} \quad (8.1.5)$$

Furthermore, we represent complete ignorance about the signal cross section

by setting the prior p.d.f.  $\pi(\sigma)$  equal to a constant:

$$\pi(\sigma) = \begin{cases} \frac{1}{\sigma_{max}} & 0 < \sigma < \sigma_{max} \\ 0 & \text{otherwise} \end{cases} \quad (8.1.6)$$

where  $\sigma_{max}$  is the upper bound of  $\sigma$  that the value of the posterior is sufficiently close to zero, and it is chosen to be 8 pb for  $s$ -channel single top.

Bayesian statistics provides a framework to incorporate systematic uncertainties into a result. If a model does depend not only on parameters of interest  $\sigma$ , but also on nuisance parameters, whose values are known with some limited accuracy, then the posterior p.d.f. for  $\sigma$  alone can be obtained by integrating over the nuisance parameters.  $\mathbf{a}$  and  $\mathbf{b}$  are such nuisance parameters in our measurement:

$$\begin{aligned} p(\sigma|\mathbf{D}) &= \frac{1}{\mathcal{N}} \int \int L(\mathbf{D}|\sigma, \mathbf{a}, \mathbf{b}) \pi(\sigma, \mathbf{a}, \mathbf{b}) d\mathbf{a} d\mathbf{b} \\ &= \frac{1}{\mathcal{N}_{\sigma_{max}}} \int \int L(\mathbf{D}|\sigma, \mathbf{a}, \mathbf{b}) \pi(\mathbf{a}, \mathbf{b}) d\mathbf{a} d\mathbf{b}. \end{aligned} \quad (8.1.7)$$

Out of the posterior p.d.f., the mode (peak position) is chosen as the measurement and the 68% interval about the mode as an estimate of its uncertainty, as shown in Figure 8.1. With a uniform prior, the posterior is proportional to the likelihood, and therefore the mode of the posterior is equal to the ML estimator. Furthermore, it has been shown that the 68% interval can be interpreted as an approximation of a frequentist one standard deviation interval [151].

The prior p.d.f.  $\pi(\mathbf{a}, \mathbf{b})$  encodes our state of knowledge, the effective signal luminosities and the predicted background yields, with the systematic uncertainties accounting for their limited accuracy. Each systematic uncertainty is sampled from the MC as a Gaussian distribution, whose mean is set to the predicted yield and width to the corresponding uncertainty. The width of the Gaussian sampling may be asymmetric in the case that the systematic uncertainty gives different plus one ( $\delta^+$ ) and minus one ( $\delta^-$ ) standard deviation shifts, typically on the shape-changing systematics as illustrated in Figure 8.2.

We apply Bayesian approach on the cross section measurement using the `top_statistics` package. In this package, the integration in Equation (8.1.7)

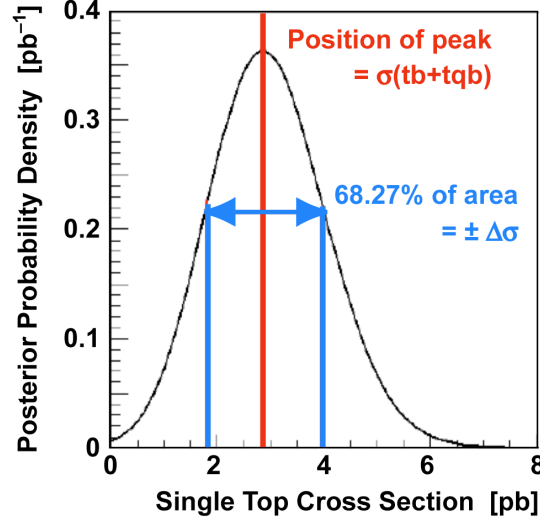


**Figure 8.1** An example of the posterior probability density function. The mode (peak position) is the measured value, while the width is the uncertainty.

is performed numerically with Monte Carlo importance sampling:

$$\begin{aligned}
 p(\sigma|\mathbf{D}) &= \frac{1}{\mathcal{N}_{\sigma_{max}}} \int \int L(\mathbf{D}|\sigma, \mathbf{a}, \mathbf{b}) \pi(\mathbf{a}, \mathbf{b}) d\mathbf{a} d\mathbf{b} \\
 &\sim \frac{1}{\mathcal{N}_{\sigma_{max}} N_{samples}} \sum_{k=1}^{N_{samples}} L(\mathbf{D}|\sigma, \mathbf{a}_k, \mathbf{b}_k)
 \end{aligned} \tag{8.1.8}$$

where  $N_{samples}$  is a large number and the  $N_{samples}$  points of  $(\mathbf{a}_k, \mathbf{b}_k)$  are randomly sampled from the prior p.d.f.  $\pi(\mathbf{a}, \mathbf{b})$ . More details can be found in Ref. [151].

## 8.2 Calibration of the Method

To validate the cross section measurement with the Matrix Element discriminant, we study the performance of the method in samples of pseudo-data. The pseudo-data samples have characteristics as close as possible to those of the real data, so that we can test what would happen if we were able to repeat the  $D\bar{O}$  experiment thousands of times. We can use such ensembles to determine whether our method is able to measure the signal cross section from an overwhelming background contribution. And by generating ensembles with different values of the signal cross

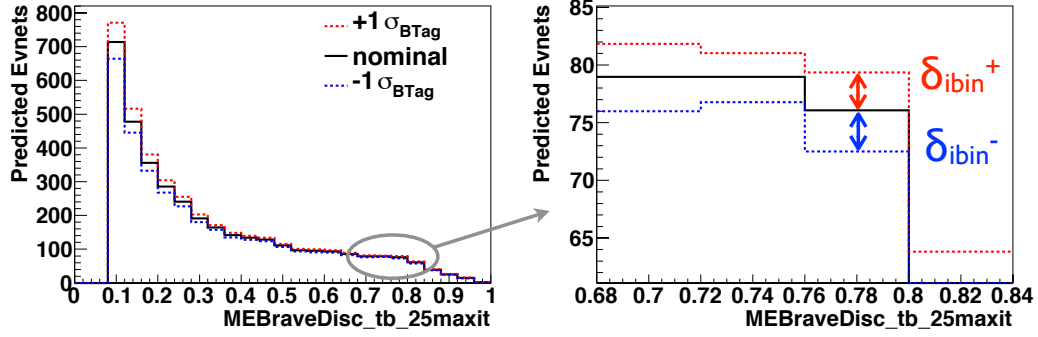


**Figure 8.2** An example of shape-changing systematic uncertainties. In each bin, the prior p.d.f.  $\pi(\mathbf{a}, \mathbf{b})$  is sampled as a Gaussian with different positive and negative widths,  $\delta_{ibin}^+$  and  $\delta_{ibin}^-$ , and with the mean equal to the predicted yields of the nominal sample.

sections, we can assess whether there is a bias in the cross section measurement.

To generate a pseudo-data sample, we vary the systematic uncertainties, and in each bin, a count is sampled from a Poisson distribution with mean of the systematics-shifted prediction. By drawing Poisson random numbers, the count in each bin is an integer, which looks exactly like data. The procedure takes all systematics as well as their correlations into account. Afterwards, we measure the signal cross section with each pseudo-data sample using Bayesian approach presented in Section 8.1. In order to improve the sensitivity, the samples are divided into four analysis channels, depending on the jet multiplicity (two or three jets), and the number of  $b$ -tagged jets (one or two), but the posterior density function and the signal cross section are obtained from the combination of all the available analysis channels.

We generate six ensembles with the same background contribution, but with different signal cross sections: for  $s$ -channel, 0.5 pb, 0.75 pb, 1.04 pb (the SM prediction), 1.5 pb, 2.5 pb, and 3.5 pb, where the  $t$ -channel is treated as background with the cross section predicted in the SM, and for  $t$ -channel, 1.5 pb, 2 pb, 2.26 pb (the SM prediction), 3.5 pb, 5 pb, and 7 pb, where the  $s$ -channel is background with the cross section predicted in the SM. For each ensemble, 10,000 pseudo-data samples are generated. Figures 8.3 and 8.5 show the peak of the posterior p.d.f. for each pseudo-data sample.

The average cross section and the average uncertainty for each ensemble are taken as the “ensemble average result.” A linear fit is performed on the ensemble

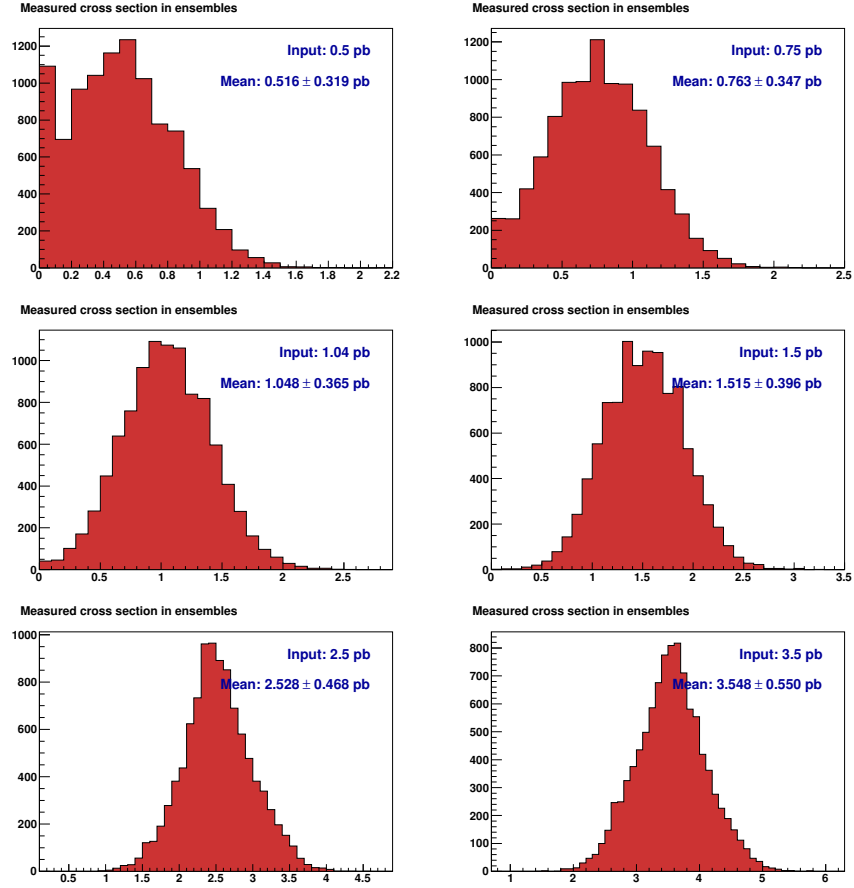


**Figure 8.3** Each plot contains 10,000 entries, consisting of the peak of the posterior p.d.f. for each pseudo-data sample for the  $s$ -channel. The ensemble average of the measured cross sections is written in each plot, and it follows the different injected signal cross sections. The input cross sections are 0.5 pb (top left), 0.75 pb (top right), 1.04 pb (the SM prediction, middle left), 1.5 pb (middle right), 2.5 pb (bottom left), 3.5 pb (bottom right).

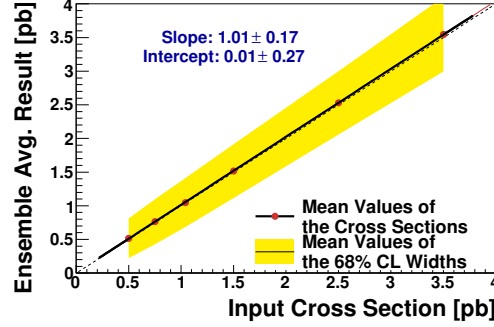


**Figure 8.4** The ensemble average of measured cross section as a function of the input  $s$ -channel cross sections. The band shows the ensemble average of the 68% intervals of the posteriors, and this interval is used as the uncertainty of the value of the cross section in the fit.

average cross sections versus the input cross sections, as shown in Figures 8.4 and 8.6 for  $s$  and  $t$ -channels respectively. The results are  $1.01 \pm 0.17$  for the slope and  $0.01 \pm 0.27$  pb for the intercept for  $s$ -channel, and  $1.01 \pm 0.15$  for the slope and  $-0.03 \pm 0.51$  for the intercept for  $t$ -channel. We conclude that the bias in the Matrix Element method is negligible, and therefore we do not have to calibrate the expected or measured cross sections.

### 8.3 Expected Cross Section

We use the ensemble average results from the ensemble with the SM signal prediction, 1.04 pb and 2.26 pb for  $s$  and  $t$ -channels respectively, as the expected results:

$$\begin{aligned}\sigma^{\text{exp}}(p\bar{p} \rightarrow tb + X) &= 1.048^{+0.383}_{-0.347} \text{ pb} \\ \sigma^{\text{exp}}(p\bar{p} \rightarrow tqb + X) &= 2.255^{+0.584}_{-0.535} \text{ pb}.\end{aligned}$$

We assume the SM  $t$ -channel when extracting the  $s$ -channel cross section, and vice versa. Figures 8.7 and 8.8 demonstrate the distributions of measured cross sections and uncertainties from the  $s$  and  $t$ -channel ensembles. The ensemble results take all the systematic effects into account, while the nominal simulation may be biased in one direction. Since the ensemble test fundamentally represents all the statistical statement we have to make, we use the ensemble result as the expected measurement.

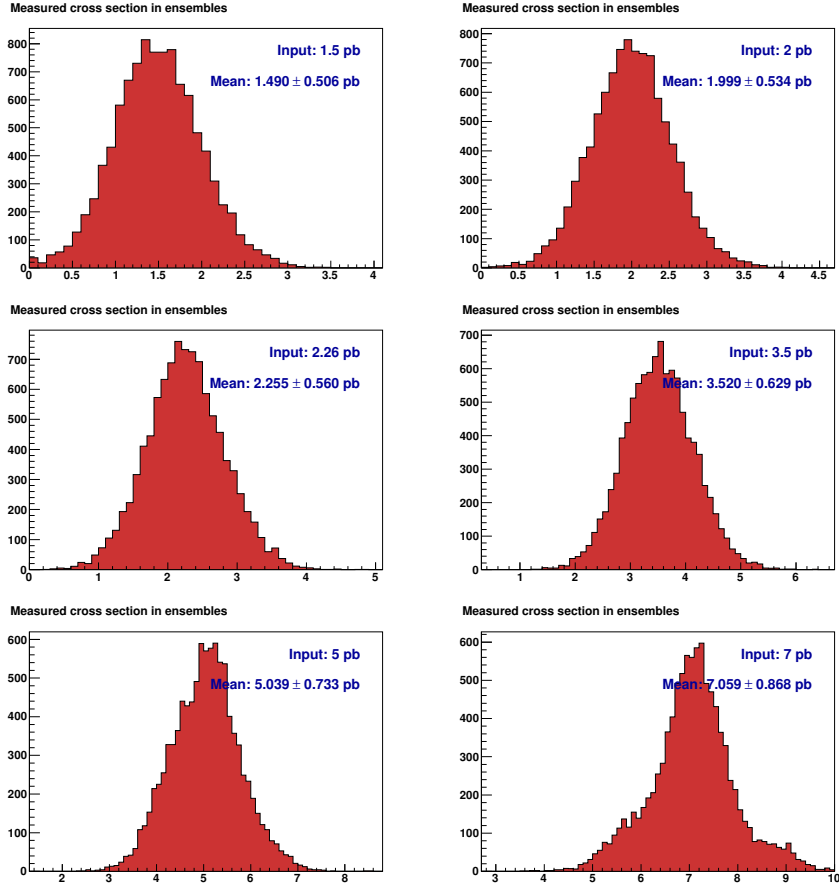


**Figure 8.5** Each plot contains 10,000 entries, consisting of the peak of the posterior p.d.f. for each pseudo-data sample for the  $t$ -channel. The ensemble average of the measured cross sections is written in each plot, and it follows the different injected signal cross sections. The input cross sections are 1.5 pb (top left), 2 pb (top right), 2.26 pb (the SM prediction, middle left), 3.5 pb (middle right), 5 pb (bottom left), 7 pb (bottom right).

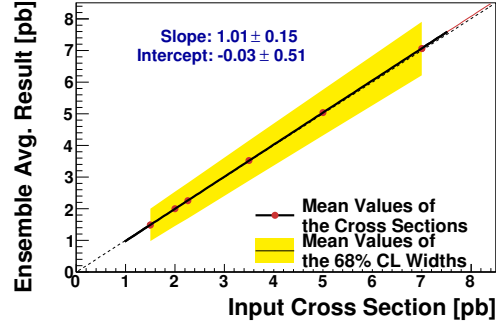


**Figure 8.6** The ensemble average of measured cross section as a function of the input  $t$ -channel cross sections. The band shows the ensemble average of the 68% intervals of the posteriors, and this interval is used as the uncertainty of the value of the cross section in the fit.

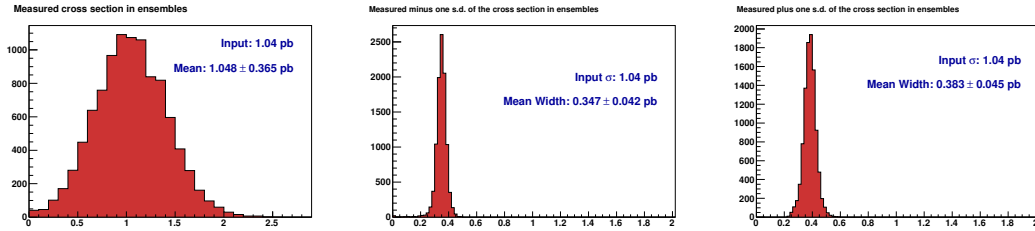


**Figure 8.7** Distributions of the measured cross sections (left), the measured negative uncertainties (central), and the measured positive uncertainties (right) for the  $s$ -channel B-MED pseudo-data samples, where the SM cross section, 1.04 pb, is used as the input signal cross section.

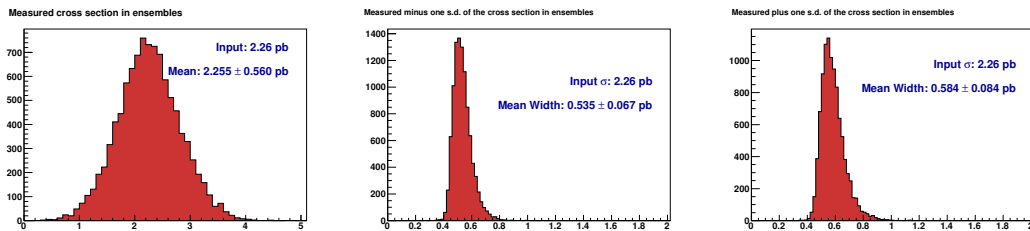


**Figure 8.8** Distributions of the measured cross sections (left), the measured negative uncertainties (central), and the measured positive uncertainties (right) for the  $t$ -channel  $p^{bl}_{\text{MED}}$  pseudo-data samples, where the SM cross section, 2.26pb, is used as the input signal cross section.

## 8.4 Measured Cross Section

The cross sections measured using data are listed as follows,

$$\begin{aligned}\sigma^{\text{obs}}(p\bar{p} \rightarrow tb + X) &= 1.269^{+0.354}_{-0.334} \text{ pb} \\ \sigma^{\text{obs}}(p\bar{p} \rightarrow tqb + X) &= 2.115^{+0.526}_{-0.493} \text{ pb}.\end{aligned}$$

The  $t$ -channel is assumed to have the cross section predicted in the SM when we measure the  $s$ -channel cross section, and vice versa. All the statistical and systematic uncertainties, as well as their correlations, are taken into account. The posterior density functions of the  $s$  and  $t$ -channel single top-quark cross sections measured in data are shown in Figures 8.9 and 8.10, respectively. Figures 8.11 and 8.12 demonstrate the ME discriminant zoomed into the signal-enriched region, and Figure 8.13 show the posterior  $\pm 1$  SD uncertainty on the background prediction versus the ME discriminant outputs. In addition, Figures 8.14(a) and 8.14(b) show the comparison between the background-subtracted data and the measured signals, where the signal contributions are visible above the  $\pm 1$  SD uncertainty. The model including a signal contribution clearly fits the data better than the background-only model does.

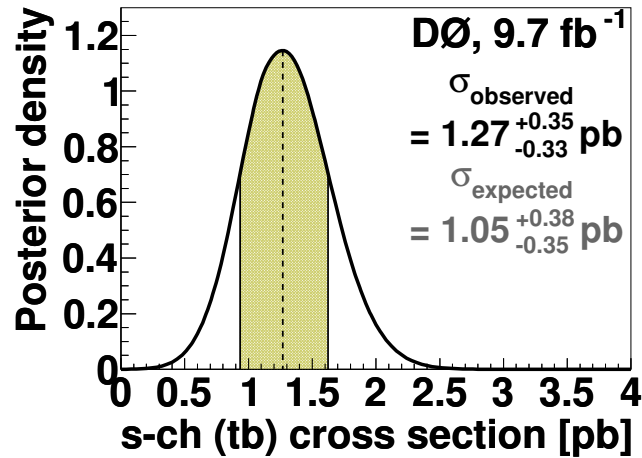


**Figure 8.9** Measured result for  $s$ -channel single top-quark cross section measurement.

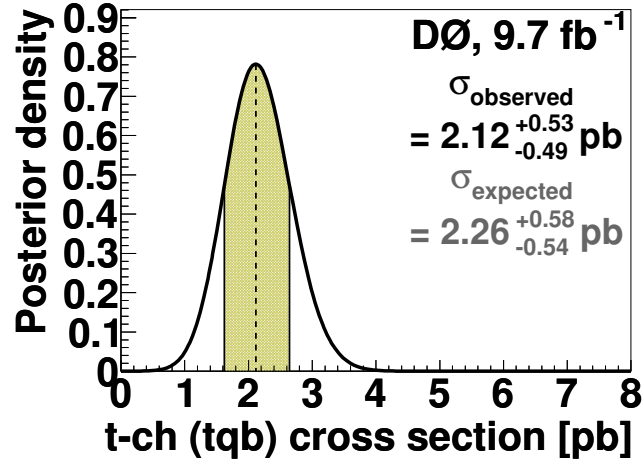


Figure 8.10 Measured result for  $t$ -channel single top-quark cross section measurement.

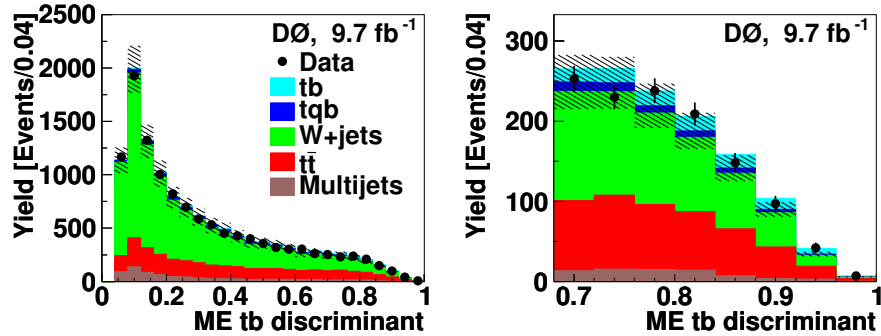
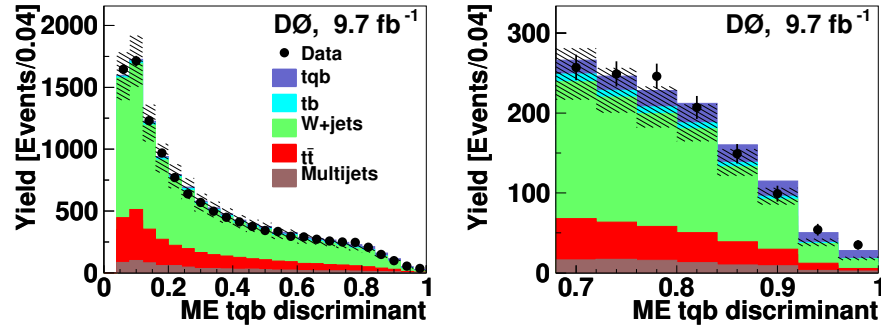
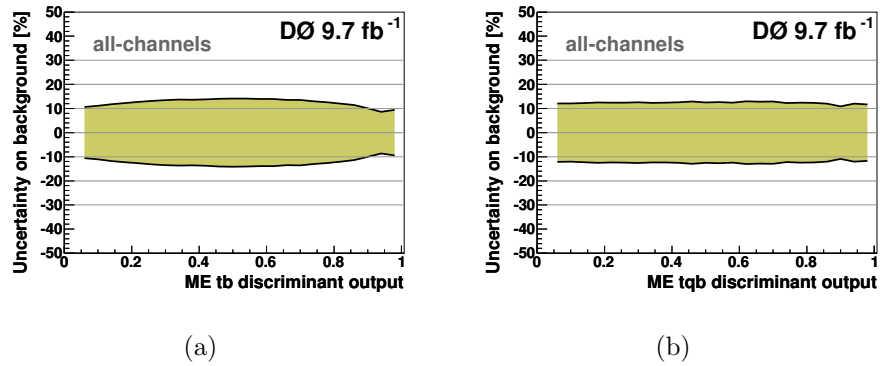


Figure 8.11 The data-MC comparisons of the  $s$ -channel B-MED for the overall Run II data, with all the analysis channels combined. The left figure shows the overall region, while the right figure zooms into the signal-enriched region. The hatched area is the posterior  $\pm 1$  SD uncertainty on the total background prediction. The signal contribution is scaled to the measured result.



**Figure 8.12** The data-MC comparisons of the  $t$ -channel  $P^{bl}_{MED}$  for the overall Run II data, with all the analysis channels combined. The left figure shows the overall region, while the right figure zooms into the signal-enriched region. The hatched area is the posterior  $\pm 1$  SD uncertainty on the total background prediction. The signal contribution is scaled to the measured result.



**Figure 8.13** The posterior  $\pm 1$  SD uncertainty on the background prediction versus the ME discriminant output for (a)  $s$ -channel and (b)  $t$ -channel.

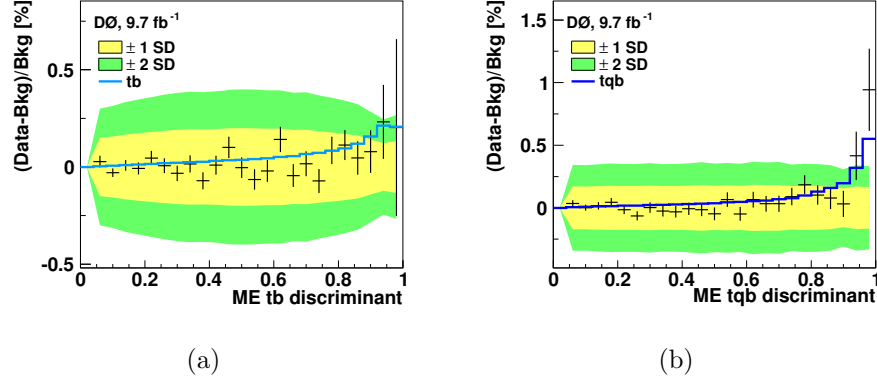


**Figure 8.14** The data after subtracting the background versus (a)  $s$ -channel and (b)  $t$ -channel ME discriminants. The signal contributions are scaled to the measured cross sections. The hatched bands show the posterior uncertainty on the background prediction, and both the  $s$  and  $t$ -channel contributions are visible above the  $\pm 1$  SD hatched band.

## 8.5 Model-independent Measurement

We perform a model-independent measurement by extracting the  $s$  and  $t$ -channel cross sections simultaneously, without imposing any constraint on the relative rates of  $s$  and  $t$ -channel production. To obtain a discriminant sensitive to both the  $s$  and  $t$ -channels, we utilize both the discriminants at one time. For each analysis channel, the events are separated into two categories,  $s$ -like and  $t$ -like, with the criteria  $P^{bl\_MED}_s > P^{bl\_MED}_t$  and  $P^{bl\_MED}_s < P^{bl\_MED}_t$ , respectively. Since  $P^{bl\_MED}$  is essentially the likelihood ratio, the comparison of  $P^{bl\_MED}$  for the  $s$  and  $t$ -channels is meaningful. We use the discriminant optimized to the  $s$ -channel,  $B - MED_s$ , for events in the  $s$ -like category, while the discriminant optimized to the  $t$ -channel,  $P^{bl\_MED}_t$ , is used for the events in the  $t$ -like category. The bin transformation described in Section 6.3.2 is performed separately in these two categories, and the transformed discriminants are shown in Figure 8.15. Finally, both the categories are used in the cross section extraction.

To extract two cross sections simultaneously, Equation (8.1.3) in Bayesian approach can be redefined as

$$d = a_1\sigma_1 + a_2\sigma_2 + \sum_{i=1}^N b_i, \quad (8.5.1)$$

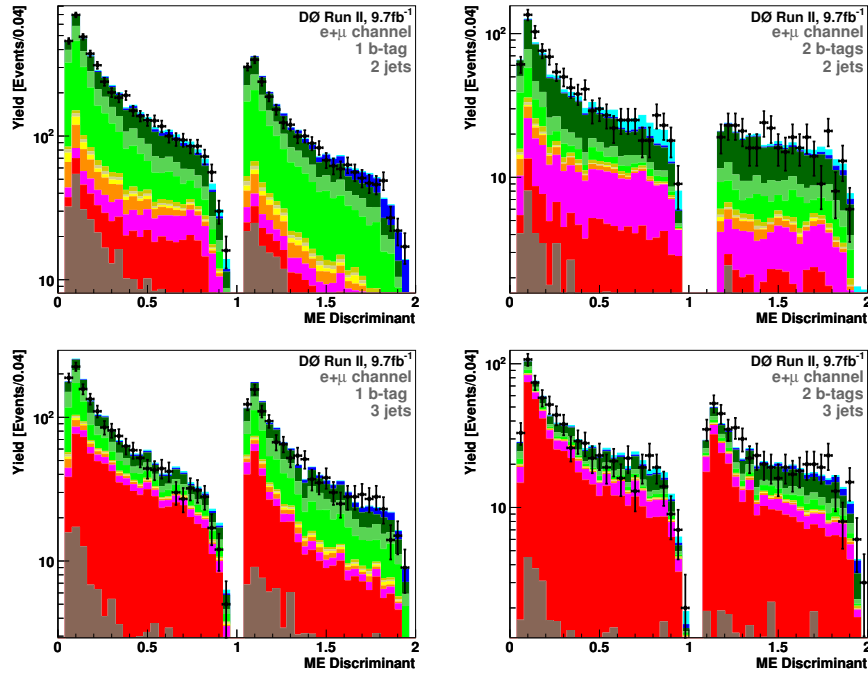


**Figure 8.15** The data-MC comparisons of the mixed discriminant with log scale for the Run II electron and muon combined samples. The upper and lower rows show the results of the two-jet and the three-jet events, respectively. The left and right columns show the results of the single-tagged and the double-tagged events. The bins between 0 and 1 show the  $s$ -like category, while the bins between 1 and 2 show the  $t$ -like category. The  $s$  and  $t$ -channel contributions are scaled to the measured results.

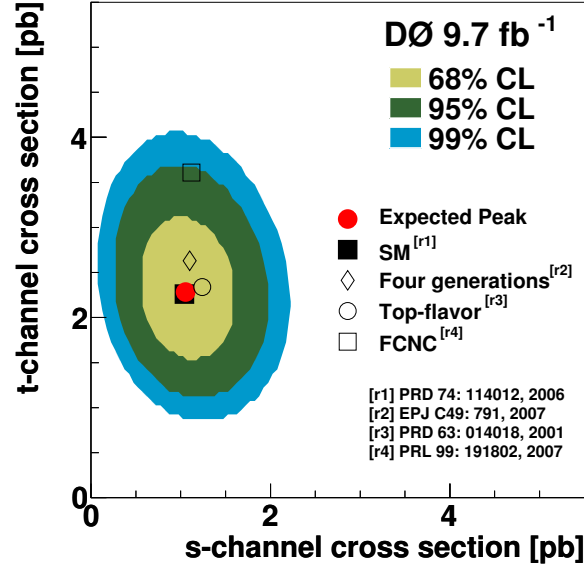
where  $a_1$  and  $a_2$  are the effective luminosities for the two signals, respectively. We assume both the prior p.d.f. for the two signal cross sections to be uniform, and establish a two-dimensional (2D) posterior p.d.f. based on this mixed discriminant. Contours of equal probabilities for given confidence levels (CL) are shown in Figures 8.16(a) and 8.17(a). To take into account the uncertainty on the individual cross sections, we derive the one-dimensional (1D) posterior p.d.f. by integrating the 2D posterior p.d.f. over the other signal, and the 1D posterior p.d.f. shown in Figures 8.16(b), 8.16(c), 8.17(b) and 8.17(c) can be analyzed as described in Section 8.1.

## 8.6 Significance of Measurement

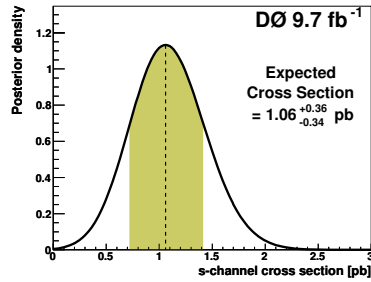
In addition to the cross section measurement, we assess the validity of the measurement concerning the data's underlying distribution. The “significance test” gives the probability to obtain a level of incompatibility with a certain hypothesis that is greater than or equal to the level observed with the actual data. For our purpose of measuring a new signal process, we define a null hypothesis,  $H_0$ , as describing only known processes, namely the backgrounds, and a statistic  $q$  as a function of the data which reflects the level of agreement between the data and the hypothesis. The statistical significance is quantified by a  $p$ -value, which in our case represents how likely the data could statistically fluctuate up to be equal to or greater than the measured value, assuming the signal process is absent.

In the observation analysis [56], we used an ensemble of background-only pseudo-data sets, and the significance of the cross section measurement was determined by how often the measured cross section in the ensemble is equal to or greater than the observed one. That calculation is heavily time-consuming, for a huge amount of the pseudo-data sets are required (e.g. 70 M pseudo-data sets for the observation analysis). To reduce the computing time, an asymptotic log-likelihood ratio (LLR) approach [152] is adopted and used in the previous  $D\bar{O}$  measurements of  $t$ -channel cross section [153], the CMS and ATLAS Higgs searches [154, 155], and this analysis.

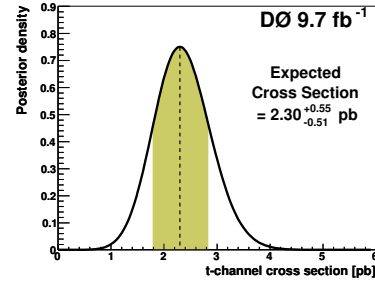
Denoting the strength parameter as  $\mu$  and the signal cross section predicted in the SM as  $\sigma_0$ , the hypothesized cross section,  $\sigma$ , can be represented as  $\sigma = \mu\sigma_0$ .



(a)

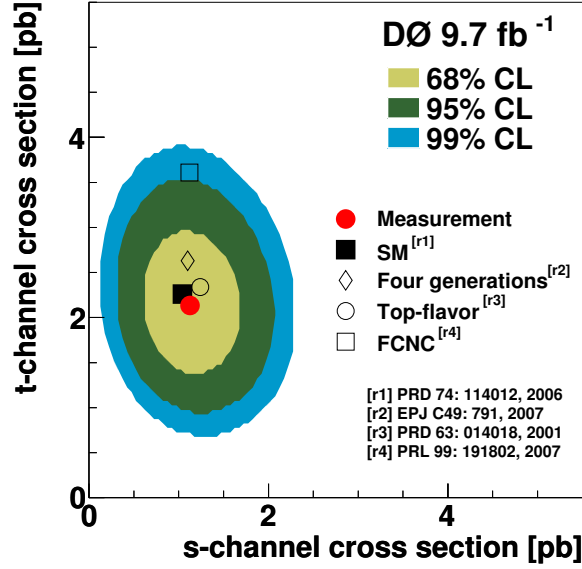


(b)

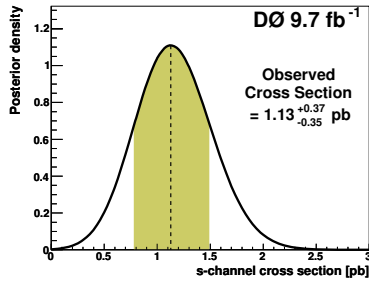


(c)

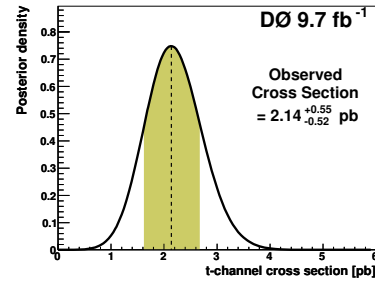
**Figure 8.16** Expected results for model-independent measurements on the  $s$  and  $t$ -channel cross sections: (a) 2D posterior p.d.f., shown along with the 1, 2 and 3 SD contours of probability, (b) 1D posterior p.d.f. for the  $s$ -channel, and (c) 1D posterior p.d.f. for the  $t$ -channel.



(a)



(b)



(c)

**Figure 8.17** Observed results for model-independent measurements on the  $s$  and  $t$ -channel cross sections: (a) 2D posterior p.d.f., shown along with the 1, 2 and 3 SD contours of probability, (b) 1D posterior p.d.f. for the  $s$ -channel, and (c) 1D posterior p.d.f. for the  $t$ -channel.

We use the profile likelihood ratio to test a hypothesized value of  $\mu$ :

$$\lambda(\mu) = \frac{L(\mu, \hat{\boldsymbol{\theta}})}{L(\hat{\mu}, \hat{\boldsymbol{\theta}})} \quad (8.6.1)$$

where  $L$  is the likelihood function,  $\boldsymbol{\theta}$  the parameters that characterize the likelihood (e.g.  $a$  and  $b_i$  in Equation (8.1.3)),  $\hat{\boldsymbol{\theta}}$  the value of  $\boldsymbol{\theta}$  that maximizes  $L$  for the specified  $\mu$  (the conditional maximum-likelihood estimator of  $\boldsymbol{\theta}$ ), and the denominator is the maximized (unconditional) likelihood function. Since  $0 \leq \lambda \leq 1$ , with  $\lambda$  near 1 implying good agreement between the data and the hypothesized value of  $\mu$ , usually it is convenient to use the statistic

$$q(\mu) = -2 \ln \lambda(\mu) \quad (8.6.2)$$

as the basis of a statistical test.

Suppose that the data are distributed according to a strength parameter  $\mu'$ , and  $\hat{\mu}$  follows a Gaussian distribution with a mean  $\mu'$  and a standard deviation  $\sigma_{\hat{\mu}}$ , Wald [156] showed that for the case of a single parameter of interest ( $\mu$ ),  $q(\mu)$  can be written as

$$q(\mu) = -2 \ln \lambda(\mu) = \frac{(\mu - \hat{\mu})^2}{\sigma_{\hat{\mu}}^2} + \mathcal{O}\left(\frac{1}{\sqrt{N}}\right) \quad (8.6.3)$$

where  $N$  represents the data sample size.

A standard method to find the variance  $\sigma_{\hat{\mu}}$  is to estimate the matrix of second derivatives of the log-likelihood function [1]. However, an alternative method is exploited here, as discussed below. We define an artificial data set  $A$  such that when it is used to evaluate the estimators for all parameters, the true parameter values are obtained. The data set  $A$  corresponding to a strength  $\mu'$  gives  $\hat{\mu} = \mu'$ , and therefore Wald's approximation Equation (8.6.3) can be written as

$$q_A(\mu) = -2 \ln \lambda_A(\mu) \simeq \frac{(\mu - \mu')^2}{\sigma_{\hat{\mu}}^2}. \quad (8.6.4)$$

Equivalently, the variance  $\sigma_{\hat{\mu}}^2$  which characterizes the distribution of  $\hat{\mu}$  is

$$\sigma_{\hat{\mu}, A}^2 = \frac{(\mu - \mu')^2}{q_A(\mu)}. \quad (8.6.5)$$

This method is found to provide similar results of the variance to the standard one [152]. Moreover, under the assumption of Wald's approximation, the test statistic  $q(\mu)$  is monotonically related to  $\hat{\mu}$ , and its median value can be found directly by using the median of  $\hat{\mu}$ , i.e.  $\mu'$ . In other words, the value of the variance is independent of the choice of the strength value  $\mu$  for evaluating  $q(\mu)$ .

As many of the Tevatron analyses, we calculate the significance based on the test statistic

$$Q = -2 \ln \frac{L_{s+b}}{L_b} \quad (8.6.6)$$

where  $L_{s+b}$  is the likelihood of the nominal signal model and  $L_b$  is that of the background-only hypothesis. Namely, the  $s+b$  corresponds to having the strength parameter  $\mu = 1$  and  $L_b$  refers to  $\mu = 0$ . The statistic  $Q$  can therefore be written as

$$Q = -2 \ln \frac{L(\mu = 1, \hat{\boldsymbol{\theta}}(1))}{L(\mu = 0, \hat{\boldsymbol{\theta}}(0))} = -2 \ln \lambda(1) + 2 \ln \lambda(0). \quad (8.6.7)$$

Assuming Wald's approximation is valid,  $Q$  can be written as

$$Q = \frac{(\hat{\mu} - 1)^2}{\sigma_{\hat{\mu}}^2} - \frac{\hat{\mu}^2}{\sigma_{\hat{\mu}}^2} = \frac{1 - 2\hat{\mu}}{\sigma_{\hat{\mu}}^2}. \quad (8.6.8)$$

Since  $\hat{\mu}$  follows a Gaussian distribution, the distribution of  $Q$  is also a Gaussian, which has a mean value of

$$E[Q] = \frac{1 - 2\mu'}{\sigma_{\hat{\mu}}^2} \quad (8.6.9)$$

and a variance of

$$V[Q] = \frac{4}{\sigma_{\hat{\mu}}^2}. \quad (8.6.10)$$

The standard deviation of  $\hat{\mu}$ ,  $\sigma_{\hat{\mu}}$ , can be estimated from Equation (8.6.5).

The  $p$ -value is quantified as the probability under the ensemble of the background-only pseudo-data sets ( $\mu' = 0$ ) that the value of  $Q$  is smaller than or equal to the observed result  $Q_{obs}$ :

$$p \text{ value} = \int_{-\infty}^{Q_{obs}} f(Q|b) dQ = \Phi \left( \frac{Q_{obs} - 1/\sigma_{\hat{\mu},b}^2}{2/\sigma_{\hat{\mu},b}^2} \right) \quad (8.6.11)$$

where  $f(Q|b)$  denotes the p.d.f. of  $Q$  under the  $b$  pseudo-data sets. The  $\sigma_{\hat{\mu},b}$  can be calculated from Equation (8.6.5) with  $\mu' = 0$  (background-only) and the

“expected” strength  $\mu_{exp} = \sigma_{exp}/\sigma_0$ , where  $\sigma_{exp}$  is estimated using the nominal Monte Carlo samples:

$$\sigma_{\hat{\mu},b}^2 = \frac{\mu_{exp}^2}{q_b(\mu_{exp})}. \quad (8.6.12)$$

In our case of a constant prior, the Bayesian posterior is proportional to the likelihood, as mentioned in Section 8.1. Therefore, the value of  $q_b(\mu_{exp})$  can be computed using the posterior p.d.f. in the background-only pseudo-data:

$$q_b(\mu_{exp}) = -2 \ln \frac{L(\mu_{exp}, \hat{\boldsymbol{\theta}})}{L(\hat{\mu}, \hat{\boldsymbol{\theta}})} = 2 \ln \frac{p(\hat{\sigma}|\mathbf{D})}{p(\sigma_{exp}|\mathbf{D})} \quad (8.6.13)$$

where  $p$  is the posterior p.d.f. and  $\hat{\sigma}$  is the mode of  $p$ .

Similarly, the ensemble of the background plus signal pseudo-data sets ( $\mu' = 1$ ) can be described by the corresponding p.d.f. of  $Q$ ,  $f(Q|s+b)$ , with the mean and the variance also from Equations (8.6.9) and (8.6.10), respectively. The expected  $p$ -value is estimated by replacing  $Q_{obs}$  in Equation (8.6.11) with the mean value of the distribution  $f(Q|s+b)$ . From Equation (8.6.9), this mean value is  $-1/\sigma_{\hat{\mu}}^2$ , and  $\sigma_{\hat{\mu}}^2$  can be evaluated using Equation (8.6.5) with  $\mu = 0$ :

$$\sigma_{\hat{\mu},s+b}^2 = \frac{1}{q_{s+b}(0)}. \quad (8.6.14)$$

Furthermore, the value of  $q_{s+b}(0)$  can be evaluated from the Bayes ratio, where the Bayes ratio is defined as

$$B_r = \frac{p(\hat{\sigma}|\mathbf{D})}{p(\sigma = 0|\mathbf{D})} \quad (8.6.15)$$

and  $q_{s+b}(0)$  can be obtained:

$$q_{s+b}(0) = -2 \ln \frac{L(0, \hat{\boldsymbol{\theta}})}{L(\hat{\mu}, \hat{\boldsymbol{\theta}})} = 2 \ln \frac{p(\hat{\sigma}|\mathbf{D})}{p(\sigma = 0|\mathbf{D})} = 2 \ln B_r. \quad (8.6.16)$$

Finally, the  $p$ -value is converted into an equivalent significance  $Z$ , defined such that a  $Z$  standard deviation upward fluctuation of a Gaussian random variable would have an upper tail area equal to the  $p$ -value:

$$Z = \Phi^{-1}(1 - p). \quad (8.6.17)$$

Here  $\Phi$  is the cumulative distribution of the Standard Gaussian.

In the measurement with two signals, significance is calculated individually. The likelihood of the background-only hypothesis relative to the first signal,  $\mu_1$ , is the expected likelihood in an ensemble with the second signal and background, where the strength of the second signal,  $\mu_2$ , is equal to unity. This can be obtained by integrating over the strength of the second signal,  $\mu_2$ ,

$$L_{s_2+b}(\mu_1) = \int L_{s_2+b}(\mu_1, \mu_2) \pi(\mu_2) d\mu_2, \quad (8.6.18)$$

where  $\pi(\mu_2)$  is assumed to be uniform. The significance for the first signal can be calculated from this likelihood, and vice versa.

Table 8.1 lists the expected and observed  $p$ -values and significances for the  $s$  and  $t$ -channel measurements, and Figures 8.18 and 8.19 show the  $s$  and  $t$ -channel significances, where the green and purple lines represent the log-likelihood ratio distributions of the background-only ( $f(Q|b)$ ) and nominal signal ( $f(Q|s+b)$ ) models, respectively. The significance of the model-independent measurements is shown in Table 8.2 and figs. 8.20 and 8.21.

Channel	$p\text{-value}_{exp}$	$p\text{-value}_{obs}$	$Z_{exp}$	$Z_{obs}$
$s$ -channel	$5.51 \times 10^{-4}$	$1.42 \times 10^{-4}$	3.26	3.63
$t$ -channel	$5.76 \times 10^{-7}$	$6.49 \times 10^{-6}$	4.86	4.36

**Table 8.1** The expected and observed significance computed using the asymptotic log-likelihood ratio approach. The  $t$ -channel is assumed to have the cross section predicted in the SM when measuring the  $s$ -channel cross section, and vice versa. Here  $Z$  is defined such that a  $Z$  standard deviation upward fluctuation of a Gaussian random variable would have an upper tail area equal to the  $p$ -value.

Channel	$p\text{-value}_{exp}$	$p\text{-value}_{obs}$	$Z_{exp}$	$Z_{obs}$
$s$ -channel	$8.05 \times 10^{-4}$	$4.02 \times 10^{-4}$	3.15	3.35
$t$ -channel	$4.51 \times 10^{-7}$	$3.06 \times 10^{-6}$	4.91	4.52

**Table 8.2** The expected and observed significance of the model-independent measurements. Here  $Z$  is defined such that a  $Z$  standard deviation upward fluctuation of a Gaussian random variable would have an upper tail area equal to the  $p$ -value.

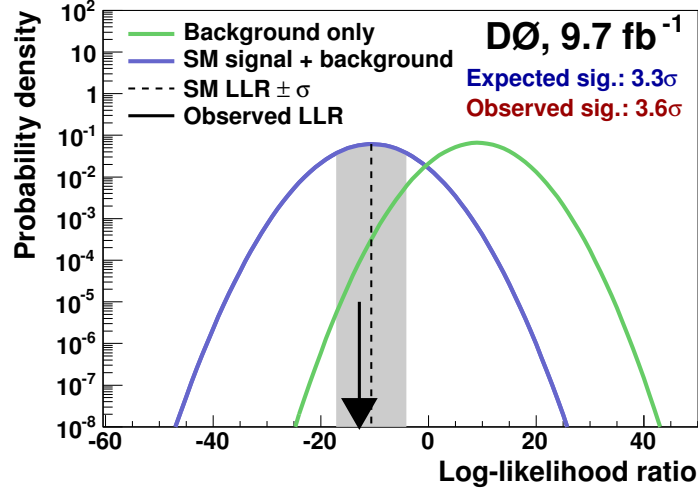


**Figure 8.18** Significance of  $s$ -channel cross section measurement. The  $t$ -channel is assumed to have the cross section predicted in the SM.

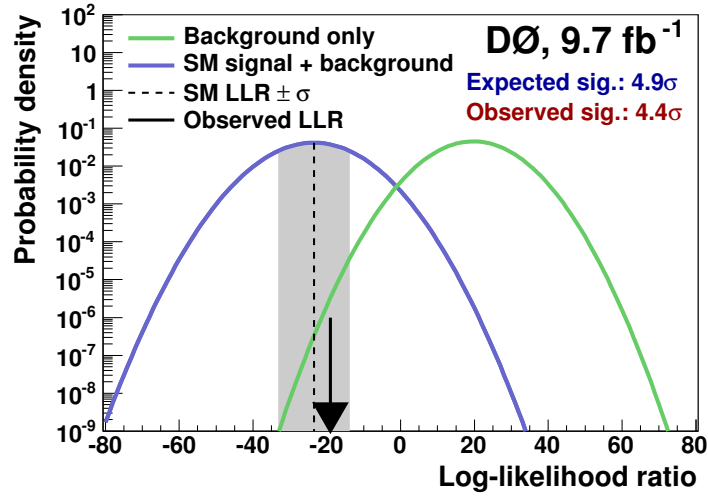


**Figure 8.19** Significance of  $t$ -channel cross section measurement. The  $s$ -channel is assumed to have the cross section predicted in the SM.

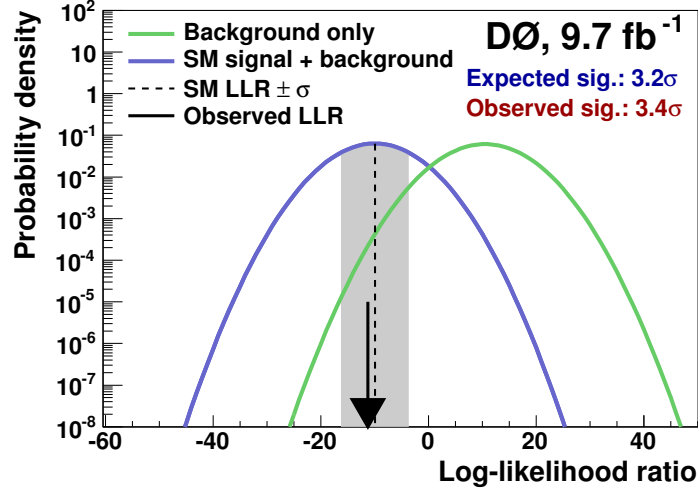


**Figure 8.20** Significance of the model-independent  $s$ -channel cross section measurement.

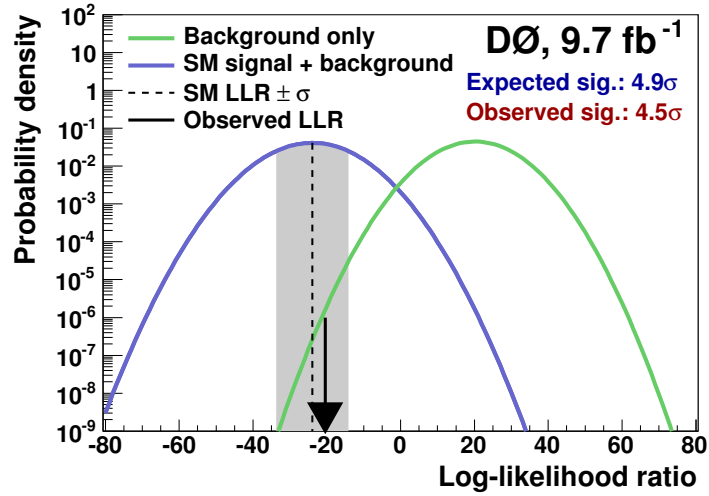


**Figure 8.21** Significance of the model-independent  $t$ -channel cross section measurement.

## 9 Conclusions and Outlook

This dissertation presents a model-independent measurement of the  $s$  and  $t$ -channel single top-quark production cross sections based on the full Tevatron Run II data collected with the DØ detector, corresponding to  $9.7 \text{ fb}^{-1}$  of integrated luminosity. We select events with an isolated electron or muon, a large apparent imbalance in transverse momentum, two or three jets, among which one or two are identified as candidates for originating from the fragmentation of  $b$  quarks. An improved Matrix-Element method is used to distinguish signal-like events from the background, and a Bayesian approach is utilized to extract the cross section, taking into account all the statistical and systematic uncertainties as well as their correlations. We performed a two-dimensional measurement, extracting the  $s$  and  $t$ -channel cross sections simultaneously. This provided a way to measure both modes without assuming the SM prediction for either. The final results are determined to be

$$\begin{aligned}\sigma(p\bar{p} \rightarrow tb + X) &= 1.13 \pm 0.36 \text{ pb} \\ \sigma(p\bar{p} \rightarrow tqb + X) &= 2.14 \pm 0.54 \text{ pb},\end{aligned}$$

corresponding to significance relative to upward fluctuations of the background of 3.4 and 4.5 SD, respectively. These results are in agreement with the SM predictions of  $1.04 \pm 0.08 \text{ pb}$  for the  $s$ -channel and  $2.26 \pm 0.12 \text{ pb}$  for the  $t$ -channel.

As Tevatron operations were terminated on September 30th, 2011, these results comprise part of legacy of the measurements at the proton-antiproton collider at a center-of-mass of 1.96 TeV. Our analysis provided first evidence for  $s$ -channel production of single top quarks.

DØ plans to define discriminants based on the Boosted Decision Trees and Bayesian Neural Network discriminants, with the goal of combining the three

measurements to extract a final result. Since the ME method is intrinsically different from both BDT and BNN, it provides complementary information and improves the sensitivity of the combined result. Figure 9.1 illustrates a correlation study among these three methods. The ME method is  $\approx 65\%$  correlated with the BDT or BNN analysis, while the correlation between the BDT and BNN is 75% [16].

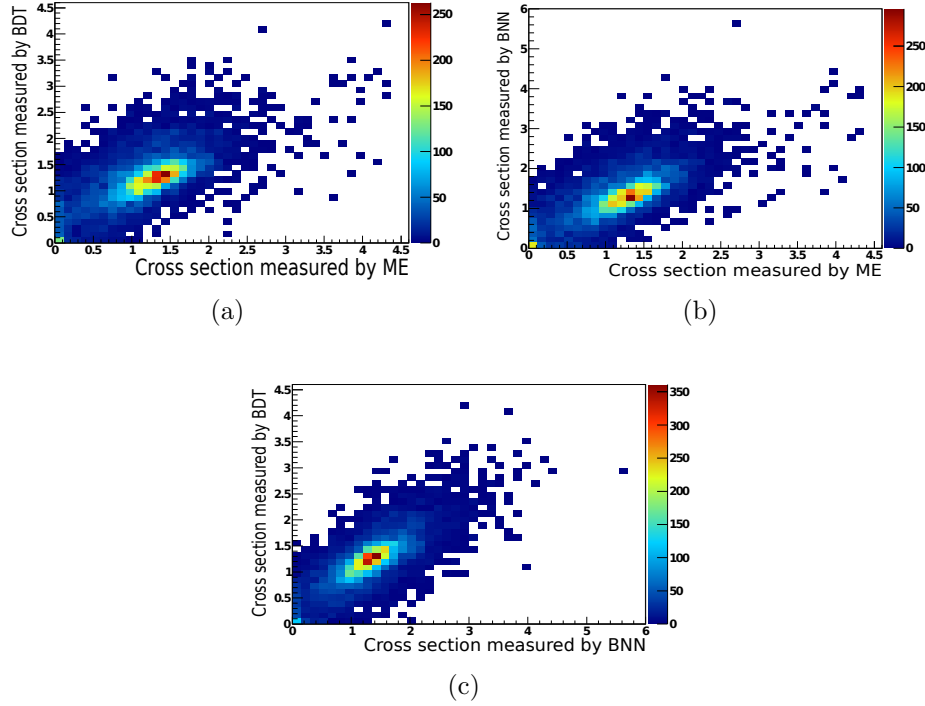


**Figure 9.1** Correlation expected for cross sections based on MC studies of pairs of discriminants: (a) BDT vs ME, (b) BNN vs ME, and (c) BDT vs BNN [16].

In addition, DØ will extract the CKM matrix element  $|V_{tb}|$  directly from these data. Since the cross section for single top-quark production is proportional to  $|V_{tb}|^2$ , the value of  $|V_{tb}|$  can be obtained without imposing assumptions on the number of quark generations or on the unitarity of the CKM matrix. In addition, separate results for  $|V_{tb}|$  from the  $s$  and  $t$ -channels will provide an opportunity to examine the dynamic structure of the  $Wtb$  coupling.

The measurements of single top-quark production cross sections at the Tevatron are in agreement with the SM. Moreover, the searches for physics beyond the SM, such as for new heavy bosons [68, 69, 70, 71], anomalous couplings [72, 73, 74],

and flavor-changing neutral currents [75, 76, 77], have yielded negative results. However, new phenomena may manifest themselves at a higher energy. The LHC, with a planned center-of-mass energy of 14 TeV, may be the place where new phenomena are discovered.

Thus far, both ATLAS and CMS have observed  $t$ -channel single top-quark production, and have an evidence for associated  $tW$  production at a center-of-mass of 7 TeV. As the production cross sections of these two channels are much larger at the LHC, precision measurements and differential studies can be performed. For example, the CKM matrix element  $|V_{tb}|$  can be further constrained [52, 54], and provide thereby a better understanding of the electroweak interaction. Since top quarks and antitop quarks have different cross sections at the LHC, that depend on different configurations of initial-state partons, the ratio of the two  $t$ -channel production cross sections can be used to examine parton density functions [157, 158]. Moreover, any new particles that couple to top quarks, such as  $W'$  and  $b'$  quark, excluded the energy range of the Tevatron, can be sought through the  $s$ -channel single top-quark production at the LHC [159]. The latest results show limits already have stronger than obtained at the Tevatron.

The ME method is currently used at the Tevatron in measurements of the top-quark mass, spin correlations in  $t\bar{t}$  production, and the  $W$  helicity in top-quark decays, in addition to measuring the single top-quark cross section, as done in our analysis. It can also be employed in other searches for small signals with large backgrounds, such as in Higgs-boson searches.

As the heaviest known elementary particle, the top quark is important to search for new physics, and to improving our understanding of the Standard Model, including electroweak symmetry breaking and the Higgs-like particle that was discovered in 2012 at the LHC. A top-quark factory such as the LHC, or the proposed International Linear Collider (ILC) provides opportunities to study the top quark, and the methods developed in this dissertation are therefore bound to such future analyses.

## Bibliography

- [1] Beringer, J. et al., “2012 Review of Particle Physics,” *Phys. Rev. D*, Vol. 86, No. 010001, 2012.
- [2] Heinson, A., “Feynman Diagrams for talks,” [http://www-d0.fnal.gov/Run2Physics/top/top\\_public\\_web\\_pages/top\\_feynman\\_diagrams.html](http://www-d0.fnal.gov/Run2Physics/top/top_public_web_pages/top_feynman_diagrams.html).
- [3] Abazov, V. M. et al., “Model-independent measurement of  $t$ -channel single top quark production in  $p\bar{p}$  collisions at  $\sqrt{s}=1.96$  TeV,” *Physics Letters B*, Vol. 705, No. 4, 11 2011, pp. 313–319.
- [4] Heinson, A. P., “Observation of Single Top Quark Production at the Tevatron Collider,” *Modern Physics Letters A*, 2010, pp. 30.
- [5] Schwanenberger, C., “Top group analyses and plans,” [http://www-clued0.fnal.gov/~schwanen/d0\\_private/html/top\\_plenary.pdf](http://www-clued0.fnal.gov/~schwanen/d0_private/html/top_plenary.pdf).
- [6] “Fermilab Tevatron website,” <http://www.fnal.gov/pub/science/accelerator/>.
- [7] “DØ Gallery,” <http://www-d0.fnal.gov/Run2Physics/displays/presentations/#gallery>.
- [8] Abazov, V. M. *et al.*, “The upgraded DØ detector,” *Nuclear Instruments and Methods in Physics Research Section A: Accelerators, Spectrometers, Detectors and Associated Equipment*, Vol. 565, No. 2, 9 2006/9/15, pp. 463–537.
- [9] “DØ Event Gallery,” <http://www-d0.fnal.gov/Run2Physics/WWW/events.htm>.

- [10] “DØ Live Event,” [http://d0.phys.washington.edu/Projects/live\\_event/](http://d0.phys.washington.edu/Projects/live_event/).
- [11] Petrillo, G., “A private communication with the JES convener,” 2011.
- [12] Bandurin, D. et al., “Jet Energy Scale Determination for D0 Run IIb,” *DØ note 6327*, 2012.
- [13] “*b*-tagging Graphic,” [http://www-d0.fnal.gov/Run2Physics/top/singletop\\_observation/](http://www-d0.fnal.gov/Run2Physics/top/singletop_observation/).
- [14] Abazov, V. M. and others (DØ Collaboration), “*b*-Jet identification in the D0 experiment,” *Nuclear Instruments and Methods in Physics Research Section A: Accelerators, Spectrometers, Detectors and Associated Equipment*, Vol. 620, No. 2-3, 2010/8/21/ 2010, pp. 490–517.
- [15] Meister, D., “The lepton+jets Selection and Determination of the Lepton Fake Rate with the Full RunIIb Data Set,” *DØ thesis*, 2012.
- [16] Bala, S. et al., “Measurement of the Single Top Production Cross Section in  $9.7 \text{ fb}^{-1}$  of Data,” *DØ note 6375*, 2012.
- [17] Halzen, F. and Martin, A. D., *Quarks and Leptons*, Wiley, 1984.
- [18] Fukuda, Y. et al., “Measurements of the Solar Neutrino Flux from Super-Kamiokande’s First 300 Days,” *Physical Review Letters*, Vol. 81, No. 6, 08 1998, pp. 1158–1162.
- [19] Aharmim, B., et al., “Electron energy spectra, fluxes, and day-night asymmetries of  $^8\text{B}$  solar neutrinos from measurements with NaCl dissolved in the heavy-water detector at the Sudbury Neutrino Observatory,” *Physical Review C*, Vol. 72, No. 5, 11 2005, pp. 055502.
- [20] Englert, F. and Brout, R., “Broken Symmetry and the Mass of Gauge Vector Mesons,” *Physical Review Letters*, Vol. 13, No. 9, 08 1964, pp. 321–323.
- [21] Higgs, P. W., “Broken Symmetries and the Masses of Gauge Bosons,” *Physical Review Letters*, Vol. 13, No. 16, 10 1964, pp. 508–509.

- [22] Guralnik, G. S., Hagen, C. R., and Kibble, T. W. B., “Global Conservation Laws and Massless Particles,” *Physical Review Letters*, Vol. 13, No. 20, 11 1964, pp. 585–587.
- [23] Kobayashi, M. and Maskawa, T., “ $CP$ -Violation in the Renormalizable Theory of Weak Interaction,” *Progress of Theoretical Physics*, Vol. 49, No. 2, 1973, pp. 652–657.
- [24] Christenson, J. H., Cronin, J. W., Fitch, V. L., and Turlay, R., “Evidence for the  $2\pi$  Decay of the  $K_2^0$  Meson,” *Physical Review Letters*, Vol. 13, No. 4, 07 1964, pp. 138–140.
- [25] Bennett, C. L. et al., “Nine-Year Wilkinson Microwave Anisotropy Probe (WMAP) Observations: Final Maps and Results Nine-Year Wilkinson Microwave Anisotropy Probe (WMAP) Observations: Final Maps and Results Nine-Year Wilkinson Microwave Anisotropy Probe (WMAP) Observations: Final Maps and Results Nine-Year Wilkinson Microwave Anisotropy Probe (WMAP) Observations: Final Maps and Results,” *arXiv:1212.5225*, 2013.
- [26] Abe, F. et al., “Observation of Top Quark Production in  $p\bar{p}$  Collisions with the Collider Detector at Fermilab,” *Physical Review Letters*, Vol. 74, No. 14, 04 1995, pp. 2626–2631.
- [27] Abachi, S. et al., “Search for High Mass Top Quark Production in  $p\bar{p}$  Collisions at  $\sqrt{s} = 1.8$  TeV,” *Physical Review Letters*, Vol. 74, No. 13, 03 1995, pp. 2422–2426.
- [28] Bigi, I., Dokshitzer, Y., Khoze, V., Kühn, J., and Zerwas, P., “Production and decay properties of ultra-heavy quarks,” *Physics Letters B*, Vol. 181, No. 1–2, 11 1986, pp. 157–163.
- [29] Moch, S. and Uwer, P., “Theoretical status and prospects for top-quark pair production at hadron colliders,” *Physical Review D*, Vol. 78, No. 3, 08 2008, pp. 034003.
- [30] Kidonakis, N. and Vogt, R., “Theoretical top quark cross section at the Fermilab Tevatron and the CERN LHC,” *Physical Review D*, Vol. 78, No. 7, 10 2008, pp. 074005.

- [31] Nadolsky, P. M. et al., “Implications of CTEQ global analysis for collider observables,” *Physical Review D*, Vol. 78, No. 1, 07 2008, pp. 013004.
- [32] Cacciari, M., Frixione, S., Mangano, M. L., Nason, P., and Ridolfi, G., “Updated predictions for the total production cross sections of top and of heavier quark pairs at the Tevatron and at the LHC,” *Journal of High Energy Physics*, Vol. 2008, No. 09, 2008, pp. 127.
- [33] Group, T. T. E. W., “Combination of the  $t\bar{t}$  production cross section measurements from the Tevatron Collider,” *DØ note 6363*, 2012.
- [34] ATLAS and CMS, “Combination of ATLAS and CMS top-quark pair cross-section measurements using proton-proton collisions at  $\sqrt{s} = 7$  TeV,” *CMS and ATLAS Note*, 2012.
- [35] Aliev, M. et al., “HATHOR –HADronic Top and Heavy quarks crOss section calculatoR,” *Computer Physics Communications*, Vol. 182, No. 4, 4 2011, pp. 1034–1046.
- [36] Cortese, S. and Petronzio, R., “The single top production channel at Tevatron energies,” *Physics Letters B*, Vol. 253, No. 3–4, 1 1991, pp. 494–498.
- [37] Stelzer, T. and Willenbrock, S., “Single-top-quark production via  $q\bar{q} \rightarrow t\bar{b}$ ,” *Physics Letters B*, Vol. 357, No. 1–2, 8 1995, pp. 125–130.
- [38] Smith, M. C. and Willenbrock, S. S., “QCD and Yukawa corrections to single-top-quark production via  $q\bar{q} \rightarrow t\bar{b}$ ,” *Physical Review D*, Vol. 54, No. 11, 12 1996, pp. 6696–6702.
- [39] Mrenna, S. and Yuan, C. P., “Effects of QCD resummation on  $W^+h$  and  $t\bar{b}$  production at the Tevatron,” *Physics Letters B*, Vol. 416, No. 1–2, 1 1998, pp. 200–207.
- [40] Heinson, A. P., Belyaev, A. S., and Boos, E. E., “Single top quarks at the Fermilab Tevatron,” *Physical Review D*, Vol. 56, No. 5, 09 1997/09/01/.
- [41] Kidonakis, N., “Single top quark production at the Fermilab Tevatron: Threshold resummation and finite-order soft gluon corrections,” *Physical Review D*, Vol. 74, No. 11, 12 2006, pp. 114012.

- [42] Kidonakis, N., “Single top and top pair production,” *arXiv:1212.2844*, 2012.
- [43] Sullivan, Z., “Understanding single-top-quark production and jets at hadron colliders,” *Physical Review D*, Vol. 70, No. 11, 12 2004.
- [44] Willenbrock, S. S. D. and Dicus, D. A., “Production of heavy quarks from  $W$ -gluon fusion,” *Physical Review D*, Vol. 34, No. 1, 07 1986.
- [45] Yuan, C. P., “New method to detect a heavy top quark at the Fermilab Tevatron,” *Physical Review D*, Vol. 41, No. 1, 01 1990, pp. 42–51.
- [46] Ellis, R. K. and Parke, S., “Top-quark production by  $W$ -gluon fusion,” *Physical Review D*, Vol. 46, No. 9, 11 1992, pp. 3785–3788.
- [47] Stelzer, T., Sullivan, Z., and Willenbrock, S., “Single-top-quark production via  $W$ -gluon fusion at next-to-leading order,” *Physical Review D*, Vol. 56, No. 9, 11 1997.
- [48] Kidonakis, N., “Next-to-next-to-leading-order collinear and soft gluon corrections for  $t$ -channel single top quark production,” *Physical Review D*, Vol. 83, No. 9, 05 2011, pp. 091503.
- [49] E. E. Boos, V. E. Bunichev, L. V. D. V. I. S. and Sherstnev, V. V., “Method for Simulating Electroweak Top-Quark Production Events in the NLO Approximation: SingleTop Event Generator,” *Physics of Atomic Nuclei*, Vol. 69, No. 8, 2006, pp. 1352–1365.
- [50] Kidonakis, N., “Two-loop soft anomalous dimensions for single top quark associated production with a  $W^-$  or  $H^-$ ,” *Physical Review D*, Vol. 82, No. 5, 09 2010, pp. 054018.
- [51] CDF, “Measurement of Single Top Quark Production in  $7.5 \text{ fb}^{-1}$  of CDF Data Using Neural Networks,” *CDF conference note*, 2012.
- [52] Aad, G. et al., “Measurement of the  $t$ -channel single top-quark production cross section in pp collisions at  $\sqrt{s} = 7 \text{ TeV}$  with the ATLAS detector,” *Physics Letters B*, Vol. 717, No. 4–5, 10 2012, pp. 330–350.
- [53] Aad, G. et al., “Evidence for the associated production of a  $W$  boson and a top quark in ATLAS at  $\sqrt{s} = 7 \text{ TeV}$ ,” *Physics Letters B*, Vol. 716, No. 1, 9 2012, pp. 142–159.

- [54] CMS, “Measurement of the single-top-quark  $t$ -channel cross section in pp collisions at  $\sqrt{s} = 7$  TeV,” *arXiv:1209.4533*, 2012.
- [55] CMS, “Evidence for associated production of a single top quark and W boson in pp collisions at  $\sqrt{s} = 7$  TeV,” *arXiv:1209.3489*, 2012.
- [56] Abazov, V. M. et al., “Observation of Single Top-Quark Production,” *Physical Review Letters*, Vol. 103, No. 9, 08 2009, pp. 092001–7.
- [57] Aaltonen, T. et al., “Observation of Electroweak Single Top-Quark Production,” *Physical Review Letters*, Vol. 103, No. 9, 08 2009, pp. 092002.
- [58] Abazov, V. M. et al., “Measurements of single top quark production cross sections and  $|V_{tb}|$  in  $p\bar{p}$  collisions at  $\sqrt{s} = 1.96$  TeV,” *Physical Review D*, Vol. 84, No. 11, 12 2011, pp. 112001.
- [59] Abazov, V. M. et al., “Precision Measurement of the Ratio  $\mathcal{B}(t \rightarrow Wb)/\mathcal{B}(t \rightarrow Wq)$  and Extraction of  $V_{tb}$ ,” *Physical Review Letters*, Vol. 107, No. 12, 09 2011, pp. 121802.
- [60] Aaltonen, T. et al., “Direct Bound on the Total Decay Width of the Top Quark in  $p\bar{p}$  Collisions at  $\sqrt{s} = 1.96$  TeV,” *Physical Review Letters*, Vol. 102, No. 4, 01 2009, pp. 042001.
- [61] Abazov, V. M. et al., “Determination of the Width of the Top Quark,” *Physical Review Letters*, Vol. 106, No. 2, 01 2011, pp. 022001.
- [62] Abazov, V. M. et al., “Improved determination of the width of the top quark,” *Physical Review D*, Vol. 85, No. 9, 05 2012, pp. 091104.
- [63] CDF, “The Measurement of Single-Top Polarization with  $3.2 \text{ fb}^{-1}$ ,” *CDF conference note*, 2009.
- [64] Atwood, D., Bar-Shalom, S., Eilam, G., and Soni, A., “ $CP$  nonconservation in  $p\bar{p} \rightarrow t\bar{b}X$  at the Fermilab Tevatron,” *Physical Review D*, Vol. 54, No. 9, 11 1996, pp. 5412–5416.
- [65] Atwood, D., Bar-Shalom, S., Eilam, G., and Soni, A., “ $CP$  violation in top physics,” *Physics Reports*, Vol. 347, No. 1–2, 6 2001, pp. 1–222.

- [66] Bala, S. et al., “Search for CP Violation in Single Top Quark Production in  $5.4 \text{ fb}^{-1}$  of Data,” *DØ note 6234*, 2012.
- [67] Tait, T. M. P. and Yuan, C. P., “Single top quark production as a window to physics beyond the standard model,” *Physical Review D*, Vol. 63, No. 1, 12 2000.
- [68] Abazov, V. M. et al., “Search for Charged Higgs Bosons Decaying into Top and Bottom Quarks in  $p\bar{p}$  Collisions,” *Physical Review Letters*, Vol. 102, No. 19, 05 2009, pp. 191802.
- [69] Abazov, V. M. et al., “Search for  $W'$  boson production in the  $W' \rightarrow t\bar{b}$  decay channel,” *Physics Letters B*, Vol. 641, No. 6, 10 2006, pp. 423–431.
- [70] Abazov, V. M. et al., “Search for  $W'$  Boson Resonances Decaying to a Top Quark and a Bottom Quark,” *Physical Review Letters*, Vol. 100, No. 21, 05 2008.
- [71] Abazov, V. M. et al., “Search for  $W' \rightarrow t\bar{b}$  resonances with left- and right-handed couplings to fermions,” *Physics Letters B*, Vol. 699, No. 3, 5 2011, pp. 145–150.
- [72] Abazov, V. M. et al., “Search for Anomalous  $Wtb$  Couplings in Single Top Quark Production,” *Physical Review Letters*, Vol. 101, No. 22, 11 2008.
- [73] Aaltonen, T. et al., “Search for the Production of Narrow  $t\bar{b}$  Resonances in  $1.9 \text{ fb}^{-1}$  of  $p\bar{p}$  Collisions at  $\sqrt{s} = 1.96 \text{ TeV}$ ,” *Physical Review Letters*, Vol. 103, No. 4, 07 2009, pp. 041801.
- [74] Abazov, V. M. et al., “Search for anomalous  $Wtb$  couplings in single top quark production in  $p\bar{p}$  collisions at  $\sqrt{s} = 1.96 \text{ TeV}$ ,” *Physics Letters B*, Vol. 708, No. 1–2, 2 2012, pp. 21–26.
- [75] Abazov, V. M. et al., “Search for Production of Single Top Quarks Via  $t\bar{c}g$  and  $t\bar{u}g$  Flavor-Changing-Neutral-Current Couplings,” *Physical Review Letters*, Vol. 99, No. 19, 11 2007, pp. 191802.
- [76] Aaltonen, T. et al., “Search for Top-Quark Production via Flavor-Changing Neutral Currents in W+1 Jet Events at CDF,” *Physical Review Letters*, Vol. 102, No. 15, 04 2009, pp. 151801.

- [77] Abazov, V. M. et al., “Search for flavor changing neutral currents via quark–gluon couplings in single top quark production using  $2.3 \text{ fb}^{-1}$  of  $p\bar{p}$  collisions,” *Physics Letters B*, Vol. 693, No. 2, 9 2010, pp. 81–87.
- [78] Abazov, V. M. et al., “Multivariate searches for single top quark production with the D0 detector,” *Physical Review D (Particles and Fields)*, Vol. 75, No. 9, 05 2007/05/01/, pp. 092007–27.
- [79] Abazov, V. M. et al., “Evidence for production of single top quarks,” *Physical Review D (Particles and Fields)*, Vol. 78, No. 1, 07 2008/07/01/, pp. 012005–47.
- [80] Gattuso, C. et al., “Accelerator Concepts Rookie Book,” Vol. version 3.6, 2010.
- [81] “Tevatron Rookie Book,” Vol. version 2.3, 2009.
- [82] Angstadt, R. et al., “The layer 0 inner silicon detector of the D0 experiment,” *Nuclear Instruments and Methods in Physics Research Section A: Accelerators, Spectrometers, Detectors and Associated Equipment*, Vol. 622, No. 1, 10 2010, pp. 298–310.
- [83] Khanov, A., “HTF: histogramming method for finding tracks. The algorithm description,” *DØ note 3778*, 2000.
- [84] Borissov, G., “Technical Details of AA Tracking,” 2003.
- [85] Greenlee, H., “The D0 Kalman Track Fit,” *DØ note 4303*, 2004.
- [86] Ariel Schwartzman, C. T., “Primary Vertex Reconstruction by Means of Adaptive Vertex Fitting,” *DØ note 4918*, 2005.
- [87] Gregorio Bernardi, E. B. and Vlimant, J.-R., “Improvements from the T42 Algorithm on Calorimeter Objects Reconstruction,” *DØ note 4335*, 2004.
- [88] Kozminski, J. et al., “Electron Likelihood in p14,” *DØ note 4449*, 2004.
- [89] Abdesselam, A., “Comparison of H-Matrices for electron identification in D0 Run II,” *DØ note 3745*, 2000.
- [90] Kumar, A. et al., “Electron Likelihood Study,” *DØ note 4769*, 2005.

- [91] Head, T., “Top quark spin correlations and leptonic forward-backward asymmetries at D0,” *DØ thesis*, 2012.
- [92] Vesterinen, M., “An Improved Energy Calibration and Monte Carlo Oversmearing for Electromagnetic Clusters,” *DØ note 6040*, March 2010.
- [93] Brandt, O. et al., “Muon Identification Certification for the Summer 2009 Extended Dataset (Run IIB-1 and -2),” *DØ note 6025*, 2010.
- [94] M. Arthaud, F. Deliot, B. T. V. S. D. V., “Muon Momentum Oversmearing for p17 Data,” *DØ note 5444*, 2007.
- [95] Blazey, G. C. et al., “Run II Jet Physics: Proceedings of the Run II QCD and Weak Boson Physics Workshop,” *DØ proceeding*, 2000.
- [96] E. Busato, B. A., “Jet Algorithms in D0 RunII Software: Description and User’s Guide,” *DØ note 4457*, 2004.
- [97] Harel, A., “Jet ID optimization,” *DØ note 4919*, 2005.
- [98] Amnon Harel, R. W., “Improved L1 Confirmation,” *DØ note 4932*, 2005.
- [99] “Jet Energy Scale Determination at D0 Run II (final p17 version),” *DØ note 5382*, December 2007.
- [100] Ye, Z. et al., “Correction for the MC-Data Difference in the Jet Response at D0,” *DØ note 6143*, 2011.
- [101] Makovec, N. and Grivaz, J.-F., “Shifting, Smearing and Removing Simulated Jets,” *DØ note 4914*, 2005.
- [102] Ochando, C. and Grivaz, J.-F., “SSR for p17,” *DØ note 5609*, 2008.
- [103] Sebastien Greder, I. R.-B., “B-tagging with combined multivariate techniques,” *DØ note 5936*, 2009.
- [104] Schwartzman, A. and Narain, M., “b-quark jet identification via Secondary Vertex Reconstruction,” *DØ note 4080*, 2003.
- [105] Daniel Bloch, Benoit Clement, D. G. S. G. I. R.-B., “Performance of the JLIP b-tagger in p14,” *DØ note 4348*, 2004.

- [106] R.Demina, A.Khanov, F., “b-tagging with Counting Signed Impact Parameter method,” *DØ note 4049*, 2002.
- [107] Bala, S. et al., “Single Top Quark Production in  $5.4 \text{ fb}^{-1}$  of Data - Signal and Background Modeling and Event Selection,” *DØ note 6099*, 2010.
- [108] Mangano, M. L., Piccinini, F., Polosa, A. D., Moretti, M., and Pittau, R., “ALPGEN, a generator for hard multiparton processes in hadronic collisions,” *Journal of High Energy Physics*, Vol. 2003, No. 07, 2003, pp. 001.
- [109] Sjöstrand, T., Mrenna, S., and Skands, P., “PYTHIA 6.4 physics and manual,” *Journal of High Energy Physics*, Vol. 2006, No. 05, 2006, pp. 026.
- [110] Edward Boos, Lev Dudko, T. O., “Complete Calculations of  $Wb\bar{b}$  and  $Wb\bar{b}$  + jet Production at Tevatron and LHC: Probing Anomalous  $Wtb$  Couplings in Single Top Production,” *Eur.Phys.J.C11*, 1999.
- [111] Rick Field, R. C. G., “Pythia Tune A, Herwig, and Jimmy in Run 2 at CDF,” *hep-ph/0510198*, 2005.
- [112] Albrow, M. et al., “Tevatron-for-LHC Report of the QCD Working Group,” *arXiv:hep-ph/0610012*, 2006.
- [113] “Pythia underlying event tunes in D0,” from the MC generators webpage: [http://www-d0.fnal.gov/computing/MonteCarlo/mc\\_generators/Pythia\\_underlying\\_event\\_tunes\\_011609.txt](http://www-d0.fnal.gov/computing/MonteCarlo/mc_generators/Pythia_underlying_event_tunes_011609.txt).
- [114] Jadach, S., Was, Z., Decker, R., and Kühn, J. H., “The decay library TAUOLA, version 2.4,” *Computer Physics Communications*, Vol. 76, No. 3, 8 1993, pp. 361–380.
- [115] Lange, D. J., “The EvtGen particle decay simulation package,” *Nuclear Instruments and Methods in Physics Research Section A: Accelerators, Spectrometers, Detectors and Associated Equipment*, Vol. 462, No. 1–2, 4 2001, pp. 152–155.
- [116] ed. A. De Roeck and Jung, H., “Matching Parton Showers and Matrix Element,” in *Proceedings of the Workshop on the Implications of HERA for LHC Physics*, 2005, pp. 288.

- [117] Gillberg, D., “Heavy Flavour Removal and Determination of Weighting Factors for ALPGEN W+jet Monte Carlo,” *DØ note 5129*, 2006.
- [118] Brun, R. and Carminati, F., “GEANT - Detector Description and Simulation Tool,” *CERN Program Library Long Writeup, Report No. W5013*, 1993.
- [119] Hamberg, R., van Neerven, W. L., and Matsuura, T., “A complete calculation of the order  $\alpha_s^2$  correction to the Drell-Yan  $K$ -factor,” *Nuclear Physics B*, Vol. 359, No. 2–3, 8 1991, pp. 343–405.
- [120] Hamberg, R., van Neerven, W. L., and Matsuura, T., “Erratum to: “A complete calculation of the order  $\alpha_s^2$  correction to the Drell-Yan  $K$ -factor”: [Nucl. Phys. B 359 (1991) 343],” *Nuclear Physics B*, Vol. 644, No. 1–2, 11 2002, pp. 403–404.
- [121] Fernando Febres Cordero, Laura Reina, D. W., “Associated production of a  $W$  or  $Z$  boson with bottom quarks at the Tevatron and the LHC,” in *the proceedings of “RADCOR 2009 - 9th International Symposium on Radiative Corrections”*, 2009.
- [122] Berger, C. F. et al., “Next-to-leading order QCD predictions for W+3-jet distributions at hadron colliders,” *Physical Review D*, Vol. 80, No. 7, 10 2009, pp. 074036.
- [123] Campbell, J. and Ellis, K., “MCFM - Monte Carlo for Femtobarn processes,” <http://mcfm.fnal.gov/>.
- [124] O. Turkot, A.W. Jung, Z. Y., “Taggability scale factors for single and double top selection,” 2012, <http://www-d0.hef.ru.nl//fullAgenda.php?id=a12814#2012-09-06>.
- [125] Reinhard Schwienhorst, E. P., “Uncertainty Calculation for Combined W+jets and QCD Backgrounds in Analyses with W+jets Signatures,” *DØ note 4597*, 2004.
- [126] Aguilo, E. et al., “Single Top Quark Production in 2.3 fb<sup>-1</sup> of Data — Signal and Background Modeling and Event Selection,” *DØ note 5810*, December 2009.

- [127] Abazov, V. M. et al., “Measurements of inclusive  $W$ +jets production rates as a function of jet transverse momentum in  $p\bar{p}$  collisions at  $\sqrt{s} = 1.96$  TeV,” *Physics Letters B*, Vol. 705, No. 3, 11 2011, pp. 200–207.
- [128] “Talk by Darren Price in Winter Physics workshop on February 4, 2013,” <https://indico.fnal.gov/materialDisplay.py?contribId=38&sessionId=4&materialId=slides&confId=6251>.
- [129] Canelli, F., “Helicity of the  $W$  Boson in Single-Lepton  $t\bar{t}$  Events,” *DØ thesis*, 2003.
- [130] Ye, Z. et al., “Correction for the MC-Data Difference in the Jet Response at DØ for Run IIB,” *DØ note 6144*, 2011.
- [131] Haefner, P. and Fiedler, F., “Muon transfer function parameters for p17 MC,” *DØ note 5214*, 2006.
- [132] Petra Haefner, F. F., “Determination of the Muon Transfer Function for Top Mass Measurements,” *DØ note 4818*, 2005.
- [133] Andeen, T. et al., “Measurement of the  $W$  boson mass using RunIIa data,” *DØ note 5868*, 2011.
- [134] Stark, J., “Understanding and modelling the CAL energy resolution,” *DØ slide on Jan. 13th, 2006*, 2006.
- [135] Maltoni, F. and Stelzer, T., “MadEvent: automatic event generation with MadGraph,” *Journal of High Energy Physics*, Vol. Volume 2003, JHEP02(2003), 2003.
- [136] H. Murayama, I. Watanabe, K. H., “HELAS: HELicity Amplitude Subroutines for Feynman Diagram Evaluations,” *KEK Report*, 2000.
- [137] Pumplin, J., Belyaev, A., Huston, J., Stump, D., and Tung, W.-K., “Parton distributions and the strong coupling: CTEQ6AB PDFs,” *Journal of High Energy Physics*, Vol. 2006, No. 02, 2006, pp. 032.
- [138] “The Les Houches Accord PDF Interface,” <http://lhpdf.hepforge.org>.
- [139] Lepage, G. P. V., “An adaptive multidimensional integration program,” *CLNS-80/447*, 1980.

- [140] “The GNU scientific library,” <http://www.gnu.org/software/gsl/>.
- [141] Neyman, J. and Pearson, E. S., “On the Problem of the Most Efficient Tests of Statistical Hypotheses,” *Phil Trans R Soc A*, Vol. 231, No. 289, 1933.
- [142] Nakamura, K. and Group, P. D., “Review of Particle Physics,” *Journal of Physics G: Nuclear and Particle Physics*, Vol. 37, No. 7A, 2010, pp. 075021.
- [143] Schellman, H., “The longitudinal shape of the luminous region at DØ,” *DØ note 5142*, 2006.
- [144] Schellman, H., “RunIIb longitudinal beam shape,” *DØ note 5540*, 2007.
- [145] Xuebing Bu, Tim Head, K. P. M. T. and Xie, Y., “Electron Identification for Summer 2010,” *DØ note 6116*, 2010.
- [146] Oleg Brandt, David Hedin, S. C., “Certification of muon identification efficiencies and treatment of systematic uncertainties for the Run IIb dataset,” *DØ note 6326*, 2012.
- [147] Déliot, F. et al., “Systematic Uncertainties in Top Quark Measurements,” *DØ note 6024*, Feb 2010.
- [148] Y. Peters, M. Begel, K. H. . D. W., “Reweighting of the fragmentation function for the D0 Monte Carlo,” *DØ note 5325*, 2007.
- [149] Barberis, E. et al., “The Matrix Method and its Error Calculation,” *DØ note 4564*, 2004.
- [150] Harel, A., “An estimate of the data over MC, b over light jet response uncertainty for RunIIa JES,” *DØ note 5654*, 2008.
- [151] Supriya Jain, Harrison Prosper, R. S., “Statistical methods implemented in the package `top_statistics`,” *DØ note 5817*, 2008.
- [152] Glen Cowan, Kyle Cranmer, E. G. O. V., “Asymptotic formulae for likelihood-based tests of new physics,” *Eur.Phys.J.C71*, 2010.
- [153] Bala, S. et al., “Measurement of the Single Top Production Cross Section in  $5.4 \text{ fb}^{-1}$  of Data,” *DØ note 6128*, 2010.

- [154] Aad, G. et al., “Search for the Higgs Boson in the  $H \rightarrow WW^* \rightarrow l^+\nu l^-\bar{\nu}$  Decay Channel in  $pp$  Collisions at  $\sqrt{s}=7$  TeV with the ATLAS Detector,” *Physical Review Letters*, Vol. 108, No. 11, 03 2012, pp. 111802.
- [155] Chatrchyan, S. et al., “Search for the standard model Higgs boson decaying into two photons in  $pp$  collisions at  $\sqrt{s} = 7$  TeV,” *Physics Letters B*, Vol. 710, No. 3, 4 2012, pp. 403–425.
- [156] Wald, A., “Tests of statistical hypotheses concerning several parameters when the number of observations is large,” *Transactions of the American Mathematical Society*, Vol. 54, No. 3, 1943, pp. 426–482.
- [157] Collaboration, A., “Measurement of the  $t$ -channel single top-quark and top-antiquark production cross-sections and their ratio in  $pp$  collisions at  $\sqrt{s} = 7$  TeV,” *ATLAS Conference Note*, 2012.
- [158] CMS, “Measurement of the single-top  $t$ -channel cross section in  $pp$  collisions at centre-of-mass energy of 8 TeV,” *CMS Conference Note*, 2012.
- [159] ATLAS, “Search for single  $b^*$ -quark production with the ATLAS detector at  $\sqrt{s} = 7$  TeV,” *arXiv:1301.1583*, 2013.
- [160] Wigmans, R., *Calorimetry: Energy Measurement in Particle Physics*, Oxford, 2000.
- [161] Abe, F. et al., “Dijet angular distribution in  $p\bar{p}$  collisions at  $\sqrt{s}=1.8$  TeV,” *Physical Review Letters*, Vol. 69, No. 20, 11 1992, pp. 2896–2900.
- [162] Wang, M. et al., “Measurement of the mass difference between top and anti-top quarks in the lepton+jets channel using the matrix element method on  $1 \text{ fb}^{-1}$  of Run IIa data (P17),” *DØ note 5825*, 2008.
- [163] Aguilo, E. et al., “Observation of Single Top Quark Production Using The Matrix Element Analysis Technique in  $2.3 \text{ fb}^{-1}$  of Data,” *DØ note 5813*, Jan 2009.
- [164] Aaltonen, T. et al., “Observation of single top quark production and measurement of  $|V_{tb}|$  with CDF,” *Physical Review D*, Vol. 82, No. 11, 12 2010.

## A Absolute MPF Response Correction

The response correction is numerically the largest correction in the jet energy scale calibration procedure, since it accounts for a number of rather sizable instrumental effects. First, particles produced via the hard scattering interact with the material before the calorimeter and lose a fraction of their energy, which can be rather significant for low momentum particles. Furthermore, charged particles bend in the magnetic field and can possibly never reach the calorimeter (e.g. central tracks with  $p_T < 0.3 \text{ GeV}/c$ ) or deposit their energy in calorimeter cells far away from the jet axis, and thus not be clustered by the jet algorithm. Most particles reaching the calorimeter (except for muons and neutrinos, which constitute a very small fraction of the jet energy) are completely absorbed and their deposited energy is transformed into a visible signal. The DØ calorimeter is non-compensating, implying it has a higher and more linear response to electromagnetic particles ( $e^\pm, \gamma$ ) than to hadrons ( $e/h > 1$ ). The energy dependence of the calorimeter response to hadrons is nearly logarithmic with respect to the incident hadron energy (because the fraction of  $\pi^0$  is slowly increasing as a function of the incident hadron energy), in combination with the non-compensating nature of the calorimeter [160]. The zero bias (the contribution from noises and pile-ups) suppression can also significantly contribute to the non-linearity of the response to hadrons, especially for low momentum jets. Finally, module-to-module inhomogeneities or poorly instrumented regions of the calorimeter (e.g. the ICD region) can result in significant distortions to the measured jet energy.

Some of these instrumental effects (e.g. the calorimeter response to hadrons) are very difficult to model accurately in the MC simulation. As a result, data and MC have different response to jets, which requires this correction to be determined separately for the data and the simulated events. While in the simulated samples it is a-priori possible to compute exactly the response correction by comparing the

measured jet energy to the particle jet energy, this information is not available in the data. The so-called Missing  $E_T$  Projection Fraction (MPF) method [161] was developed to measure the calorimeter response to jets in the data. In addition, applying the MPF method to the simulated samples, where the true jet response is known, allows us to study the biases of the method and develop suitable correction procedures for the data.

The absolute response correction is determined using central calorimeter jets. As its name suggests, it provides the absolute scale for jet energy calibration. Forward jets are subsequently calibrated with respect to this scale.

## A.1 Missing $E_T$ Projection Fraction Method

Consider a two-body process  $X$ +jets, where  $X(=\gamma, Z \text{ or jet})$  is referred to as the “tag object,” and the jet is the “probe object.” The response of the “probe object” is the one we are estimating.

At the particle level, the transverse momenta of the tag object ( $\vec{p}_{T,\text{tag}}$ ) and of the hadronic recoil ( $\vec{p}_{T,\text{recoil}}$ ) are balanced,

$$\vec{p}_{T,\text{tag}} + \vec{p}_{T,\text{recoil}} = 0. \quad (\text{A.1.1})$$

The probe jet is a part of the hadronic recoil but may not constitute all of it. As already discussed, in a real calorimeter the responses of the tag object ( $R_{\text{tag}}$ ) and of the hadronic recoil ( $R_{\text{recoil}}$ ) might be different (an obvious case is when the tag object is a photon), which results in a transverse momentum imbalance as measured by the calorimeter:

$$\vec{p}_{T,\text{tag}}^{\text{meas}} + \vec{p}_{T,\text{recoil}}^{\text{meas}} = -\vec{E}_T^{\text{meas}}, \quad (\text{A.1.2})$$

where  $\vec{p}_{T,\text{tag}}^{\text{meas}} = R_{\text{tag}}\vec{p}_{T,\text{tag}}$  is the measured transverse momentum of the tag object,  $\vec{p}_{T,\text{recoil}}^{\text{meas}} = R_{\text{recoil}}\vec{p}_{T,\text{recoil}}$  is the measured transverse momentum of the hadronic recoil, and  $\vec{E}_T^{\text{meas}}$  is the measured  $E_T$  in the event (Section 3 of Ref. [12]).

From Equations (A.1.1) and (A.1.2), the following expression is obtained,

$$\frac{R_{\text{recoil}}}{R_{\text{tag}}} = 1 + \frac{\vec{E}_T^{\text{meas}} \cdot \vec{n}_{T,\text{tag}}}{p_{T,\text{tag}}^{\text{meas}}}. \quad (\text{A.1.3})$$

It shows that the response of the hadronic recoil relative to the response of the tag object can be estimated from the projection of  $\vec{\cancel{E}}_T$  onto the tag object direction in the transverse plane ( $\vec{n}_{T,\text{tag}}$ ) and  $p_{T,\text{tag}}^{\text{meas}}$ .

In the ideal case where the probe jet is identical to the hadronic recoil, we can replace  $R_{\text{recoil}}$  by  $R_{\text{jet}}$  in Equation (A.1.3). In practice, however, the presence of additional jets in the event (some of which might not even be reconstructed), makes this idealized situation impossible to achieve. Nonetheless, by requiring exactly two reconstructed objects (the tag and the probe) back-to-back in azimuth, it is possible to improve the approximation that  $R_{\text{jet}} \simeq R_{\text{recoil}}$ . On the other hand, as we will see, residual effects at the percent level have to be corrected. To avoid the confusion with the true response of the particle jet ( $R_{\text{jet}}$ ), we will refer to the jet response estimated with the MPF method as  $R_{\text{MPF}}^{\text{sample}}$ , where the superscript will be used to indicate which sample has been used to estimate the jet response. The latter information is important since the MPF response is an event-wide quantity and therefore depends on the actual sample used (via e.g. the parton flavor composition, color flow, etc.). In addition, the corrections applied to the tag object  $p_T$  are also propagated to  $\cancel{E}_T$  (Equation (A.2.5)).

The absolute response is derived from Equation (A.1.3) using  $\gamma$ +jet events, assuming the photon momentum has been corrected to the particle level. Therefore,  $R_{\text{tag}} \equiv R_\gamma = 1$  and Equation (A.1.3) can be rewritten as:

$$R_{\text{MPF}}^{\gamma\text{meas}+\text{jet}} = 1 + \frac{\vec{\cancel{E}}_T^{\text{meas}} \cdot \vec{n}_{T\gamma}}{p_{T\gamma}^{\text{meas}}}. \quad (\text{A.1.4})$$

The most important dependence of the jet response we are interested in is the jet energy. Unfortunately, the poor jet energy resolution will cause a bias in the estimated jet response when binning in terms of the measured probe jet energy. To measure the energy dependence of the jet response with minimal impact from resolution effects, we therefore use the energy estimator  $E'$ , defined as:

$$E' = p_{T\gamma}^{\text{meas}} \cosh(\eta_{\text{jet}}), \quad (\text{A.1.5})$$

where  $\eta_{\text{jet}}$  is the jet pseudorapidity with respect to the reconstructed hard-scattering primary vertex in the event. The variable  $E'$  is strongly correlated with the particle level jet energy, since it is calculated using the photon transverse momentum and the jet direction, the quantities measured more precisely than the jet energy

itself. The energy dependence of the jet response is well described by a quadratic logarithmic function:

$$R(E') = p_0 + p_1 \log(E'/E_0) + p_2 \log^2(E'/E_0), \quad (\text{A.1.6})$$

where  $E_0 = 100$  GeV and  $p_i$  ( $i = 0, 1, 2$ ) are free parameters to be determined.

## A.2 Corrections for Biases

In reality, the measurement of the MPF response is affected by the bias in the measured photon transverse momentum,  $p_{T\gamma}^{\text{meas}}$ , as well as the presence of the dijet background events. The former bias is addressed by the correction described in Section 5 of Ref. [12]. The absolute response measurement in the data, referred as  $R_{\text{MPF,CC}}^{\text{mixture}}$ , is corrected by a suitable average correction,  $k_{\text{R}}^\gamma$ , such that the desired MPF response measurement is obtained,

$$R_{\text{MPF,CC}}^{\gamma + \text{jet, data}} = R_{\text{MPF,CC}}^{\text{mixture}} k_{\text{R,CC}}^\gamma. \quad (\text{A.2.1})$$

The  $k_{\text{R}}^\gamma$  correction factor includes both the photon energy scale and the background corrections. After applying this correction ( $k_{\text{R}}^\gamma$ ), the JES procedures in both the data and the simulated sample are completely identical.

First, the MPF response measurement in the data must be corrected for the bias caused by the dijet contamination. In general, the measured MPF response in the selected  $\gamma + \text{jet}$  sample with a jet at  $\eta_{\text{jet}}^{\text{det}}$  can be expressed as a linear combination of the MPF responses for  $\gamma + \text{jet}$  signal and dijet background, weighted by the respective fractions:

$$R_{\text{MPF},\eta}^{\text{mixture}} = \rho_\eta R_{\text{MPF},\eta}^{\gamma + \text{jet}} + (1 - \rho_\eta) R_{\text{MPF},\eta}^{\text{dijet}}, \quad (\text{A.2.2})$$

where both the MPF responses are with respect to the measured photon  $p_{\text{T}}$ , and  $\rho_\eta$  is the sample purity. The relative difference between the MPF response of the mixture sample and the MPF response of the pure sample is given by:

$$c_{\text{bckg},\eta} \equiv \frac{R_{\text{MPF},\eta}^{\text{mixture}}}{R_{\text{MPF},\eta}^{\gamma + \text{jet}}} - 1 = (1 - \rho_\eta) \left( \frac{R_{\text{MPF},\eta}^{\text{dijet}}}{R_{\text{MPF},\eta}^{\gamma + \text{jet}}} - 1 \right). \quad (\text{A.2.3})$$

Consequently, the response correction factor,  $k_{\text{R},\eta}^\gamma$ , can be expressed in terms of the background correction,  $c_{\text{bckg},\eta}$ ,

$$k_{\text{R},\eta}^\gamma = \frac{1}{1 + c_{\text{bckg},\eta}}. \quad (\text{A.2.4})$$

The details of deriving this correction factor is described in Section 7 of Ref. [12].

The photon energy scale correction is applied to the reconstructed EM object in the analysis chain, and the missing energy is corrected accordingly,

$$\vec{\cancel{E}}_{\text{T}}^{\text{corr}} = \vec{\cancel{E}}_{\text{T}}^{\text{meas}} + \vec{p}_{T\gamma}^{\text{meas}} - \vec{p}_{T\gamma}, \quad (\text{A.2.5})$$

where  $\vec{p}_{T\gamma}^{\text{meas}}$  is the uncorrected (raw) transverse momentum of the EM cluster, and  $\vec{p}_{T\gamma}$  is the true photon transverse momentum.

Since all the reconstructed EM clusters are already calibrated in the data using  $Z \rightarrow e^+e^-$  events, the photon energy scale correction should account only for the difference between the EM cluster energy and the true photon energy. The corrections for the electron energy loss in the material in front of the calorimeter as a function of  $\eta^{\text{det}}$  and  $p_{\text{T}}$  are derived in the simulated sample and applied to the data. Specifically, photons interact less with the material than electrons, and as a result the electron energy scale correction overcorrects the photon  $p_{\text{T}}$ . This effect is particularly sizable for the low momentum photons.

We derive the photon energy scale correction with respect to electron energy using the simulated samples from  $W$ -mass group, and parametrize this scale factor,  $c_{\text{scale}}$ , as a quadratic logarithmic function (Section 5 of Ref. [12]). Then  $c_{\text{scale}}$  is applied to the reconstructed electromagnetic object in our selection,

$$p_{\text{T}}^{\text{corr}} = \frac{1}{1 - c_{\text{scale}}} p_{\text{T}}^{\text{reco}} \quad (\text{A.2.6})$$

(in case of no background,  $p_{\text{T}}^{\text{corr}} = p_{T\gamma}$ ). The energy of the EM cluster is corrected to the photon particle level, and the missing energy is corrected accordingly. Therefore, a modified version of Equation (A.1.4) is obtained,

$$R_{\text{MPF,CC}}^{\gamma + \text{jet}} = 1 + \frac{\vec{\cancel{E}}_{\text{T}}^{\text{corr}} \cdot \vec{n}_{T\gamma}}{p_{T\gamma}^{\text{corr}}}, \quad (\text{A.2.7})$$

and is used in the response measurement, where  $\vec{\cancel{E}}_{\text{T}}^{\text{corr}}$  is defined in Equation (A.2.5).

### A.3 Results in the Data

The absolute MPF responses measured in data as a function of  $E'$  are shown in Figure A.1 for  $R_{\text{cone}} = 0.7$  jets (left) and for  $R_{\text{cone}} = 0.5$  jets (right) for all run periods. Figure A.2 and Figure A.3 show the responses for each epoch separately. The measured MPF response is fitted using the function in Equation (A.1.6).

One can see that at low and medium  $E'$  values, the central response in Run IIb1 is slightly higher than that for Run IIb4 data, especially for  $R_{\text{cone}} = 0.7$  jets. We confirm this conclusion by requiring exactly one primary vertex and comparing the two responses again in Figure A.4.

Since jets do not enter directly the calculation of the MPF response, the dependence on  $R_{\text{cone}}$  is expected to be very small. In fact, the MPF response for  $R_{\text{cone}} = 0.7$  is about 1.7% higher at  $E' \sim 100$  GeV than for  $R_{\text{cone}} = 0.5$ , in both the data and the MC simulation. The measured MPF response is fitted using the parameterization in Equation (A.1.6), and the fitted parameters are summarized in Table A.1.

Type	$R_{\text{cone}}$	Epoch	$p_0$	$p_1$	$p_2$	$\chi^2/NDF$
data	0.7	Run IIa	$0.7294 \pm 0.0015$	$0.0761 \pm 0.0033$	$-0.0134 \pm 0.0027$	n/a
data	0.7	Run IIb	$0.7825 \pm 0.0009$	$0.0775 \pm 0.0024$	$-0.0112 \pm 0.0021$	1.83
data	0.7	Run IIb1	$0.7879 \pm 0.0019$	$0.0779 \pm 0.0050$	$-0.0069 \pm 0.0043$	1.00
data	0.7	Run IIb2	$0.7813 \pm 0.0015$	$0.0723 \pm 0.0042$	$-0.0157 \pm 0.0035$	2.06
data	0.7	Run IIb3	$0.7862 \pm 0.0020$	$0.0730 \pm 0.0052$	$-0.0180 \pm 0.0044$	3.00
data	0.7	Run IIb4	$0.7792 \pm 0.0019$	$0.0857 \pm 0.0051$	$-0.0052 \pm 0.0043$	1.52
data	0.5	Run IIa	$0.7350 \pm 0.0015$	$0.0766 \pm 0.0034$	$-0.0155 \pm 0.0028$	n/a
data	0.5	Run IIb	$0.7901 \pm 0.0009$	$0.0818 \pm 0.0024$	$-0.0132 \pm 0.0020$	2.26
data	0.5	Run IIb1	$0.7958 \pm 0.0018$	$0.0836 \pm 0.0051$	$-0.0103 \pm 0.0043$	0.83
data	0.5	Run IIb2	$0.7883 \pm 0.0014$	$0.0771 \pm 0.0039$	$-0.0165 \pm 0.0032$	1.93
data	0.5	Run IIb3	$0.7933 \pm 0.0020$	$0.0759 \pm 0.0055$	$-0.0185 \pm 0.0045$	2.45
data	0.5	Run IIb4	$0.7866 \pm 0.0018$	$0.0891 \pm 0.0050$	$-0.0085 \pm 0.0041$	1.46

**Table A.1** Fitted parameters for the MPF response parameterization given in Equation (A.1.6). Run IIa parameterization is provided for reference.

The results of the absolute response in the simulated sample can be found in Section 7.3 of Ref. [12].

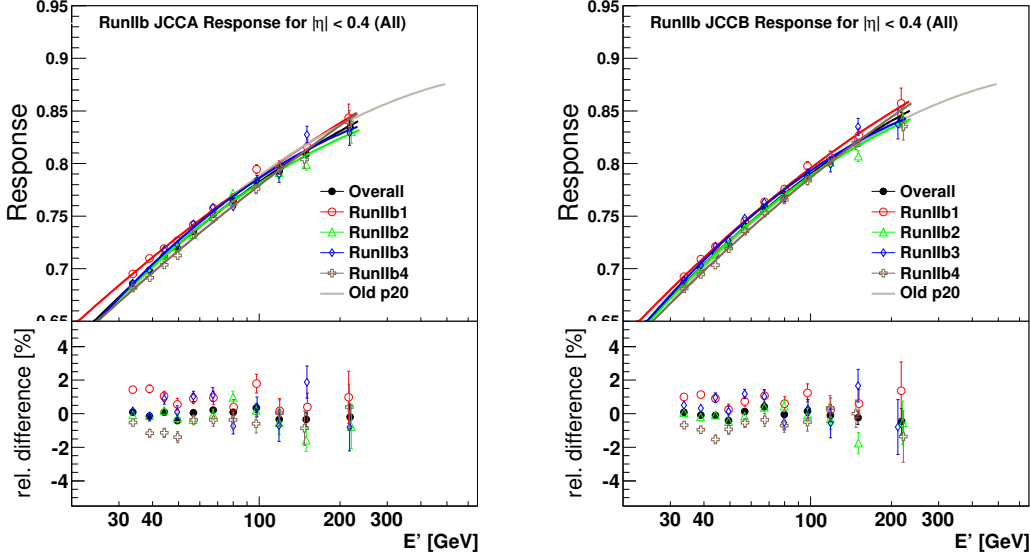


**Figure A.1** Absolute MPF response for  $R_{\text{cone}} = 0.7$  jets (left) and for  $R_{\text{cone}} = 0.5$  jets (right) as a function of  $E'$ . The solid lines indicate the fit to the function in Equation (A.1.6). The lower plots show the relative difference of the points with respect to the fitted function of the overall Run IIB data.

## A.4 Uncertainties

The main sources of the uncertainties in the MPF response measurement for  $R_{\text{cone}} = 0.7$  jets are shown in Figure A.6, while for  $R_{\text{cone}} = 0.5$  they are shown in Figure A.7. Both the statistical uncertainty of the fit and the uncertainty on the photon energy scale are included. The relative difference between the fits and the measured responses in Run IIB1–4 data are shown in Figure A.5.

As shown in the plots, the photon energy scale uncertainty is dominating up to  $E' \simeq 70 - 80$  GeV. The statistical uncertainty, shown as the red curve in Figure A.6, is estimated taking into account the full covariance matrix from the fit, and dominates at  $E' > 80$  GeV.

The uncertainty on the photon energy scale correction, shown as the blue curve in Figure A.6, has two main contributions, which are added in quadrature. The first contribution is the uncertainty on the determination of the absolute electron energy scale, which has been estimated to be 0.5% using the  $Z \rightarrow e^+e^-$  invariant mass. The second contribution is related to the uncertainties on the MC simulation of the relative energy scale between photons and electrons, as a result

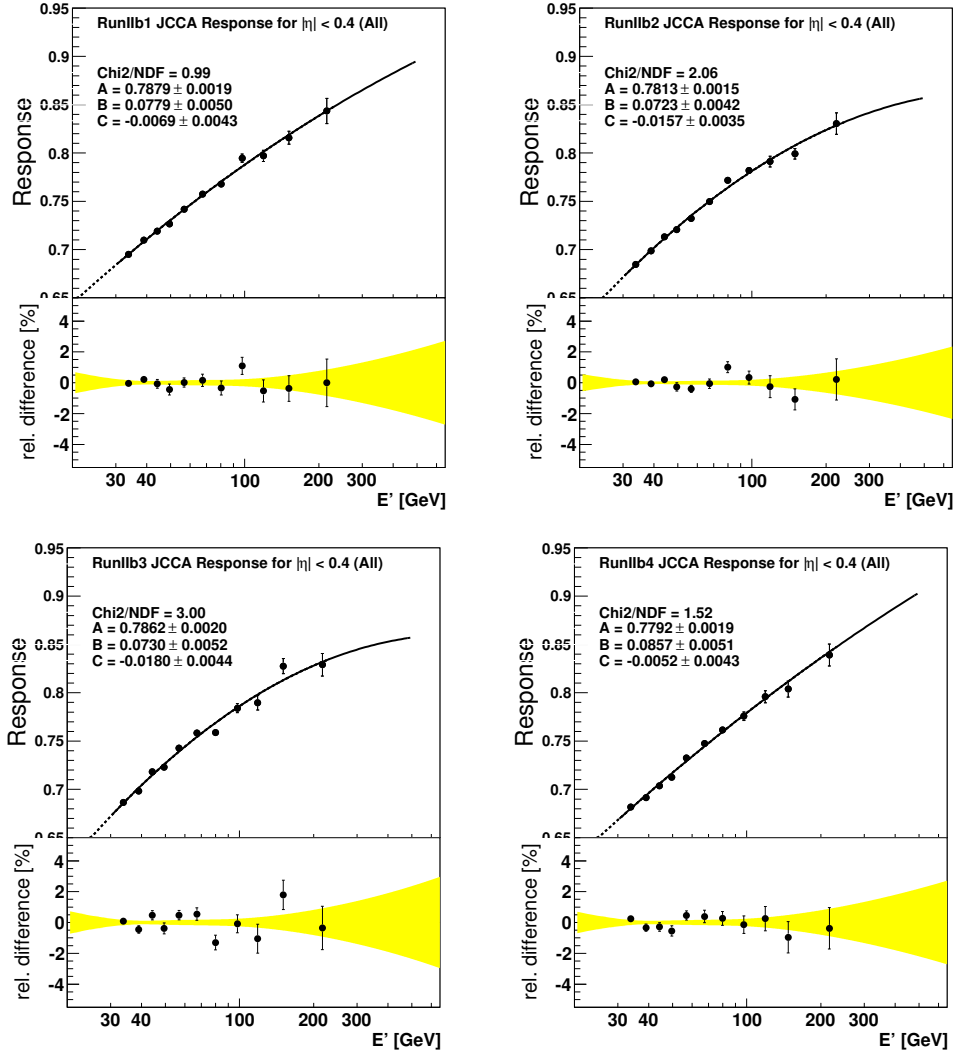


**Figure A.2** Absolute MPF response for  $R_{\text{cone}} = 0.7$  jets as a function of  $E'$ . The solid lines indicate the fit to the function in Equation (A.1.6). The lower plots show the relative difference of the points with respect to the fitted function, with a yellow band showing statistical uncertainty of the fit.

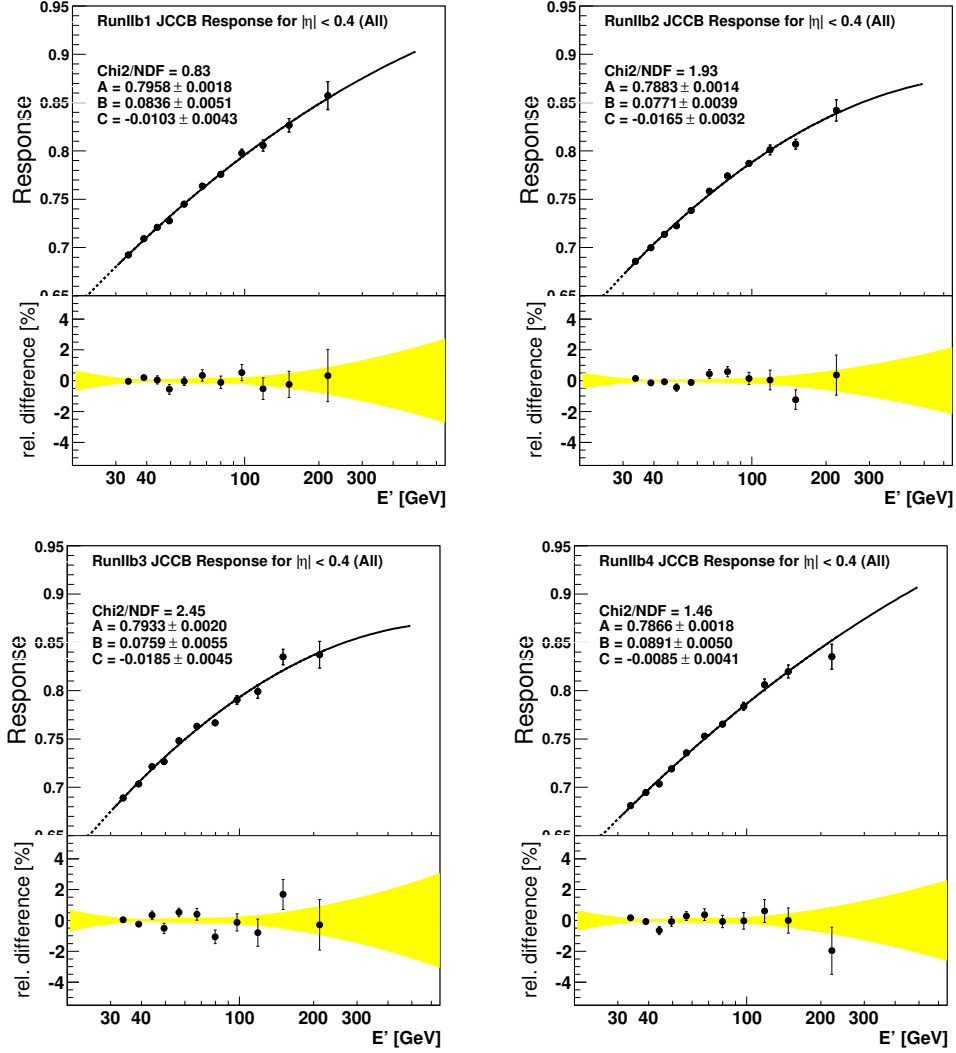


**Figure A.3** Absolute MPF response for  $R_{\text{cone}} = 0.5$  jets as a function of  $E'$ . The solid lines indicate the fit to the function in Equation (A.1.6). The lower plots show the relative difference of the points with respect to the fitted function.

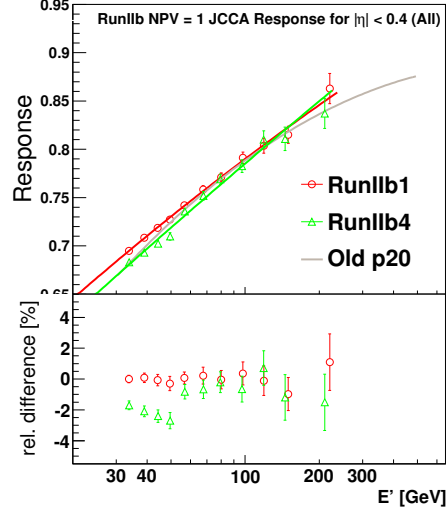


**Figure A.4** Comparison of absolute responses measured with Run I Ib1 and Run I Ib4 data using the events with exactly one primary vertex.

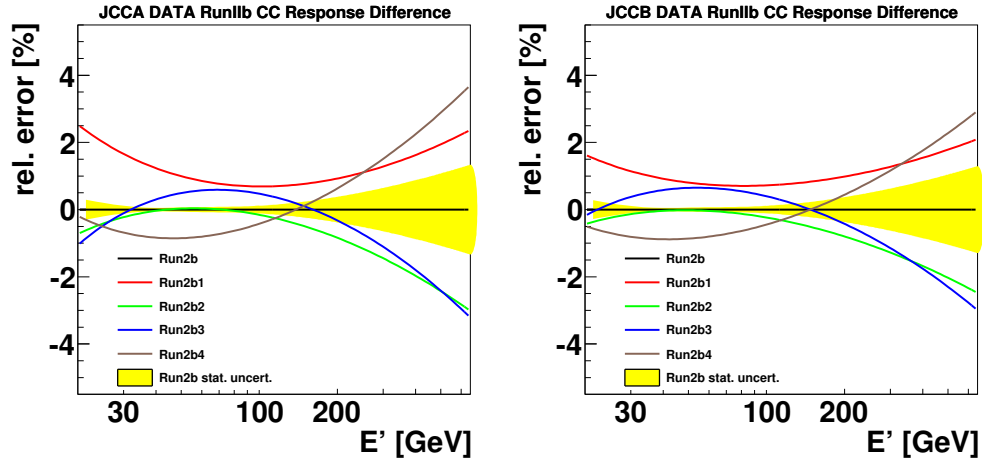


**Figure A.5** The relative difference of the absolute MPF responses for  $R_{\text{cone}} = 0.7$  jets (left) and for  $R_{\text{cone}} = 0.5$  jets (right) as a function of  $E'$ . The solid lines indicate the fit to the function in Equation (A.1.6). The yellow band shows the statistic uncertainty of the overall Run I Ib fit.

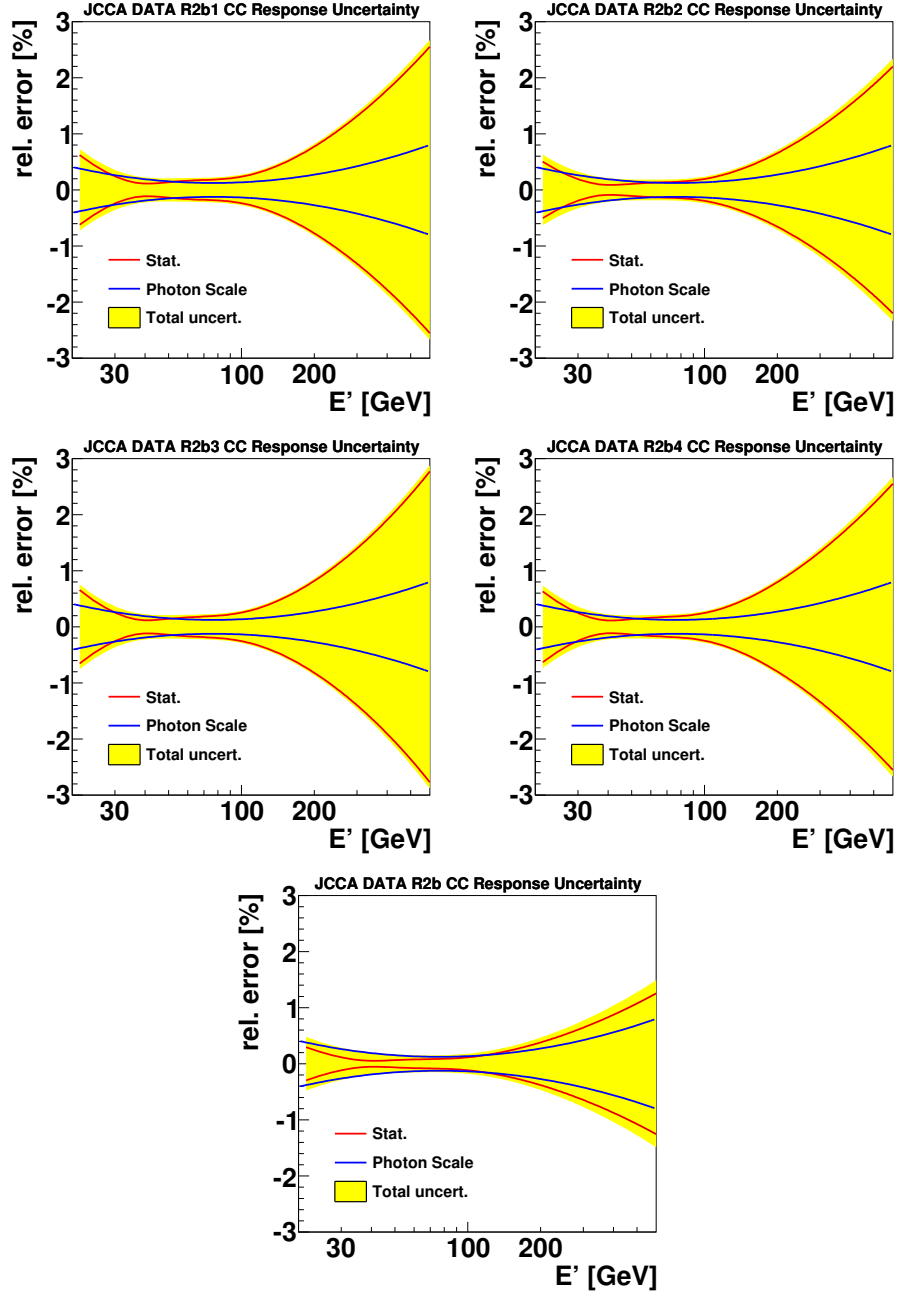


**Figure A.6** Relative uncertainties on the absolute MPF response measurement in data for  $R_{\text{cone}} = 0.7$  jets as a function of  $E'$ .

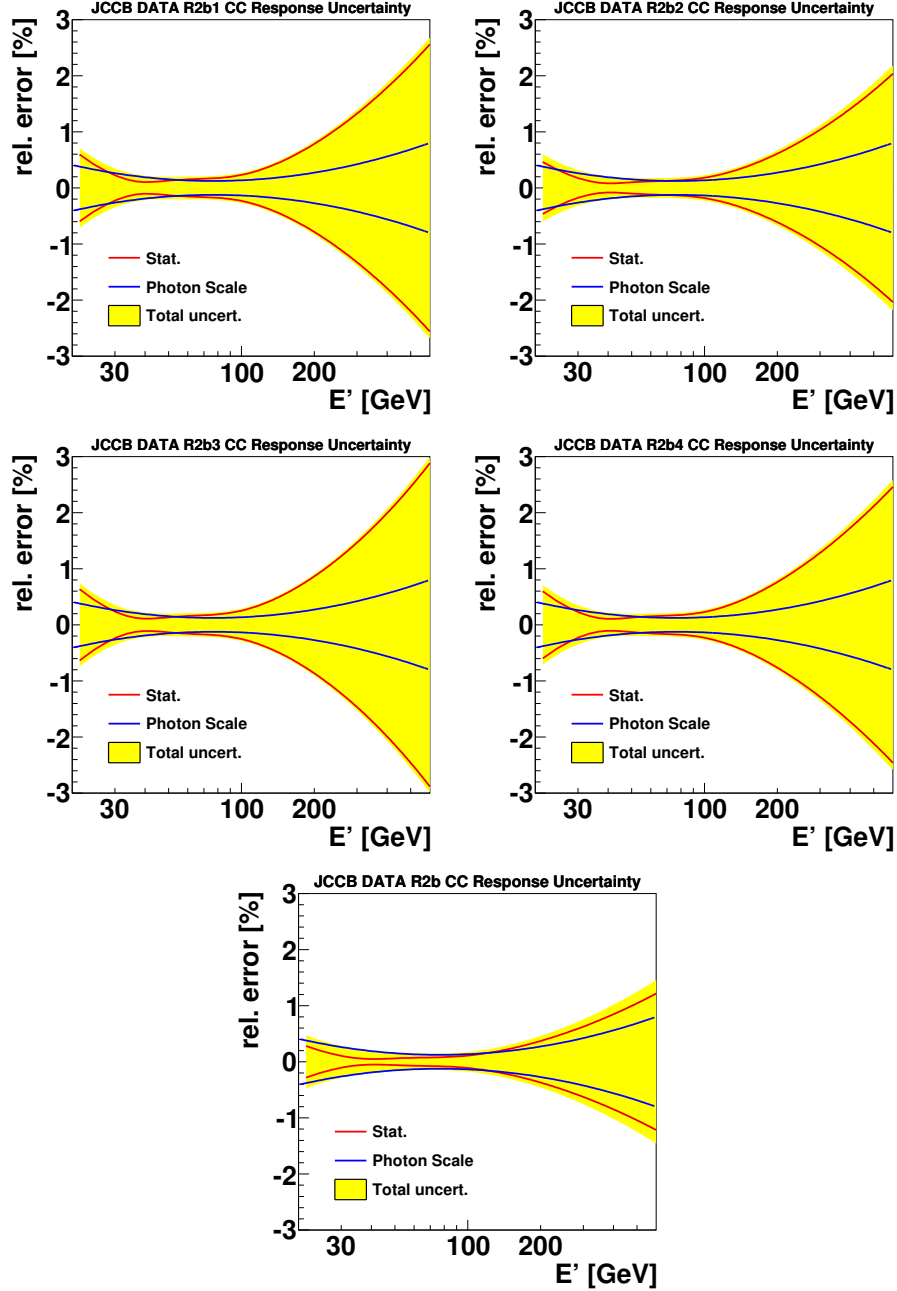


**Figure A.7** Relative uncertainties on the absolute MPF response measurement in data for  $R_{\text{cone}} = 0.5$  jets as a function of  $E'$ .

of the different interactions with matters.

## B Trigger Efficiency Measurement

We use the “inclusive” triggers, meaning no explicit trigger requirement, to select the data in this analysis for both the electron and muon channels. The signal acceptance significantly increases in the muon channel by using the inclusive trigger instead of the muon “Super-OR” triggers, since the efficiency of the muon “Super-OR” triggers is approximately 70% (Super-OR is an OR of the “Single-Lepton-OR” and “Lepton+Jets-OR” trigger selections). In this appendix, we show that the inclusive trigger efficiency for our selected events is 100% within the assigned systematic uncertainties and thus no additional trigger efficiency correction factors are needed in our simulated samples.

The inclusive trigger requirement is very close to the “Mega-OR” triggers which were used in the previous single top-quark analyses [126, 107], and therefore we follow the same procedure to measure the trigger efficiencies as described in Appendix 1 of Refs. [126, 107]. Specifically, we show the efficiency of the inclusive trigger requirement is 100% by comparing the ratio of Super-OR selected data to the inclusive selected data, and the ratio of the simulated events with the Super-OR trigger turn-on curves applied to the 100% efficient simulation. The corrections of the Super-OR trigger requirement on the simulated samples were measured with the tag-and-probe method on  $Z \rightarrow \ell\ell$  events. In particular, we subtract the multijet background contribution from the data in these comparisons, for the trigger efficiencies are different for the signal-selected data and multijet events, which come from an orthogonal dataset as described in Section 5.1.

Figures B.1 to B.6 show the ratios of Super-OR to “inclusive trigger” efficiencies in “Data-multijet” samples (left column), the ratios of the simulation with Super-OR trigger efficiencies to 100% efficiencies (central column), and the ratio of the data ratios to the simulation ratios (right column). This double ratio

represents the efficiency of the inclusive trigger requirement. All the samples are taken in the “pre-tagged” stage. The topological variables sensitive to the trigger requirement ( $p_T(\text{jet1})$ ,  $p_T(\text{jet2})$ ,  $p_T(\text{lepton})$ ,  $\cancel{E}_T$ ,  $M_T(W)$ , and  $H_T(\text{alljets})$ ) are plotted. The vertical (green) lines delineate the relevant regions containing 90% of the data (with 5% of the data on either side). The horizontal yellow lines indicate the 100% efficiencies, and the red ones are drawn at  $100\pm 3\%$  levels for the electron channel, but at  $100\pm 5\%$  levels for the muon channel.

From the left and central columns of these plots, we verify the efficiency of the Super-OR trigger is only about 75% in the muon channel. The right columns show the overall inclusive trigger efficiency is consistent with 100% estimation within the uncertainty. The double ratios in the right columns are sometimes above 1, indicating we have fewer event yields in the “Data-multijet” sample than expected from the simulation. This does not mean the trigger efficiency is greater than 100%, but rather is a result of the uncertainty in the multijet background contributions. The Super-OR trigger requirement reduces the multijet background contributions significantly, and therefore we have to re-estimate the multijet backgrounds for the Super-OR samples. Owing to the different sets of multijet background normalization, it is possible to have the double ratios greater than 100%.

Since almost all of the double ratio points are in between the 97% and 103% lines for the electron channel, and in between the 95% and 105% lines for the muon channel, we assign systematic uncertainties of 3% and 5% to our trigger efficiency, for the electron and muon channels respectively. In the cross section measurement described in DØ note 6366, we model this uncertainty as a Gaussian with mean 1 and width 0.03 (0.05 for the muon channel), and allow it to vary only below 1, i.e. the efficiencies are not allowed to be larger than 100%.

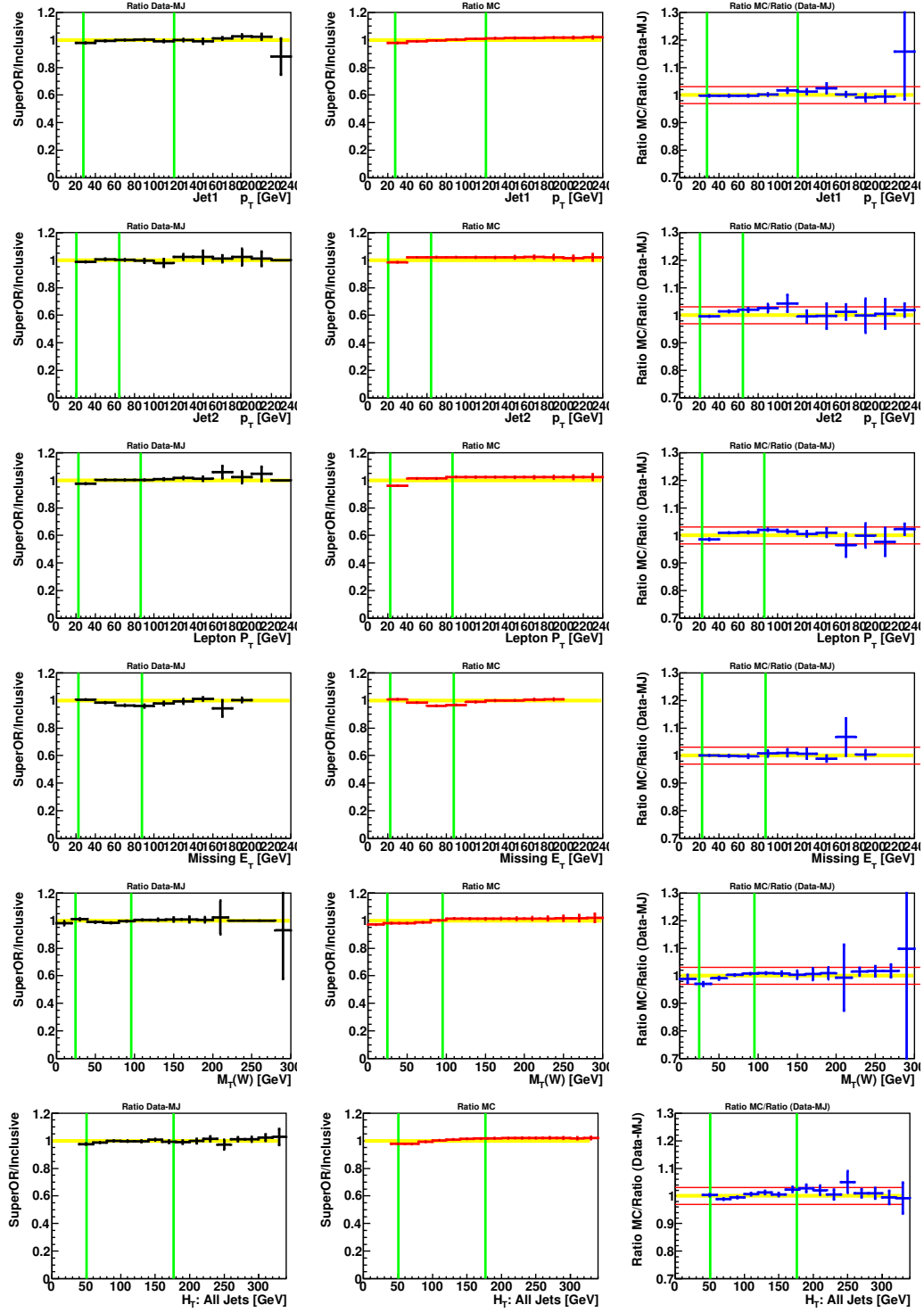


**Figure B.1** Run I Ib1 electron channel: Ratios of Super-OR fired events to the inclusive trigger fired events in “Data-multijet” (left column); ratios of Super-OR corrected MC yields to the 100% MC yields (central column); ratios of the previous two ratios, namely the inclusive trigger efficiency (right column). The rows show these ratios for the six chosen variables.

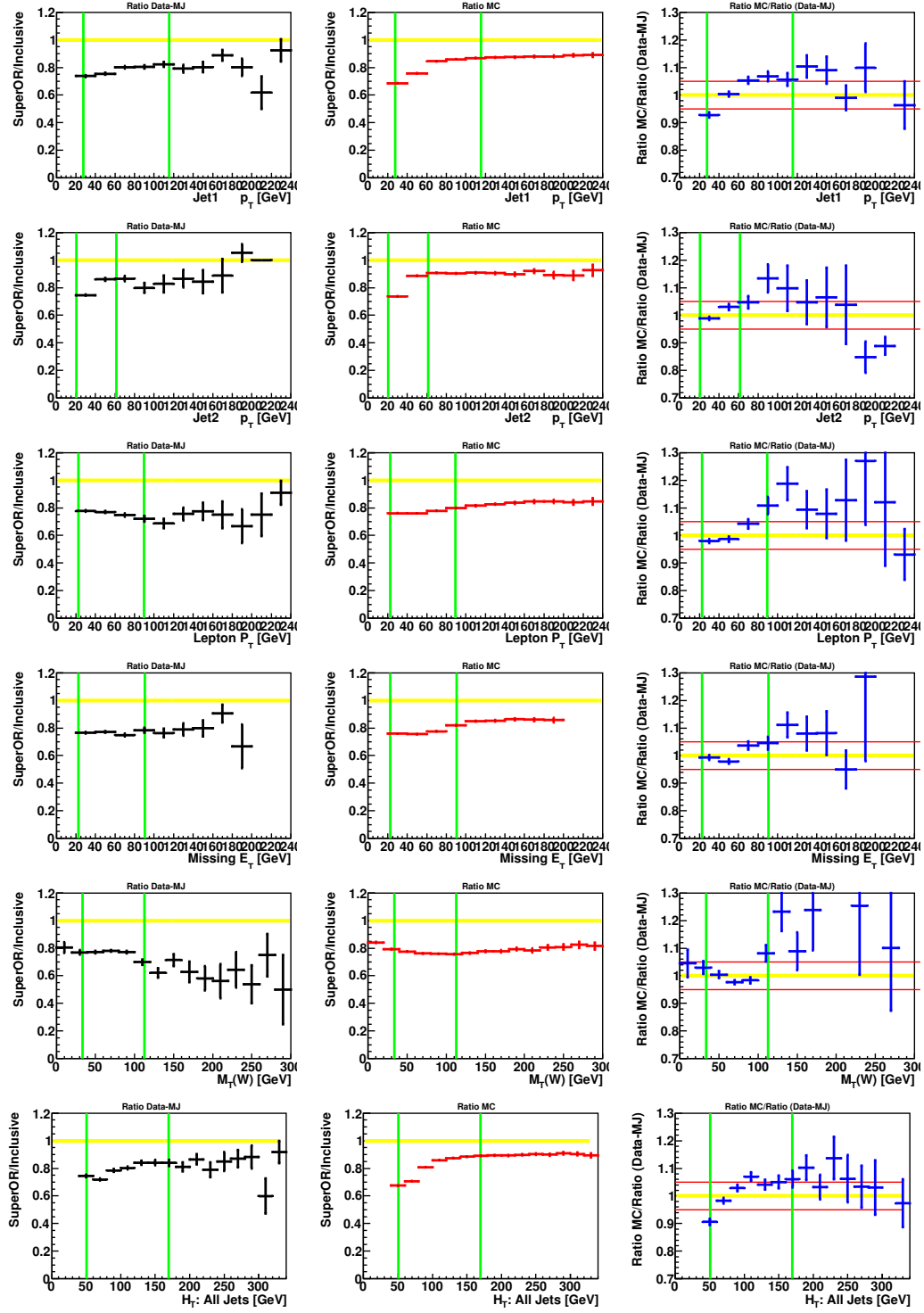


**Figure B.2** Run IIb1 muon channel: Ratios of Super-OR fired events to the inclusive trigger fired events in “Data-multijet” (left column); ratios of Super-OR corrected MC yields to the 100% MC yields (central column); ratios of the previous two ratios, namely the inclusive trigger efficiency (right column). The rows show these ratios for the six chosen variables.

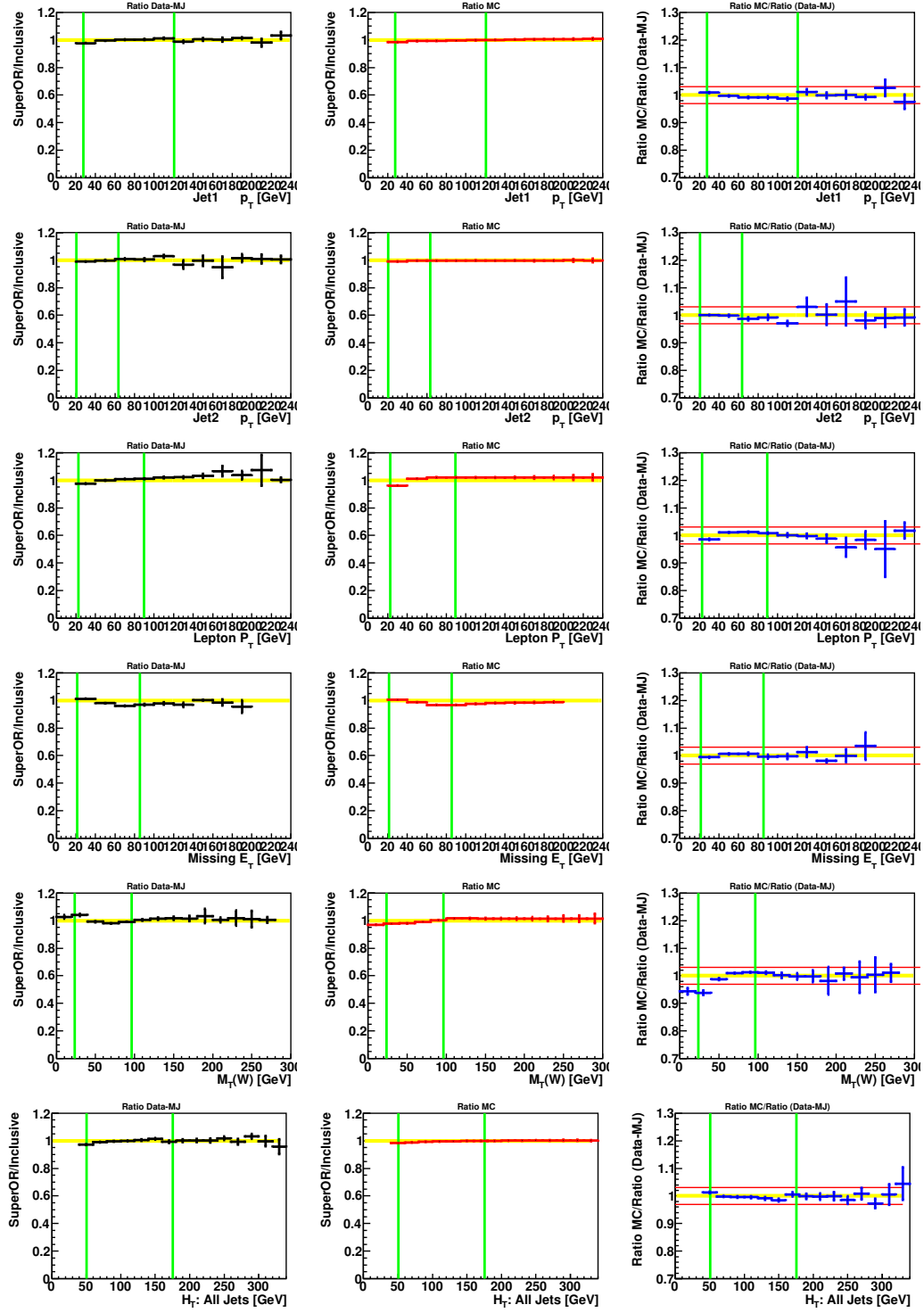


**Figure B.3** Run I Ib2 electron channel: Ratios of Super-OR fired events to the inclusive trigger fired events in “Data-multijet” (left column); ratios of Super-OR corrected MC yields to the 100% MC yields (central column); ratios of the previous two ratios, namely the inclusive trigger efficiency (right column). The rows show these ratios for the six chosen variables.

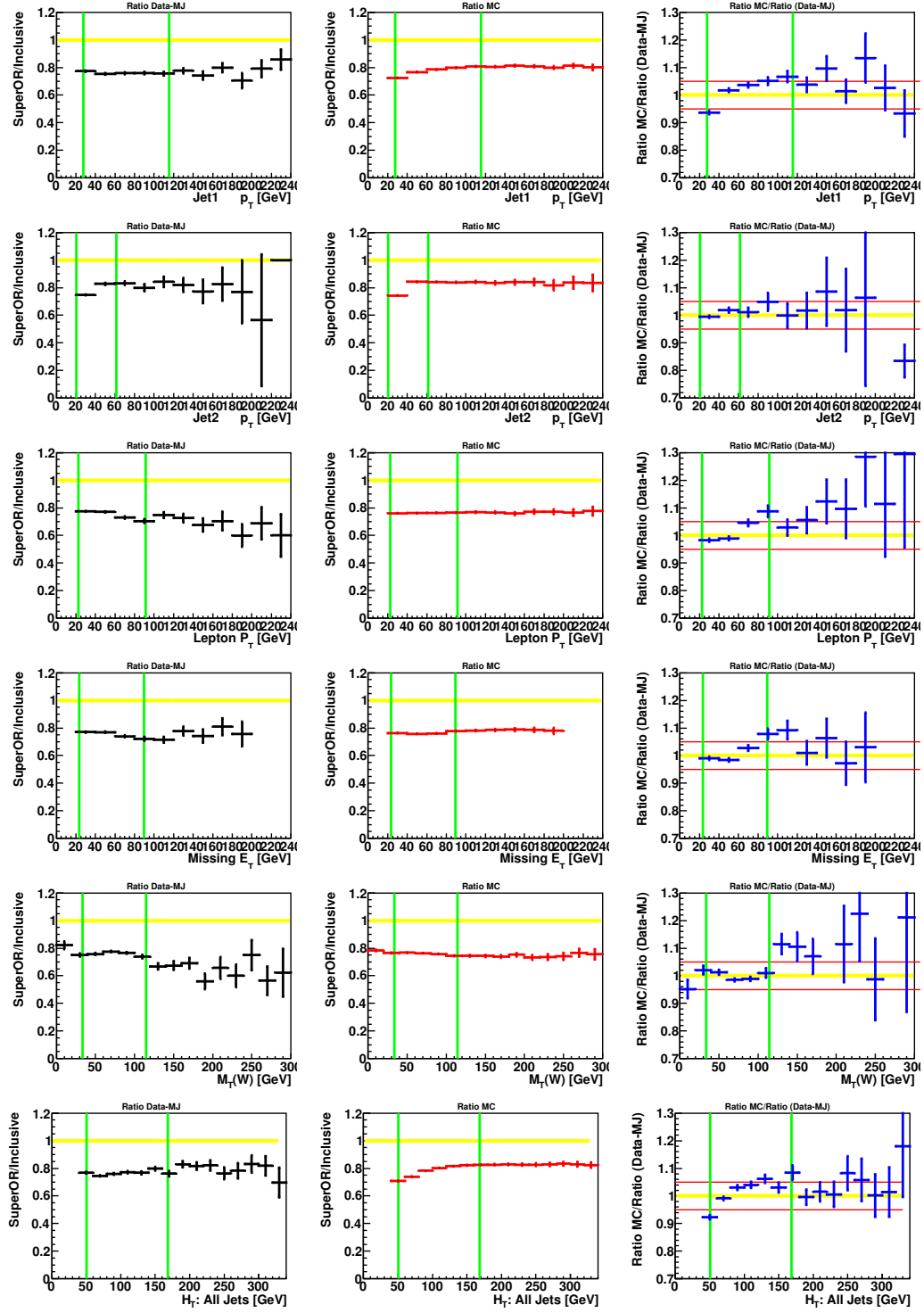


**Figure B.4** Run IIb2 muon channel: Ratios of Super-OR fired events to the inclusive trigger fired events in “Data-multijet” (left column); ratios of Super-OR corrected MC yields to the 100% MC yields (central column); ratios of the previous two ratios, namely the inclusive trigger efficiency (right column). The rows show these ratios for the six chosen variables.

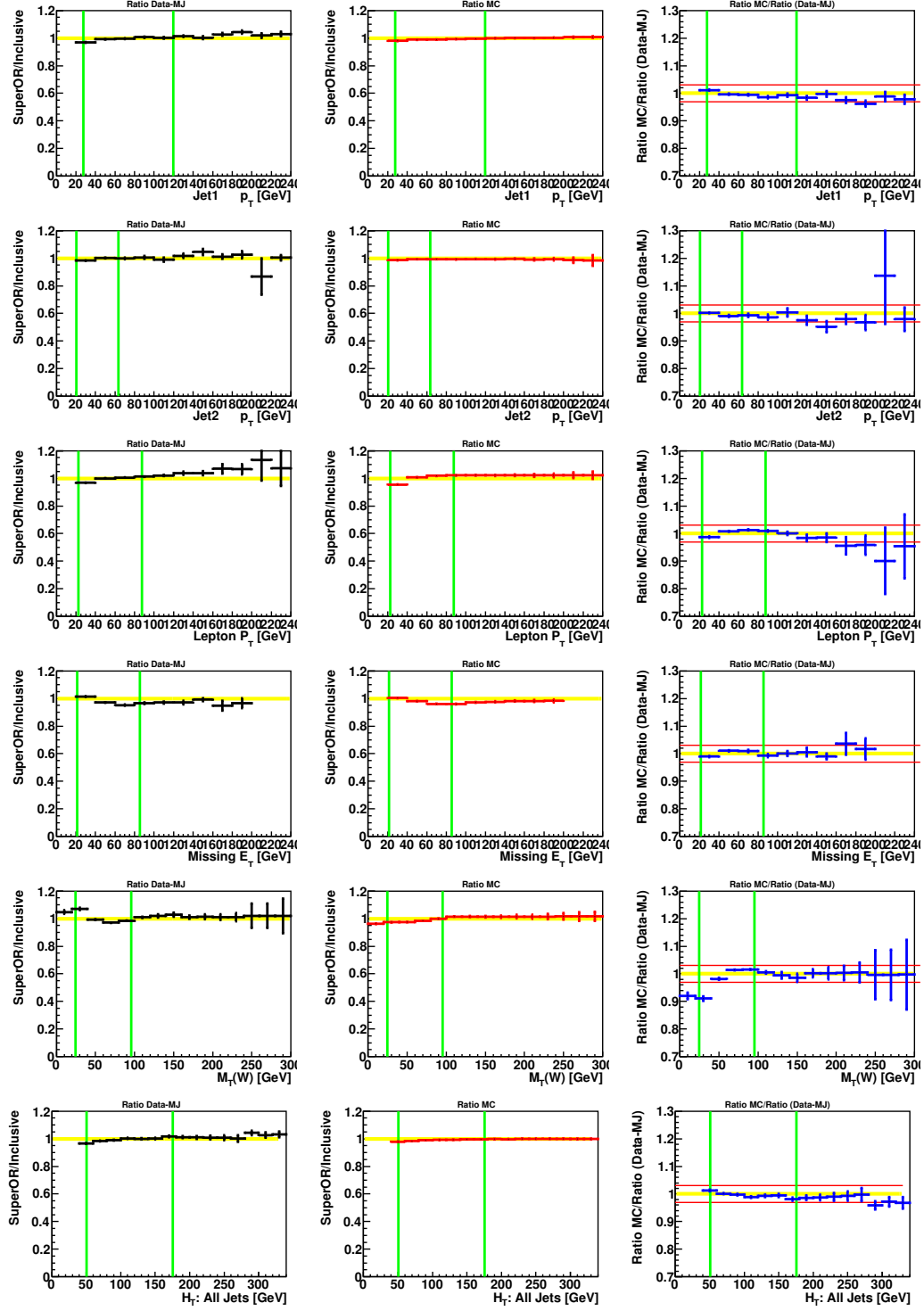


**Figure B.5** Run I Ib3 electron channel: Ratios of Super-OR fired events to the inclusive trigger fired events in “Data-multijet” (left column); ratios of Super-OR corrected MC yields to the 100% MC yields (central column); ratios of the previous two ratios, namely the inclusive trigger efficiency (right column). The rows show these ratios for the six chosen variables.

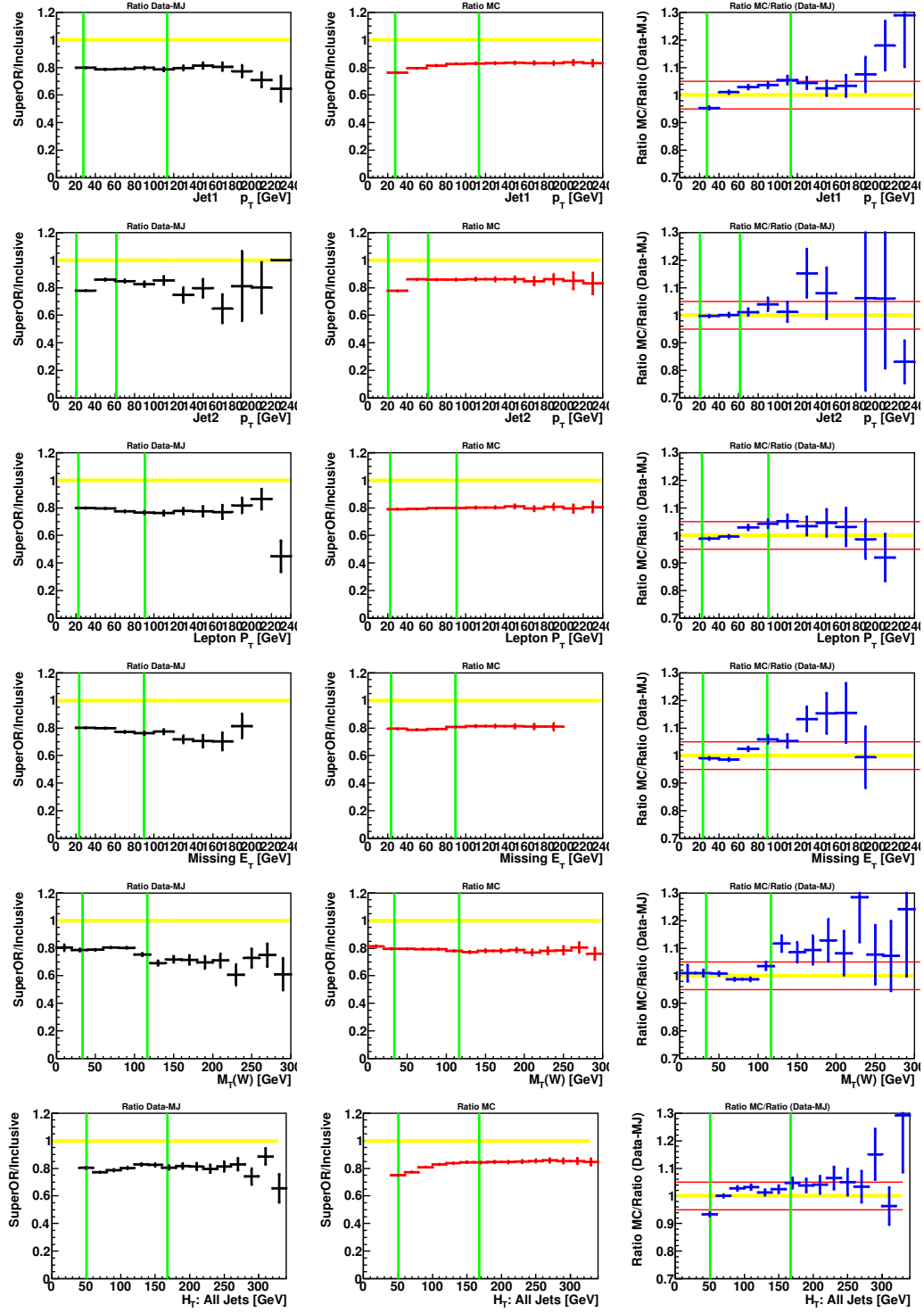


**Figure B.6** Run IIb3 muon channel: Ratios of Super-OR fired events to the inclusive trigger fired events in “Data-multijet” (left column); ratios of Super-OR corrected MC yields to the 100% MC yields (central column); ratios of the previous two ratios, namely the inclusive trigger efficiency (right column). The rows show these ratios for the six chosen variables.

# C Muon Angular Corrections

## C.1 Muon $\eta^{\text{det}}$ Corrections

To cope with the muon angular mismodeling, we apply a bin-by-bin reweighting on the muon detector  $\eta$  distribution for all the simulated samples. The resulting plots are shown in Figure C.1, and more details can be found in [126, 107].

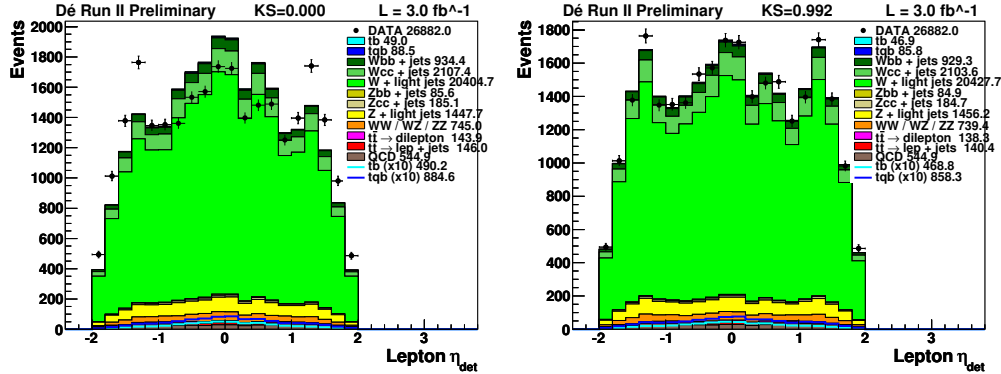


**Figure C.1** The muon detector  $\eta$  distributions for the Run IIb2 two-jet samples. The left plot shows the distribution before the bin-by-bin muon detector  $\eta$  reweighting, while the right one shows the one after the reweighting. As indicated in these plots, the data-MC agreement is improved after reweighting.

## C.2 Muon Angular Cuts

The simulated samples do not model well the data in the distribution of the  $\Delta\phi(\mu, \cancel{E}_T)$  in the muon channel, especially when the reconstructed muon and  $\cancel{E}_T$  are back-to-back in the transverse plane, as shown in Figure C.2. In this appendix,

we show where this disagreement comes from, and how we fix the issue without losing many signal events.

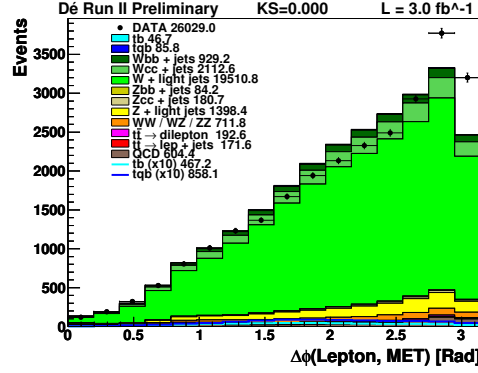


**Figure C.2** The mismodeled  $\Delta\phi(\mu, \cancel{E}_T)$  distribution for Run IIb muon two-jet channel at the pre-tagged stage. All the Run IIb1, IIb2, and IIb3 simulation have the same features.

To investigate where the mismodeling comes from, we make plots of the muon related variables, as shown in Figure C.3:

- **Lepton  $\chi^2$  Probability:** The  $\chi^2$  probability of the global muon fit
- **Lepton DCA:** The  $d_{ca}$  of the track associated with the muon
- **Lepton DCA Significance:** The significance of the  $d_{ca}$  mentioned above
- **Lepton  $\eta^{\text{det}}$ :** The detector pseudorapidity of the muon
- **Number of CFT Hits**
- **Number of SMT Hits**
- **TrackQPt:** The muon track curvature
- **Track Curvature Significance**

We observe the simulation is mismodeled in the region with low Lepton  $\chi^2$  Probability, the ICD region, and the region when the absolute value of the muon Track Curvature Significance is small. In particular, the mismodeling in the low Lepton  $\chi^2$  Probability region is significant, which means the simulation does not well model the bad global-fit muons.

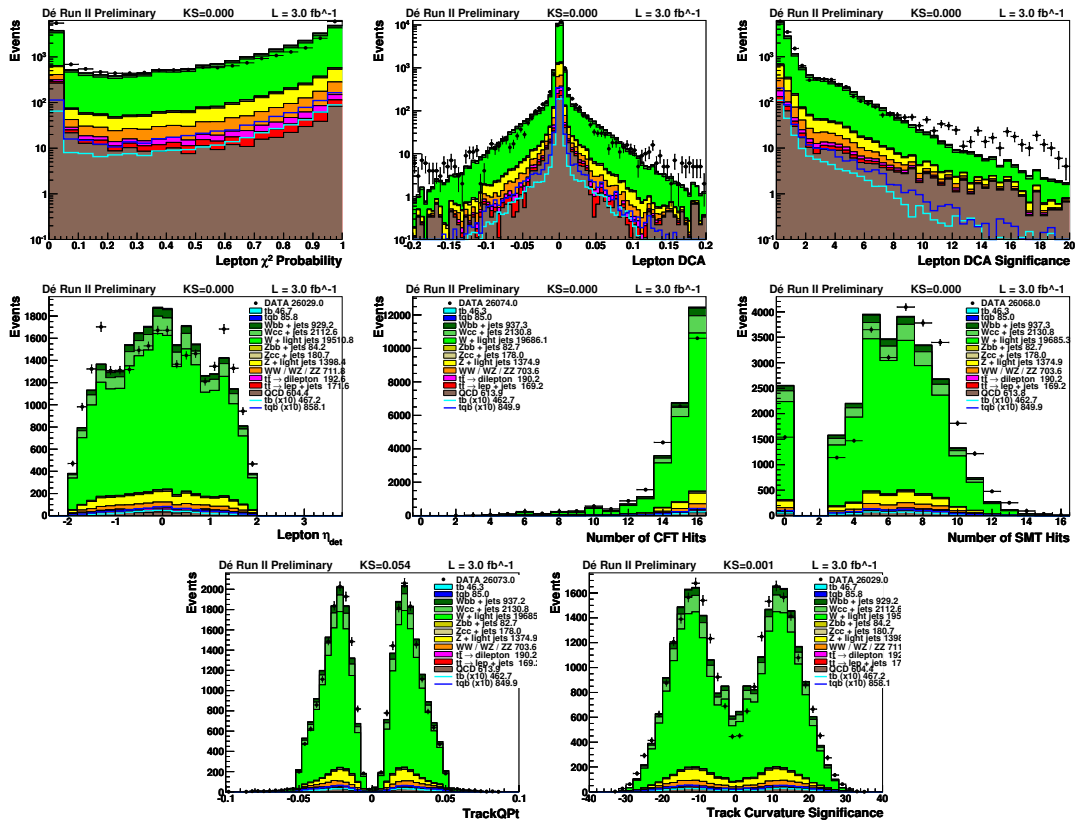


Figure C.3 The muon related variables for the Run IIB2 muon two-jet channel.

We cut off the events with Lepton  $\chi^2$  Probability  $< 0.05$ , and the simulation is much improved, as shown in Figure C.4. It verifies that the source of the  $\Delta\phi(\mu, \cancel{E}_T)$  mismodeling is from the bad global-fit muons. However, with this cut we lose 15% of the signal events that we cannot afford. Therefore, we have to look for another cuts to fix the issue without losing too many signals.

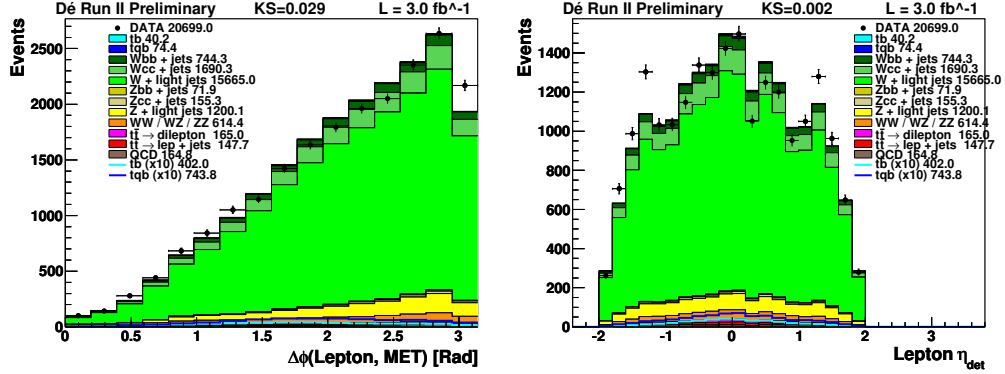


Figure C.4 The  $\Delta\phi(\mu, \cancel{E}_T)$  and Lepton  $\eta^{\text{det}}$  with the cut Lepton  $\chi^2$  Probability  $> 0.05$ . The simulation improves.

We make plots of events with  $\Delta\phi(\mu, \cancel{E}_T) > 2.95$ , where the simulation mismodels the data, and find out the Lepton  $\eta^{\text{det}}$  and the muon Track Curvature Significance are badly mismodeled in parts of the distributions, as shown in Figure C.5.

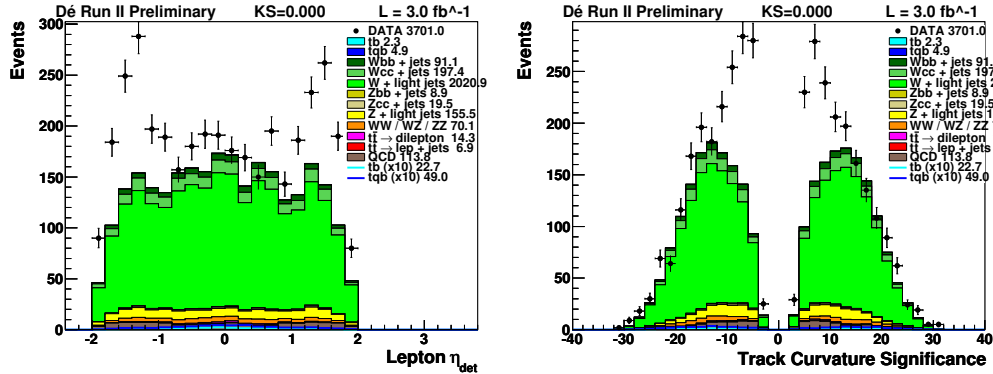
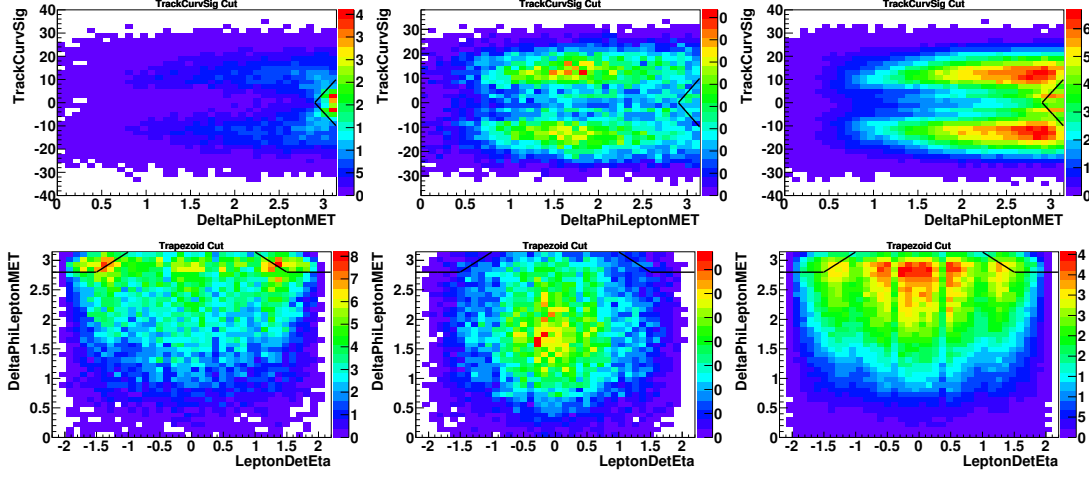


Figure C.5 Events with  $\Delta\phi(\mu, \cancel{E}_T) > 2.95$ .

By investigating the two-dimensional distributions of the muon Track Curvature Significance versus  $\Delta\phi(\mu, \cancel{E}_T)$ , and the Lepton  $\eta^{\text{det}}$  versus  $\Delta\phi(\mu, \cancel{E}_T)$ , as

shown in Figure C.6, we optimize a triangle cut and a trapezoid cut to get rid of the mismodeled regions, while retaining as many signal events as possible.



**Figure C.6** Two-dimensional distributions: The muon track curvature significance versus  $\Delta\phi(\mu, \cancel{E}_T)$  (upper row), and the  $\Delta\phi(\mu, \cancel{E}_T)$  versus the lepton  $\eta^{\text{det}}$  (lower row), for the data (left column), the  $tb$  signal (central column), and  $wlp$  simulated sample (right column).

With these optimized cuts, we lose only 3% of the signal, and have reasonable agreement between the data and the simulation, as shown in Figure C.7.

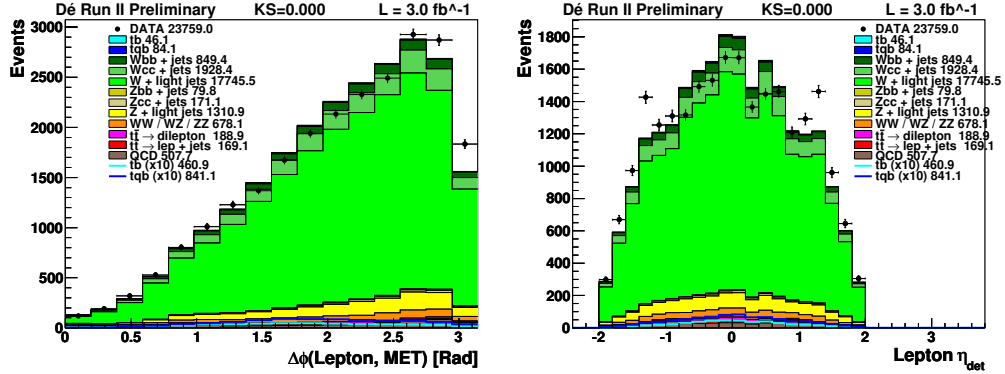


**Figure C.7** The distributions of  $\Delta\phi(\mu, \cancel{E}_T)$  and Lepton  $\eta^{\text{det}}$  with the final triangle and trapezoid cuts.

We apply the trapezoid cut after applying the muon  $\eta^{\text{det}}$  reweighting, in order to avoid possible biases on the reweighting.

## D Control Plots

Figures D.1 to D.11 show various kinematic distributions in the pre-tagged and tagged samples. The kinematic variable  $Q \times \eta$  is defined as the product of the lepton charge and the pseudorapidity of the leading light quark jet, and the light quark jet is defined as the leading jet that is not  $b$ -tagged. Thus, there are no light quark jets in the two-jet, double-tagged events, and  $Q \times \eta$  is not defined.

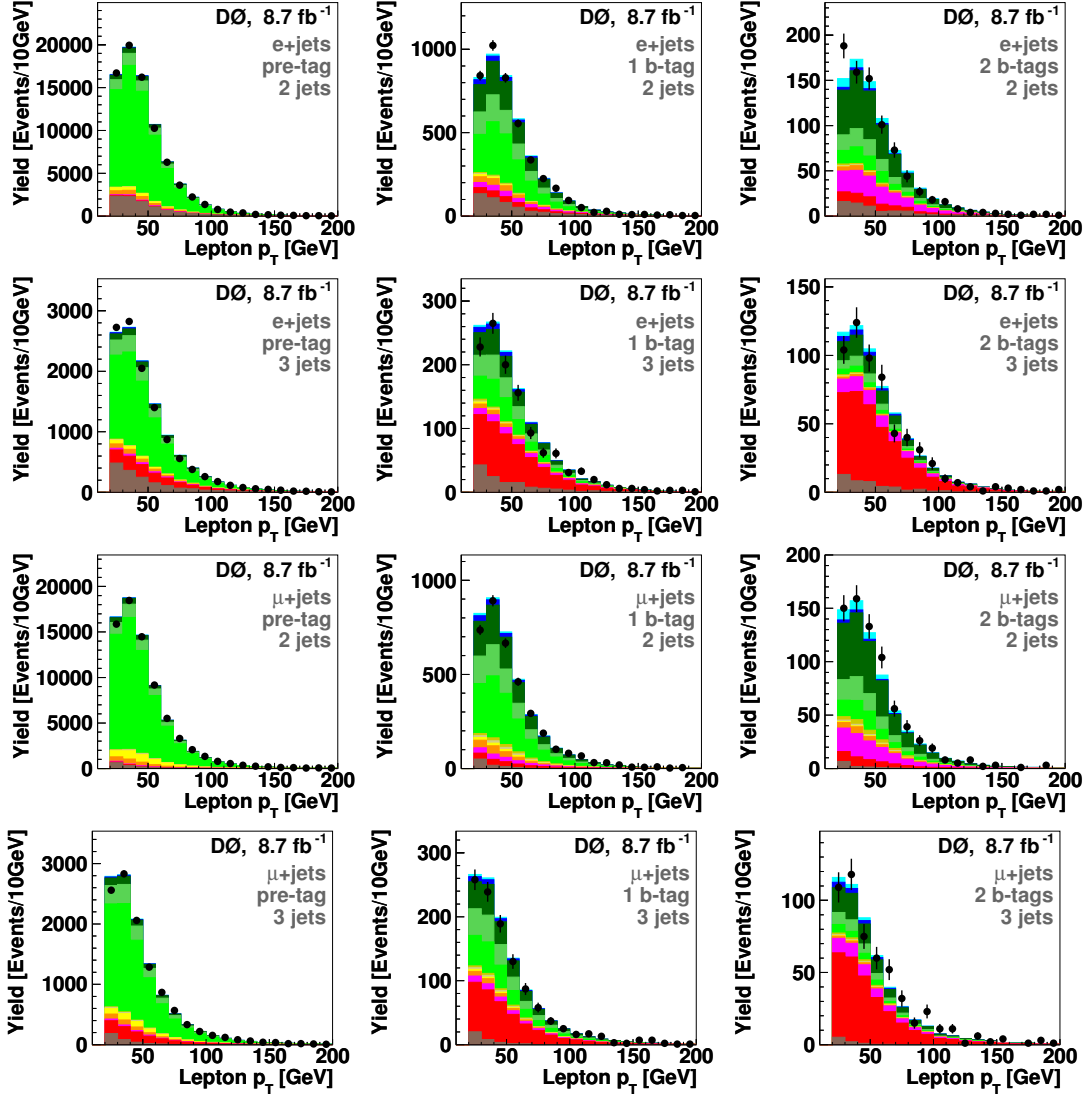


**Figure D.1** The transverse momentum of the lepton for pre-tagged (left), single-tagged (central), and double-tagged (right) for Run IIb, electron and muon channels, two-jet and three-jet events.

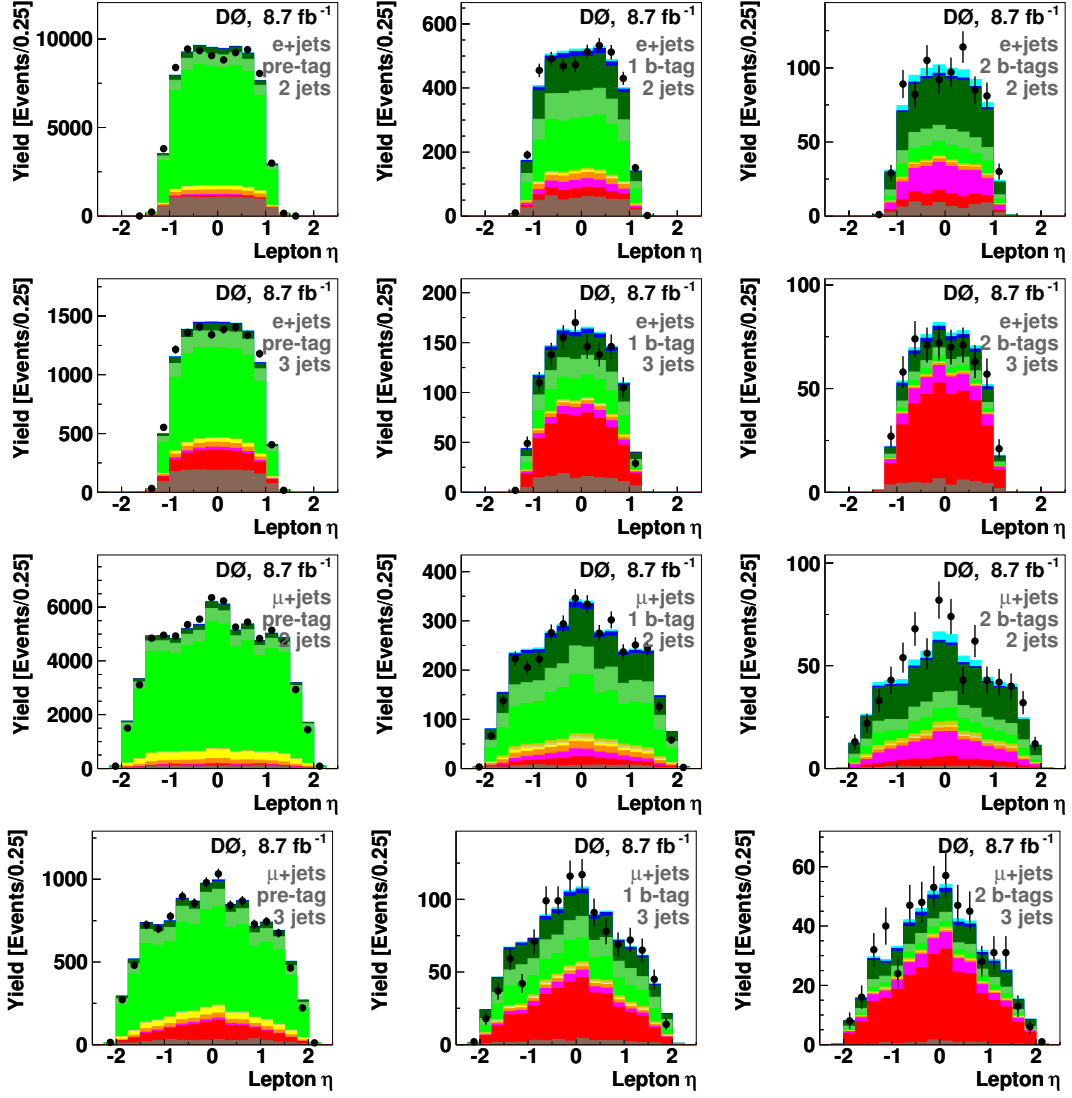


**Figure D.2** The pseudorapidity of the lepton for pre-tagged (left), single-tagged (central), and double-tagged (right) for Run IIb, electron and muon channels, two-jet and three-jet events.

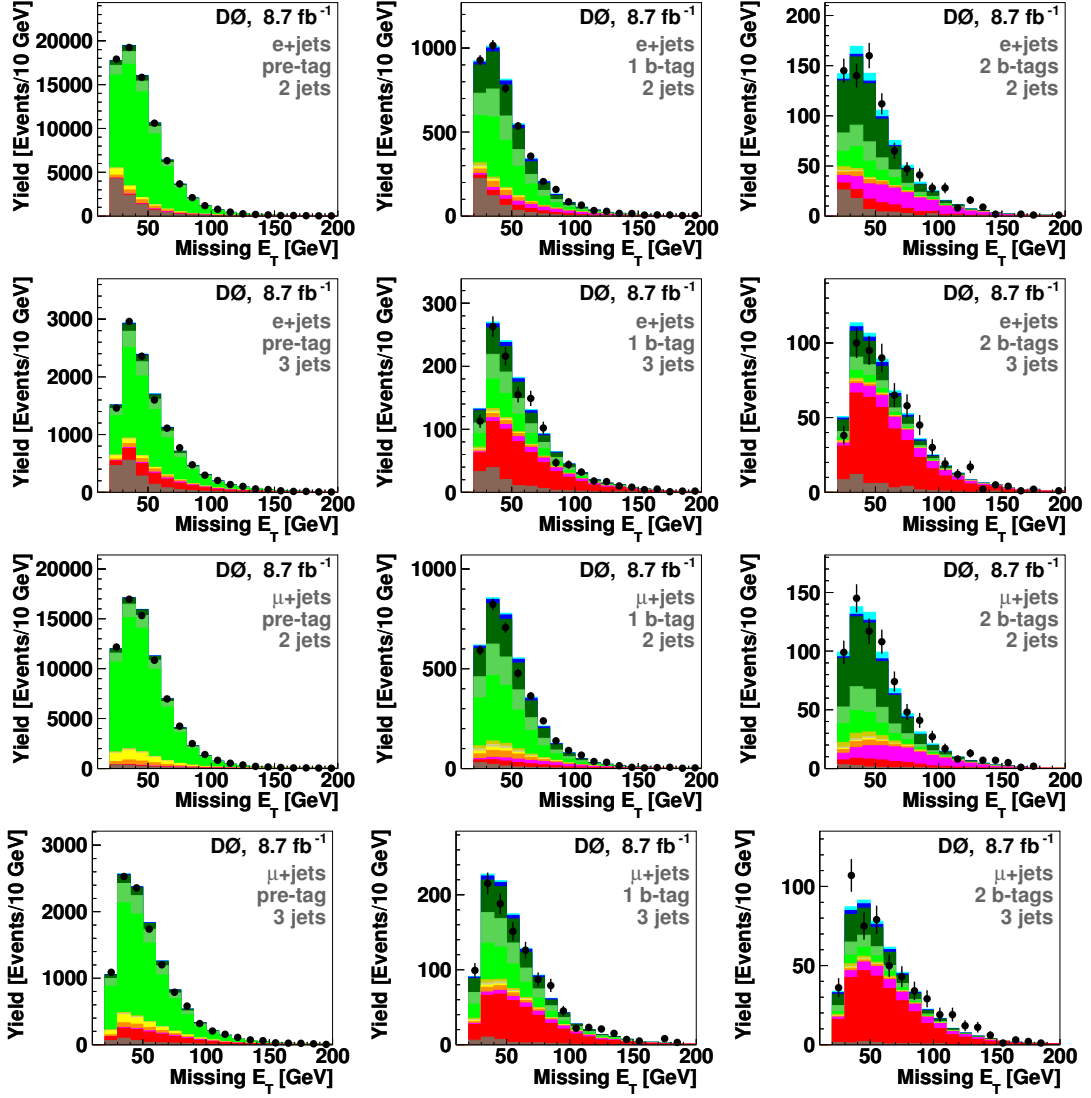


**Figure D.3** The missing transverse energy for pre-tagged (left), single-tagged (central), and double-tagged (right) for Run IIb, electron and muon channels, two-jet and three-jet events.

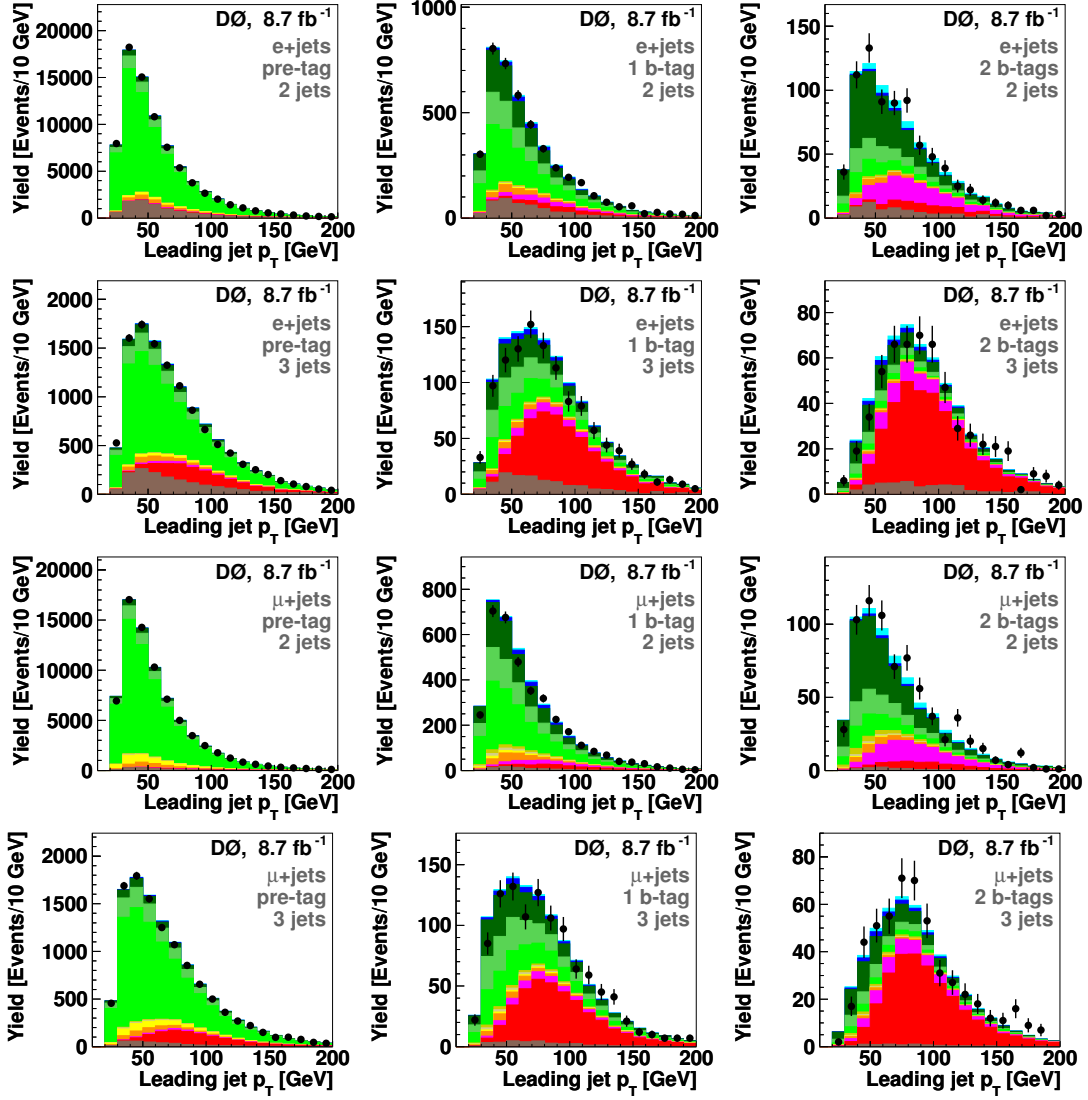


**Figure D.4** The transverse energy of the leading jet for pre-tagged (left), single-tagged (central), and double-tagged (right) for Run IIb, electron and muon channels, two-jet and three-jet events.

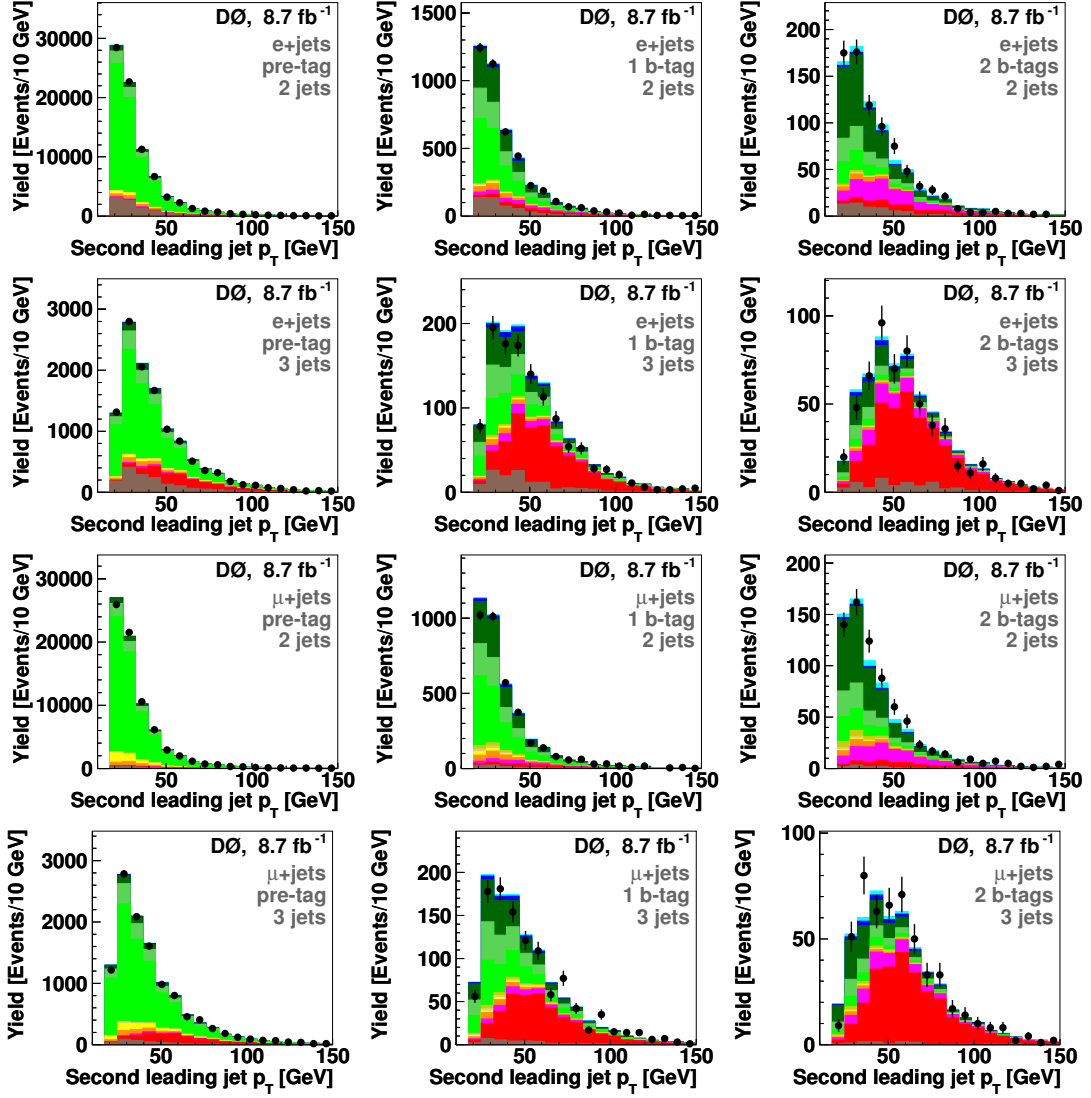


**Figure D.5** The transverse energy of the second leading jet for pre-tagged (left), single-tagged (central), and double-tagged (right) for Run IIb, electron and muon channels, two-jet and three-jet events.

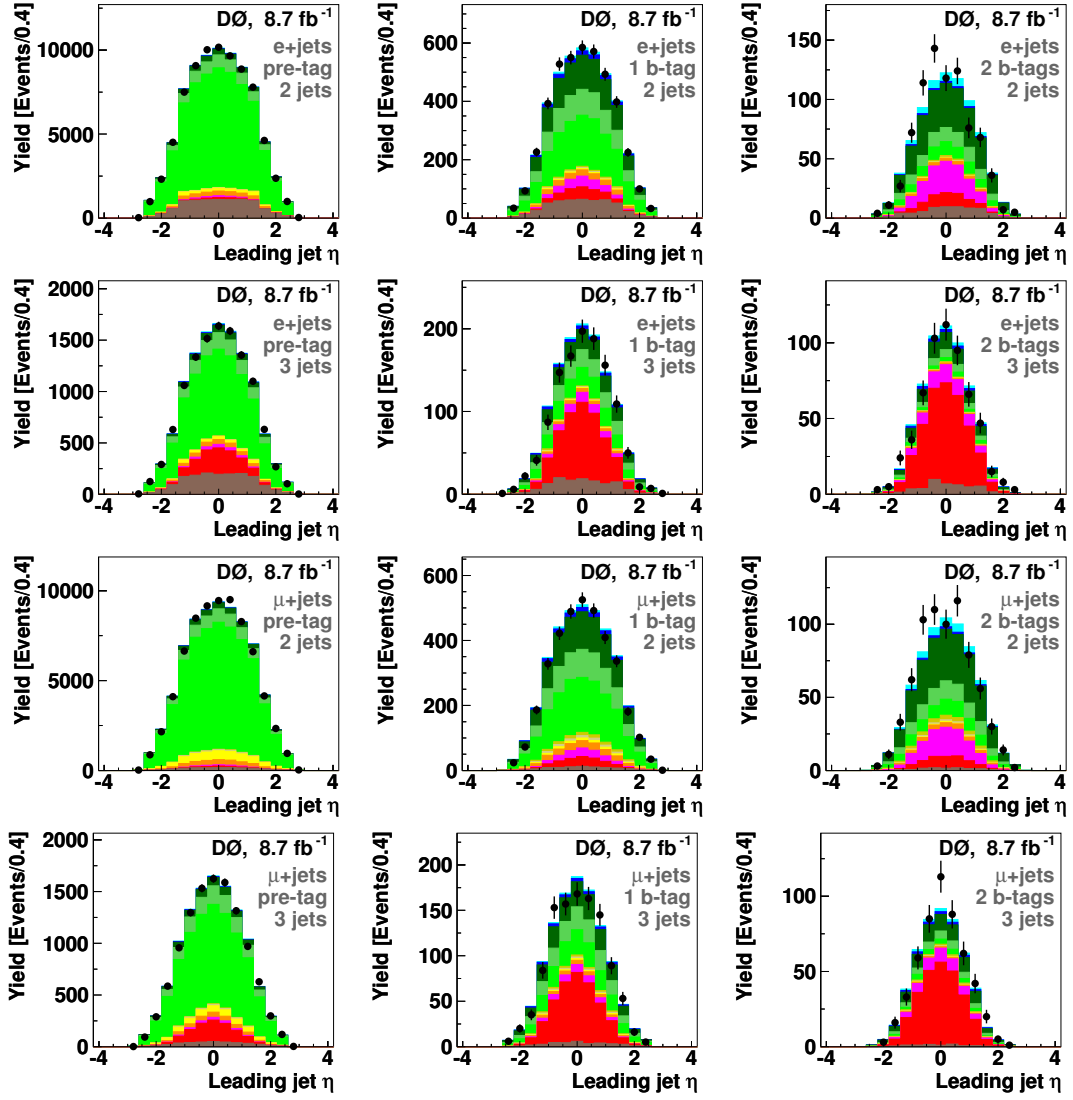


**Figure D.6** The pseudorapidity of the leading jet for pre-tagged (left), single-tagged (central), and double-tagged (right) for Run IIb, electron and muon channels, two-jet and three-jet events.

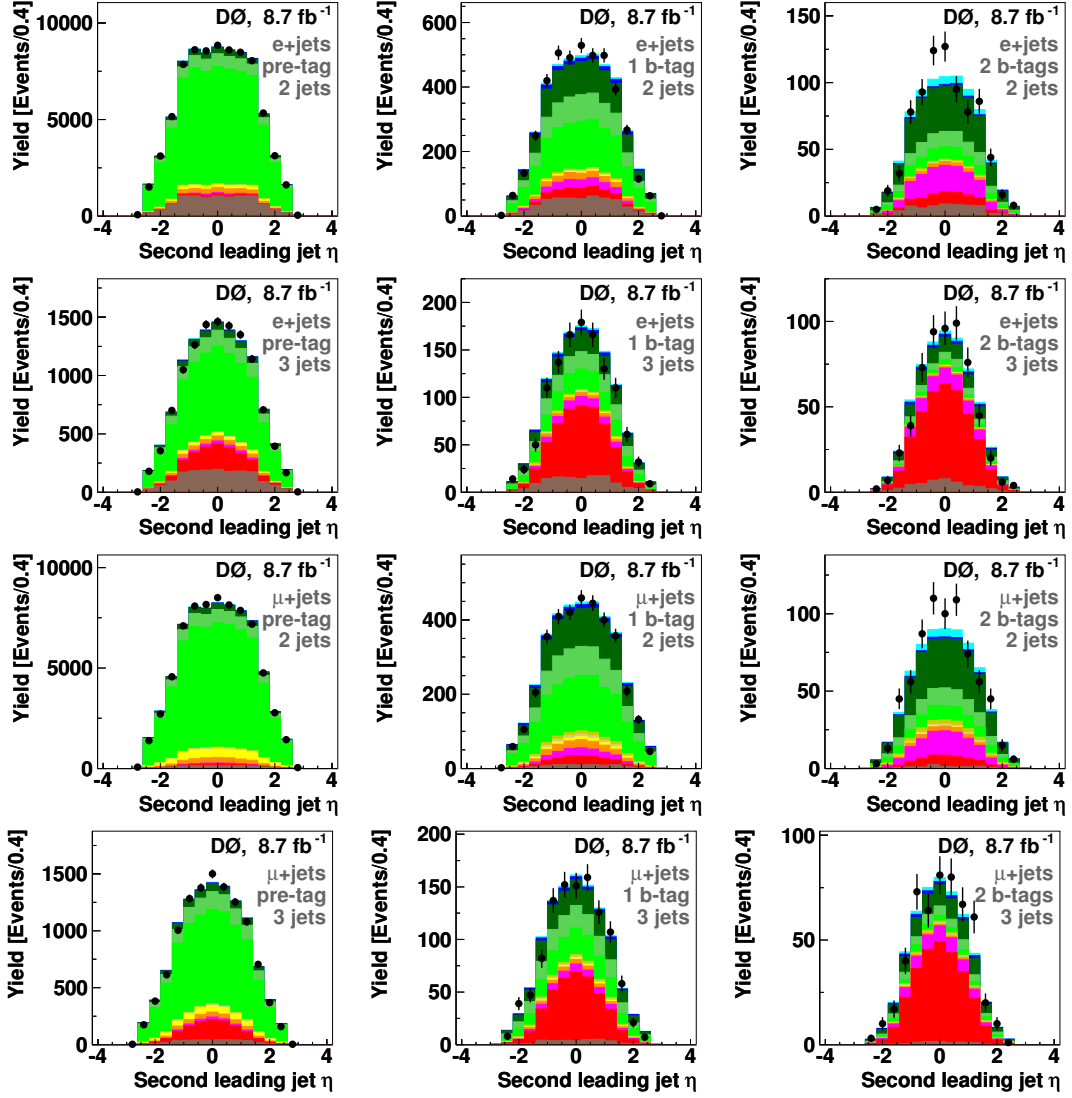


Figure D.7 The pseudorapidity of the second leading jet for pre-tagged (left), single-tagged (central), and double-tagged (right) for Run IIb, electron and muon channels, two-jet and three-jet events.

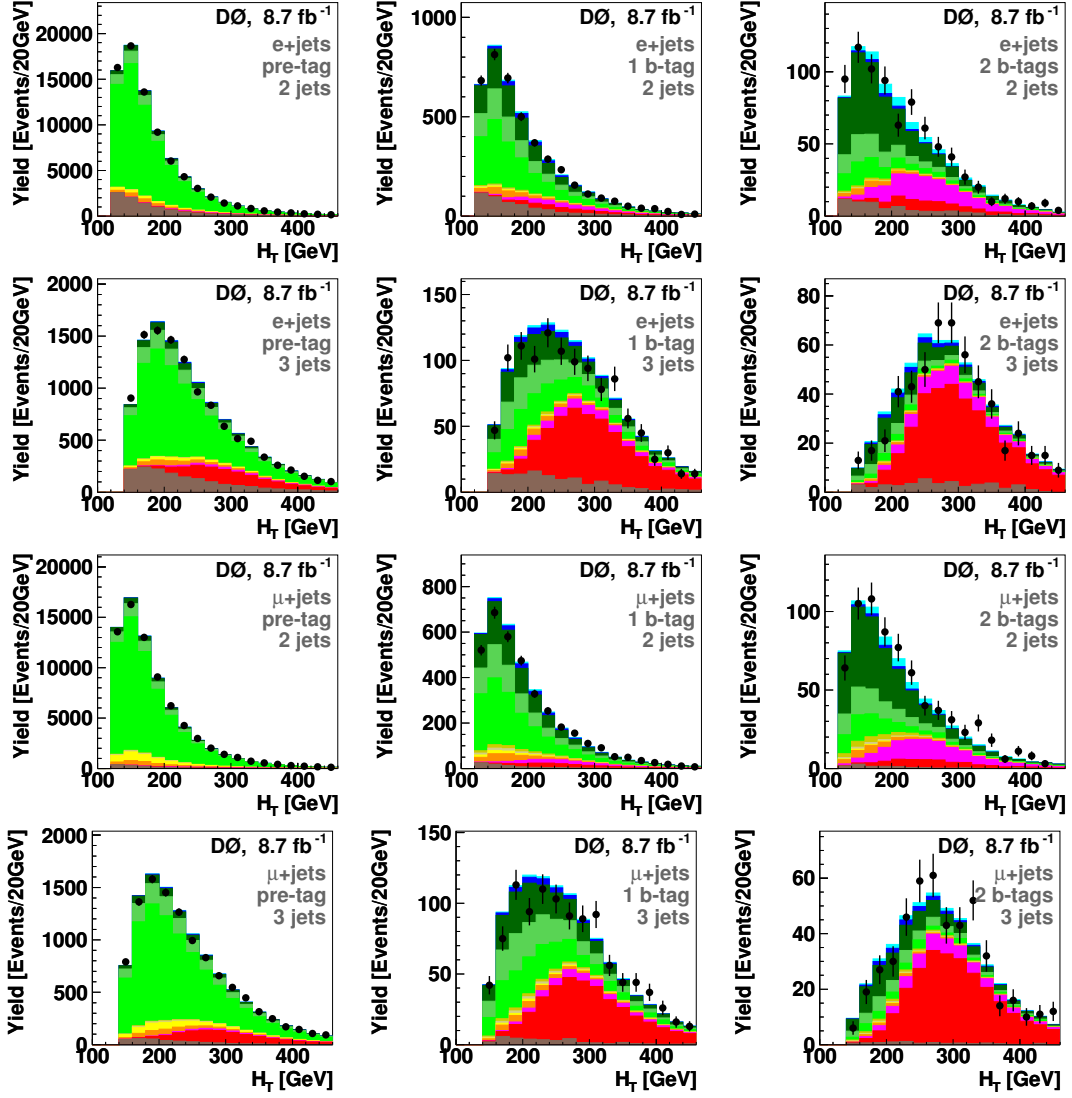
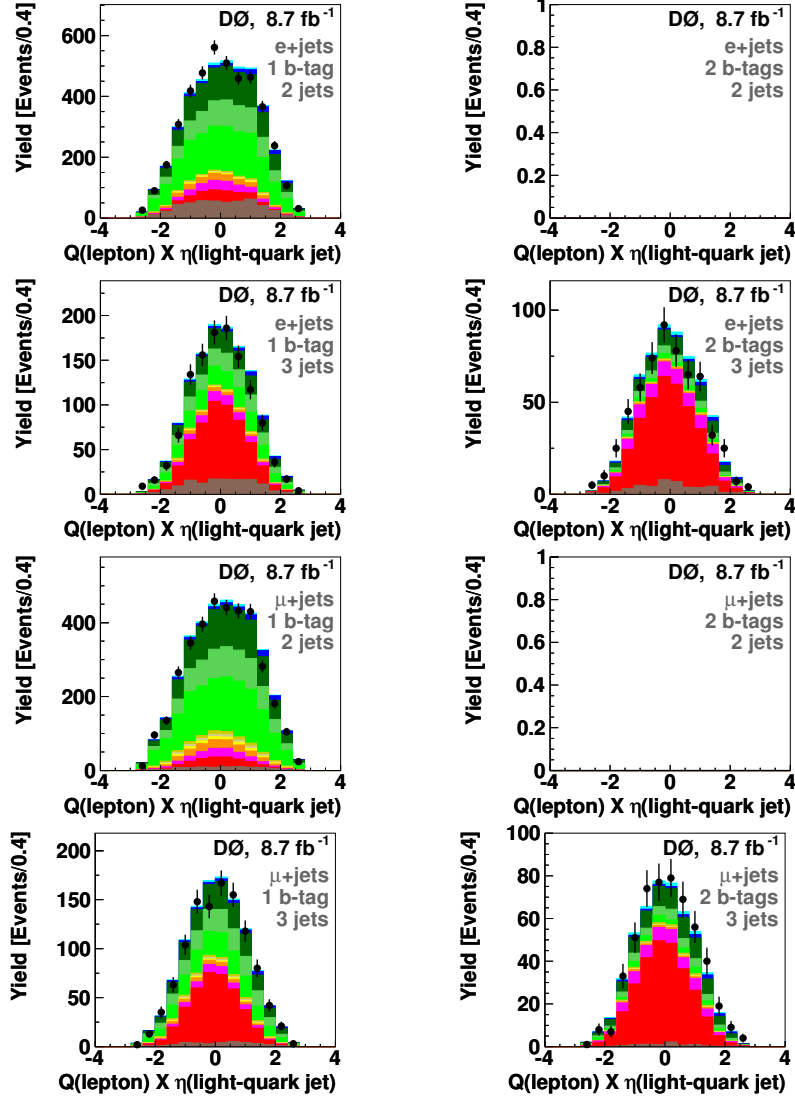


Figure D.8 The scalar transverse energy sum for pre-tagged (left), single-tagged (central), and double-tagged (right) for Run IIb, electron and muon channels, two-jet and three-jet events.



**Figure D.9** The pseudorapidity of the light quark jet times lepton charge for single-tagged (left) and double-tagged (right) for Run IIb, electron and muon channels, two-jet and three-jet events.

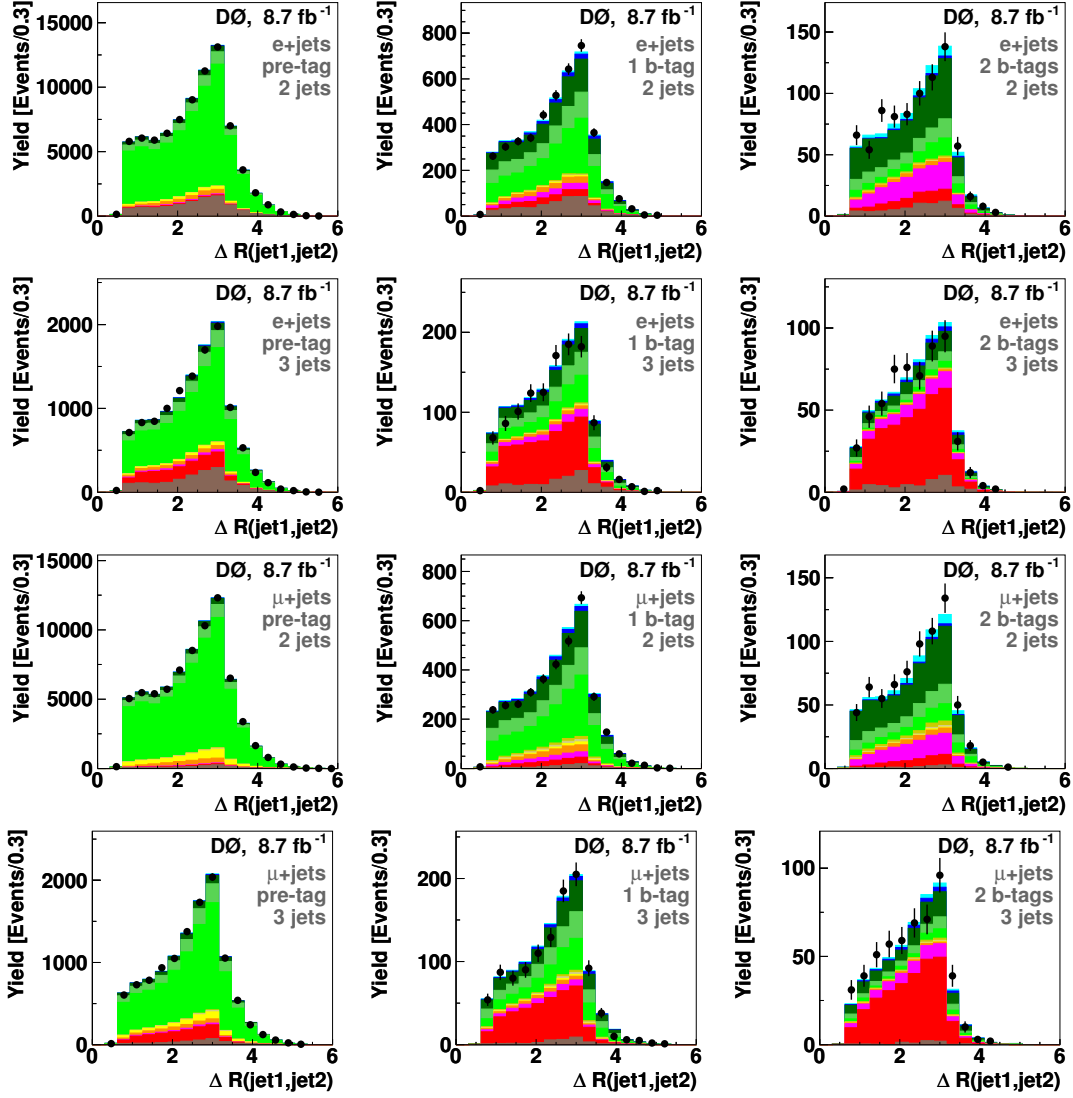


Figure D.10 The angular distance  $\Delta R$  between the leading two jets for pre-tagged (left), single-tagged (central), and double-tagged (right) for Run IIb, electron and muon channels, two-jet and three-jet events.

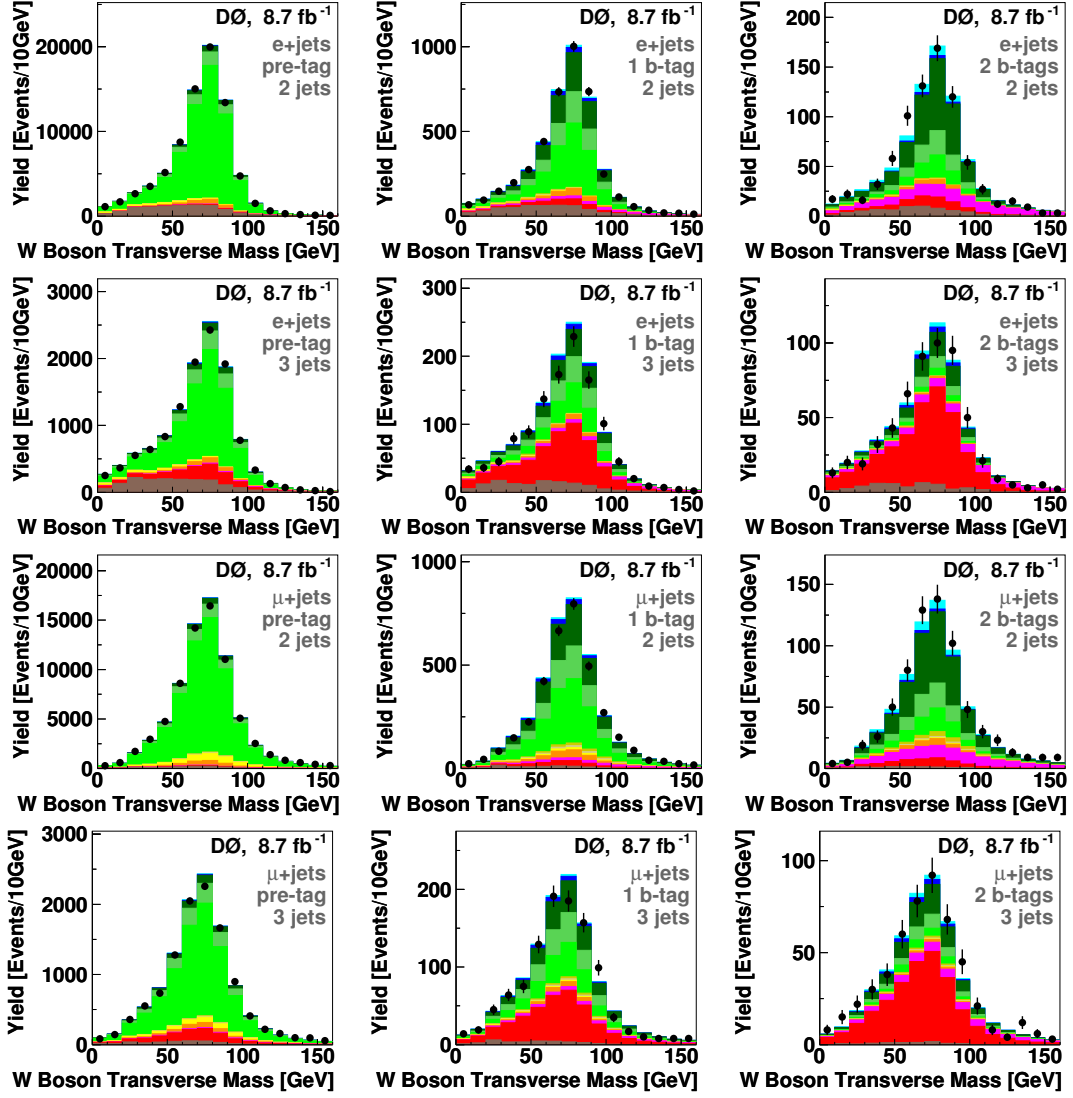
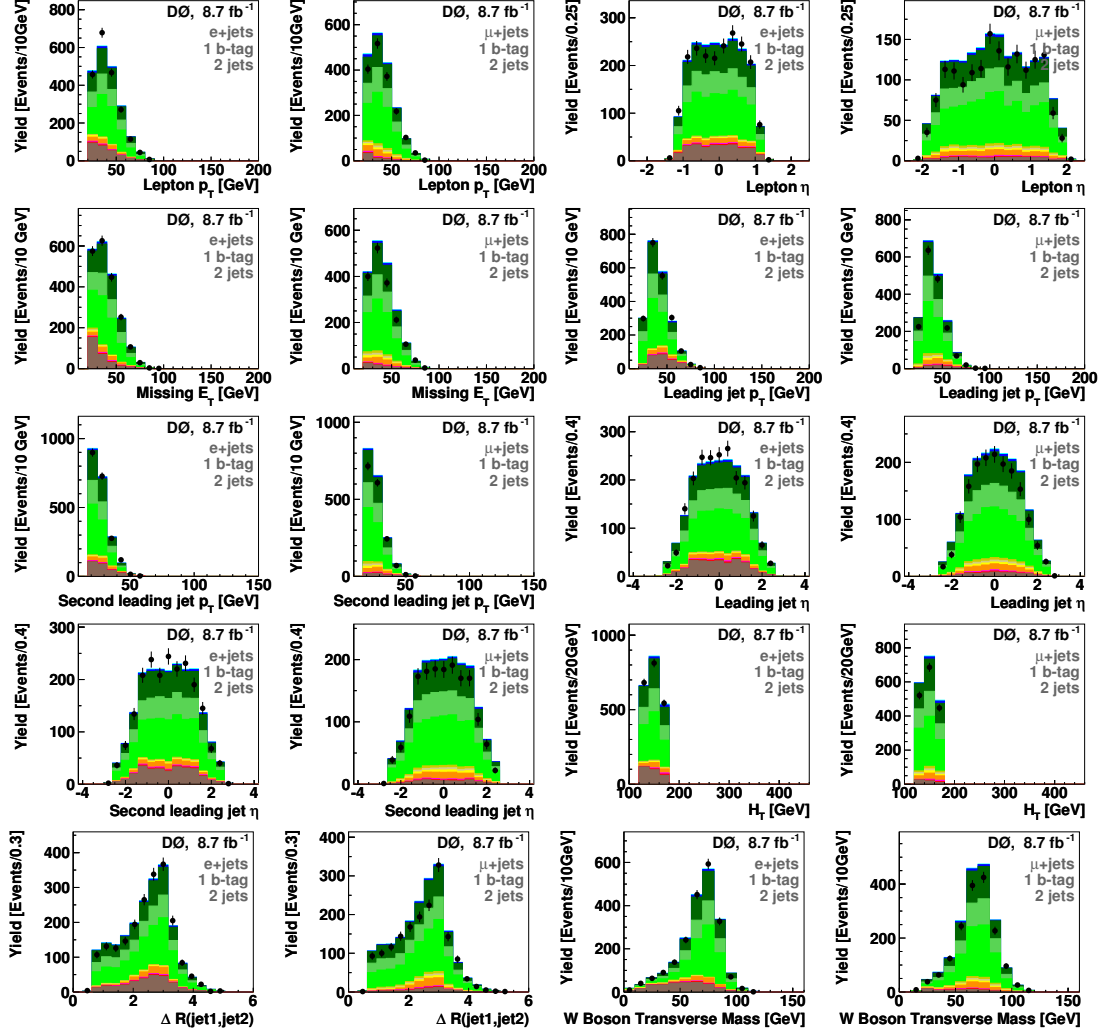
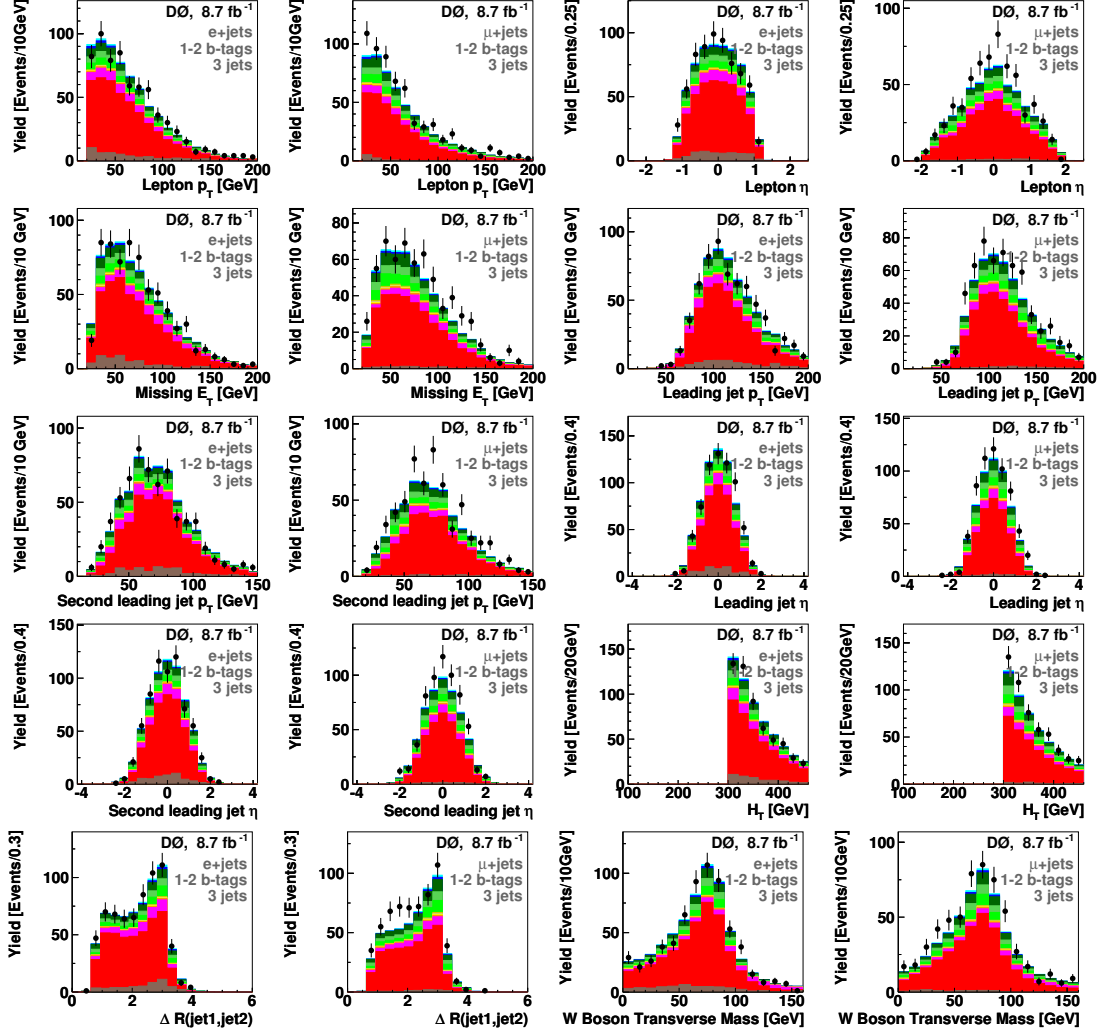


Figure D.11 The transverse mass of the W boson from the top quark for pre-tagged (left), single-tagged (central), and double-tagged (right) for Run IIb, electron and muon channels, two-jet and three-jet events.

## E Cross-Check Plots

Figure E.1 shows some kinematic distributions in the  $W$ +jets enriched sample (2 jets, 1  $b$ -tag,  $H_T < 175$  GeV). Figure E.2 shows some kinematic distributions in the  $t\bar{t}$  enriched sample (3 jets,  $\geq 1$   $b$ -tag,  $H_T > 300$  GeV).

Figure E.1 Cross-check plots for several variables in the  $W$ +Jets enriched samples.

Figure E.2 Cross-check plots for several variables in the  $t\bar{t}$  enriched samples.

## F Differential Cross Section

The differential cross section integral in the matrix element method is complicated. Based on the concept described in Section 6.1.2, we discuss further details of the calculation in this appendix. Appendix F.1 explicitly demonstrates the hard scattering part in Equation (6.1.2), Appendix F.2 shows the general idea of the phase space, and Appendix F.3 presents how to evaluate the neutrino four-momentum by the energy and momentum conservation laws. We demonstrate the full integral of the differential cross section in Appendix F.4, while the process-optimized Jacobian determinants coming from the phase transformation, and the sampling techniques are explained in Appendices I and J, respectively.

### F.1 Hard Scatter Differential Cross Sections

In a  $2 \rightarrow n$  process, the differential cross section is given by

$$d\sigma = \frac{(2\pi)^4 |\mathcal{M}|^2}{4\sqrt{(p_1 \cdot p_2)^2 - m_1^2 m_2^2}} d\Phi_n(p_1 + p_2; p_3, \dots, p_{n+2}). \quad (\text{F.1.1})$$

We assume the incoming partons,  $p_1$  and  $p_2$ , are moving along the  $z$ -axis; in other words, the two incoming partons have no transverse momenta. Moreover, the masses of the incoming partons are negligible compared to their energies. Therefore, their four-momenta can be written as

$$p_1 = (E_{beam}\xi_1, 0, 0, E_{beam}\xi_1) \quad (\text{F.1.2})$$

$$p_2 = (E_{beam}\xi_2, 0, 0, -E_{beam}\xi_2) \quad (\text{F.1.3})$$

where the  $E_{beam}$  is the beam energy, 980 GeV at the Tevatron, and the  $\xi_1$  and  $\xi_2$  are the momentum fractions of the  $p_1$  and  $p_2$ , respectively.

Under this assumption, the flux factor in the hard scattering cross section can be written in terms of the beam energy and the two momentum fractions,

$$\frac{1}{\sqrt{(p_1 \cdot p_2)^2 - m_1^2 m_2^2}} \rightarrow \frac{1}{\sqrt{(p_1 \cdot p_2)^2}} = \frac{1}{2E_{beam}^2 \xi_1 \xi_2}. \quad (\text{F.1.4})$$

## F.2 Phase Space

For a  $2 \rightarrow n$  process, the phase space element is constrained by a  $\delta$ -function due to the energy-momentum conservation of the whole system

$$d\Phi_n(p_1 + p_2; p_3, \dots, p_{n+2}) = \delta^4(p_1 + p_2 - \sum_{i=3}^{n+2} p_i) \prod_{i=1}^{n+2} \frac{d^4 p_i}{(2\pi)^3}. \quad (\text{F.2.1})$$

With a known mass value for each parton, we have a  $\delta$ -function which kills the integral over energy:

$$\begin{aligned} \int d^4 p &= \int \int d^3 \mathbf{p} dE \delta(E^2 - \mathbf{p}^2 - m^2) \\ &= \int \int \frac{d^3 \mathbf{p} d(E^2 - \mathbf{p}^2 - m^2)}{2E} \delta(E^2 - \mathbf{p}^2 - m^2) \\ &= \int \frac{d^3 \mathbf{p}}{2E} \delta(E^2 - \mathbf{p}^2 - m^2). \end{aligned} \quad (\text{F.2.2})$$

Therefore, the phase space of the  $n$ -body final state can be written as

$$\begin{aligned} d\Phi_n(p_1 + p_2; p_3, \dots, p_{n+2}) &= \delta^4(p_1 + p_2 - \sum_{i=3}^{n+2} p_i) \prod_{i=3}^{n+2} \frac{d^3 \mathbf{p}_i}{(2\pi)^3 2E_i} \\ &= \delta^4(p_1 + p_2 - \sum_{i=3}^{n+2} p_i) \prod_{i=3, i \neq 4}^{n+2} \frac{\mathbf{p}_i^2 d\mathbf{p}_i d\Omega_i}{(2\pi)^3 2E_i} \frac{d^3 \mathbf{p}_4}{(2\pi)^3 2E_4}. \end{aligned} \quad (\text{F.2.3})$$

For the  $ggg$  process, we remove the energy and the momentum conservations of the whole system and the neutrino term in the phase space, because only the

events with large missing energy will pass our selection:

$$d\Phi_3(p_1 + p_2; p_3, p_5, p_6) = \prod_{i=3, i \neq 4}^6 \frac{\mathbf{p}_i^2 d\mathbf{p}_i d\Omega_i}{(2\pi)^3 2E_i}. \quad (\text{F.2.4})$$

### F.3 Energy and Momentum Conservation and Neutrino Four-Momentum

Technically, we are integrating over the four-momenta of the final state partons whose corresponding reconstructed objects can be measured, i.e. all the partons except neutrinos, and the longitudinal momentum of the whole system. These integration variables are listed in Table 6.6 and the details of the change of variables and the sampling are demonstrated in Appendices I and J. The rest of the parton four-momenta can be derived by these variables.

First of all, given the values of the integration variables, the only missing quantity is the neutrino in the final state, and we can derive the four-momentum of the neutrino by energy and momentum conservation:

$$p_{tot}^x = p_1^x + p_2^x = \sum_{i=3}^{n+2} p_i^x = 0 \Rightarrow p_4^x = - \sum_{i=3, i \neq 4}^{n+2} p_i^x \quad (\text{F.3.1})$$

$$p_{tot}^y = p_1^y + p_2^y = \sum_{i=3}^{n+2} p_i^y = 0 \Rightarrow p_4^y = - \sum_{i=3, i \neq 4}^{n+2} p_i^y \quad (\text{F.3.2})$$

$$p_{tot}^z = p_1^z + p_2^z = \sum_{i=3}^{n+2} p_i^z \Rightarrow p_4^z = p_{tot}^z - \sum_{i=3, i \neq 4}^{n+2} p_i^z \quad (\text{F.3.3})$$

$$= E_{beam}(\xi_1 - \xi_2) - \sum_{i=3, i \neq 4}^{n+2} p_i^z.$$

Since the mass of neutrinos is negligible, the neutrino energy is equal to the magnitude of its momentum,  $E_4 = \mathbf{p}_4$ .

Now we know all the four-momenta of the final state partons, and therefore

the total energy of the whole system can be calculated:

$$E_{tot} = E_1 + E_2 = E_{beam}(\xi_1 + \xi_2) = \sum_{i=3, i \neq 4}^{n+2} E_i. \quad (\text{F.3.4})$$

Sequentially, we can derive the four-momenta of the initial state parton, given the assumptions we made in Appendix F.1:

$$\begin{aligned} \xi_1 &= \frac{E_{tot} + p_{tot}^z}{2E_{beam}} \\ \xi_2 &= \frac{E_{tot} - p_{tot}^z}{2E_{beam}}. \end{aligned} \quad (\text{F.3.5})$$

As a result, we have the four-momenta of all the initial and the final state partons, and can use these variables to evaluate the differential cross section via the corresponding matrix element.

## F.4 The Full Integrals

In summary, the full integral to calculate the differential cross section of a  $2 \rightarrow n$  process is illustrated below:

$$\begin{aligned} \frac{d\sigma}{dx}(p\bar{p} \rightarrow x) &= \sum_{jet-parton} \sum_{i,j} \int_y f_i(\xi_1, Q^2) f_j(\xi_2, Q^2) \frac{(2\pi)^4 |\mathcal{M}(p_1(i)p_2(j) \rightarrow y)|^2}{8E_{beam}^2 \xi_1 \xi_2} W(x, y) \\ &\times \prod_{k=3, k \neq 4}^{n+2} \delta(\Omega_k^x - \Omega_k^y) \Theta_{parton}(y) \delta^4(p_1 + p_2 - \sum_{k=3}^{n+2} p_k) \prod_{k=3, k \neq 4}^{n+2} \frac{\mathbf{p}_k^2 d\Omega_k}{(2\pi)^3 2E_k} \frac{1}{(2\pi)^3 2E_4} \frac{S}{|J|} dy_{transf} \end{aligned} \quad (\text{F.4.1})$$

where  $\frac{1}{|J|}$  is the Jacobian determinant, and the forms of  $|J|$  are described in Appendix I.  $S$  is the sampling factor shown in Appendix J, and  $dy_{transf}$  is the trans-

formed phase space. For instance, for the single top-quark two-jet process,

$$dy_{transf} = du_{34} du_{345} du_6 dp_{tot}^z$$

$$S = \left[ (s_{34} - m_W^2)^2 + m_W^2 \Gamma_W^2 \right] \Delta r_{34} \times \left[ (s_{345} - m_t^2)^2 + m_t^2 \Gamma_t^2 \right] \Delta r_{345}$$

$$\times \frac{\Delta r_6}{\frac{1}{\sqrt{2\pi}\sigma_6} e^{-\frac{(\Delta E_6 - \mu_6)^2}{2\sigma_6^2}}}.$$

(F.4.2)

## G Supplements of Transfer Functions

We present more details about the jet transfer functions, including plots and parameters, in Appendix G.1. Additionally, the parameters of the muon and the fake electron transfer functions, as explained in Sections 6.1.3.2 and 6.1.3.4, are listed in Appendices G.2 and G.4, respectively. We re-derive the Run IIb jet transfer functions for this analysis, while the Run IIa jet, all the muon, and the electron transfer functions are taken from the top-quark mass analysis [162]. Moreover, the fake electron transfer function is the same as the one used in the previous single top-quark analysis [163].

### G.1 Jet

The jet transfer functions are determined using fully simulated  $t\bar{t}$  ALPGEN+PYTHIA Monte Carlo events, which are the same as used in the standard  $D\bar{O}$  analysis. The semileptonic top decay channel is chosen to include both light and  $b$  jets in the final state, and the events with top mass 150, 160, 165, 170, 172.5, 175, 180, 185, and 190 GeV are used for gaining more statistics. All the jet corrections used in the standard analysis are applied. In addition to the standard selection, we require exactly two jets matching to the light quarks from the  $W$  boson decay, and the other two jets matching to the  $b$  quarks from the top decay. Furthermore, a selection of  $|\Delta E| = |E_{jet} - E_{parton}| < 100$  GeV is applied to exclude the outliers in the fit.

As mentioned in Section 6.1.3.1, the jet transfer function has the form of

$$W_{jet}(E_x, E_y) = \frac{1}{\sqrt{2\pi}(c_2+c_3c_5)} \left\{ \exp \left[ -\frac{1}{2} \left( \frac{(E_x-E_y)-c_1}{c_2} \right)^2 \right] + c_3 \exp \left[ -\frac{1}{2} \left( \frac{(E_x-E_y)-c_4}{c_5} \right)^2 \right] \right\} \quad (\text{G.1.1})$$

where  $E_x$  is the energy of jet and  $E_y$  is the energy of parton.  $c_i$  can be written as a linear function of  $E_y$ :

$$c_i = a_i + b_i \times E_y. \quad (\text{G.1.2})$$

The 10 parameters,  $a_i$  and  $b_i$ , for each jet type in each  $|\eta^{\text{det}}|$  region are derived by minimizing the likelihood function

$$-\ln \mathcal{L} = -\sum_{i=1}^n \ln W_{jet}(E_x, E_y) \quad (\text{G.1.3})$$

for  $n$  selected jets. The parameter  $a_3$  is fixed to zero to constrain the area of the second Gaussian. Examples of the  $\Delta E$  distributions are shown in Figures G.1 to G.3.

From the comparison between the fully simulated MC events and the pseudo-data generated using the transfer functions, we find the peaks of the dijet and the three-jet invariant masses have different biases for Run IIb1 and Run IIb2 events. Hence, we derive the transfer functions separately for Run IIb1, IIb2, and IIb3. The parameters are listed in Tables G.2 to G.4, while the parameters for Run IIa are listed in Table G.1. Moreover, the shape of the transfer functions are shown in Figures G.4 to G.6.

## G.2 Muons

The parameters of the muon transfer functions are listed in Tables G.5 and G.6 for Run IIa and Run IIb, respectively. As an example, the Run IIb transfer functions for different parton transverse momenta are illustrated in Figure G.7.

## G.3 Electrons

The parameters of the electron transfer functions are listed in Equation (6.1.15), and a couple of examples of the the electron transfer functions are shown in Figure G.8.

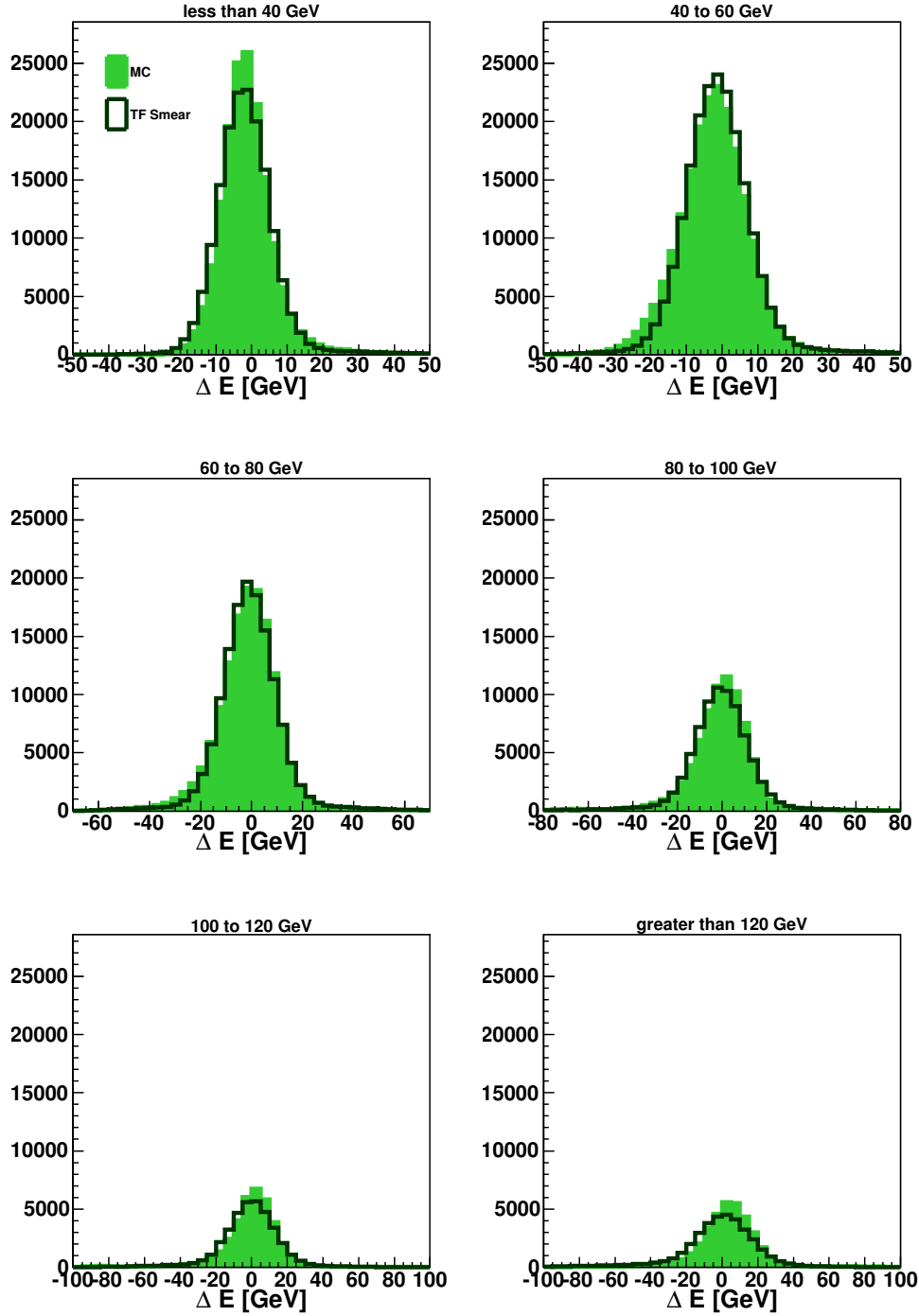


**Figure G.1** Distributions in  $\Delta E$  and transfer functions for light quarks in the range  $|\eta^{\text{det}}| < 0.4$  for Run IIB1, where the filled histograms are the  $\Delta E$  distribution of the fully simulated MC, and the open histograms are the pseudo-data generated with the transfer functions.

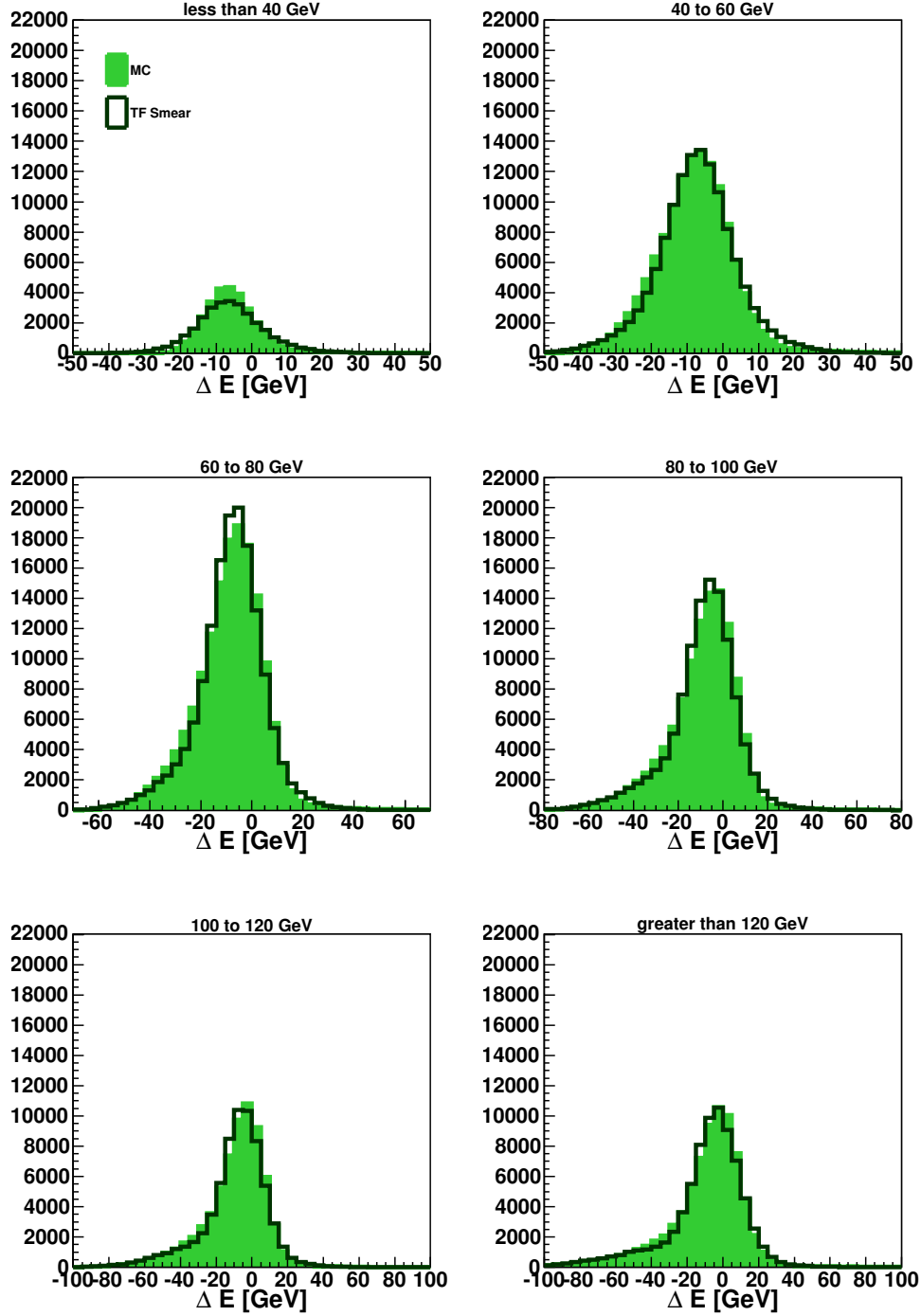


**Figure G.2** Distributions in  $\Delta E$  and transfer functions for  $b$  quarks in the range  $|\eta^{\text{det}}| < 0.4$  for Run IIb1, where the filled histograms are the  $\Delta E$  distribution of the fully simulated MC, and the open histograms are the pseudo-data generated with the transfer functions.

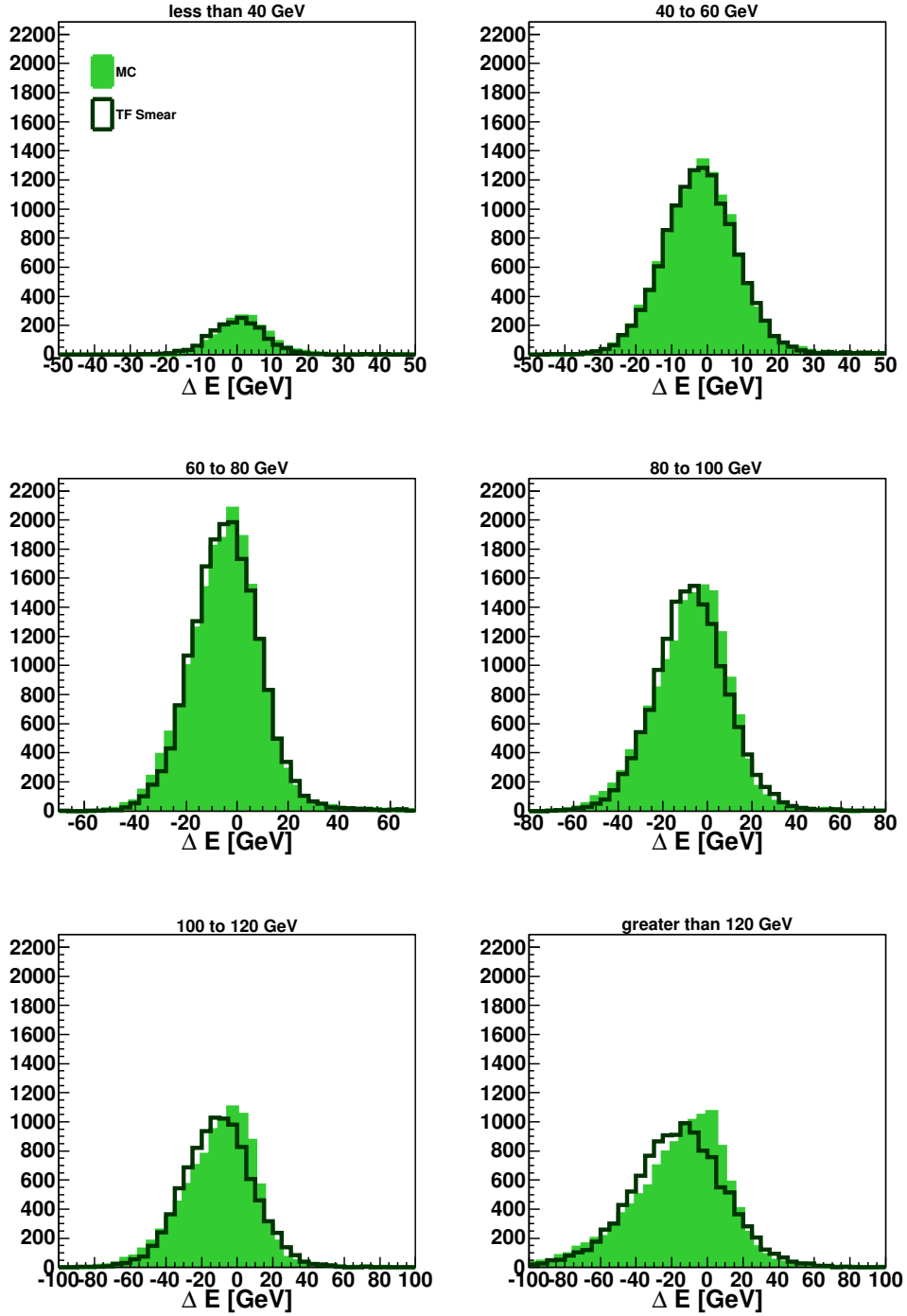


**Figure G.3** Distributions in  $\Delta E$  and transfer functions for  $b$  quarks with soft muons in the range  $|\eta^{\text{det}}| < 0.4$  for Run IIb1, where the filled histograms are the  $\Delta E$  distribution of the fully simulated MC, and the open histograms are the pseudo-data generated with the transfer functions.

$ \eta  < 0.4$	$l$ -jets		$b$ -jets		$b$ -jets with $\mu$	
$c_i = a_i + b_i \times E_y$	$a_i$	$b_i$	$a_i$	$b_i$	$a_i$	$b_i$
$c_1$	-0.81397	-0.02446	-5.80920	-0.02477	6.06311	-0.14391
$c_2$	3.60354	0.12846	3.69481	0.13338	1.99522	0.16667
$c_3$	0.	0.00039	0.	0.00058	0.	0.00015
$c_4$	26.47995	-0.24888	18.36126	-0.37502	44.06745	-0.40448
$c_5$	18.23981	0.16656	19.05745	0.10427	19.18532	0.15875

$0.4 \leq  \eta  < 0.8$	$l$ -jets		$b$ -jets		$b$ -jets with $\mu$	
$c_i = a_i + b_i \times E_y$	$a_i$	$b_i$	$a_i$	$b_i$	$a_i$	$b_i$
$c_1$	2.29687	-0.07739	-4.40726	-0.05399	9.42177	-0.17755
$c_2$	3.42214	0.14056	4.29494	0.14359	2.54109	0.16789
$c_3$	0.	0.00184	0.	0.00028	-0.00553	0.00102
$c_4$	4.34407	0.03785	21.21285	-0.12398	51.13812	-0.16163
$c_5$	14.94574	0.07996	21.38071	-0.02846	22.34586	0.06302

$0.8 \leq  \eta  < 1.6$	$l$ -jets		$b$ -jets		$b$ -jets with $\mu$	
$c_i = a_i + b_i \times E_y$	$a_i$	$b_i$	$a_i$	$b_i$	$a_i$	$b_i$
$c_1$	10.99137	-0.33563	4.12021	-0.25001	12.46998	-0.21734
$c_2$	4.15912	0.10325	1.80734	0.16880	4.58380	0.14364
$c_3$	0.	0.01875	0.	0.00826	-0.00553	0.00137
$c_4$	8.50616	-0.02495	2.56024	-0.02178	22.26436	-0.06097
$c_5$	10.82890	0.07564	13.54106	0.07845	18.73070	0.06950

$1.6 \leq  \eta  < 2.5$	$l$ -jets		$b$ -jets		$b$ -jets with $\mu$	
$c_i = a_i + b_i \times E_y$	$a_i$	$b_i$	$a_i$	$b_i$	$a_i$	$b_i$
$c_1$	18.03868	-0.26917	13.40536	-0.30090	$2.3849 \times 10^{-05}$	-0.13321
$c_2$	4.72508	0.13742	5.73795	0.12405	$3.6712 \times 10^{-05}$	0.17239
$c_3$	0.	0.00522	0.	0.00682	0.	0.00827
$c_4$	23.79935	-0.06444	10.91089	-0.05382	17.66395	-0.14506
$c_5$	18.72477	0.06337	17.89102	0.07194	15.12039	0.12867

**Table G.1** RunIIa transfer-function parameters for light jets,  $b$  jets, and soft muon tagged  $b$  jets, for four regions of detector  $|\eta|$ . Note the RunIIa parameters are not updated.

$ \eta  < 0.4$	$l$ -jets		$b$ -jets		$b$ -jets with $\mu$	
$c_i = a_i + b_i \times E_y$	$a_i$	$b_i$	$a_i$	$b_i$	$a_i$	$b_i$
$c_1$	-3.15336	0.03122	3.49955	-0.22828	5.19671	-0.14198
$c_2$	4.74917	0.06362	5.53942	0.18477	1.44956	0.15833
$c_3$	0.	0.00049	0.	0.05296	0.	0.00018
$c_4$	18.54499	-0.24832	-9.01929	0.04152	51.63531	-0.57143
$c_5$	17.80504	0.17724	5.06492	0.04485	20.39062	0.13360

$0.4 \leq  \eta  < 0.8$	$l$ -jets		$b$ -jets		$b$ -jets with $\mu$	
$c_i = a_i + b_i \times E_y$	$a_i$	$b_i$	$a_i$	$b_i$	$a_i$	$b_i$
$c_1$	-2.37916	0.02221	4.83195	-0.24168	5.92263	-0.15221
$c_2$	4.50603	0.07835	5.43388	0.18248	1.33181	0.16609
$c_3$	0.	0.00049	0.	0.04052	0.	0.00050
$c_4$	21.26791	-0.27143	-9.45410	0.04374	40.	-0.8
$c_5$	18.68937	0.16361	4.74531	0.05604	0.	0.4

$0.8 \leq  \eta  < 1.6$	$l$ -jets		$b$ -jets		$b$ -jets with $\mu$	
$c_i = a_i + b_i \times E_y$	$a_i$	$b_i$	$a_i$	$b_i$	$a_i$	$b_i$
$c_1$	3.27476	-0.04306	19.20891	-0.35806	8.00016	-0.13930
$c_2$	5.34971	0.12045	5.42841	0.24400	8.54300	0.12847
$c_3$	0.	0.00057	0.	0.09871	0.	0.001
$c_4$	27.06298	-0.19952	-5.70107	-0.05365	60.	-0.8
$c_5$	20.78713	0.13228	2.29423	0.15094	10.	0.2

$1.6 \leq  \eta  < 2.5$	$l$ -jets		$b$ -jets		$b$ -jets with $\mu$	
$c_i = a_i + b_i \times E_y$	$a_i$	$b_i$	$a_i$	$b_i$	$a_i$	$b_i$
$c_1$	19.72068	-0.26720	20.88181	-0.39546	38.19490	-0.45210
$c_2$	3.61382	0.14168	6.85892	0.09498	9.17963	0.07415
$c_3$	0.	0.00675	0.	0.01164	0.	0.00822
$c_4$	21.22876	-0.06988	8.74802	-0.08015	22.19751	-0.14513
$c_5$	20.00924	0.03722	17.63719	0.05536	14.33219	0.08175

**Table G.2** Run IIb1 transfer-function parameters for light jets,  $b$  jets, and soft muon tagged  $b$  jets, for four regions of detector  $|\eta|$ .

$ \eta  < 0.4$	$l$ -jets		$b$ -jets		$b$ -jets with $\mu$	
$c_i = a_i + b_i \times E_y$	$a_i$	$b_i$	$a_i$	$b_i$	$a_i$	$b_i$
$c_1$	-3.04666	0.03295	3.57851	-0.22658	4.98535	-0.13919
$c_2$	4.91712	0.06117	5.58559	0.18547	1.48182	0.16070
$c_3$	0.	0.00050	0.	0.05147	0.	0.00023
$c_4$	18.96732	-0.24561	-8.88103	0.04209	42.43060	-0.44193
$c_5$	17.60159	0.18413	5.10860	0.04415	15.65203	0.18272

$0.4 \leq  \eta  < 0.8$	$l$ -jets		$b$ -jets		$b$ -jets with $\mu$	
$c_i = a_i + b_i \times E_y$	$a_i$	$b_i$	$a_i$	$b_i$	$a_i$	$b_i$
$c_1$	-2.22855	0.02521	4.43854	-0.23041	5.92263	-0.15221
$c_2$	4.83727	0.07341	5.15434	0.18744	1.33181	0.16609
$c_3$	0.	0.00053	0.	0.03849	0.	0.00050
$c_4$	21.25433	-0.26655	-9.23839	0.04346	40.	-0.8
$c_5$	18.99669	0.15960	4.86087	0.05485	0.	0.4

$0.8 \leq  \eta  < 1.6$	$l$ -jets		$b$ -jets		$b$ -jets with $\mu$	
$c_i = a_i + b_i \times E_y$	$a_i$	$b_i$	$a_i$	$b_i$	$a_i$	$b_i$
$c_1$	3.64149	-0.04366	22.49952	-0.37503	8.00016	-0.13930
$c_2$	5.48246	0.11992	6.00012	0.26100	8.54300	0.12847
$c_3$	0.	0.00060	0.	0.15379	0.	0.001
$c_4$	27.60015	-0.20688	-4.44720	-0.06674	60.	-0.8
$c_5$	20.78339	0.13327	2.49658	0.15440	10.	0.2

$1.6 \leq  \eta  < 2.5$	$l$ -jets		$b$ -jets		$b$ -jets with $\mu$	
$c_i = a_i + b_i \times E_y$	$a_i$	$b_i$	$a_i$	$b_i$	$a_i$	$b_i$
$c_1$	19.39697	-0.26395	19.19868	-0.36715	42.67352	-0.48993
$c_2$	3.72269	0.14235	6.84438	0.10086	13.19712	0.04483
$c_3$	0.	0.00702	0.	0.01062	0.	0.00917
$c_4$	20.33988	-0.06607	8.39593	-0.07261	21.71256	-0.15539
$c_5$	20.42434	0.03447	18.15532	0.05103	14.68744	0.08633

**Table G.3** Run IIb2 transfer-function parameters for light jets,  $b$  jets, and soft muon tagged  $b$  jets, for four regions of detector  $|\eta|$ .

$ \eta  < 0.4$	$l$ -jets		$b$ -jets		$b$ -jets with $\mu$	
$c_i = a_i + b_i \times E_y$	$a_i$	$b_i$	$a_i$	$b_i$	$a_i$	$b_i$
$c_1$	-2.99078	0.03344	9.04120	-0.27982	6.02732	-0.13720
$c_2$	4.97725	0.06055	7.35648	0.19182	1.66887	0.15557
$c_3$	0.	0.00054	0.	0.08381	0.	0.00036
$c_4$	19.87114	-0.23995	-7.30323	0.03164	40.12658	-0.43209
$c_5$	18.89541	0.16652	5.05067	0.04719	16.93613	0.15418

$0.4 \leq  \eta  < 0.8$	$l$ -jets		$b$ -jets		$b$ -jets with $\mu$	
$c_i = a_i + b_i \times E_y$	$a_i$	$b_i$	$a_i$	$b_i$	$a_i$	$b_i$
$c_1$	-2.20022	0.02474	9.35998	-0.27878	6.51418	-0.14565
$c_2$	4.87848	0.07337	7.19660	0.18408	1.67951	0.15868
$c_3$	0.	0.00057	0.	0.05900	0.	0.00029
$c_4$	22.34631	-0.26033	-7.75118	0.03415	43.38112	-0.39625
$c_5$	20.15927	0.14580	4.65072	0.05924	19.03889	0.15078

$0.8 \leq  \eta  < 1.6$	$l$ -jets		$b$ -jets		$b$ -jets with $\mu$	
$c_i = a_i + b_i \times E_y$	$a_i$	$b_i$	$a_i$	$b_i$	$a_i$	$b_i$
$c_1$	3.80016	-0.04618	29.40841	-0.39180	12.59581	-0.19726
$c_2$	5.69836	0.11796	9.15025	0.27074	3.06590	0.15916
$c_3$	0.	0.00062	0.	0.29667	0.	0.00027
$c_4$	28.12396	-0.19600	-2.29435	-0.08055	43.00534	-0.12726
$c_5$	22.03076	0.12306	2.94050	0.15494	24.64031	0.05245

$1.6 \leq  \eta  < 2.5$	$l$ -jets		$b$ -jets		$b$ -jets with $\mu$	
$c_i = a_i + b_i \times E_y$	$a_i$	$b_i$	$a_i$	$b_i$	$a_i$	$b_i$
$c_1$	19.32919	-0.24619	15.07680	-0.29950	35.82517	-0.39079
$c_2$	4.04187	0.14351	3.94481	0.13487	9.92004	0.08898
$c_3$	0.	0.00566	0.	0.00716	0.	0.00536
$c_4$	22.91672	-0.07328	11.40218	-0.07113	23.65697	-0.13659
$c_5$	21.85386	0.03099	20.16943	0.04198	17.96512	0.06800

**Table G.4** Run IIb3 transfer-function parameters for light jets,  $b$  jets, and soft muon tagged  $b$  jets, for four regions of detector  $|\eta|$ .

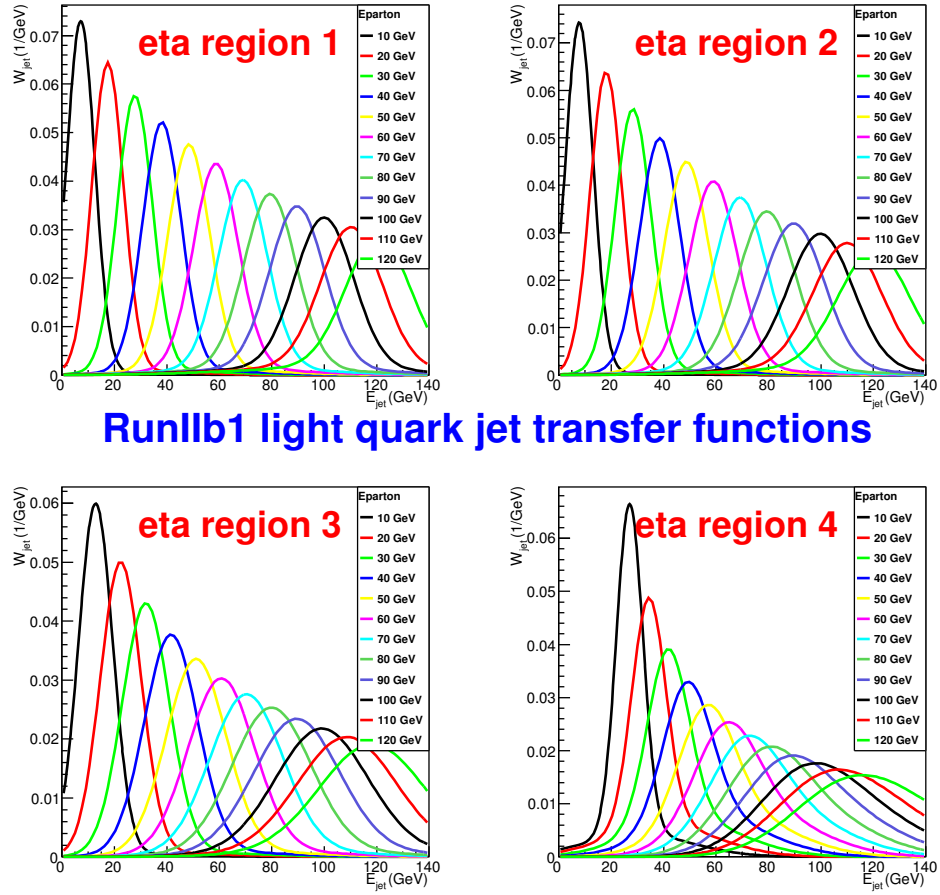


**Figure G.4** Transfer functions for light quark jets for different parton energies and for the following detector regions: (1)  $|\eta^{\text{det}}| < 0.4$ , (2)  $0.4 < |\eta^{\text{det}}| < 0.8$ , (3)  $0.8 < |\eta^{\text{det}}| < 1.6$ , (4)  $1.6 < |\eta^{\text{det}}| < 2.5$

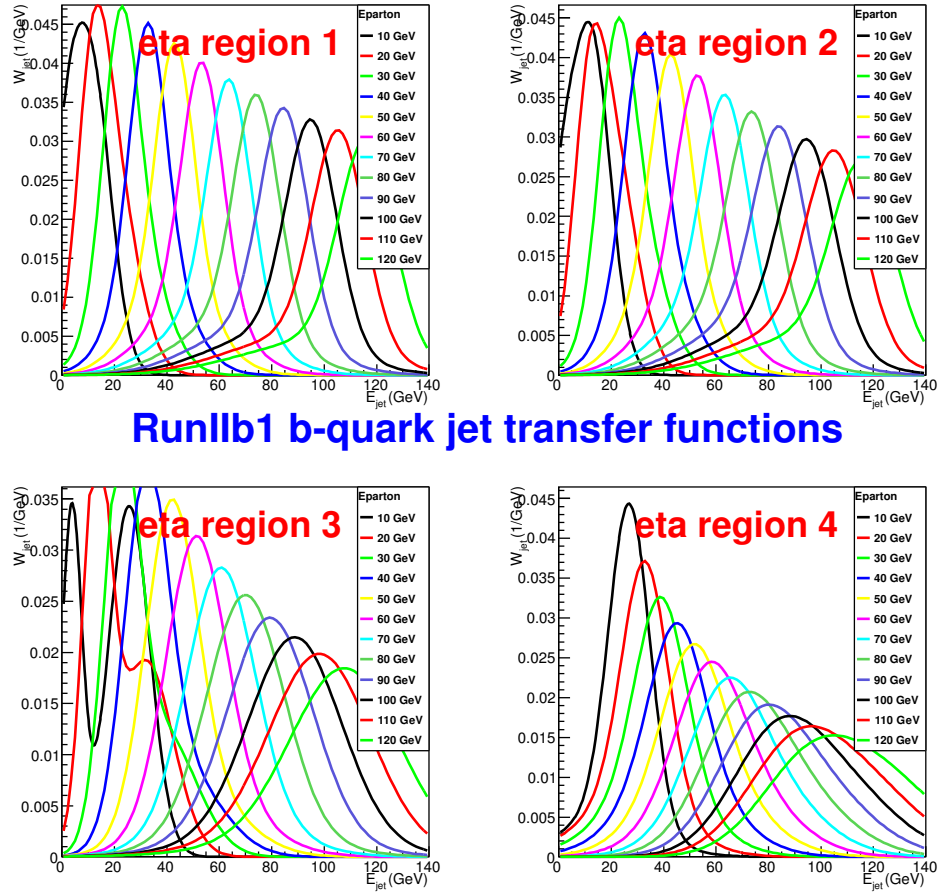


**Figure G.5** Transfer functions for  $b$  quark jets for different parton energies and for the following detector regions: (1)  $|\eta^{det}| < 0.4$ , (2)  $0.4 < |\eta^{det}| < 0.8$ , (3)  $0.8 < |\eta^{det}| < 1.6$ , (4)  $1.6 < |\eta^{det}| < 2.5$

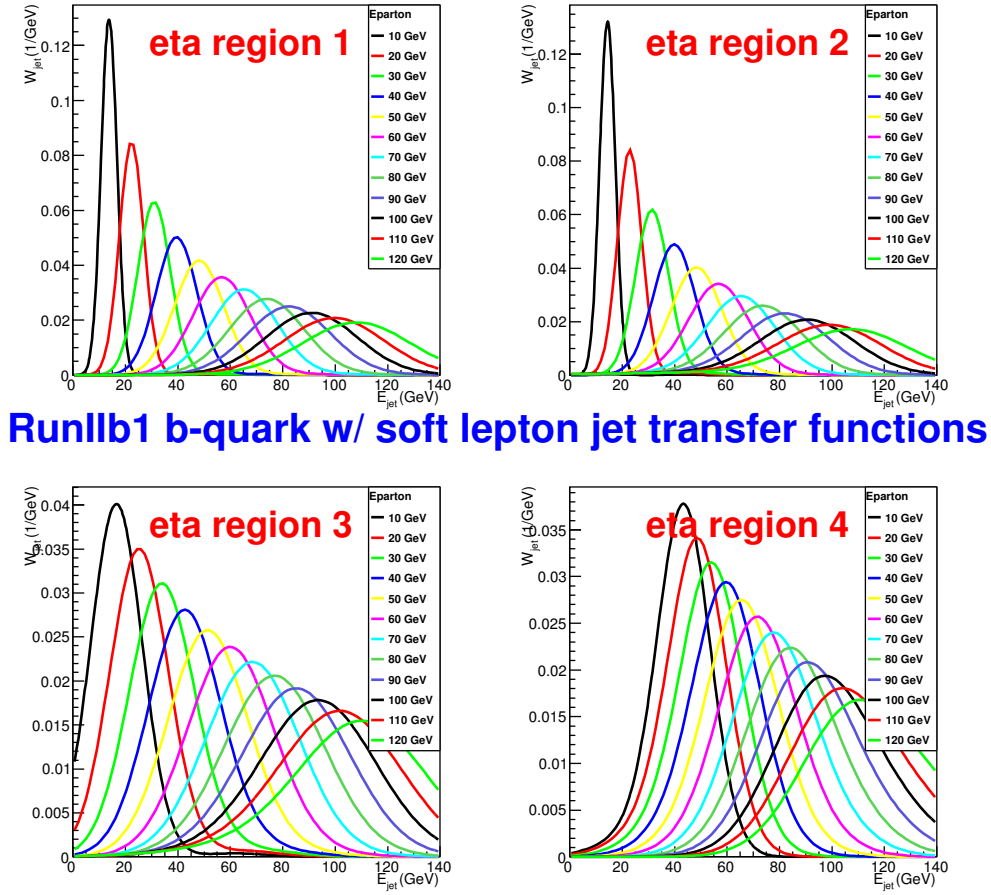


**Figure G.6** Transfer functions for light quark jets for different parton energies and for the following detector regions: (1)  $|\eta^{\text{det}}| < 0.4$ , (2)  $0.4 < |\eta^{\text{det}}| < 0.8$ , (3)  $0.8 < |\eta^{\text{det}}| < 1.6$ , (4)  $1.6 < |\eta^{\text{det}}| < 2.5$

parameters	with SMT hits		without SMT hits	
	pre-shutdown	post-shutdown	pre-shutdown	post-shutdown
$\sigma_0(0)$	$3.158 \times 10^{-3}$	$3.273 \times 10^{-3}$	$5.255 \times 10^{-3}$	$4.756 \times 10^{-3}$
$\sigma_0(1)$	$-2.769 \times 10^{-2}$	$-2.091 \times 10^{-2}$	$-5.269 \times 10^{-2}$	$-3.106 \times 10^{-2}$
$c_0(0)$	$4.239 \times 10^{-3}$	$9.403 \times 10^{-3}$	$2.037 \times 10^{-2}$	$2.065 \times 10^{-2}$
$c_0(1)$	$1.381 \times 10^{-1}$	$3.871 \times 10^{-1}$	$-1.730 \times 10^{-1}$	$-1.783 \times 10^{-1}$
$\eta_0(0)$	1.4	1.4	1.4	1.4
$\eta_0(1)$	0.	0.	0.	0.

**Table G.5** Run IIa muon transfer-function parameters, for pre-2004-shutdown and post-2004-shutdown data taking periods, and for the cases with and without SMT hits associated with muon tracks.

parameters	with SMT hits	without SMT hits
$\sigma_0(0)$	$2.082 \times 10^{-3}$	$3.620 \times 10^{-3}$
$\sigma_0(1)$	$1.125 \times 10^{-2}$	$1.388 \times 10^{-2}$
$c_0(0)$	$7.668 \times 10^{-3}$	$2.070 \times 10^{-2}$
$c_0(1)$	$7.851 \times 10^{-2}$	$7.042 \times 10^{-1}$
$\eta_0(0)$	1.4	1.4
$\eta_0(1)$	0.	0.

**Table G.6** Run IIb muon transfer-function parameters, for the cases with and without SMT hits associated with muon tracks.

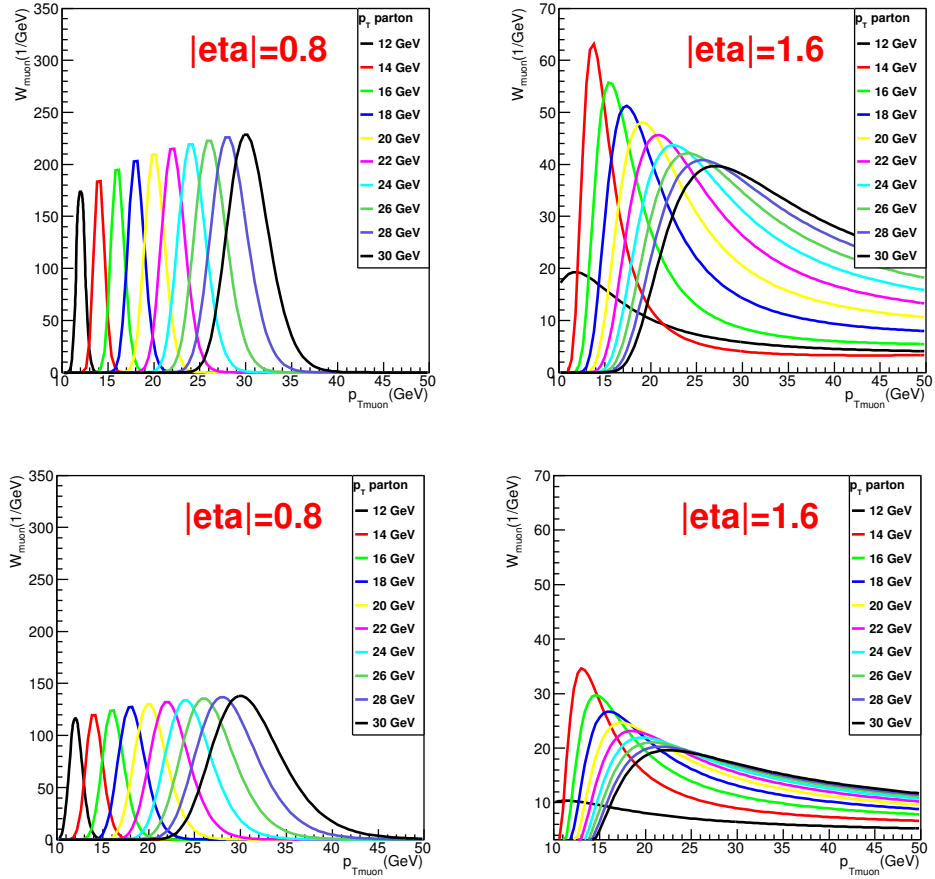


**Figure G.7** The muon transfer functions for different parton transverse momenta for Run IIb; the upper plots are the transfer functions with SMT hits, while the lower plots are the ones without SMT hits.

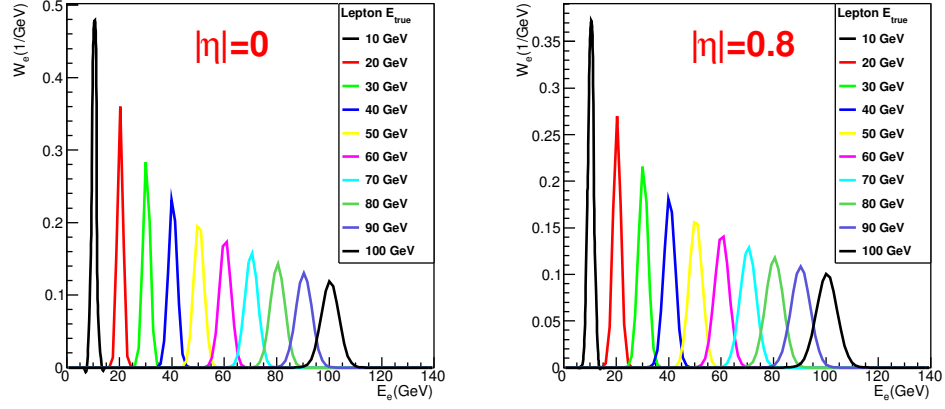


**Figure G.8** The electron transfer functions for different true electron energies.

## G.4 Fake Electrons

The parameters of the fake electron transfer functions are listed in Table G.7, and the plots are shown in Figure G.9.

$c_i = a_i + b_i \times E_y$	$a_i$	$b_i$
$c_1$	-8.15876	-0.09250
$c_2$	4.18329	0.03538
$c_3$	-2.15539	0.17162

**Table G.7** The parameters of the fake electron transfer functions.

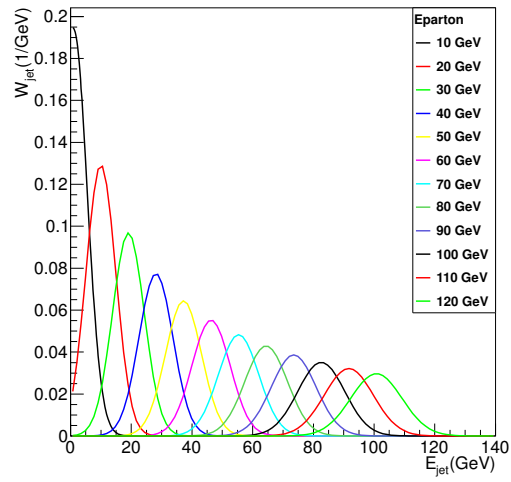


**Figure G.9** The fake electron transfer functions for different parton energies.

## H The Normalization of the Probabilities

As discussed in Section 6.1.4, the differential cross section evaluated in Section 6.1.2 should be normalized properly. The normalization constants derived and used in this analysis are listed in Tables H.1 to H.4. The difference between Run IIa and Run IIb are due to the different selections and transfer functions, while the one between Run IIb1, IIb2, and IIb3 are mainly due to the different jet transfer functions.

Two Jets			Three Jets		
Process	e+jets (pb)	$\mu$ +jets (pb)	Process	e+jets (pb)	$\mu$ +jets (pb)
$tb$	0.0759	0.0996	$tbq$	0.093	0.137
$tq$	0.149	0.209	$tqb$	0.0949	0.147
			$tqg$	0.0684	0.133
$Wbb$	0.325	0.466	$Wbbq$	0.255	0.41
$Wcg$	1.4	2.09	$Wugg$	2.9	5.58
$Wgg$	17.7	25.6			
$WW$	0.537	0.752			
$WZ$	0.031	0.0462			
$ggg$	$8.17 \times 10^{11}$	$1.44 \times 10^{12}$			
$t\bar{t}$	0.00265	0.00347	$t\bar{t}$	0.944	1.36

**Table H.1** The normalization constants for the Run IIa samples.

Two Jets			Three Jets		
Process	e+jets (pb)	$\mu$ +jets (pb)	Process	e+jets (pb)	$\mu$ +jets (pb)
$tb$	0.0593	0.0739	$tbg$	0.0551	0.0686
$tq$	0.103	0.135	$tqb$	0.0601	0.0772
			$tqg$	0.0369	0.0337
$Wbb$	0.224	0.322	$Wbbg$	0.126	0.172
$Wcg$	0.71	1.02	$Wugg$	1.05	1.82
$Wgg$	7.94	11			
$WW$	0.371	0.509			
$WZ$	0.0219	0.0324			
$ggg$	$1.0 \times 10^{11}$	$2.21 \times 10^{11}$			
$t\bar{t}$	0.00214	0.00267	$t\bar{t}$	0.769	0.937

**Table H.2** The normalization constants for the Run IIb1 samples.

Two Jets			Three Jets		
Process	e+jets (pb)	$\mu$ +jets (pb)	Process	e+jets (pb)	$\mu$ +jets (pb)
$tb$	0.0594	0.0741	$tbg$	0.0576	0.0706
$tq$	0.103	0.135	$tqb$	0.06	0.0775
			$tqg$	0.0392	0.0495
$Wbb$	0.227	0.317	$Wbbg$	0.128	0.175
$Wcg$	0.724	1.04	$Wugg$	1.08	1.86
$Wgg$	8.12	11.3			
$WW$	0.374	0.513			
$WZ$	0.022	0.0325			
$ggg$	$1.02 \times 10^{11}$	$2.26 \times 10^{11}$			
$t\bar{t}$	0.00215	0.00267	$t\bar{t}$	0.772	0.944

**Table H.3** The normalization constants for the Run IIb2 samples.

Two Jets			Three Jets		
Process	e+jets (pb)	$\mu$ +jets (pb)	Process	e+jets (pb)	$\mu$ +jets (pb)
$tb$	0.0603	0.0755	$tbg$	0.0597	0.0728
$tq$	0.103	0.135	$tqb$	0.064	0.0824
			$tqg$	0.0397	0.0538
$Wbb$	0.263	0.368	$Wbbg$	0.145	0.203
$Wcg$	0.739	1.06	$Wugg$	1.11	1.91
$Wgg$	8.32	11.6			
$WW$	0.373	0.513			
$WZ$	0.0228	0.0337			
$ggg$	$1.05 \times 10^{11}$	$2.31 \times 10^{11}$			
$t\bar{t}$	0.00217	0.00269	$t\bar{t}$	0.802	0.987

**Table H.4** The normalization constants for the Run IIb3 samples.

# I Integration Variable Remapping

As mentioned in Section 6.2.3.2, the phase space of integration is transformed to minimize the computing time. A Jacobian determinant is required for this change of variables. In this appendix, the details of these Jacobian determinants are further described. The complete Jacobians for each process are demonstrated and simplified in Appendix I.1, while the explicit formulae of these Jacobians are shown in Appendix I.2.

## I.1 Jacobians

### I.1.1 Jacobian for Single Top-Quark Two-Jet Processes

In general, the integration variables for the two-jet processes are the magnitudes of the momenta of the lepton ( $|\mathbf{p}_3|$ ) and the two quarks ( $|\mathbf{p}_5|$  and  $|\mathbf{p}_6|$ ), as well as the longitudinal momentum of the whole system ( $p_{tot}^z$ ). For the phase space transformation, we pick the squared invariant masses of the  $W$  ( $s_{34}$ ) boson and the top quark ( $s_{345}$ ), the magnitude of the momentum of the  $b$  quark associated with the top quark ( $|\mathbf{p}_6|$ ), and the longitudinal momentum of the whole system ( $p_{tot}^z$ ) specifically for the single top-quark two-jet processes,  $tb$  and  $tq$ . Hence, the phase space transformation is

$$dy_{singletop-2jets} = d|\mathbf{p}_3|d|\mathbf{p}_5|d|\mathbf{p}_6|dp_{tot}^z \rightarrow ds_{34}ds_{345}d|\mathbf{p}_6|dp_{tot}^z. \quad (\text{I.1.1})$$

And the corresponding Jacobian determinant is shown below:

$$|J| = \begin{vmatrix} \frac{\partial s_{34}}{\partial |\mathbf{p}_3|} & \frac{\partial s_{34}}{\partial |\mathbf{p}_5|} & \frac{\partial s_{34}}{\partial |\mathbf{p}_6|} & \frac{\partial s_{34}}{\partial p_{tot}^z} \\ \frac{\partial s_{345}}{\partial |\mathbf{p}_3|} & \frac{\partial s_{345}}{\partial |\mathbf{p}_5|} & \frac{\partial s_{345}}{\partial |\mathbf{p}_6|} & \frac{\partial s_{345}}{\partial p_{tot}^z} \\ \frac{\partial |\mathbf{p}_6|}{\partial |\mathbf{p}_3|} & \frac{\partial |\mathbf{p}_6|}{\partial |\mathbf{p}_5|} & \frac{\partial |\mathbf{p}_6|}{\partial |\mathbf{p}_6|} & \frac{\partial |\mathbf{p}_6|}{\partial p_{tot}^z} \\ \frac{\partial p_{tot}^z}{\partial |\mathbf{p}_3|} & \frac{\partial p_{tot}^z}{\partial |\mathbf{p}_5|} & \frac{\partial p_{tot}^z}{\partial |\mathbf{p}_6|} & \frac{\partial p_{tot}^z}{\partial p_{tot}^z} \end{vmatrix} = \begin{vmatrix} \frac{\partial s_{34}}{\partial |\mathbf{p}_3|} & \frac{\partial s_{34}}{\partial |\mathbf{p}_5|} & \frac{\partial s_{34}}{\partial |\mathbf{p}_6|} & \frac{\partial s_{34}}{\partial p_{tot}^z} \\ \frac{\partial s_{345}}{\partial |\mathbf{p}_3|} & \frac{\partial s_{345}}{\partial |\mathbf{p}_5|} & \frac{\partial s_{345}}{\partial |\mathbf{p}_6|} & \frac{\partial s_{345}}{\partial p_{tot}^z} \\ 0 & 0 & 1 & 0 \\ 0 & 0 & 0 & 1 \end{vmatrix} = \begin{vmatrix} \frac{\partial s_{34}}{\partial |\mathbf{p}_3|} & \frac{\partial s_{34}}{\partial |\mathbf{p}_5|} \\ \frac{\partial s_{345}}{\partial |\mathbf{p}_3|} & \frac{\partial s_{345}}{\partial |\mathbf{p}_5|} \end{vmatrix}. \quad (\text{I.1.2})$$

### I.1.2 Jacobian for $W+2$ Jets Processes

For the phase space transformation of the  $W+2$  Jets processes,  $Wbb$ ,  $Wcg$ , and  $Wgg$ , the magnitude of the momentum of the lepton is replaced by the squared invariant mass of the  $W$  boson, while the rest of the variables are unchanged,

$$dy_{W+2jets} = d|\mathbf{p}_3|d|\mathbf{p}_5|d|\mathbf{p}_6|dp_{tot}^z \rightarrow ds_{34}d|\mathbf{p}_5|d|\mathbf{p}_6|dp_{tot}^z. \quad (\text{I.1.3})$$

The Jacobian can be written and simplified as follow,

$$|J| = \begin{vmatrix} \frac{\partial s_{34}}{\partial |\mathbf{p}_3|} & \frac{\partial s_{34}}{\partial |\mathbf{p}_5|} & \frac{\partial s_{34}}{\partial |\mathbf{p}_6|} & \frac{\partial s_{34}}{\partial p_{tot}^z} \\ \frac{\partial |\mathbf{p}_5|}{\partial |\mathbf{p}_3|} & \frac{\partial |\mathbf{p}_5|}{\partial |\mathbf{p}_5|} & \frac{\partial |\mathbf{p}_5|}{\partial |\mathbf{p}_6|} & \frac{\partial |\mathbf{p}_5|}{\partial p_{tot}^z} \\ \frac{\partial |\mathbf{p}_6|}{\partial |\mathbf{p}_3|} & \frac{\partial |\mathbf{p}_6|}{\partial |\mathbf{p}_5|} & \frac{\partial |\mathbf{p}_6|}{\partial |\mathbf{p}_6|} & \frac{\partial |\mathbf{p}_6|}{\partial p_{tot}^z} \\ \frac{\partial p_{tot}^z}{\partial |\mathbf{p}_3|} & \frac{\partial p_{tot}^z}{\partial |\mathbf{p}_5|} & \frac{\partial p_{tot}^z}{\partial |\mathbf{p}_6|} & \frac{\partial p_{tot}^z}{\partial p_{tot}^z} \end{vmatrix} = \begin{vmatrix} \frac{\partial s_{34}}{\partial |\mathbf{p}_3|} & \frac{\partial s_{34}}{\partial |\mathbf{p}_5|} & \frac{\partial s_{34}}{\partial |\mathbf{p}_6|} & \frac{\partial s_{34}}{\partial p_{tot}^z} \\ 0 & 1 & 0 & 0 \\ 0 & 0 & 1 & 0 \\ 0 & 0 & 0 & 1 \end{vmatrix} = \left| \frac{\partial s_{34}}{\partial |\mathbf{p}_3|} \right|. \quad (\text{I.1.4})$$

### I.1.3 Jacobian for Diboson Two-Jet Processes

Similarly, the squared invariant masses of the  $W$  ( $s_{34}$ ) and the  $W/Z$  ( $s_{56}$ ) bosons are chosen as two of the integration variables for the diboson processes,  $WW$  and  $WZ$ . The  $|\mathbf{p}_6|$  and  $p_{tot}^z$  are used for the rest of the integration variables.

$$dy_{diboson-2jets} = d|\mathbf{p}_3|d|\mathbf{p}_5|d|\mathbf{p}_6|dp_{tot}^z \rightarrow ds_{34}ds_{56}d|\mathbf{p}_6|dp_{tot}^z. \quad (\text{I.1.5})$$

The Jacobian can be written and simplified as follows,

$$|J| = \begin{vmatrix} \frac{\partial s_{34}}{\partial |\mathbf{p}_3|} & \frac{\partial s_{34}}{\partial |\mathbf{p}_5|} & \frac{\partial s_{34}}{\partial |\mathbf{p}_6|} & \frac{\partial s_{34}}{\partial p_{tot}^z} \\ \frac{\partial s_{56}}{\partial |\mathbf{p}_3|} & \frac{\partial s_{56}}{\partial |\mathbf{p}_5|} & \frac{\partial s_{56}}{\partial |\mathbf{p}_6|} & \frac{\partial s_{56}}{\partial p_{tot}^z} \\ \frac{\partial |\mathbf{p}_6|}{\partial |\mathbf{p}_3|} & \frac{\partial |\mathbf{p}_6|}{\partial |\mathbf{p}_5|} & \frac{\partial |\mathbf{p}_6|}{\partial |\mathbf{p}_6|} & \frac{\partial |\mathbf{p}_6|}{\partial p_{tot}^z} \\ \frac{\partial p_{tot}^z}{\partial |\mathbf{p}_3|} & \frac{\partial p_{tot}^z}{\partial |\mathbf{p}_5|} & \frac{\partial p_{tot}^z}{\partial |\mathbf{p}_6|} & \frac{\partial p_{tot}^z}{\partial p_{tot}^z} \end{vmatrix} = \begin{vmatrix} \frac{\partial s_{34}}{\partial |\mathbf{p}_3|} & \frac{\partial s_{34}}{\partial |\mathbf{p}_5|} \\ \frac{\partial s_{56}}{\partial |\mathbf{p}_3|} & \frac{\partial s_{56}}{\partial |\mathbf{p}_5|} \end{vmatrix}. \quad (\text{I.1.6})$$

#### I.1.4 Jacobian for $t\bar{t}$ Two-Jet Processes

The  $t\bar{t}$  process is a particular one because of the missing jets (Section 6.2.4). In addition to the regular integration variables for the two-jet processes,  $|\mathbf{p}_3|$ ,  $|\mathbf{p}_5|$ ,  $|\mathbf{p}_6|$  and  $p_{tot}^z$ , we have to integrate over the phase space of the  $W$  boson (parton 7), of which the decay products are missing. Moreover, we assume this  $W$  boson is always on-shell, with the mass 80.4 GeV. Therefore, the phase space has seven degrees of freedom, and the additional three are the three-momentum of the  $W$  boson.

Among the two  $W$  bosons decaying from the top quarks, the one mentioned above is considered as a final-state parton, and its three-momentum is directly used in the integration. As a consequence, we can choose the squared invariant masses of the other  $W$  and the two quarks as three of the integration variables, for the kinematic equation is not too complicated in this case. The phase space transformation is therefore shown below,

$$dy_{t\bar{t}-2jets} = d|\mathbf{p}_3|d|\mathbf{p}_5|d|\mathbf{p}_6|d|\mathbf{p}_7|d\cos\theta_7d\phi_7dp_{tot}^z \rightarrow ds_{34}ds_{345}ds_{67}d|\mathbf{p}_7|d\cos\theta_7d\phi_7dp_{tot}^z. \quad (\text{I.1.7})$$

And the Jacobian can be written and simplified as follows,

$$|J| = \begin{vmatrix} \frac{\partial s_{34}}{\partial |\mathbf{p}_3|} & \frac{\partial s_{34}}{\partial |\mathbf{p}_5|} & \frac{\partial s_{34}}{\partial |\mathbf{p}_6|} & \frac{\partial s_{34}}{\partial |\mathbf{p}_7|} & \frac{\partial s_{34}}{\partial \cos\theta_7} & \frac{\partial s_{34}}{\partial \phi_7} & \frac{\partial s_{34}}{\partial p_{tot}^z} \\ \frac{\partial s_{345}}{\partial |\mathbf{p}_3|} & \frac{\partial s_{345}}{\partial |\mathbf{p}_5|} & \frac{\partial s_{345}}{\partial |\mathbf{p}_6|} & \frac{\partial s_{345}}{\partial |\mathbf{p}_7|} & \frac{\partial s_{345}}{\partial \cos\theta_7} & \frac{\partial s_{345}}{\partial \phi_7} & \frac{\partial s_{345}}{\partial p_{tot}^z} \\ \frac{\partial s_{67}}{\partial |\mathbf{p}_3|} & \frac{\partial s_{67}}{\partial |\mathbf{p}_5|} & \frac{\partial s_{67}}{\partial |\mathbf{p}_6|} & \frac{\partial s_{67}}{\partial |\mathbf{p}_7|} & \frac{\partial s_{67}}{\partial \cos\theta_7} & \frac{\partial s_{67}}{\partial \phi_7} & \frac{\partial s_{67}}{\partial p_{tot}^z} \\ \frac{\partial |\mathbf{p}_7|}{\partial |\mathbf{p}_3|} & \frac{\partial |\mathbf{p}_7|}{\partial |\mathbf{p}_5|} & \frac{\partial |\mathbf{p}_7|}{\partial |\mathbf{p}_6|} & \frac{\partial |\mathbf{p}_7|}{\partial |\mathbf{p}_7|} & \frac{\partial |\mathbf{p}_7|}{\partial \cos\theta_7} & \frac{\partial |\mathbf{p}_7|}{\partial \phi_7} & \frac{\partial |\mathbf{p}_7|}{\partial p_{tot}^z} \\ \frac{\partial \cos\theta_7}{\partial |\mathbf{p}_3|} & \frac{\partial \cos\theta_7}{\partial |\mathbf{p}_5|} & \frac{\partial \cos\theta_7}{\partial |\mathbf{p}_6|} & \frac{\partial \cos\theta_7}{\partial |\mathbf{p}_7|} & \frac{\partial \cos\theta_7}{\partial \cos\theta_7} & \frac{\partial \cos\theta_7}{\partial \phi_7} & \frac{\partial \cos\theta_7}{\partial p_{tot}^z} \\ \frac{\partial \phi_7}{\partial |\mathbf{p}_3|} & \frac{\partial \phi_7}{\partial |\mathbf{p}_5|} & \frac{\partial \phi_7}{\partial |\mathbf{p}_6|} & \frac{\partial \phi_7}{\partial |\mathbf{p}_7|} & \frac{\partial \phi_7}{\partial \cos\theta_7} & \frac{\partial \phi_7}{\partial \phi_7} & \frac{\partial \phi_7}{\partial p_{tot}^z} \\ \frac{\partial p_{tot}^z}{\partial |\mathbf{p}_3|} & \frac{\partial p_{tot}^z}{\partial |\mathbf{p}_5|} & \frac{\partial p_{tot}^z}{\partial |\mathbf{p}_6|} & \frac{\partial p_{tot}^z}{\partial |\mathbf{p}_7|} & \frac{\partial p_{tot}^z}{\partial \cos\theta_7} & \frac{\partial p_{tot}^z}{\partial \phi_7} & \frac{\partial p_{tot}^z}{\partial p_{tot}^z} \end{vmatrix} = \begin{vmatrix} \frac{\partial s_{34}}{\partial |\mathbf{p}_3|} & \frac{\partial s_{34}}{\partial |\mathbf{p}_5|} & \frac{\partial s_{34}}{\partial |\mathbf{p}_6|} \\ \frac{\partial s_{345}}{\partial |\mathbf{p}_3|} & \frac{\partial s_{345}}{\partial |\mathbf{p}_5|} & \frac{\partial s_{345}}{\partial |\mathbf{p}_6|} \\ \frac{\partial s_{67}}{\partial |\mathbf{p}_3|} & \frac{\partial s_{67}}{\partial |\mathbf{p}_5|} & \frac{\partial s_{67}}{\partial |\mathbf{p}_6|} \end{vmatrix}. \quad (\text{I.1.8})$$

### I.1.5 Jacobian for Single Top-Quark Three-Jet Processes

The general integration variables for the three-jet processes are the magnitudes of the momenta of the lepton ( $|\mathbf{p}_3|$ ) and the three quarks ( $|\mathbf{p}_5|$ ,  $|\mathbf{p}_6|$ , and  $|\mathbf{p}_7|$ ), as well as the longitudinal momentum of the whole system ( $p_{tot}^z$ ). In particular, for the single top-quark three-jet processes,  $tbq$ ,  $tqq$ , and  $tqb$ , the phase space transformation makes  $|\mathbf{p}_3|$  and  $|\mathbf{p}_5|$  be replaced by the squared invariant masses of the  $W$  boson ( $s_{34}$ ) and the top quark ( $s_{345}$ ), while  $|\mathbf{p}_6|$ ,  $|\mathbf{p}_7|$ , and  $p_{tot}^z$  are unchanged:

$$dy_{single\text{top-}3\text{jets}} = d|\mathbf{p}_3|d|\mathbf{p}_5|d|\mathbf{p}_6|d|\mathbf{p}_7|dp_{tot}^z \rightarrow ds_{34}ds_{345}d|\mathbf{p}_6|d|\mathbf{p}_7|dp_{tot}^z. \quad (\text{I.1.9})$$

The Jacobian is written and simplified below,

$$|J| = \begin{vmatrix} \frac{\partial s_{34}}{\partial |\mathbf{p}_3|} & \frac{\partial s_{34}}{\partial |\mathbf{p}_5|} & \frac{\partial s_{34}}{\partial |\mathbf{p}_6|} & \frac{\partial s_{34}}{\partial |\mathbf{p}_7|} & \frac{\partial s_{34}}{\partial p_{tot}^z} \\ \frac{\partial s_{345}}{\partial |\mathbf{p}_3|} & \frac{\partial s_{345}}{\partial |\mathbf{p}_5|} & \frac{\partial s_{345}}{\partial |\mathbf{p}_6|} & \frac{\partial s_{345}}{\partial |\mathbf{p}_7|} & \frac{\partial s_{345}}{\partial p_{tot}^z} \\ \frac{\partial |\mathbf{p}_6|}{\partial |\mathbf{p}_3|} & \frac{\partial |\mathbf{p}_6|}{\partial |\mathbf{p}_5|} & \frac{\partial |\mathbf{p}_6|}{\partial |\mathbf{p}_6|} & \frac{\partial |\mathbf{p}_6|}{\partial |\mathbf{p}_7|} & \frac{\partial |\mathbf{p}_6|}{\partial p_{tot}^z} \\ \frac{\partial |\mathbf{p}_7|}{\partial |\mathbf{p}_3|} & \frac{\partial |\mathbf{p}_7|}{\partial |\mathbf{p}_5|} & \frac{\partial |\mathbf{p}_7|}{\partial |\mathbf{p}_6|} & \frac{\partial |\mathbf{p}_7|}{\partial |\mathbf{p}_7|} & \frac{\partial |\mathbf{p}_7|}{\partial p_{tot}^z} \\ \frac{\partial p_{tot}^z}{\partial |\mathbf{p}_3|} & \frac{\partial p_{tot}^z}{\partial |\mathbf{p}_5|} & \frac{\partial p_{tot}^z}{\partial |\mathbf{p}_6|} & \frac{\partial p_{tot}^z}{\partial |\mathbf{p}_7|} & \frac{\partial p_{tot}^z}{\partial p_{tot}^z} \end{vmatrix} = \begin{vmatrix} \frac{\partial s_{34}}{\partial |\mathbf{p}_3|} & \frac{\partial s_{34}}{\partial |\mathbf{p}_5|} \\ \frac{\partial s_{345}}{\partial |\mathbf{p}_3|} & \frac{\partial s_{345}}{\partial |\mathbf{p}_5|} \end{vmatrix}. \quad (\text{I.1.10})$$

### I.1.6 Jacobian for $W+3$ Jets Processes

Similar to Appendix I.1.2, the magnitude of the momentum of the lepton,  $|\mathbf{p}_3|$  is replaced by the squared invariant mass of the  $W$  boson for the phase space transformation of the  $W+3$  Jets processes,  $Wbbg$  and  $Wugg$ .

$$dy_{W+3jets} = d|\mathbf{p}_3|d|\mathbf{p}_5|d|\mathbf{p}_6|d|\mathbf{p}_7|dp_{tot}^z \rightarrow ds_{34}d|\mathbf{p}_5|d|\mathbf{p}_6|d|\mathbf{p}_7|dp_{tot}^z. \quad (\text{I.1.11})$$

And the Jacobian and its simplification are listed below,

$$|J| = \begin{vmatrix} \frac{\partial s_{34}}{\partial |\mathbf{p}_3|} & \frac{\partial s_{34}}{\partial |\mathbf{p}_5|} & \frac{\partial s_{34}}{\partial |\mathbf{p}_6|} & \frac{\partial s_{34}}{\partial |\mathbf{p}_7|} & \frac{\partial s_{34}}{\partial p_{tot}^z} \\ \frac{\partial |\mathbf{p}_5|}{\partial |\mathbf{p}_3|} & \frac{\partial |\mathbf{p}_5|}{\partial |\mathbf{p}_5|} & \frac{\partial |\mathbf{p}_5|}{\partial |\mathbf{p}_6|} & \frac{\partial |\mathbf{p}_5|}{\partial |\mathbf{p}_7|} & \frac{\partial |\mathbf{p}_5|}{\partial p_{tot}^z} \\ \frac{\partial |\mathbf{p}_6|}{\partial |\mathbf{p}_3|} & \frac{\partial |\mathbf{p}_6|}{\partial |\mathbf{p}_5|} & \frac{\partial |\mathbf{p}_6|}{\partial |\mathbf{p}_6|} & \frac{\partial |\mathbf{p}_6|}{\partial |\mathbf{p}_7|} & \frac{\partial |\mathbf{p}_6|}{\partial p_{tot}^z} \\ \frac{\partial |\mathbf{p}_7|}{\partial |\mathbf{p}_3|} & \frac{\partial |\mathbf{p}_7|}{\partial |\mathbf{p}_5|} & \frac{\partial |\mathbf{p}_7|}{\partial |\mathbf{p}_6|} & \frac{\partial |\mathbf{p}_7|}{\partial |\mathbf{p}_7|} & \frac{\partial |\mathbf{p}_7|}{\partial p_{tot}^z} \\ \frac{\partial p_{tot}^z}{\partial |\mathbf{p}_3|} & \frac{\partial p_{tot}^z}{\partial |\mathbf{p}_5|} & \frac{\partial p_{tot}^z}{\partial |\mathbf{p}_6|} & \frac{\partial p_{tot}^z}{\partial |\mathbf{p}_7|} & \frac{\partial p_{tot}^z}{\partial p_{tot}^z} \end{vmatrix} = \left| \frac{\partial s_{34}}{\partial |\mathbf{p}_3|} \right|. \quad (\text{I.1.12})$$

### I.1.7 Jacobian for $t\bar{t}$ 3 Jet Processes

As discussed in Appendix I.1.4, we can afford to use three squared invariant masses as the integration variables with our approximation method for the  $t\bar{t}$  three-jet process (Section 6.2.4). These three squared invariant masses are of the  $W$  boson which decays to a lepton and a neutrino ( $s_{34}$ ), and of the two top quarks ( $s_{345}$  and  $s_{67}$ ). The magnitude of the momentum of the non-decaying  $W$  boson ( $|\mathbf{p}_7|$ ) and the longitudinal momentum of the whole system ( $p_{tot}^z$ ) are kept as the rest of the integration variables.

$$dy_{t\bar{t}-3jets} = d|\mathbf{p}_3|d|\mathbf{p}_5|d|\mathbf{p}_6|d|\mathbf{p}_7|dp_{tot}^z \rightarrow ds_{34}ds_{345}ds_{67}d|\mathbf{p}_7|dp_{tot}^z. \quad (\text{I.1.13})$$

The Jacobian and its simplification are summarized below,

$$|J| = \begin{vmatrix} \frac{\partial s_{34}}{\partial |\mathbf{p}_3|} & \frac{\partial s_{34}}{\partial |\mathbf{p}_5|} & \frac{\partial s_{34}}{\partial |\mathbf{p}_6|} & \frac{\partial s_{34}}{\partial |\mathbf{p}_7|} & \frac{\partial s_{34}}{\partial p_{tot}^z} \\ \frac{\partial s_{345}}{\partial |\mathbf{p}_3|} & \frac{\partial s_{345}}{\partial |\mathbf{p}_5|} & \frac{\partial s_{345}}{\partial |\mathbf{p}_6|} & \frac{\partial s_{345}}{\partial |\mathbf{p}_7|} & \frac{\partial s_{345}}{\partial p_{tot}^z} \\ \frac{\partial s_{67}}{\partial |\mathbf{p}_3|} & \frac{\partial s_{67}}{\partial |\mathbf{p}_5|} & \frac{\partial s_{67}}{\partial |\mathbf{p}_6|} & \frac{\partial s_{67}}{\partial |\mathbf{p}_7|} & \frac{\partial s_{67}}{\partial p_{tot}^z} \\ \frac{\partial |\mathbf{p}_7|}{\partial |\mathbf{p}_3|} & \frac{\partial |\mathbf{p}_7|}{\partial |\mathbf{p}_5|} & \frac{\partial |\mathbf{p}_7|}{\partial |\mathbf{p}_6|} & \frac{\partial |\mathbf{p}_7|}{\partial |\mathbf{p}_7|} & \frac{\partial |\mathbf{p}_7|}{\partial p_{tot}^z} \\ \frac{\partial p_{tot}^z}{\partial |\mathbf{p}_3|} & \frac{\partial p_{tot}^z}{\partial |\mathbf{p}_5|} & \frac{\partial p_{tot}^z}{\partial |\mathbf{p}_6|} & \frac{\partial p_{tot}^z}{\partial |\mathbf{p}_7|} & \frac{\partial p_{tot}^z}{\partial p_{tot}^z} \end{vmatrix} = \begin{vmatrix} \frac{\partial s_{34}}{\partial |\mathbf{p}_3|} & \frac{\partial s_{34}}{\partial |\mathbf{p}_5|} & \frac{\partial s_{34}}{\partial |\mathbf{p}_6|} \\ \frac{\partial s_{345}}{\partial |\mathbf{p}_3|} & \frac{\partial s_{345}}{\partial |\mathbf{p}_5|} & \frac{\partial s_{345}}{\partial |\mathbf{p}_6|} \\ \frac{\partial s_{67}}{\partial |\mathbf{p}_3|} & \frac{\partial s_{67}}{\partial |\mathbf{p}_5|} & \frac{\partial s_{67}}{\partial |\mathbf{p}_6|} \end{vmatrix}. \quad (\text{I.1.14})$$

## I.2 Jacobian Evaluation

In the previous section, the Jacobian determinants for all the processes are listed and simplified. The next step is to explicitly express these Jacobians with the final state parton four-momenta. Because of the energy-momentum conservation law, the expression of each derivative in the Jacobians is universal, no matter to which process the derivative belongs. In other words, the final expressions of the derivatives in this section can be applied on all the processes in this analysis.

### I.2.1 Jacobian about the $W$ mass squared, $s_{34}$

The  $W$  mass squared,  $s_{34}$ , is defined as

$$s_{34} = m_3^2 + m_4^2 + 2E_3E_4 - 2p_3^x p_4^x - 2p_3^y p_4^y - 2p_3^z p_4^z. \quad (\text{I.2.1})$$

Since the masses of the  $W$  decay products are negligible compared to their energy,  $m_i = 0$ ,  $|\mathbf{p}_i| = E_i$ . The neutrino four-momentum is defined in terms of all the other particles by the conservation laws, and the following equations can therefore be obtained.

For the two-jet final state,

$$\begin{aligned}
s_{34} &= 2|\mathbf{p}_3||\mathbf{p}_4| - 2p_3^x p_4^x - 2p_3^y p_4^y - 2p_3^z p_4^z \\
&= 2|\mathbf{p}_3| \sqrt{(-p_3^x - p_5^x - p_6^x)^2 + (-p_3^y - p_5^y - p_6^y)^2 + (p_{tot}^z - p_3^z - p_5^z - p_6^z)^2} \\
&\quad - 2p_3^x(-p_3^x - p_5^x - p_6^x) - 2p_3^y(-p_3^y - p_5^y - p_6^y) - 2p_3^z(p_{tot}^z - p_3^z - p_5^z - p_6^z)
\end{aligned} \tag{I.2.2}$$

while for the three-jet final state,

$$\begin{aligned}
s_{34} &= 2|\mathbf{p}_3||\mathbf{p}_4| - 2p_3^x p_4^x - 2p_3^y p_4^y - 2p_3^z p_4^z \\
&= 2|\mathbf{p}_3| \sqrt{(-p_3^x - p_5^x - p_6^x - p_7^x)^2 + (-p_3^y - p_5^y - p_6^y - p_7^y)^2 + (p_{tot}^z - p_3^z - p_5^z - p_6^z - p_7^z)^2} \\
&\quad - 2p_3^x(-p_3^x - p_5^x - p_6^x - p_7^x) - 2p_3^y(-p_3^y - p_5^y - p_6^y - p_7^y) - 2p_3^z(p_{tot}^z - p_3^z - p_5^z - p_6^z - p_7^z).
\end{aligned} \tag{I.2.3}$$

Therefore, the partial derivative of  $s_{34}$  with respect to  $|\mathbf{p}_3|$  can be evaluated. The expressions of this derivative are exactly the same for both the two-jet and the three-jet final states in terms of  $|\mathbf{p}_3|$  and  $|\mathbf{p}_4|$ :

$$\frac{\partial s_{34}}{\partial |\mathbf{p}_3|} = 2(|\mathbf{p}_3| + |\mathbf{p}_4|)(1 - \hat{\mathbf{p}}_3 \cdot \hat{\mathbf{p}}_4) \tag{I.2.4}$$

where  $\hat{\mathbf{p}}_3 \cdot \hat{\mathbf{p}}_4$  is the dot product of the unit three-momenta of parton 3 (lepton) and parton 4 (neutrino).

Similarly, we can also evaluate the partial derivative of  $s_{34}$  with respect to  $|\mathbf{p}_5|$ . Note this derivative is not zero, since  $s_{34}$  is expressed by  $|\mathbf{p}_5|$  as well (Equations (I.2.2) and (I.2.3)) due to the term of neutrino,

$$\frac{\partial s_{34}}{\partial |\mathbf{p}_5|} = 2|\mathbf{p}_3|(\hat{\mathbf{p}}_3 \cdot \hat{\mathbf{p}}_5 - \hat{\mathbf{p}}_4 \cdot \hat{\mathbf{p}}_5). \tag{I.2.5}$$

In some cases, for example the  $t\bar{t}$ , we need the partial derivative of  $s_{34}$  with respect to  $|\mathbf{p}_6|$ . This derivative can be obtained by replacing  $|\mathbf{p}_6|$  to  $|\mathbf{p}_5|$  in

Equation (I.2.5) since  $|\mathbf{p}_5|$  and  $|\mathbf{p}_6|$  are symmetric in Equations (I.2.2) and (I.2.3),

$$\frac{\partial s_{34}}{\partial |\mathbf{p}_6|} = 2|\mathbf{p}_3|(\hat{\mathbf{p}}_3 \cdot \hat{\mathbf{p}}_6 - \hat{\mathbf{p}}_4 \cdot \hat{\mathbf{p}}_6). \quad (\text{I.2.6})$$

### I.2.2 Jacobian about the top mass squared, $s_{345}$

The top mass squared,  $s_{345}$ , is defined as

$$\begin{aligned} s_{345} = & m_3^2 + m_4^2 + m_5^2 + 2E_3E_4 + 2E_3E_5 + 2E_4E_5 \\ & - 2p_3^x p_4^x - 2p_3^x p_5^x - 2p_4^x p_5^x - 2p_3^y p_4^y - 2p_3^y p_5^y - 2p_4^y p_5^y - 2p_3^z p_4^z - 2p_3^z p_5^z - 2p_4^z p_5^z. \end{aligned} \quad (\text{I.2.7})$$

Similar to Equations (I.2.2) and (I.2.3),  $s_{345}$  can be simplified and expressed as the three-momenta of  $\vec{\mathbf{p}}_3$ ,  $\vec{\mathbf{p}}_5$ , and  $\vec{\mathbf{p}}_6$  (as well as  $\vec{\mathbf{p}}_7$  for the three-jet processes). Therefore, the derivatives can be evaluated and expressed as follows,

$$\frac{\partial s_{345}}{\partial |\mathbf{p}_3|} = 2(|\mathbf{p}_3| + |\mathbf{p}_4| + |\mathbf{p}_5|)(1 - \hat{\mathbf{p}}_3 \cdot \hat{\mathbf{p}}_4) \quad (\text{I.2.8})$$

$$\frac{\partial s_{345}}{\partial |\mathbf{p}_5|} = 2(|\mathbf{p}_3| + |\mathbf{p}_4| + |\mathbf{p}_5|)(1 - \hat{\mathbf{p}}_5 \cdot \hat{\mathbf{p}}_4) \quad (\text{I.2.9})$$

$$\frac{\partial s_{345}}{\partial |\mathbf{p}_6|} = -2(|\mathbf{p}_3| + |\mathbf{p}_5|)(\hat{\mathbf{p}}_4 \cdot \hat{\mathbf{p}}_6) + 2(\vec{\mathbf{p}}_3 + \vec{\mathbf{p}}_5) \cdot \hat{\mathbf{p}}_6. \quad (\text{I.2.10})$$

### I.2.3 Jacobian about the $Z$ (or the second $W$ ) mass squared,

$$s_{56}$$

The squared invariant mass of the second  $W$  boson in the  $WW$  process and the  $Z$  boson in the  $WZ$  process is defined as

$$s_{56} = m_5^2 + m_6^2 + 2E_5E_6 - 2p_5^x p_6^x - 2p_5^y p_6^y - 2p_5^z p_6^z. \quad (\text{I.2.11})$$

Note there is no neutrino momentum ( $\vec{\mathbf{p}}_4$ ) in  $s_{56}$ . Moreover, it is independent on the lepton momentum ( $\vec{\mathbf{p}}_3$ ):

$$\frac{\partial s_{56}}{\partial |\mathbf{p}_3|} = 0. \quad (\text{I.2.12})$$

And the derivative with respect to  $|\mathbf{p}_5|$  can be directly evaluated:

$$\frac{\partial s_{56}}{\partial |\mathbf{p}_5|} = 2(|\mathbf{p}_6| - \hat{\mathbf{p}}_5 \cdot \vec{\mathbf{p}}_6). \quad (\text{I.2.13})$$

#### I.2.4 Jacobian about the second top mass squared, $s_{67}$

The squared invariant mass of the second top quark in the  $t\bar{t}$  processes is defined as,

$$s_{67} = m_6^2 + m_7^2 + 2E_6E_7 - 2p_6^xp_7^x - 2p_6^yp_7^y - 2p_6^zp_7^z. \quad (\text{I.2.14})$$

However, the simplification of  $s_{67}$  is slightly different from the other cases, since the  $W$  boson decaying from the top quark does not decay in our approximation (Section 6.2.4), and its mass is not negligible. Consequently, Equation (I.2.14) can be written as,

$$s_{67} = m_7^2 + 2|\mathbf{p}_6|E_7 - 2p_6^xp_7^x - 2p_6^yp_7^y - 2p_6^zp_7^z. \quad (\text{I.2.15})$$

Similar to  $s_{56}$  in Appendix I.2.3,  $s_{67}$  has no dependence on the momentum of the lepton ( $\vec{\mathbf{p}}_3$ ) and the quark from the other quark ( $\vec{\mathbf{p}}_5$ ),

$$\frac{\partial s_{67}}{\partial |\mathbf{p}_3|} = 0 \quad (\text{I.2.16})$$

$$\frac{\partial s_{67}}{\partial |\mathbf{p}_5|} = 0. \quad (\text{I.2.17})$$

But the derivative of  $s_{67}$  with respect to  $|\mathbf{p}_6|$  is not zero,

$$\frac{\partial s_{67}}{\partial |\mathbf{p}_6|} = 2(E_7 - \hat{\mathbf{p}}_6 \cdot \vec{\mathbf{p}}_7). \quad (\text{I.2.18})$$

## J Distribution Sampling

As mentioned in Section 6.2.3.2, once a squared invariant mass of the  $W$  boson or the top quark is chosen as one of the integration variables, a Breit-Wigner sampling is sequentially performed to integrate over such a variable.

Similarly, when the magnitude of the momentum of a final-state parton is chosen as a integration variable, for example,  $|\mathbf{p}_6|$  in the single top-quark processes, we actually integrate over the energy difference between the parton and the corresponding reconstructed jet (under our assumption of the negligible masses, the Jacobian of this change is a unity),  $\Delta E_6 = (E_6)_x - (E_6)_y$ . Consequently, we can perform a Gaussian sampling in the integration. In fact, the energy difference is supposed to be a transfer-function distribution; however, the form of the transfer function is too complicated, and therefore a Gaussian sampling is implemented instead.

We describe the details of the Breit-Wigner sampling in Appendix J.1 and of the Gaussian sampling in Appendix J.2. Note it is important to obtain correct terms, or the whole integration will be meaningless.

### J.1 Breit-Wigner Distribution Sampling

Since the matrix element contains a Breit-Wigner peak as a function of the squared invariant mass,  $s$ , and we are choosing it to be one of our integration variables, we would like to sample this variable according to a Breit-Wigner distribution as shown below:

$$h(s) = \frac{1}{(s - m_0^2)^2 + \Gamma_0^2 m_0^2} \quad (\text{J.1.1})$$

where  $m_0$  and  $\Gamma_0$  are the on-shell mass and the resonance width, respectively. By doing so, the region around the peak of the  $h(s)$ ,  $m_0^2$ , has finer sampling, and the computing-time is much reduced while the integration precision is kept.

If we have a uniformly distributed random number,  $r$ , we can convert it to a Breit-Wigner sampling,  $s$ , by the “inverse transform sampling;” i.e. by evaluating the inverse of the cumulative distribution function (cdf) of  $h(s)$ . The cdf of the Breit-Wigner distribution is written as follows,

$$\begin{aligned} r &= \int h(s) ds \\ &= \int \frac{ds}{(s - m_0^2)^2 + \Gamma_0^2 m_0^2} \\ &= \frac{1}{m_0 \Gamma_0} \tan^{-1} \left( \frac{s - m_0^2}{m_0 \Gamma_0} \right). \end{aligned} \tag{J.1.2}$$

And  $s$  can be evaluated by reversing the cdf,

$$s = m_0^2 + m_0 \Gamma_0 \tan(m_0 \Gamma_0 r). \tag{J.1.3}$$

Because the integration variable,  $s$ , is not uniformly sampled, we are effectively performing the integration  $\int f(s) dr$  ( $= \int f(s) h(s) ds$ ) instead of  $\int f(s) ds$ , where the  $f(s)$  is the real integrand. Hence, we have to take the additional  $h(s)$  out of the integration. In other words, this procedure is a change of variable,  $ds \rightarrow dr$ , and the Jacobian determinant is  $1/h(s)$ . This can be achieved as follows,

$$\begin{aligned} dr &= h(s) ds \\ \Rightarrow \int f(s) ds &= \int f(s) \frac{dr}{h(s)} = \int f(s) \left[ (s - m_0^2)^2 + m_0^2 \Gamma_0^2 \right] dr. \end{aligned} \tag{J.1.4}$$

Moreover, when we generate a uniformly distributed random number,  $u$ , we generate it between 0 and 1, and scale it appropriately to get  $r$ . The scale factor,  $\Delta r$ , is defined below,

$$r = (r_{max} - r_{min}) \times u + r_{min} = \Delta r \times u \tag{J.1.5}$$

where  $r_{max}$  and  $r_{min}$  can be estimated from

$$\begin{aligned} r_{max} &= \frac{1}{m_0 \Gamma_0} \tan^{-1} \left( \frac{s_{max} - m_0^2}{m_0 \Gamma_0} \right) \\ r_{min} &= \frac{1}{m_0 \Gamma_0} \tan^{-1} \left( \frac{s_{min} - m_0^2}{m_0 \Gamma_0} \right). \end{aligned} \quad (\text{J.1.6})$$

The  $s_{min}$  is constrained by the minimum of the possible squared invariant mass, for example,  $(m_{lepton} + m_{neutrino})^2$  for the squared  $W$  invariant mass. Similarly, the  $s_{max}$  is the maximum of  $s$ , which is  $(E_{beam} - \sum_{other \text{ partons}} m)^2$  in our example.

Taking this scaling into account, our integral can be written as follow,

$$\begin{aligned} dr &= \Delta r du \\ \Rightarrow \int f(s) ds &= \int f(s) \frac{dr}{h(s)} = \int f(s) \left[ (s - m_0^2)^2 + m_0^2 \Gamma_0^2 \right] \Delta r du. \end{aligned} \quad (\text{J.1.7})$$

## J.2 Gaussian Distribution Sampling

The integration variable  $\Delta E$  is sampled according to a Gaussian distribution,

$$g(\Delta E) = \frac{1}{\sqrt{2\pi}\sigma} e^{-\frac{(\Delta E - \mu)^2}{2\sigma^2}} \quad (\text{J.2.1})$$

where the mean value  $\mu$  is zero and the width  $\sigma$  is comparable with the width of the main Gaussian of the jet transfer functions (between 20 to 30 GeV). The region near the reconstructed energy is finer sampled, since the parton energy is more likely being close to than being far from the reconstructed one.

Similar to the B-W sampling described in Appendix J.1, we use the inverse transform sampling to generate the normally distributed variable  $\Delta E$ :

$$\begin{aligned} r &= \int g(\Delta E) d\Delta E \\ &= \int_{-\infty}^{\Delta E} \frac{1}{\sqrt{2\pi}\sigma} e^{-\frac{(\Delta E' - \mu)^2}{2\sigma^2}} d\Delta E' \\ &= \frac{1}{2} \left[ 1 + \operatorname{erf} \left( \frac{\Delta E - \mu}{\sqrt{2}\sigma} \right) \right] \end{aligned} \quad (\text{J.2.2})$$

where  $r$  is a uniformly distributed random number. Then  $\Delta E$  can be evaluated by reversing the cdf,

$$\Delta E = \mu + \sqrt{2}\sigma \text{erf}^{-1}(2r - 1). \quad (\text{J.2.3})$$

Again, we are effectively performing the integration  $\int f(\Delta E)dr (= \int f(\Delta E)g(\Delta E)d\Delta E)$  instead of  $\int f(\Delta E)d\Delta E$ ; therefore we have to take the  $g(\Delta E)$  out:

$$\begin{aligned} dr &= g(\Delta E)d\Delta E \\ \Rightarrow \int f(\Delta E)d\Delta E &= \int f(\Delta E)\frac{dr}{g(\Delta E)} = \int f(\Delta E)\frac{dr}{\frac{1}{\sqrt{2\pi}\sigma}e^{-\frac{(\Delta E-\mu)^2}{2\sigma^2}}}. \end{aligned} \quad (\text{J.2.4})$$

We uniformly generate a random number  $u$  within the interval (0,1) and scale it by  $\Delta r$ ,

$$r = (r_{max} - r_{min}) \times u + r_{min} = \Delta r \times u \quad (\text{J.2.5})$$

where  $r_{max}$  and  $r_{min}$  are defined below,

$$\begin{aligned} r_{max} &= \frac{1}{2} \left[ 1 + \text{erf} \left( \frac{\Delta E_{max} - \mu}{\sqrt{2}\sigma} \right) \right] \\ r_{min} &= \frac{1}{2} \left[ 1 + \text{erf} \left( \frac{\Delta E_{min} - \mu}{\sqrt{2}\sigma} \right) \right]. \end{aligned} \quad (\text{J.2.6})$$

The  $\Delta E_{max}$  and  $\Delta E_{min}$  are set to be 100 GeV and -100 GeV, respectively, for the energy difference of the parton and its corresponding jet is hardly larger than 100 GeV, and we cut off the events with  $|\Delta E| > 100$  GeV in while deriving the jet transfer functions.

The integral is therefore written as,

$$\begin{aligned} dr &= \Delta r du \\ \Rightarrow \int f(\Delta E)d\Delta E &= \int f(\Delta E)\frac{dr}{g(\Delta E)} = \int f(\Delta E)\frac{\Delta r du}{\frac{1}{\sqrt{2\pi}\sigma}e^{-\frac{(\Delta E-\mu)^2}{2\sigma^2}}}. \end{aligned} \quad (\text{J.2.7})$$

## K The Yield Fractions in the Likelihood Functions

The Appendix explicitly shows how to calculate the yield fractions, as mentioned in Section 6.3. These  $c_i$  coefficients are set a priori based on the theoretical cross sections and efficiencies. They do not involve any fit to data. They are supposed to give the correct mix for each probability in the discriminant: such that if we have more  $Wbb$  events then that probability weighs more in the discriminant.

The yield of each two-jet process is defined as follows,

$$\begin{aligned}
 y_{tb} &= \text{yield}(tb) \\
 y_{tq} &= \text{yield}(tqb) \\
 y_{Wbb} &= \text{yield}(Wbb) + \text{yield}(Wcc) + \text{yield}(Zbb) + \text{yield}(Zcc) \\
 y_{Wcg} &= \text{yield}(Wcj) \\
 y_{Wgg} &= \text{yield}(Wjj) - \text{yield}(Wcj) + \text{yield}(Zjj) \\
 y_{WW} &= \frac{\sigma_{WW}}{\sigma_{WW} + \sigma_{WZ}} \text{yield}(Diboson) \\
 y_{WZ} &= \frac{\sigma_{WZ}}{\sigma_{WW} + \sigma_{WZ}} \text{yield}(Diboson) \\
 y_{ggg} &= \text{yield}(Multijet) \\
 y_{t\bar{t}} &= \text{yield}(t\bar{t} \rightarrow \ell + jets) + \text{yield}(t\bar{t} \rightarrow \ell\ell)
 \end{aligned} \tag{K.0.1}$$

where  $y_{tb}$  is the yield we are going to use for the  $tb$  process,  $\text{yield}(tb)$  is the yield of the  $tb$  MC sample, and so on.  $\sigma_{WW}$  and  $\sigma_{WZ}$  are the normalization terms of the  $WW$  and  $WZ$  probabilities, as listed in Tables H.1 to H.4.

Similarly, the yield of each three-jet process is defined below,

$$\begin{aligned}
 y_{tbq} &= \text{yield}(tb) \\
 y_{tqb} &= \frac{\sigma_{tqb}}{\sigma_{tqb} + \sigma_{tqg}} \text{yield}(tqb) \\
 y_{tqg} &= \frac{\sigma_{tqg}}{\sigma_{tqb} + \sigma_{tqg}} \text{yield}(tqb) \\
 y_{Wbbg} &= \text{yield}(Wbb) + \text{yield}(Wcc) + \text{yield}(Zbb) + \text{yield}(Zcc) \\
 y_{Wugg} &= \text{yield}(Wcj) + \text{yield}(Wjj) + \text{yield}(Zjj) + \text{yield}(Diboson) + \text{yield}(Multijet) \\
 y_{t\bar{t}} &= \text{yield}(t\bar{t} \rightarrow \ell + jets) + \text{yield}(t\bar{t} \rightarrow \ell\ell).
 \end{aligned}
 \tag{K.0.2}$$

The normalization term of the yield fraction is defined as the sum over the yields of the signal or the background processes,

$$y_{total} = \sum_{H \text{ proc } i} y_i
 \tag{K.0.3}$$

where  $y_i$  is the yield defined in Equations (K.0.1) and (K.0.2).  $H$  is the signal or the background hypothesis, and the matrix element processes belonging to a certain hypothesis are categorized in Table 6.7.

Hence, the yield fraction  $c_i$  can be obtained by the following equation,

$$c_i = \frac{y_i}{y_{total}}
 \tag{K.0.4}$$

and the values of the yield fractions used in this analysis are listed in Tables K.1 to K.8.

For example, the only signal process for the  $s$ -channel discriminant in the two-jet channel is  $tb$ , so in that case,  $c_{tb} = 1$ . The sum of the  $c_i$  coefficients for all the backgrounds (in this case also including the  $tq$  channel) also adds up to 1. For the  $s + t$  channel discriminant, it is the sum of the  $s$  and  $t$ -channels  $c_{tb} + c_{tq}$  that adds up to 1, and in that case the sum of all the backgrounds  $c_{Wbb} + c_{Wcg} + c_{Wgg} + c_{WW} + c_{WZ} + c_{ggg}$  that adds up to 1.

Process	$D_s$		$D_t$		$D_{st}$	
	e+jets	$\mu$ +jets	e+jets	$\mu$ +jets	e+jets	$\mu$ +jets
$t\bar{b}$	1	1	0.016	0.014	0.34	0.32
$tq$	0.031	0.029	1	1	0.66	0.68
$Wbb$	0.39	0.42	0.39	0.42	0.4	0.43
$Wcg$	0.15	0.15	0.15	0.15	0.16	0.15
$Wgg$	0.28	0.3	0.28	0.31	0.29	0.31
$WW$	0.031	0.032	0.031	0.032	0.032	0.033
$WZ$	0.0018	0.0019	0.0018	0.002	0.0018	0.002
$t\bar{t}$	0.06	0.045	0.061	0.046	0.062	0.047
$ggg$	0.06	0.021	0.061	0.021	0.062	0.022

**Table K.1** The coefficients,  $c_i$ , of discriminants  $D_s$ ,  $D_t$ , and  $D_{st}$  for p17 two-jet single-tagged samples.

Process	$D_s$		$D_t$		$D_{st}$	
	e+jets	$\mu$ +jets	e+jets	$\mu$ +jets	e+jets	$\mu$ +jets
$tbg$	1	1	0.015	0.013	0.31	0.3
$tqb$	0.018	0.016	0.58	0.53	0.4	0.37
$tqg$	0.013	0.015	0.42	0.47	0.29	0.33
$Wbbg$	0.32	0.37	0.33	0.37	0.33	0.38
$Wugg$	0.37	0.38	0.38	0.39	0.39	0.4
$t\bar{t}$	0.27	0.22	0.27	0.22	0.28	0.22

**Table K.2** The coefficients,  $c_i$ , of discriminants  $D_s$ ,  $D_t$ , and  $D_{st}$  for p17 three-jet single-tagged samples.

Process	$D_s$		$D_t$		$D_{st}$	
	e+jets	$\mu$ +jets	e+jets	$\mu$ +jets	e+jets	$\mu$ +jets
$t\bar{b}$	1	1	0.072	0.069	0.86	0.86
$tq$	0.012	0.012	1	1	0.14	0.14
$Wbb$	0.63	0.66	0.6	0.62	0.64	0.66
$Wcg$	0.029	0.031	0.027	0.029	0.029	0.031
$Wgg$	0.054	0.06	0.05	0.056	0.054	0.06
$WW$	0.029	0.04	0.027	0.038	0.029	0.041
$WZ$	0.0017	0.0025	0.0016	0.0023	0.0017	0.0025
$t\bar{t}$	0.21	0.19	0.2	0.18	0.21	0.19
$ggg$	0.031	0.012	0.029	0.011	0.032	0.012

**Table K.3** The coefficients,  $c_i$ , of discriminants  $D_s$ ,  $D_t$ , and  $D_{st}$  for p17 two-jet double-tagged samples.

Process	$D_s$		$D_t$		$D_{st}$	
	e+jets	$\mu$ +jets	e+jets	$\mu$ +jets	e+jets	$\mu$ +jets
$tbg$	1	1	0.036	0.037	0.53	0.54
$tqb$	0.019	0.016	0.58	0.53	0.27	0.24
$tqg$	0.013	0.015	0.42	0.47	0.2	0.22
$Wbbg$	0.29	0.33	0.28	0.32	0.3	0.34
$Wugg$	0.084	0.1	0.084	0.1	0.087	0.11
$t\bar{t}$	0.6	0.54	0.6	0.54	0.62	0.56

**Table K.4** The coefficients,  $c_i$ , of discriminants  $D_s$ ,  $D_t$ , and  $D_{st}$  for p17 three-jet double-tagged samples.

Process	$D_s$		$D_t$		$D_{st}$	
	e+jets	$\mu$ +jets	e+jets	$\mu$ +jets	e+jets	$\mu$ +jets
$t\bar{b}$	1	1	0.015	0.014	0.31	0.3
$tq$	0.032	0.032	1	1	0.69	0.7
$Wbb$	0.35	0.41	0.36	0.42	0.36	0.42
$Wcg$	0.17	0.18	0.17	0.18	0.17	0.18
$Wgg$	0.19	0.22	0.19	0.23	0.19	0.23
$WW$	0.039	0.045	0.04	0.046	0.04	0.046
$WZ$	0.0023	0.0029	0.0024	0.0029	0.0024	0.003
$t\bar{t}$	0.1	0.087	0.11	0.088	0.11	0.089
$ggg$	0.12	0.024	0.12	0.025	0.13	0.025

**Table K.5** The coefficients,  $c_i$ , of discriminants  $D_s$ ,  $D_t$ , and  $D_{st}$  for p20 two-jet single-tagged samples.

Process	$D_s$		$D_t$		$D_{st}$	
	e+jets	$\mu$ +jets	e+jets	$\mu$ +jets	e+jets	$\mu$ +jets
$tbg$	1	1	0.012	0.012	0.3	0.3
$tqb$	0.016	0.016	0.61	0.62	0.43	0.43
$tqg$	0.01	0.01	0.39	0.38	0.27	0.27
$Wbbg$	0.25	0.32	0.25	0.32	0.25	0.32
$Wugg$	0.3	0.27	0.3	0.27	0.31	0.27
$t\bar{t}$	0.43	0.39	0.43	0.4	0.44	0.4

**Table K.6** The coefficients,  $c_i$ , of discriminants  $D_s$ ,  $D_t$ , and  $D_{st}$  for p20 three-jet single-tagged samples.

Process	$D_s$		$D_t$		$D_{st}$	
	e+jets	$\mu$ +jets	e+jets	$\mu$ +jets	e+jets	$\mu$ +jets
$t\bar{b}$	1	1	0.061	0.06	0.77	0.76
$tq$	0.019	0.02	1	1	0.23	0.24
$Wbb$	0.47	0.54	0.45	0.52	0.47	0.55
$Wcg$	0.043	0.041	0.041	0.039	0.043	0.041
$Wgg$	0.062	0.082	0.06	0.078	0.064	0.083
$WW$	0.029	0.037	0.028	0.036	0.03	0.038
$WZ$	0.0018	0.0024	0.0017	0.0023	0.0018	0.0024
$t\bar{t}$	0.3	0.26	0.29	0.25	0.31	0.27
$ggg$	0.08	0.017	0.077	0.016	0.082	0.017

**Table K.7** The coefficients,  $c_i$ , of discriminants  $D_s$ ,  $D_t$ , and  $D_{st}$  for p20 two-jet double-tagged samples.

Process	$D_s$		$D_t$		$D_{st}$	
	e+jets	$\mu$ +jets	e+jets	$\mu$ +jets	e+jets	$\mu$ +jets
$tbg$	1	1	0.023	0.025	0.47	0.47
$tqb$	0.016	0.017	0.61	0.62	0.33	0.33
$tqg$	0.01	0.011	0.39	0.38	0.21	0.2
$Wbbg$	0.16	0.22	0.16	0.22	0.17	0.22
$Wugg$	0.13	0.09	0.13	0.09	0.13	0.092
$t\bar{t}$	0.68	0.67	0.68	0.67	0.7	0.68

**Table K.8** The coefficients,  $c_i$ , of discriminants  $D_s$ ,  $D_t$ , and  $D_{st}$  for p20 three-jet double-tagged samples.

# L Different Types of Discriminants

In addition to the discriminant described in Section 6.3.1, we tried a few different discriminants and chose the one which is most sensitive to the signal. We describe here the six different discriminants that were tested and their comparison.

## L.1 Basic Discriminant with no $b$ -ID Information

This discriminant does not include any  $b$ -ID information, it is simply built from the ME probabilities:

$$\mathcal{L}(H|x) = \sum_{H \text{ proc } i} c_i P_i(x) \quad (\text{L.1.1})$$

where  $P_i$  is defined in Eq. 6.1.1.

## L.2 $P^{bl}$ -based Matrix Element Discriminant

This discriminant incorporates the  $b$ -tagging information from the  $b_l$  tagger by giving a weight to each jet-parton permutation, as described in Section 6.3.1.1. The  $P_{bl}$  probability is computed and the discriminant is built from the likelihoods:

$$\mathcal{L}(H|x) = \sum_{H \text{ proc } i} c_i P_i^{bl}(x) \quad (\text{L.2.1})$$

where  $P_i^{bl}$  is defined in Eq. 6.3.4 for a given ME process  $i$ , like  $tb$  or  $t\bar{t}$ , etc.

This discriminant is the most efficient in separating  $t$ -channel single top-quark from the backgrounds.

### L.3 $P^{bl \times bc}$ -based Matrix Element Discriminant

The  $b$ -ID output variable,  $b_l$ , helps us to distinguish the  $b$  jets from the light jets. However, the  $c$  jets often have similar features to the  $b$  ones, and the  $b$ -ID output variables,  $b_l$ , are not sensitive to separate  $b$  and  $c$  jets. To improve the  $b$ - $c$  separation, the  $b$ -ID group developed a  $b_c$  discriminant [103], which combined with the original  $b_l$  produces a  $b_l \times b_c$  discriminant. This  $P^{bl \times bc}$  discriminant is built exactly as the one based on  $P^{bl}$ , but replacing everywhere  $b_l$  values with the  $b_l \times b_c$  ones.

### L.4 B-weighted Matrix Element Discriminant

This is the discriminant chosen to discriminate  $s$ -channel single top-quark production from the backgrounds in this analysis. It is built by multiplying each ME probability by a weight  $B(x)$  derived from the  $b_l$  MVA output of the jets. It does not affect each jet-parton assignment, as the previous two.

$$\mathcal{L}(H|x) = \sum_{H \text{ proc } i} c_i B_i(x) P_i(x) \quad (\text{L.4.1})$$

where  $B_i$  and  $P_i$  are defined in Eq. 6.3.8 and in Eq. 6.3.3, respectively.

### L.5 $B^{bl \times bc}$ -weighted Matrix Element Discriminant

This is the same as the B-MED discriminant, but using the output of the  $bl \times bc$  MVA tagger instead of the  $bl$  MVA tagger.

### L.6 CDF's Event Probability Discriminant

We also test the event probability discriminant developed by the CDF experiment [164]. It is exactly the same as the B-MED for the two- $b$ -tagged channel,

but slightly different in the one- $b$ -tagged channel:

$$B^{CDF}(x) = \begin{cases} b_{l,1st} & \text{for processes with at least one } b \text{ final state} \\ (1 - b_{l,1st}) & \text{for processes with no } b \text{ final state} \end{cases}. \quad (\text{L.6.1})$$

The signal and the background likelihoods are defined in this case as

$$\mathcal{L}(H|x) = \sum_{H \text{ proc } i} c_i B_{CDF,i}(x) P_i(x) \quad (\text{L.6.2})$$

and the EPD is built accordingly.

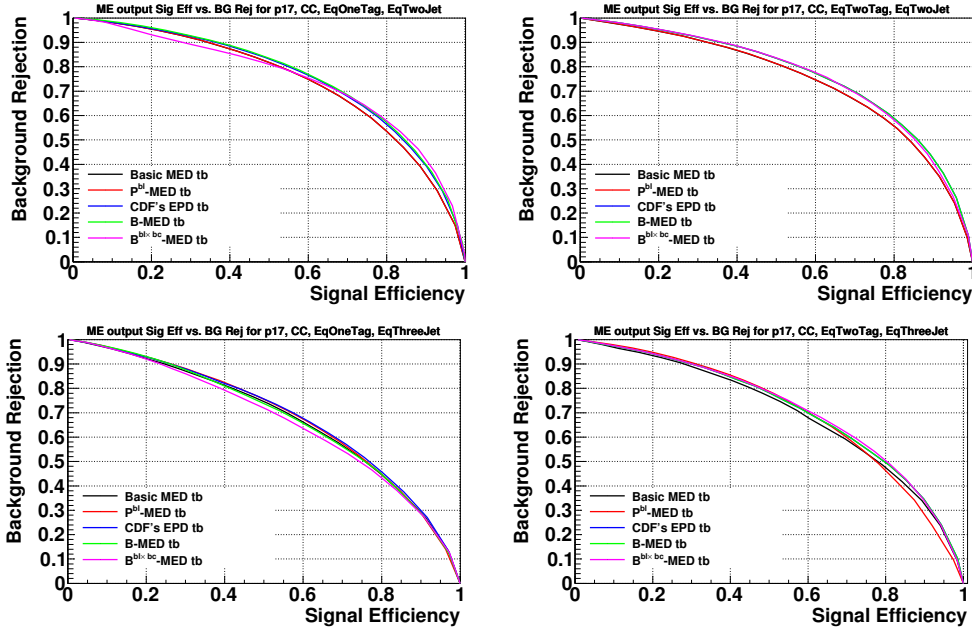
## L.7 Comparison of different discriminants

Among all the alternatives of the probabilities and the likelihoods developed, we have six types of the ME discriminants, as summarized in Table L.1. We study here the performance of these discriminants, to choose the one which is most sensitive to the  $s$ -channel signal for the cross section measurement.

Discriminant	Likelihood $\mathcal{L}(H x)$
Basic	$\sum c_i P_i(x)$
$P^{bl}$ _MED	$\sum c_i P_i^{bl}(x)$
$P^{bl \times bc}$ _MED	$\sum c_i P_i^{bl \times bc}(x)$
B-MED	$\sum c_i B_i(x) P_i(x)$
$B^{bl \times bc}$ -MED	$\sum c_i B_i^{bl \times bc}(x) P_i(x)$
CDF's EPD	$\sum c_i B_i^{CDF}(x) P_i(x)$

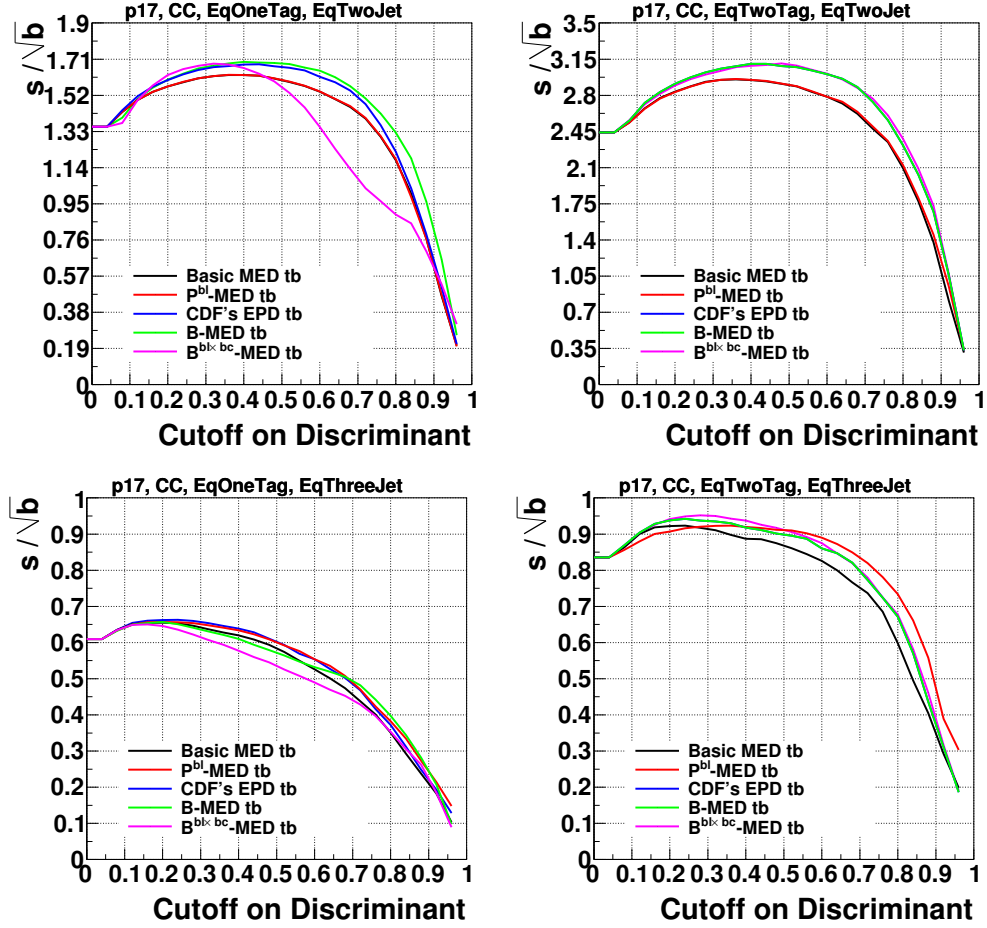
**Table L.1** The summary table of the definitions of all the ME discriminants. The  $\sum$  in the table is to sum over all the processes  $i$  which are included in the  $H$  hypothesis, as categorized in Table 6.7. The  $P_i(x)$  is defined in Equation (6.3.3), and the  $P_i^{bl}(x)$  in Equation (6.3.4).

Figure L.1 illustrates the signal efficiency and the background rejection of each discriminant. All the efficiency curves are very similar. However, the discriminants do have different values for the figure of merit  $s/\sqrt{b}$  as a function of the cutoff on the discriminant output, as shown in Figure L.2. Since we do not place any cuts on the discriminant outputs, the best figure of merit in our case is the one with the highest value at every point. As a result, the B-MED is chosen for this measurement.



**Figure L.1** Background rejection vs signal efficiency of the  $s$ -channel discriminant for the Run II electron and muon combined samples. The first and the second rows show the results of the two-jet and the three-jet events, respectively. The left column shows the results of the single-tagged events, while the right column the double-tagged ones. The  $P^{bl \times bc}$  discriminant is not plotted, for it is very similar to the  $P^{bl}$  discriminant.

It is worth discussing the similarity between all the discriminants in Figure L.1. In the single top-quark analysis, most of the two-jet processes are symmetric respect to the final state quark flavors. For instance, the  $Wbb$  process has two  $b$  quarks and no light ones. Hence, the  $b$ -ID related weights,  $w_j$  in Eq. 6.3.4, are the same in both the jet-parton assignments and therefore do not help out disentangling the correct assignment. As a result, the  $P^{bl}$  and the  $P^{bl \times bc}$  are the same as the probability without  $b$ -ID information,  $P$  in Eq. 6.3.3, in this kind of two-jet processes. However, the probabilities calculated with  $b$ -ID outputs are



**Figure L.2** The figure of merit,  $s/\sqrt{b}$  vs the cutoff on discriminants, of the  $s$ -channel discriminant for the Run II electron and muon combined samples. The first and the second rows show the results of the two-jet and the three-jet events, respectively. The left column shows the results of the single-tagged events, while the right column the double-tagged ones. The  $P^{bl \times bc}$  discriminant is not plotted, for it is very similar to the  $P^{bl}$  discriminant.

still sensitive in the three-jet events.

# M Updates from the Previous Matrix Element Analysis

The code used for this analysis is available in CVS: `topd0root_me` v06-00-01 and `btags_cert` v.09-00-02. In this appendix the new development and updates that are different from the previous analysis [163] are summarized.

- New Developments

- **$b$ -ID output information**

The previous analysis did not use the  $b$ -ID output information in the construction of the discriminant. The probability Equation (6.3.3) and the “Basic Discriminant” in Table L.1 are equivalent to the discriminant used before.

- **$t\bar{t}$  modeling**

The special  $t\bar{t}$  matrix elements in Figures 6.4 and 6.6 were used in the previous analysis, but all the studies have been repeated for this analysis to validate the assumption. Furthermore, The  $t\bar{t}$  model described in Section 6.2.4 (in particular, Figures 6.7 and 6.8) is completely new.

- **New discriminants**

Only the “Basic Discriminant” described in Table L.1 was used in the previous analysis, and the other discriminants are newly developed.

- Updates

- **Jet transfer functions**

The jet transfer functions are re-derived for this analysis, as described in Appendix G.1.

- **Direct  $b$ -tagging**

The direct  $b$ -tagging is first implemented in the single top-quark matrix element analysis; in the previous one, the permutation  $b$ -tagging was used.

- **Top quark mass and width**

The mass and width of the top quark in the matrix element and the Breit-Wigner sampling are updated. The updated values, 172.5 GeV for the mass and 1.3292 GeV for the width, are consistent with the MC simulation.

- Main Bug Fixes

- **Muon transfer functions**

The widths of the muon transfer functions, the  $\sigma$  in Tables G.5 and G.6, for the two detector  $\eta$  regions were swapped by mistake. It affected the muon energy resolution by 25%.

- **Random variable correlation**

The integration variables  $\mathbf{p}_i$  were fully correlated for the uncorrelated dimensions in all  $W$ +Jets processes and three-jet single top-quark processes. It is fixed in the current analysis, and the sensitivity of the low  $H_T$  ( $W$ +Jets dominated) regions is consequently improved.

- **$ggg$  Jacobian and normalization**

All the Gaussian sampling factors,  $g(\Delta E)$  in Eq. J.2.7 were missing, and the differential cross section of the  $ggg$  process was small. The “RAMBO” (RAndom Momenta and BOosts) was introduced to evaluate the corresponding normalization constant, to make the probability comparable with the other processes. However, the differential cross section and its normalization were not consistent, and the  $ggg$  probability had no physical interpretation. In this analysis, the missing sampling factors are fixed, and the normalization constant is evaluated with the same matrix element as the differential cross section evaluation. (Namely, the RAMBO algorithm is removed in this analysis.)

- **$t\bar{t}$  three-jet Jacobian**

The Jacobian for the  $t\bar{t}$  three-jet process had a wrong sign in the previous analysis, and therefore the probability and the likelihood was wrong. Now it is corrected.

## N Tables of the Normalization Systematic Uncertainties

Tables N.1 to N.16 show the systematic uncertainties which only affect the normalization. A systematic uncertainty is assumed to be fully correlated between all signal or background samples within the same systematic source, and for all the analysis channels. The exceptions to this assumption are the systematic uncertainties on the theoretical cross sections, which are used to normalize our background simulation. In addition, the lepton ID and trigger uncertainties are independent between the electron and muon channels and between the Run IIa and Run IIb samples, and the trigger uncertainties are independent between each jet multiplicity as well.

Since the  $W$ +jets simulated samples are normalized to the data, these samples are not affected by any of these normalization-related systematic uncertainties, except the uncertainty on the taggability, which is applied after the normalization. In addition, because the  $W$ +jets and multijet backgrounds are normalized to the data simultaneously using the Matrix Method, their normalization uncertainties are anti-correlated. The negative sign in the “Matrix Method” row for the multijet sample indicates the anti-correlation.

The uncertainties on the heavy flavor correction are anti-correlated with respect to the ones on the  $b$ -ID scale factor corrections, as demonstrated in Section 5.5. The anti-correlation is taken into account in the cross section measurement.

	Run IIa Electron Channel Single-Tagged Two-Jet Percentage Errors												
	$t\bar{t}l\bar{l}$	$t\bar{t}\ell j$	$Wb\bar{b}$	$Wc\bar{c}$	$Wlp$	$Zb\bar{b}$	$Zc\bar{c}$	$Zlp$	diboson	multijet	$tb$	$tqb$	$tb + tqb$
Xsect.	9	9	—	—	—	3.3	3.3	3.3	7	—	3.8	5.3	4.8
Branching frac.	1.5	1.5	—	—	—	—	—	—	—	—	1.5	1.5	1.5
ISR/FSR	4.3	4.3	—	—	—	—	—	—	—	—	0.8	0.8	0.8
Jet frag. and higher order	1.6	1.6	—	—	—	—	—	—	—	—	0.7	0.7	0.7
Electron ID	2.8	2.8	—	—	—	2.8	2.8	2.8	2.8	—	2.8	2.8	2.8
Luminosity	6.1	6.1	—	—	—	6.1	6.1	6.1	6.1	—	6.1	6.1	6.1
PDF	—	—	—	—	—	—	—	—	—	—	2.0	2.0	2.0
Prim. vertex	1.4	1.4	—	—	—	1.4	1.4	1.4	1.4	—	1.4	1.4	1.4
$\lambda_{HF}^W$	—	—	12.0	12.0	—	—	—	—	—	—	—	—	—
$\lambda_{HF}^Z$	—	—	—	—	—	12.0	12.0	—	—	—	—	—	—
Taggability	10.0	6.4	5.9	5.5	6.0	13.1	11.0	9.2	6.4	—	7.5	5.6	6.2
Triggers	5.0	5.0	—	—	—	5.0	5.0	5.0	5.0	—	5.0	5.0	5.0
IKS	—	—	1.8	1.8	1.8	—	—	—	—	-30.0	—	—	—
b-jet frag.	2.0	2.0	—	—	—	2.0	—	—	—	—	2.0	2.0	2.0
Color Reconnection	1.0	1.0	—	—	—	—	—	—	—	—	1.0	1.0	1.0
Lumi. rewtg.	1.0	1.0	—	—	—	1.0	1.0	1.0	1.0	—	1.0	1.0	1.0

**Table N.1** Systematic uncertainties for Run IIa Electron Channel Single-Tagged Two-Jet events.

	Run IIa Electron Channel Double-Tagged Two-Jet Percentage Errors												
	$t\bar{t}l\bar{l}$	$t\bar{t}\ell j$	$Wb\bar{b}$	$Wc\bar{c}$	$Wlp$	$Zb\bar{b}$	$Zc\bar{c}$	$Zlp$	diboson	multijet	$tb$	$tqb$	$tb + tqb$
Xsect.	9	9	—	—	—	3.3	3.3	3.3	7	—	3.8	5.3	4.8
Branching frac.	1.5	1.5	—	—	—	—	—	—	—	—	1.5	1.5	1.5
ISR/FSR	4.3	4.3	—	—	—	—	—	—	—	—	0.8	0.8	0.8
Jet frag. and higher order	1.6	1.6	—	—	—	—	—	—	—	—	0.7	0.7	0.7
Electron ID	2.8	2.8	—	—	—	2.8	2.8	2.8	2.8	—	2.8	2.8	2.8
Luminosity	6.1	6.1	—	—	—	6.1	6.1	6.1	6.1	—	6.1	6.1	6.1
PDF	—	—	—	—	—	—	—	—	—	—	2.0	2.0	2.0
Prim. vertex	1.4	1.4	—	—	—	1.4	1.4	1.4	1.4	—	1.4	1.4	1.4
$\lambda_{HF}^W$	—	—	12.0	12.0	—	—	—	—	—	—	—	—	—
$\lambda_{HF}^Z$	—	—	—	—	—	12.0	12.0	—	—	—	—	—	—
Taggability	4.1	4.2	4.1	3.8	4.4	4.0	3.9	3.3	4.1	—	4.1	4.5	4.2
Triggers	5.0	5.0	—	—	—	5.0	5.0	5.0	5.0	—	5.0	5.0	5.0
IKS	—	—	1.8	1.8	1.8	—	—	—	—	-30.0	—	—	—
b-jet frag.	2.0	2.0	—	—	—	2.0	—	—	—	—	2.0	2.0	2.0
Color Reconnection	1.0	1.0	—	—	—	—	—	—	—	—	1.0	1.0	1.0
Lumi. rewtg.	1.0	1.0	—	—	—	1.0	1.0	1.0	1.0	—	1.0	1.0	1.0

**Table N.2** Systematic uncertainties for Run IIa Electron Channel Double-Tagged Two-Jet events.

Run IIa Electron Channel Single-Tagged Three-Jet Percentage Errors													
	$t\bar{t}l\ell$	$t\bar{t}\ell j$	$Wb\bar{b}$	$Wc\bar{c}$	$Wlp$	$Zb\bar{b}$	$Zc\bar{c}$	$Zlp$	diboson	multijet	$tb$	$tqb$	$tb + tqb$
Xsect.	9	9	—	—	—	3.3	3.3	3.3	7	—	3.8	5.3	4.8
Branching frac.	1.5	1.5	—	—	—	—	—	—	—	—	1.5	1.5	1.5
ISR/FSR	2.2	2.2	—	—	—	—	—	—	—	—	-5.9	-5.9	-5.9
Jet frag. and higher order	1.7	1.7	—	—	—	—	—	—	—	—	3.7	3.7	3.7
Electron ID	2.8	2.8	—	—	—	2.8	2.8	2.8	2.8	—	2.8	2.8	2.8
Luminosity	6.1	6.1	—	—	—	6.1	6.1	6.1	6.1	—	6.1	6.1	6.1
PDF	—	—	—	—	—	—	—	—	—	—	2.0	2.0	2.0
Prim. vertex	1.4	1.4	—	—	—	1.4	1.4	1.4	1.4	—	1.4	1.4	1.4
$\lambda_{HF}^W$	—	—	12.0	12.0	—	—	—	—	—	—	—	—	—
$\lambda_{HF}^Z$	—	—	—	—	—	12.0	12.0	—	—	—	—	—	—
Taggability	20.6	12.0	8.7	8.4	9.2	16.3	20.7	23.8	9.3	—	9.4	8.6	8.8
Triggers	5.0	5.0	—	—	—	5.0	5.0	5.0	5.0	—	5.0	5.0	5.0
IKS	—	—	1.8	1.8	1.8	—	—	—	—	-30.0	—	—	—
b-jet frag.	2.0	2.0	—	—	—	2.0	—	—	—	—	2.0	2.0	2.0
Color Reconnection	1.0	1.0	—	—	—	—	—	—	—	—	1.0	1.0	1.0
Lumi. rewtg.	1.0	1.0	—	—	—	1.0	1.0	1.0	1.0	—	1.0	1.0	1.0

**Table N.3** Systematic uncertainties for Run IIa Electron Channel Single-Tagged Three-Jet events.

Run IIa Electron Channel Double-Tagged Three-Jet Percentage Errors													
	$t\bar{t}l\ell$	$t\bar{t}\ell j$	$Wb\bar{b}$	$Wc\bar{c}$	$Wlp$	$Zb\bar{b}$	$Zc\bar{c}$	$Zlp$	diboson	multijet	$tb$	$tqb$	$tb + tqb$
Xsect.	9	9	—	—	—	3.3	3.3	3.3	7	—	3.8	5.3	4.8
Branching frac.	1.5	1.5	—	—	—	—	—	—	—	—	1.5	1.5	1.5
ISR/FSR	2.2	2.2	—	—	—	—	—	—	—	—	-5.9	-5.9	-5.9
Jet frag. and higher order	1.7	1.7	—	—	—	—	—	—	—	—	3.7	3.7	3.7
Electron ID	2.8	2.8	—	—	—	2.8	2.8	2.8	2.8	—	2.8	2.8	2.8
Luminosity	6.1	6.1	—	—	—	6.1	6.1	6.1	6.1	—	6.1	6.1	6.1
PDF	—	—	—	—	—	—	—	—	—	—	2.0	2.0	2.0
Prim. vertex	1.4	1.4	—	—	—	1.4	1.4	1.4	1.4	—	1.4	1.4	1.4
$\lambda_{HF}^W$	—	—	12.0	12.0	—	—	—	—	—	—	—	—	—
$\lambda_{HF}^Z$	—	—	—	—	—	12.0	12.0	—	—	—	—	—	—
Taggability	16.1	7.7	6.6	6.1	7.3	11.6	9.4	10.2	6.3	—	6.9	7.0	7.0
Triggers	5.0	5.0	—	—	—	5.0	5.0	5.0	5.0	—	5.0	5.0	5.0
IKS	—	—	1.8	1.8	1.8	—	—	—	—	-30.0	—	—	—
b-jet frag.	2.0	2.0	—	—	—	2.0	—	—	—	—	2.0	2.0	2.0
Color Reconnection	1.0	1.0	—	—	—	—	—	—	—	—	1.0	1.0	1.0
Lumi. rewtg.	1.0	1.0	—	—	—	1.0	1.0	1.0	1.0	—	1.0	1.0	1.0

**Table N.4** Systematic uncertainties for Run IIa Electron Channel Double-Tagged Three-Jet events.

	Run IIa Muon Channel Single-Tagged Two-Jet Percentage Errors												
	$t\bar{t}l\bar{l}$	$t\bar{t}l j$	$Wb\bar{b}$	$Wc\bar{c}$	$Wlp$	$Zb\bar{b}$	$Zc\bar{c}$	$Zlp$	diboson	multijet	$tb$	$tqb$	$tb + tqb$
Xsect.	9	9	—	—	—	3.3	3.3	3.3	7	—	3.8	5.3	4.8
Branching frac.	1.5	1.5	—	—	—	—	—	—	—	—	1.5	1.5	1.5
ISR/FSR	4.3	4.3	—	—	—	—	—	—	—	—	0.8	0.8	0.8
Jet frag. and higher order	1.6	1.6	—	—	—	—	—	—	—	—	0.7	0.7	0.7
Muon ID	2.1	2.1	—	—	—	2.1	2.1	2.1	2.1	—	2.1	2.1	2.1
Luminosity	6.1	6.1	—	—	—	6.1	6.1	6.1	6.1	—	6.1	6.1	6.1
PDF	—	—	—	—	—	—	—	—	—	—	2.0	2.0	2.0
Prim. vertex	1.4	1.4	—	—	—	1.4	1.4	1.4	1.4	—	1.4	1.4	1.4
$\lambda_{HF}^W$	—	—	12.0	12.0	—	—	—	—	—	—	—	—	—
$\lambda_{HF}^Z$	—	—	—	—	—	12.0	12.0	—	—	—	—	—	—
Taggability	7.5	5.3	4.9	4.6	4.8	5.7	5.4	6.0	5.2	—	5.8	4.5	4.9
Triggers	5.0	5.0	—	—	—	5.0	5.0	5.0	5.0	—	5.0	5.0	5.0
IKS	—	—	1.8	1.8	1.8	—	—	—	—	-30.0	—	—	—
b-jet frag.	2.0	2.0	—	—	—	2.0	—	—	—	—	2.0	2.0	2.0
Color Reconnection	1.0	1.0	—	—	—	—	—	—	—	—	1.0	1.0	1.0
Lumi. rewtg.	1.0	1.0	—	—	—	1.0	1.0	1.0	1.0	—	1.0	1.0	1.0

**Table N.5** Systematic uncertainties for Run IIa Muon Channel Single-Tagged Two-Jet events.

	Run IIa Muon Channel Double-Tagged Two-Jet Percentage Errors												
	$t\bar{t}l\bar{l}$	$t\bar{t}l j$	$Wb\bar{b}$	$Wc\bar{c}$	$Wlp$	$Zb\bar{b}$	$Zc\bar{c}$	$Zlp$	diboson	multijet	$tb$	$tqb$	$tb + tqb$
Xsect.	9	9	—	—	—	3.3	3.3	3.3	7	—	3.8	5.3	4.8
Branching frac.	1.5	1.5	—	—	—	—	—	—	—	—	1.5	1.5	1.5
ISR/FSR	4.3	4.3	—	—	—	—	—	—	—	—	0.8	0.8	0.8
Jet frag. and higher order	1.6	1.6	—	—	—	—	—	—	—	—	0.7	0.7	0.7
Muon ID	2.1	2.1	—	—	—	2.1	2.1	2.1	2.1	—	2.1	2.1	2.1
Luminosity	6.1	6.1	—	—	—	6.1	6.1	6.1	6.1	—	6.1	6.1	6.1
PDF	—	—	—	—	—	—	—	—	—	—	2.0	2.0	2.0
Prim. vertex	1.4	1.4	—	—	—	1.4	1.4	1.4	1.4	—	1.4	1.4	1.4
$\lambda_{HF}^W$	—	—	12.0	12.0	—	—	—	—	—	—	—	—	—
$\lambda_{HF}^Z$	—	—	—	—	—	12.0	12.0	—	—	—	—	—	—
Taggability	3.4	3.4	3.3	3.3	4.0	3.7	3.3	5.4	3.3	—	3.3	3.2	3.3
Triggers	5.0	5.0	—	—	—	5.0	5.0	5.0	5.0	—	5.0	5.0	5.0
IKS	—	—	1.8	1.8	1.8	—	—	—	—	-30.0	—	—	—
b-jet frag.	2.0	2.0	—	—	—	2.0	—	—	—	—	2.0	2.0	2.0
Color Reconnection	1.0	1.0	—	—	—	—	—	—	—	—	1.0	1.0	1.0
Lumi. rewtg.	1.0	1.0	—	—	—	1.0	1.0	1.0	1.0	—	1.0	1.0	1.0

**Table N.6** Systematic uncertainties for Run IIa Muon Channel Double-Tagged Two-Jet events.

	Run IIa Muon Channel Single-Tagged Three-Jet Percentage Errors												
	$t\bar{t}l\bar{l}$	$t\bar{t}l\bar{j}$	$Wb\bar{b}$	$Wc\bar{c}$	$Wl\bar{p}$	$Zb\bar{b}$	$Zc\bar{c}$	$Zl\bar{p}$	diboson	multijet	$tb$	$tqb$	$tb + tqb$
Xsect.	9	9	—	—	—	3.3	3.3	3.3	7	—	3.8	5.3	4.8
Branching frac.	1.5	1.5	—	—	—	—	—	—	—	—	1.5	1.5	1.5
ISR/FSR	2.2	2.2	—	—	—	—	—	—	—	—	-5.9	-5.9	-5.9
Jet frag. and higher order	1.7	1.7	—	—	—	—	—	—	—	—	3.7	3.7	3.7
Muon ID	2.1	2.1	—	—	—	2.1	2.1	2.1	2.1	—	2.1	2.1	2.1
Luminosity	6.1	6.1	—	—	—	6.1	6.1	6.1	6.1	—	6.1	6.1	6.1
PDF	—	—	—	—	—	—	—	—	—	—	2.0	2.0	2.0
Prim. vertex	1.4	1.4	—	—	—	1.4	1.4	1.4	1.4	—	1.4	1.4	1.4
$\lambda_{HF}^W$	—	—	12.0	12.0	—	—	—	—	—	—	—	—	—
$\lambda_{HF}^Z$	—	—	—	—	—	12.0	12.0	—	—	—	—	—	—
Taggability	16.8	8.6	6.9	6.7	7.0	8.0	6.1	8.6	8.7	—	8.0	6.6	7.0
Triggers	5.0	5.0	—	—	—	5.0	5.0	5.0	5.0	—	5.0	5.0	5.0
IKS	—	—	1.8	1.8	1.8	—	—	—	—	-30.0	—	—	—
b-jet frag.	2.0	2.0	—	—	—	2.0	—	—	—	—	2.0	2.0	2.0
Color Reconnection	1.0	1.0	—	—	—	—	—	—	—	—	1.0	1.0	1.0
Lumi. rewtg.	1.0	1.0	—	—	—	1.0	1.0	1.0	1.0	—	1.0	1.0	1.0

**Table N.7** Systematic uncertainties for Run IIa Muon Channel Single-Tagged Three-Jet events.

	Run IIa Muon Channel Double-Tagged Three-Jet Percentage Errors												
	$t\bar{t}l\bar{l}$	$t\bar{t}l\bar{j}$	$Wb\bar{b}$	$Wc\bar{c}$	$Wl\bar{p}$	$Zb\bar{b}$	$Zc\bar{c}$	$Zl\bar{p}$	diboson	multijet	$tb$	$tqb$	$tb + tqb$
Xsect.	9	9	—	—	—	3.3	3.3	3.3	7	—	3.8	5.3	4.8
Branching frac.	1.5	1.5	—	—	—	—	—	—	—	—	1.5	1.5	1.5
ISR/FSR	2.2	2.2	—	—	—	—	—	—	—	—	-5.9	-5.9	-5.9
Jet frag. and higher order	1.7	1.7	—	—	—	—	—	—	—	—	3.7	3.7	3.7
Muon ID	2.1	2.1	—	—	—	2.1	2.1	2.1	2.1	—	2.1	2.1	2.1
Luminosity	6.1	6.1	—	—	—	6.1	6.1	6.1	6.1	—	6.1	6.1	6.1
PDF	—	—	—	—	—	—	—	—	—	—	2.0	2.0	2.0
Prim. vertex	1.4	1.4	—	—	—	1.4	1.4	1.4	1.4	—	1.4	1.4	1.4
$\lambda_{HF}^W$	—	—	12.0	12.0	—	—	—	—	—	—	—	—	—
$\lambda_{HF}^Z$	—	—	—	—	—	12.0	12.0	—	—	—	—	—	—
Taggability	12.9	6.2	6.3	4.8	5.7	6.1	8.7	5.2	11.8	—	5.3	5.6	5.4
Triggers	5.0	5.0	—	—	—	5.0	5.0	5.0	5.0	—	5.0	5.0	5.0
IKS	—	—	1.8	1.8	1.8	—	—	—	—	-30.0	—	—	—
b-jet frag.	2.0	2.0	—	—	—	2.0	—	—	—	—	2.0	2.0	2.0
Color Reconnection	1.0	1.0	—	—	—	—	—	—	—	—	1.0	1.0	1.0
Lumi. rewtg.	1.0	1.0	—	—	—	1.0	1.0	1.0	1.0	—	1.0	1.0	1.0

**Table N.8** Systematic uncertainties for Run IIa Muon Channel Double-Tagged Three-Jet events.

	Run IIb Electron Channel Single-Tagged Two-Jet Percentage Errors												
	$t\bar{t}l\bar{l}$	$t\bar{t}l\bar{j}$	$Wb\bar{b}$	$Wc\bar{c}$	$Wlp$	$Zb\bar{b}$	$Zc\bar{c}$	$Zlp$	diboson	multijet	$tb$	$tqb$	$tb + tqb$
Xsect.	9	9	—	—	—	3.3	3.3	3.3	7	—	7.7	5.3	4.8
Branching frac.	1.5	1.5	—	—	—	—	—	—	—	—	1.5	1.5	1.5
ISR/FSR	4.3	4.3	—	—	—	—	—	—	—	—	0.8	0.8	0.8
Jet frag. and higher order	1.6	1.6	—	—	—	—	—	—	—	—	0.7	0.7	0.7
Electron ID	0.7	0.7	—	—	—	0.7	0.7	0.7	0.7	—	0.7	0.7	0.7
Luminosity	4.7	4.7	—	—	—	4.7	4.7	4.7	4.7	—	4.7	4.7	4.7
PDF	—	—	—	—	—	—	—	—	—	—	2.0	2.0	2.0
Prim. vertex	1.4	1.4	—	—	—	1.4	1.4	1.4	1.4	—	1.4	1.4	1.4
Heavy Flavor Correction	-20.0	-20.0	-20.0	-20.0	-20.0	-20.0	-20.0	-20.0	-20.0	—	-20.0	-20.0	-20.0
Taggability	2.0	2.0	2.0	2.0	2.0	2.0	2.0	2.0	2.0	—	2.0	2.0	2.0
Triggers	3.0	3.0	—	—	—	3.0	3.0	3.0	3.0	—	3.0	3.0	3.0
Matrix Method	—	—	1.5	1.5	1.5	—	—	—	—	-9.2	—	—	—
b-jet frag.	2.0	2.0	—	—	—	2.0	—	—	—	—	2.0	2.0	2.0
Color Reconnection	1.0	1.0	—	—	—	—	—	—	—	—	1.0	1.0	1.0
Lumi. rewtg.	1.0	1.0	—	—	—	1.0	1.0	1.0	1.0	—	1.0	1.0	1.0

**Table N.9** Systematic uncertainties for Run IIb Electron Channel Single-Tagged Two-Jet events.

	Run IIb Electron Channel Double-Tagged Two-Jet Percentage Errors												
	$t\bar{t}l\bar{l}$	$t\bar{t}l\bar{j}$	$Wb\bar{b}$	$Wc\bar{c}$	$Wlp$	$Zb\bar{b}$	$Zc\bar{c}$	$Zlp$	diboson	multijet	$tb$	$tqb$	$tb + tqb$
Xsect.	9	9	—	—	—	3.3	3.3	3.3	7	—	7.7	5.3	4.8
Branching frac.	1.5	1.5	—	—	—	—	—	—	—	—	1.5	1.5	1.5
ISR/FSR	4.3	4.3	—	—	—	—	—	—	—	—	0.8	0.8	0.8
Jet frag. and higher order	1.6	1.6	—	—	—	—	—	—	—	—	0.7	0.7	0.7
Electron ID	0.7	0.7	—	—	—	0.7	0.7	0.7	0.7	—	0.7	0.7	0.7
Luminosity	4.7	4.7	—	—	—	4.7	4.7	4.7	4.7	—	4.7	4.7	4.7
PDF	—	—	—	—	—	—	—	—	—	—	2.0	2.0	2.0
Prim. vertex	1.4	1.4	—	—	—	1.4	1.4	1.4	1.4	—	1.4	1.4	1.4
Heavy Flavor Correction	-20.0	-20.0	-20.0	-20.0	-20.0	-20.0	-20.0	-20.0	-20.0	—	-20.0	-20.0	-20.0
Taggability	2.0	2.0	2.0	2.0	2.0	2.0	2.0	2.0	2.0	—	2.0	2.0	2.0
Triggers	3.0	3.0	—	—	—	3.0	3.0	3.0	3.0	—	3.0	3.0	3.0
Matrix Method	—	—	1.5	1.5	1.5	—	—	—	—	-9.2	—	—	—
b-jet frag.	2.0	2.0	—	—	—	2.0	—	—	—	—	2.0	2.0	2.0
Color Reconnection	1.0	1.0	—	—	—	—	—	—	—	—	1.0	1.0	1.0
Lumi. rewtg.	1.0	1.0	—	—	—	1.0	1.0	1.0	1.0	—	1.0	1.0	1.0

**Table N.10** Systematic uncertainties for Run IIb Electron Channel Double-Tagged Two-Jet events.

	Run IIb Electron Channel Single-Tagged Three-Jet Percentage Errors												
	$t\bar{t}l\bar{l}$	$t\bar{t}l\bar{j}$	$Wb\bar{b}$	$Wc\bar{c}$	$Wlp$	$Zb\bar{b}$	$Zc\bar{c}$	$Zlp$	diboson	multijet	$tb$	$tqb$	$tb + tqb$
Xsect.	9	9	—	—	—	3.3	3.3	3.3	7	—	7.7	5.3	4.8
Branching frac.	1.5	1.5	—	—	—	—	—	—	—	—	1.5	1.5	1.5
ISR/FSR	2.2	2.2	—	—	—	—	—	—	—	—	-5.9	-5.9	-5.9
Jet frag. and higher order	1.7	1.7	—	—	—	—	—	—	—	—	3.7	3.7	3.7
Electron ID	0.7	0.7	—	—	—	0.7	0.7	0.7	0.7	—	0.7	0.7	0.7
Luminosity	4.7	4.7	—	—	—	4.7	4.7	4.7	4.7	—	4.7	4.7	4.7
PDF	—	—	—	—	—	—	—	—	—	—	2.0	2.0	2.0
Prim. vertex	1.4	1.4	—	—	—	1.4	1.4	1.4	1.4	—	1.4	1.4	1.4
Heavy Flavor Correction	-20.0	-20.0	-20.0	-20.0	-20.0	-20.0	-20.0	-20.0	-20.0	—	-20.0	-20.0	-20.0
Taggability	2.0	2.0	2.0	2.0	2.0	2.0	2.0	2.0	2.0	—	2.0	2.0	2.0
Triggers	3.0	3.0	—	—	—	3.0	3.0	3.0	3.0	—	3.0	3.0	3.0
Matrix Method	—	—	2.5	2.5	2.5	—	—	—	—	-9.5	—	—	—
b-jet frag.	2.0	2.0	—	—	—	2.0	—	—	—	—	2.0	2.0	2.0
Color Reconnection	1.0	1.0	—	—	—	—	—	—	—	—	1.0	1.0	1.0
Lumi. rewtg.	1.0	1.0	—	—	—	1.0	1.0	1.0	1.0	—	1.0	1.0	1.0

**Table N.11** Systematic uncertainties for Run IIb Electron Channel Single-Tagged Three-Jet events.

	Run IIb Electron Channel Double-Tagged Three-Jet Percentage Errors												
	$t\bar{t}l\bar{l}$	$t\bar{t}l\bar{j}$	$Wb\bar{b}$	$Wc\bar{c}$	$Wlp$	$Zb\bar{b}$	$Zc\bar{c}$	$Zlp$	diboson	multijet	$tb$	$tqb$	$tb + tqb$
Xsect.	9	9	—	—	—	3.3	3.3	3.3	7	—	7.7	5.3	4.8
Branching frac.	1.5	1.5	—	—	—	—	—	—	—	—	1.5	1.5	1.5
ISR/FSR	2.2	2.2	—	—	—	—	—	—	—	—	-5.9	-5.9	-5.9
Jet frag. and higher order	1.7	1.7	—	—	—	—	—	—	—	—	3.7	3.7	3.7
Electron ID	0.7	0.7	—	—	—	0.7	0.7	0.7	0.7	—	0.7	0.7	0.7
Luminosity	4.7	4.7	—	—	—	4.7	4.7	4.7	4.7	—	4.7	4.7	4.7
PDF	—	—	—	—	—	—	—	—	—	—	2.0	2.0	2.0
Prim. vertex	1.4	1.4	—	—	—	1.4	1.4	1.4	1.4	—	1.4	1.4	1.4
Heavy Flavor Correction	-20.0	-20.0	-20.0	-20.0	-20.0	-20.0	-20.0	-20.0	-20.0	—	-20.0	-20.0	-20.0
Taggability	2.0	2.0	2.0	2.0	2.0	2.0	2.0	2.0	2.0	—	2.0	2.0	2.0
Triggers	3.0	3.0	—	—	—	3.0	3.0	3.0	3.0	—	3.0	3.0	3.0
Matrix Method	—	—	2.5	2.5	2.5	—	—	—	—	-9.5	—	—	—
b-jet frag.	2.0	2.0	—	—	—	2.0	—	—	—	—	2.0	2.0	2.0
Color Reconnection	1.0	1.0	—	—	—	—	—	—	—	—	1.0	1.0	1.0
Lumi. rewtg.	1.0	1.0	—	—	—	1.0	1.0	1.0	1.0	—	1.0	1.0	1.0

**Table N.12** Systematic uncertainties for Run IIb Electron Channel Double-Tagged Three-Jet events.

	Run IIb Muon Channel Single-Tagged Two-Jet Percentage Errors												
	$t\bar{t}\ell\ell$	$t\bar{t}\ell j$	$Wb\bar{b}$	$Wc\bar{c}$	$Wlp$	$Zb\bar{b}$	$Zc\bar{c}$	$Zlp$	diboson	multijet	$t\bar{b}$	$t\bar{q}b$	$t\bar{b} + t\bar{q}b$
Xsect.	9	9	—	—	—	3.3	3.3	3.3	7	—	7.7	5.3	4.8
Branching frac.	1.5	1.5	—	—	—	—	—	—	—	—	1.5	1.5	1.5
ISR/FSR	4.3	4.3	—	—	—	—	—	—	—	—	0.8	0.8	0.8
Jet frag. and higher order	1.6	1.6	—	—	—	—	—	—	—	—	0.7	0.7	0.7
Muon ID	1.7	1.7	—	—	—	1.7	1.7	1.7	1.7	—	1.7	1.7	1.7
Luminosity	4.7	4.7	—	—	—	4.7	4.7	4.7	4.7	—	4.7	4.7	4.7
PDF	—	—	—	—	—	—	—	—	—	—	2.0	2.0	2.0
Prim. vertex	1.4	1.4	—	—	—	1.4	1.4	1.4	1.4	—	1.4	1.4	1.4
Heavy Flavor Correction	-20.0	-20.0	-20.0	-20.0	-20.0	-20.0	-20.0	-20.0	-20.0	—	-20.0	-20.0	-20.0
Taggability	2.0	2.0	2.0	2.0	2.0	2.0	2.0	2.0	2.0	—	2.0	2.0	2.0
Triggers	5.0	5.0	—	—	—	5.0	5.0	5.0	5.0	—	5.0	5.0	5.0
Matrix Method	—	—	1.1	1.1	1.1	—	—	—	—	-42.1	—	—	—
b-jet frag.	2.0	2.0	—	—	—	2.0	—	—	—	—	2.0	2.0	2.0
Color Reconnection	1.0	1.0	—	—	—	—	—	—	—	—	1.0	1.0	1.0
Lumi. rewtg.	1.0	1.0	—	—	—	1.0	1.0	1.0	1.0	—	1.0	1.0	1.0

**Table N.13** Systematic uncertainties for Run IIb Muon Channel Single-Tagged Two-Jet events.

	Run IIb Muon Channel Double-Tagged Two-Jet Percentage Errors												
	$t\bar{t}\ell\ell$	$t\bar{t}\ell j$	$Wb\bar{b}$	$Wc\bar{c}$	$Wlp$	$Zb\bar{b}$	$Zc\bar{c}$	$Zlp$	diboson	multijet	$t\bar{b}$	$t\bar{q}b$	$t\bar{b} + t\bar{q}b$
Xsect.	9	9	—	—	—	3.3	3.3	3.3	7	—	7.7	5.3	4.8
Branching frac.	1.5	1.5	—	—	—	—	—	—	—	—	1.5	1.5	1.5
ISR/FSR	4.3	4.3	—	—	—	—	—	—	—	—	0.8	0.8	0.8
Jet frag. and higher order	1.6	1.6	—	—	—	—	—	—	—	—	0.7	0.7	0.7
Muon ID	1.7	1.7	—	—	—	1.7	1.7	1.7	1.7	—	1.7	1.7	1.7
Luminosity	4.7	4.7	—	—	—	4.7	4.7	4.7	4.7	—	4.7	4.7	4.7
PDF	—	—	—	—	—	—	—	—	—	—	2.0	2.0	2.0
Prim. vertex	1.4	1.4	—	—	—	1.4	1.4	1.4	1.4	—	1.4	1.4	1.4
Heavy Flavor Correction	-20.0	-20.0	-20.0	-20.0	-20.0	-20.0	-20.0	-20.0	-20.0	—	-20.0	-20.0	-20.0
Taggability	2.0	2.0	2.0	2.0	2.0	2.0	2.0	2.0	2.0	—	2.0	2.0	2.0
Triggers	5.0	5.0	—	—	—	5.0	5.0	5.0	5.0	—	5.0	5.0	5.0
Matrix Method	—	—	1.1	1.1	1.1	—	—	—	—	-42.1	—	—	—
b-jet frag.	2.0	2.0	—	—	—	2.0	—	—	—	—	2.0	2.0	2.0
Color Reconnection	1.0	1.0	—	—	—	—	—	—	—	—	1.0	1.0	1.0
Lumi. rewtg.	1.0	1.0	—	—	—	1.0	1.0	1.0	1.0	—	1.0	1.0	1.0

**Table N.14** Systematic uncertainties for Run IIb Muon Channel Double-Tagged Two-Jet events.

	Run IIb Muon Channel Single-Tagged Three-Jet Percentage Errors												
	$t\bar{t}l\bar{l}$	$t\bar{t}l j$	$Wb\bar{b}$	$Wc\bar{c}$	$Wlp$	$Zb\bar{b}$	$Zc\bar{c}$	$Zlp$	diboson	multijet	$tb$	$tqb$	$tb + tqb$
Xsect.	9	9	—	—	—	3.3	3.3	3.3	7	—	7.7	5.3	4.8
Branching frac.	1.5	1.5	—	—	—	—	—	—	—	—	1.5	1.5	1.5
ISR/FSR	2.2	2.2	—	—	—	—	—	—	—	—	-5.9	-5.9	-5.9
Jet frag. and higher order	1.7	1.7	—	—	—	—	—	—	—	—	3.7	3.7	3.7
Muon ID	1.7	1.7	—	—	—	1.7	1.7	1.7	1.7	—	1.7	1.7	1.7
Luminosity	4.7	4.7	—	—	—	4.7	4.7	4.7	4.7	—	4.7	4.7	4.7
PDF	—	—	—	—	—	—	—	—	—	—	2.0	2.0	2.0
Prim. vertex	1.4	1.4	—	—	—	1.4	1.4	1.4	1.4	—	1.4	1.4	1.4
Heavy Flavor Correction	-20.0	-20.0	-20.0	-20.0	-20.0	-20.0	-20.0	-20.0	-20.0	—	-20.0	-20.0	-20.0
Taggability	2.0	2.0	2.0	2.0	2.0	2.0	2.0	2.0	2.0	—	2.0	2.0	2.0
Triggers	5.0	5.0	—	—	—	5.0	5.0	5.0	5.0	—	5.0	5.0	5.0
Matrix Method	—	—	2.2	2.2	2.2	—	—	—	—	-40.0	—	—	—
b-jet frag.	2.0	2.0	—	—	—	2.0	—	—	—	—	2.0	2.0	2.0
Color Reconnection	1.0	1.0	—	—	—	—	—	—	—	—	1.0	1.0	1.0
Lumi. rewtg.	1.0	1.0	—	—	—	1.0	1.0	1.0	1.0	—	1.0	1.0	1.0

**Table N.15** Systematic uncertainties for Run IIb Muon Channel Single-Tagged Three-Jet events.

	Run IIb Muon Channel Double-Tagged Three-Jet Percentage Errors												
	$t\bar{t}l\bar{l}$	$t\bar{t}l j$	$Wb\bar{b}$	$Wc\bar{c}$	$Wlp$	$Zb\bar{b}$	$Zc\bar{c}$	$Zlp$	diboson	multijet	$tb$	$tqb$	$tb + tqb$
Xsect.	9	9	—	—	—	3.3	3.3	3.3	7	—	7.7	5.3	4.8
Branching frac.	1.5	1.5	—	—	—	—	—	—	—	—	1.5	1.5	1.5
ISR/FSR	2.2	2.2	—	—	—	—	—	—	—	—	-5.9	-5.9	-5.9
Jet frag. and higher order	1.7	1.7	—	—	—	—	—	—	—	—	3.7	3.7	3.7
Muon ID	1.7	1.7	—	—	—	1.7	1.7	1.7	1.7	—	1.7	1.7	1.7
Luminosity	4.7	4.7	—	—	—	4.7	4.7	4.7	4.7	—	4.7	4.7	4.7
PDF	—	—	—	—	—	—	—	—	—	—	2.0	2.0	2.0
Prim. vertex	1.4	1.4	—	—	—	1.4	1.4	1.4	1.4	—	1.4	1.4	1.4
Heavy Flavor Correction	-20.0	-20.0	-20.0	-20.0	-20.0	-20.0	-20.0	-20.0	-20.0	—	-20.0	-20.0	-20.0
Taggability	2.0	2.0	2.0	2.0	2.0	2.0	2.0	2.0	2.0	—	2.0	2.0	2.0
Triggers	5.0	5.0	—	—	—	5.0	5.0	5.0	5.0	—	5.0	5.0	5.0
Matrix Method	—	—	2.2	2.2	2.2	—	—	—	—	-40.0	—	—	—
b-jet frag.	2.0	2.0	—	—	—	2.0	—	—	—	—	2.0	2.0	2.0
Color Reconnection	1.0	1.0	—	—	—	—	—	—	—	—	1.0	1.0	1.0
Lumi. rewtg.	1.0	1.0	—	—	—	1.0	1.0	1.0	1.0	—	1.0	1.0	1.0

**Table N.16** Systematic uncertainties for Run IIb Muon Channel Double-Tagged Three-Jet events.

## O Shape-Changing Systematic Uncertainties

The shape-changing systematic uncertainties affect both the normalization and shape of the discriminant distributions. In this analysis, the uncertainties on the jet energy scale (JES), jet energy resolution (JER), jet identification (JETID), jet vertex confirmation (VC), flavor-dependent jet energy scale (SDC),  $V$ +jets angular corrections (AC), and  $b$ -tagging scale factors (BTag) fall into this category. On one hand, the corrections applied in the *cafe* analysis chain, including JES, JER, JETID, and SDC, can influence both the event kinematics and the event weights. On the other hand, the corrections which are applied after the *cafe* analysis chain can only change the event weights, i.e. VC, AC, and BTag.

The changes on the normalization component of these systematic uncertainties are listed in Table O.1, and the changes on the discriminant shapes are shown in Figure O.1 to Figure O.16. The discriminant is detailed in Chapter 6.

Normalization Uncertainties									
		Run IIa, 1 fb <sup>-1</sup>				Run IIb, 8.7 fb <sup>-1</sup>			
		1-tag		2-tags		1-tag		2-tags	
		2 jets	3 jets	2 jets	3 jets	2 jets	3 jets	2 jets	3 jets
<b>JES</b>	Signal ( <i>e</i> )	2.8 %	4.4 %	3.9 %	1.5 %	0.4 %	4.0 %	0.1 %	3.0 %
	Bkgd. ( <i>e</i> )	3.7 %	5.8 %	7.0 %	4.7 %	0.6 %	0.4 %	1.2 %	0.5 %
	Signal ( $\mu$ )	6.8 %	6.7 %	7.9 %	3.6 %	< 0.1 %	3.7 %	0.2 %	2.4 %
	Bkgd. ( $\mu$ )	1.8 %	4.1 %	6.2 %	5.1 %	0.7 %	0.9 %	1.2 %	1.1 %
<b>JER</b>	Signal ( <i>e</i> )	4.9 %	1.1 %	10.8 %	5.5 %	0.3 %	1.1 %	0.5 %	0.6 %
	Bkgd. ( <i>e</i> )	5.5 %	9.4 %	11.2 %	10.7 %	0.6 %	0.3 %	0.9 %	0.5 %
	Signal ( $\mu$ )	6.2 %	2.3 %	7.1 %	3.4 %	0.4 %	0.8 %	0.8 %	0.6 %
	Bkgd. ( $\mu$ )	4.2 %	6.9 %	7.9 %	7.0 %	0.8 %	0.6 %	1.0 %	0.6 %
<b>JETID</b>	Signal ( <i>e</i> )	0.6 %	0.6 %	0.9 %	2.1 %	0.7 %	1.3 %	0.7 %	1.3 %
	Bkgd. ( <i>e</i> )	0.8 %	1.4 %	2.2 %	1.1 %	0.2 %	< 0.1 %	< 0.1 %	0.3 %
	Signal ( $\mu$ )	4.5 %	3.3 %	4.8 %	2.9 %	0.8 %	1.3 %	0.7 %	1.4 %
	Bkgd. ( $\mu$ )	0.8 %	1.1 %	0.7 %	0.2 %	0.1 %	0.1 %	< 0.1 %	< 0.1 %
<b>SDC</b>	Signal ( <i>e</i> )	0.5 %	0.8 %	0.5 %	0.8 %	0.1 %	1.3 %	0.3 %	1.2 %
	Bkgd. ( <i>e</i> )	< 0.1 %	< 0.1 %	< 0.1 %	< 0.1 %	0.2 %	< 0.1 %	0.6 %	0.3 %
	Signal ( $\mu$ )	0.5 %	0.8 %	0.5 %	0.8 %	0.1 %	1.2 %	0.2 %	1.3 %
	Bkgd. ( $\mu$ )	< 0.1 %	< 0.1 %	< 0.1 %	< 0.1 %	0.3 %	0.1 %	0.7 %	0.3 %
<b>VC</b>	Signal ( <i>e</i> )	< 0.1 %	< 0.1 %	< 0.1 %	< 0.1 %	4.8 %	4.5 %	9.5 %	9.1 %
	Bkgd. ( <i>e</i> )	< 0.1 %	< 0.1 %	< 0.1 %	< 0.1 %	5.2 %	4.8 %	7.5 %	9.4 %
	Signal ( $\mu$ )	< 0.1 %	< 0.1 %	< 0.1 %	< 0.1 %	5.1 %	4.6 %	10.5 %	10.2 %
	Bkgd. ( $\mu$ )	< 0.1 %	< 0.1 %	< 0.1 %	< 0.1 %	6.6 %	5.8 %	8.6 %	10.5 %
<b>AC</b>	Signal ( <i>e</i> )	< 0.1 %	< 0.1 %	< 0.1 %	< 0.1 %	< 0.1 %	< 0.1 %	< 0.1 %	< 0.1 %
	Bkgd. ( <i>e</i> )	0.2 %	0.2 %	0.2 %	0.2 %	< 0.1 %	0.1 %	< 0.1 %	< 0.1 %
	Signal ( $\mu$ )	< 0.1 %	< 0.1 %	< 0.1 %	< 0.1 %	< 0.1 %	< 0.1 %	< 0.1 %	< 0.1 %
	Bkgd. ( $\mu$ )	0.3 %	0.1 %	0.3 %	0.3 %	< 0.1 %	0.2 %	< 0.1 %	0.1 %
<b>BTag</b>	Signal ( <i>e</i> )	7.1 %	10.1 %	8.2 %	8.7 %	2.0 %	0.9 %	8.8 %	7.6 %
	Bkgd. ( <i>e</i> )	5.0 %	7.8 %	7.0 %	9.5 %	5.5 %	3.1 %	7.4 %	7.3 %
	Signal ( $\mu$ )	6.6 %	9.5 %	8.2 %	8.5 %	2.0 %	1.0 %	8.7 %	7.6 %
	Bkgd. ( $\mu$ )	4.9 %	7.5 %	6.6 %	8.9 %	6.6 %	3.9 %	7.5 %	7.4 %

**Table O.1** The yield differences on the shape-changing systematic uncertainties on the signals and the combined backgrounds.

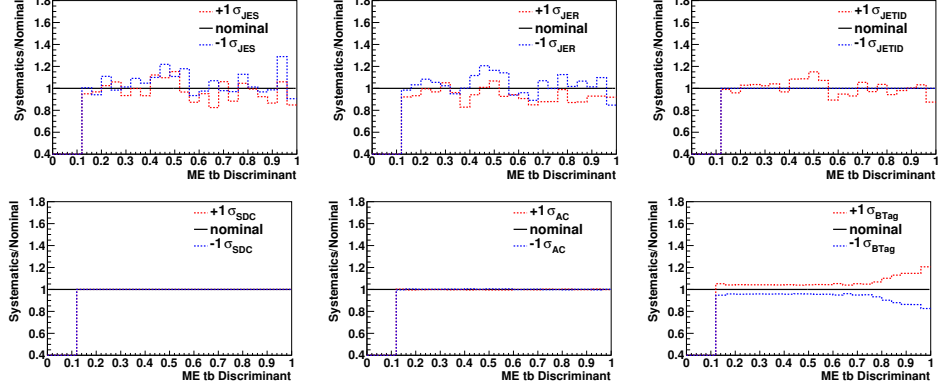


**Figure O.1** The effects of the shape-changing systematic uncertainties on the ME  $tb$  discriminant for Run IIa e+jets two-jet single-tagged sample. The  $y$ -axis shows the ratio of the systematic shifted sample to the nominal sample. For the JETID uncertainty, we take the upward-shifted variation and symmetrize it when measuring the cross section.

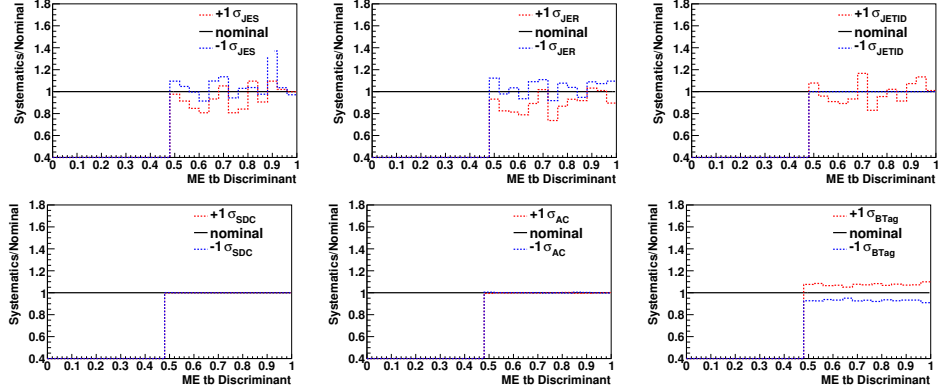


**Figure O.2** The effects of the shape-changing systematic uncertainties on the ME  $tb$  discriminant for Run IIa e+jets two-jet double-tagged sample. The  $y$ -axis shows the ratio of the systematic shifted sample to the nominal sample. For the JETID uncertainty, we take the upward-shifted variation and symmetrize it when measuring the cross section.

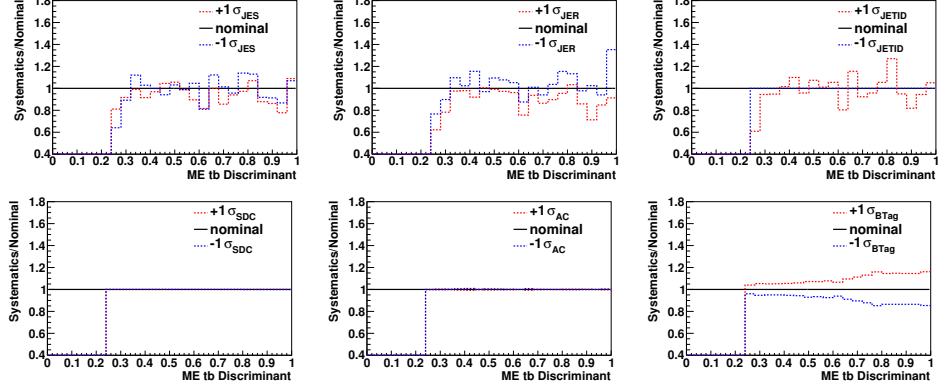


**Figure O.3** The effects of the shape-changing systematic uncertainties on the ME  $tb$  discriminant for Run IIa  $e$ +jets three-jet single-tagged sample. The  $y$ -axis shows the ratio of the systematic shifted sample to the nominal sample. For the JETID uncertainty, we take the upward-shifted variation and symmetrize it when measuring the cross section.

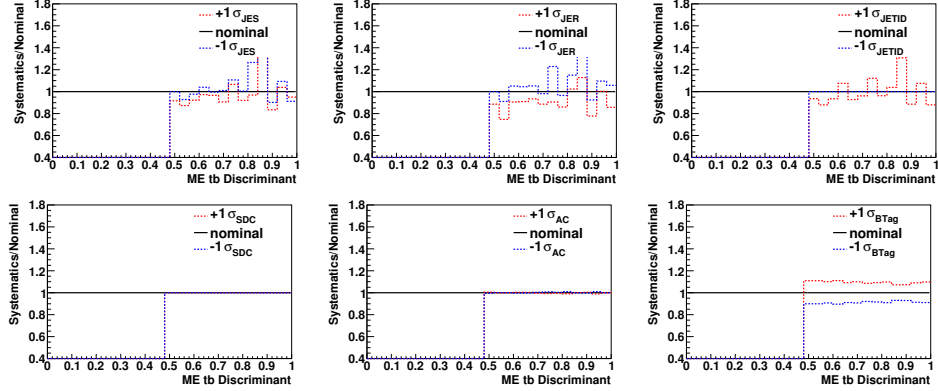


**Figure O.4** The effects of the shape-changing systematic uncertainties on the ME  $tb$  discriminant for Run IIa  $e$ +jets three-jet double-tagged sample. The  $y$ -axis shows the ratio of the systematic shifted sample to the nominal sample. For the JETID uncertainty, we take the upward-shifted variation and symmetrize it when measuring the cross section.

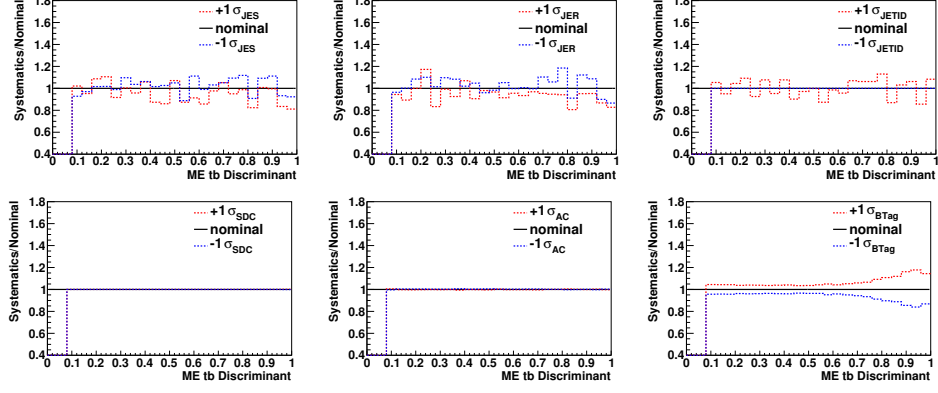


**Figure O.5** The effects of the shape-changing systematic uncertainties on the ME  $tb$  discriminant for Run IIa  $\mu$ +jets two-jet single-tagged sample. The  $y$ -axis shows the ratio of the systematic shifted sample to the nominal sample. For the JETID uncertainty, we take the upward-shifted variation and symmetrize it when measuring the cross section.

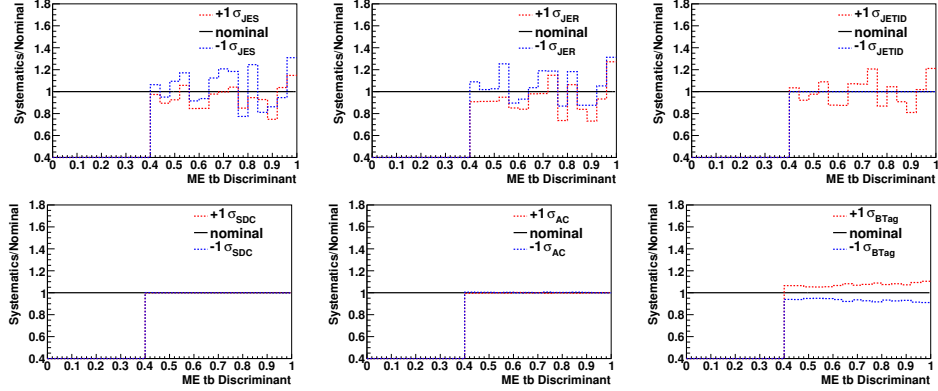


**Figure O.6** The effects of the shape-changing systematic uncertainties on the ME  $tb$  discriminant for Run IIa  $\mu$ +jets two-jet double-tagged sample. The  $y$ -axis shows the ratio of the systematic shifted sample to the nominal sample. For the JETID uncertainty, we take the upward-shifted variation and symmetrize it when measuring the cross section.

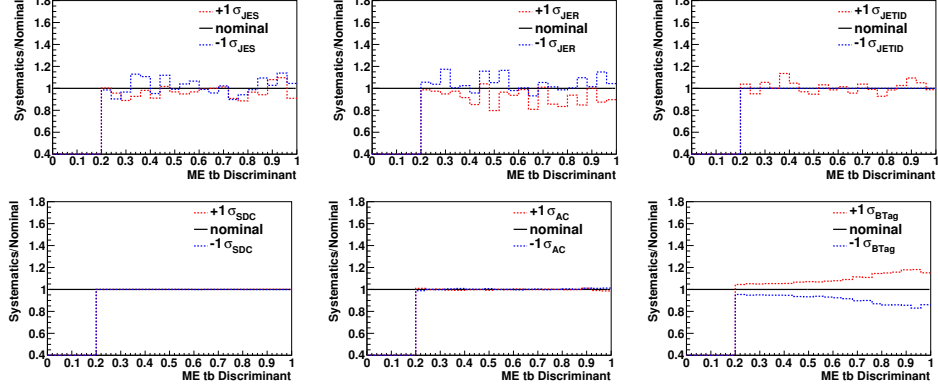


**Figure O.7** The effects of the shape-changing systematic uncertainties on the ME  $t\bar{b}$  discriminant for Run IIa  $\mu$ +jets three-jet single-tagged sample. The  $y$ -axis shows the ratio of the systematic shifted sample to the nominal sample. For the JETID uncertainty, we take the upward-shifted variation and symmetrize it when measuring the cross section.

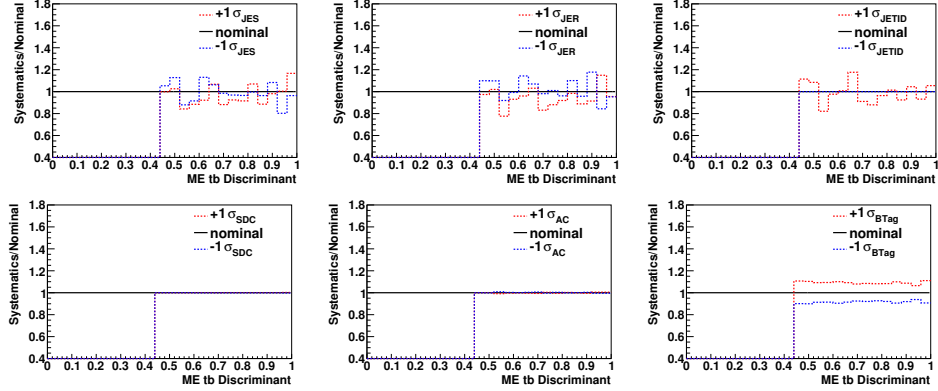


**Figure O.8** The effects of the shape-changing systematic uncertainties on the ME  $t\bar{b}$  discriminant for Run IIa  $\mu$ +jets three-jet double-tagged sample. The  $y$ -axis shows the ratio of the systematic shifted sample to the nominal sample. For the JETID uncertainty, we take the upward-shifted variation and symmetrize it when measuring the cross section.

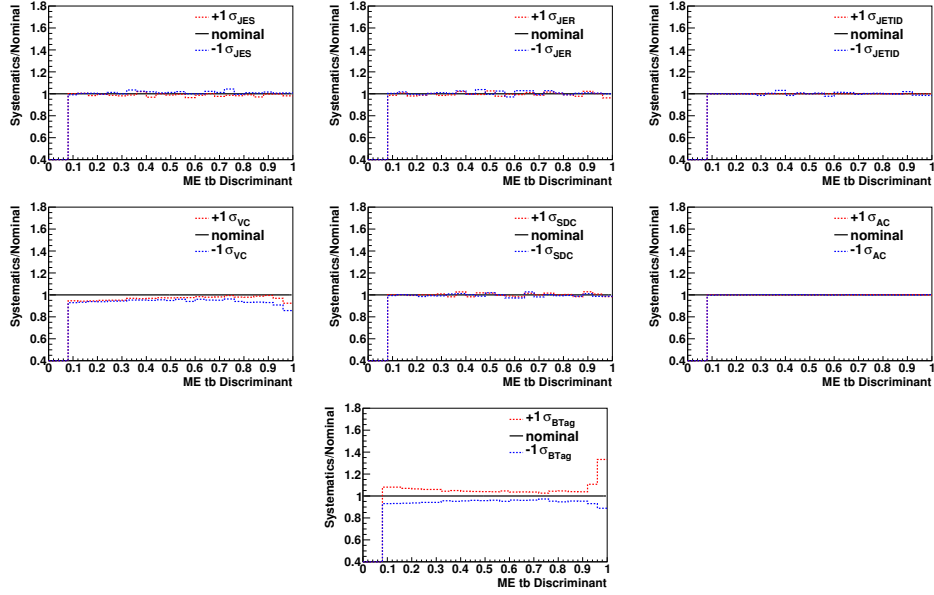


**Figure O.9** The effects of the shape-changing systematic uncertainties on the ME  $tb$  discriminant for Run IIb  $e$ +jets two-jet single-tagged sample. The  $y$ -axis shows the ratio of the systematic shifted sample to the nominal sample. For the JETID uncertainty, we take the downward-shifted variation and symmetrize it when measuring the cross section.

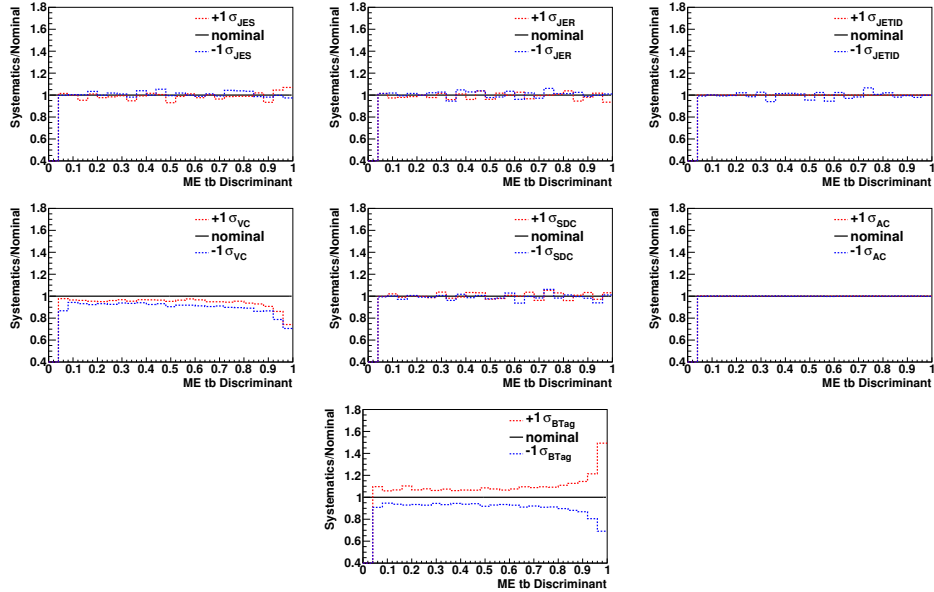


**Figure O.10** The effects of the shape-changing systematic uncertainties on the ME  $tb$  discriminant for Run IIb  $e$ +jets two-jet double-tagged sample. The  $y$ -axis shows the ratio of the systematic shifted sample to the nominal sample. For the JETID uncertainty, we take the downward-shifted variation and symmetrize it when measuring the cross section.

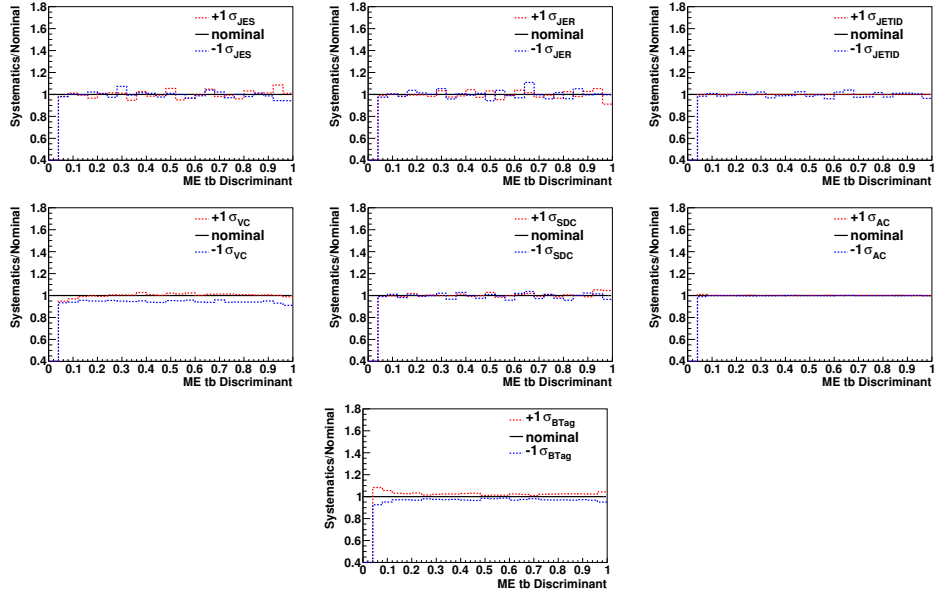


**Figure O.11** The effects of the shape-changing systematic uncertainties on the ME  $tb$  discriminant for Run IIb  $e$ +jets three-jet single-tagged sample. The  $y$ -axis shows the ratio of the systematic shifted sample to the nominal sample. For the JETID uncertainty, we take the downward-shifted variation and symmetrize it when measuring the cross section.

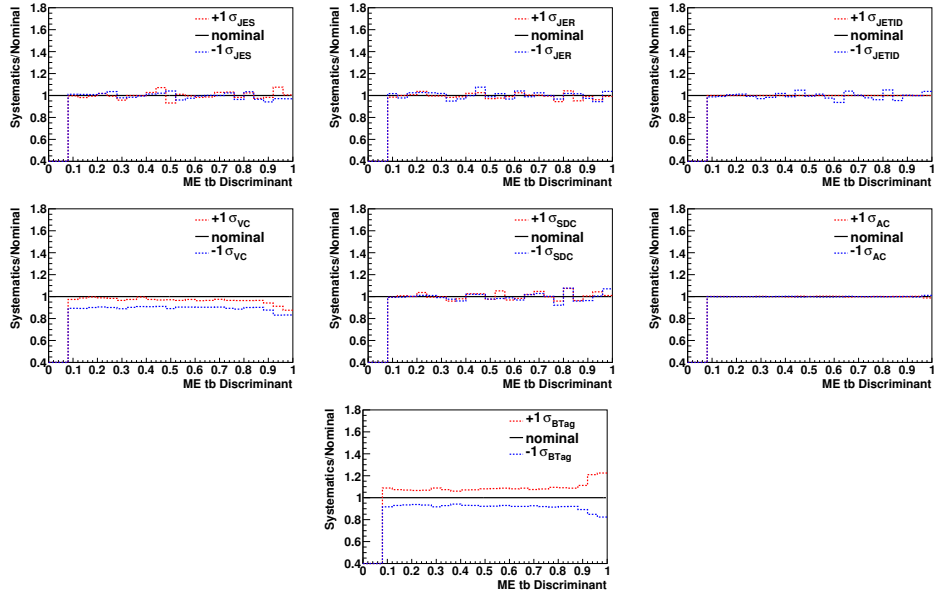


**Figure O.12** The effects of the shape-changing systematic uncertainties on the ME  $tb$  discriminant for Run IIb  $e^+ \text{jets}$  three-jet double-tagged sample. The  $y$ -axis shows the ratio of the systematic shifted sample to the nominal sample. For the JETID uncertainty, we take the downward-shifted variation and symmetrize it when measuring the cross section.

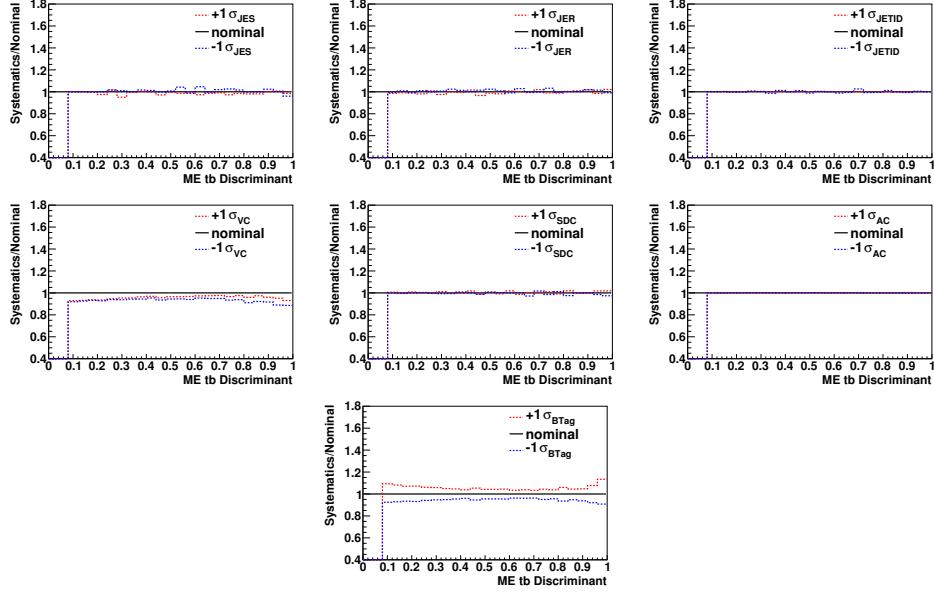


**Figure O.13** The effects of the shape-changing systematic uncertainties on the ME  $tb$  discriminant for Run IIB  $\mu$ +jets two-jet single-tagged sample. The  $y$ -axis shows the ratio of the systematic shifted sample to the nominal sample. For the JETID uncertainty, we take the downward-shifted variation and symmetrize it when measuring the cross section.

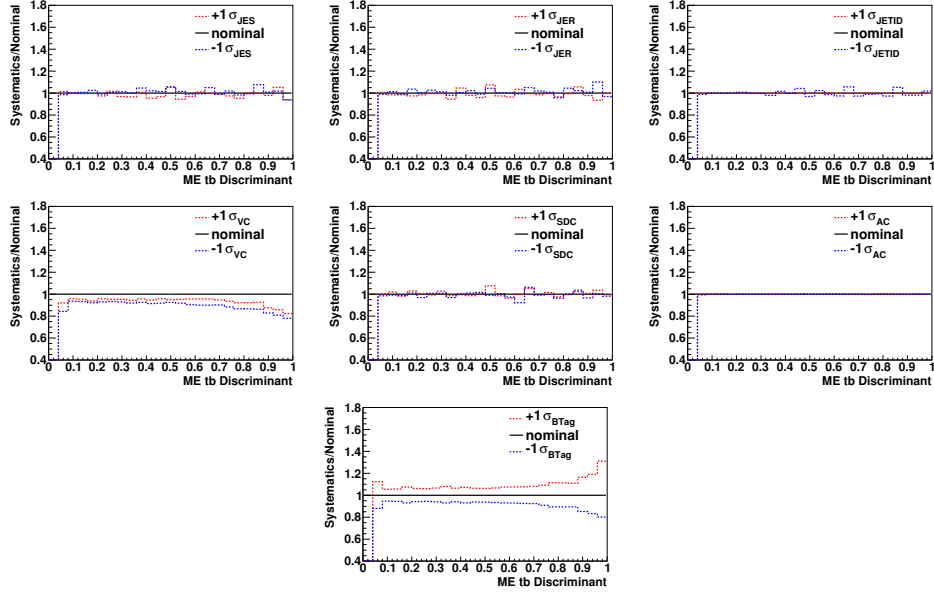


**Figure O.14** The effects of the shape-changing systematic uncertainties on the ME  $tb$  discriminant for Run IIB  $\mu$ +jets two-jet double-tagged sample. The  $y$ -axis shows the ratio of the systematic shifted sample to the nominal sample. For the JETID uncertainty, we take the downward-shifted variation and symmetrize it when measuring the cross section.

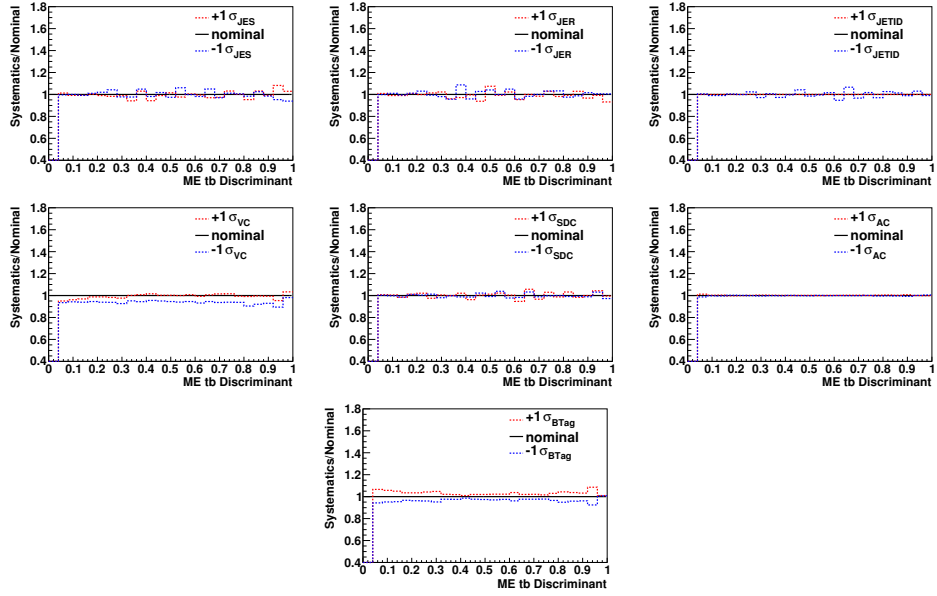


**Figure O.15** The effects of the shape-changing systematic uncertainties on the ME  $tb$  discriminant for Run IIb  $\mu$ +jets three-jet single-tagged sample. The  $y$ -axis shows the ratio of the systematic shifted sample to the nominal sample. For the JETID uncertainty, we take the downward-shifted variation and symmetrize it when measuring the cross section.

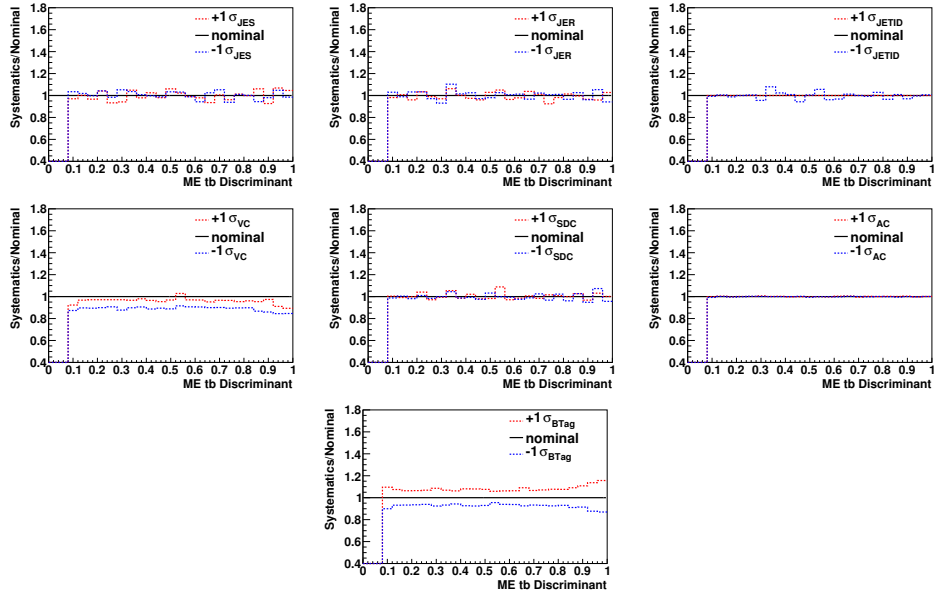


**Figure O.16** The effects of the shape-changing systematic uncertainties on the ME  $tb$  discriminant for Run IIb  $\mu$ +jets three-jet double-tagged sample. The  $y$ -axis shows the ratio of the systematic shifted sample to the nominal sample. For the JETID uncertainty, we take the downward-shifted variation and symmetrize it when measuring the cross section.